

Cover Page



Universiteit Leiden

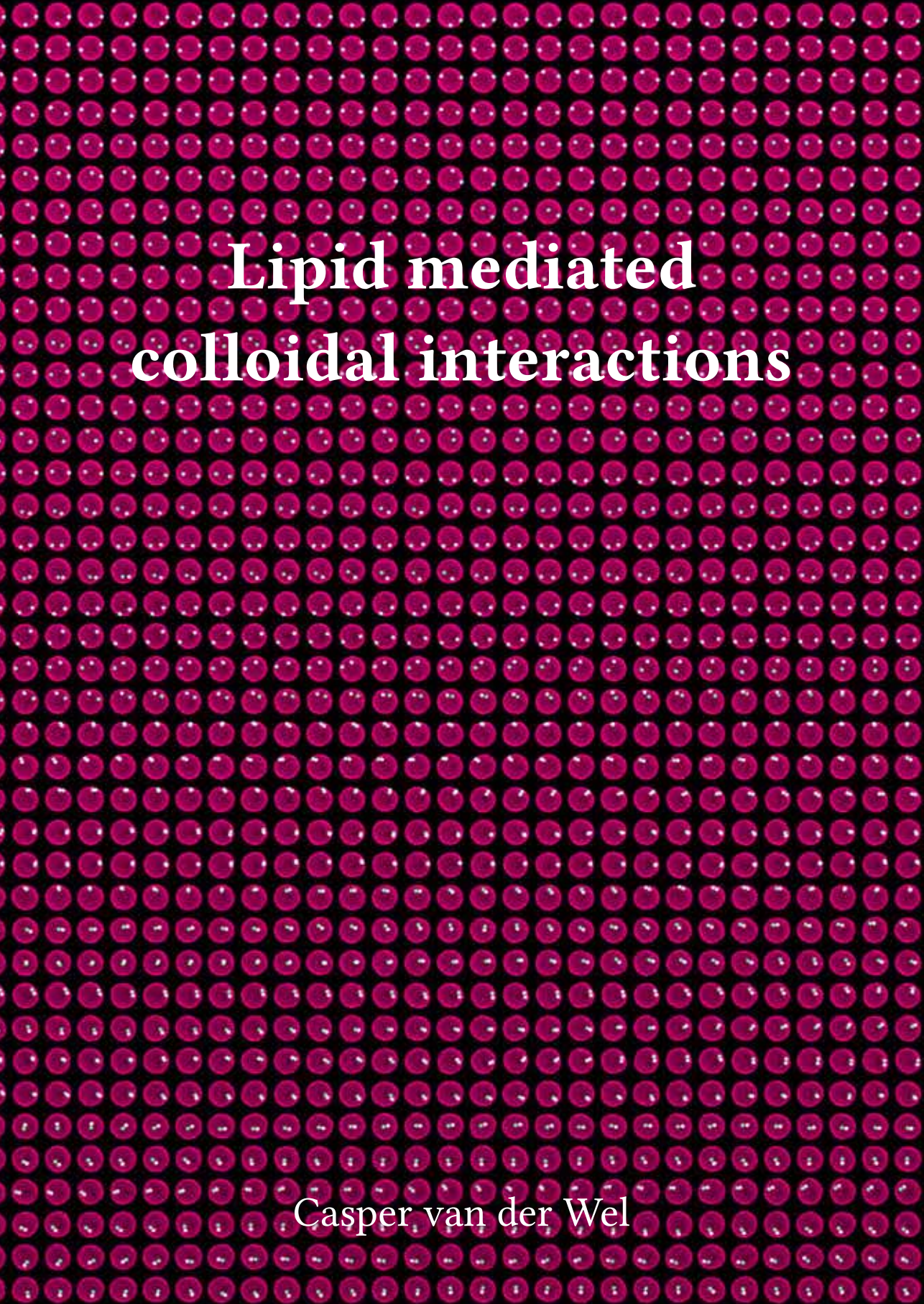


The handle <http://hdl.handle.net/1887/56250> holds various files of this Leiden University dissertation

Author: Wel, Casper van der

Title: Lipid mediated colloidal interactions

Date: 2017-10-05

The background of the slide is a repeating pattern of lipid bilayers. Each bilayer is represented by two rows of purple circles, with a white dot in the center of each circle, symbolizing the hydrophilic and hydrophobic parts of the lipid molecules respectively. The bilayers are arranged in a grid, creating a textured, grid-like appearance.

Lipid mediated colloidal interactions

Casper van der Wel

Lipid mediated colloidal interactions

Proefschrift

ter verkrijging van
de graad van Doctor aan de Universiteit Leiden,
op gezag van Rector Magnificus prof. mr. C.J.J.M. Stolker,
volgens besluit van het College voor Promoties
te verdedigen op donderdag 5 oktober 2017
klokke 16:15 uur


door

Casper Michiel van der Wel
geboren te Hilversum in 1988

Promotor: Prof. dr. T. Schmidt
Co-promotores: Dr. D.J. Kraft
Dr. D. Heinrich

Promotiecommissie: Dr. T. Idema (*Technische Universiteit Delft*)
Prof. dr. W.K. Kegel (*Universiteit Utrecht*)
Prof. dr. A.M. Dogterom
Prof. dr. E.R. Eliel
Prof. dr. M.A.G.J. Orrit
Dr. S. Semrau

Casimir PhD series, Delft-Leiden, 2017-27
ISBN 978-90-8593-311-3

 This thesis is licensed under the open source CC-BY-SA 4.0 license, excluding Figures 1.2, 1.3, and 1.5, and Chapters 2, 4, 6, and 7. An electronic version of this thesis can be found at openaccess.leidenuniv.nl. Supporting videos are accessible at goo.gl/KqUeIa or via QR codes printed in the margin.

The work described in this thesis was supported by the Netherlands Organisation for Scientific Research (NWO/OCW), as part of the Frontiers of Nanoscience (NanoFront) program.

The cover shows a time sequence of two particles (in green) wrapped by a vesicle (in magenta). The overlap of green and magenta gives a white colour, which confirms that the particles are wrapped by the membrane. The magnification is 618 times: if this thesis were 0.3 mm wide, the images would be approximately at the correct scale. The time difference between two images is 0.2 s horizontally and 14.4 s vertically.

Contents

1	Introduction	1
1.1	Lipid membranes: a biological view	2
1.2	Lipid membranes: a physical view	4
1.3	Lipids in self-assembly	6
I	Methods of single particle tracking	9
2	Tracking of colloidal clusters with sub-pixel accuracy and precision	11
2.1	Introduction	12
2.2	Methods	13
2.3	Results and Discussion	19
2.4	Conclusion	27
2.5	Supporting Figures	31
3	Force measurement from sparse trajectories in curved geometries	31
3.1	Introduction	32
3.2	Methods	32
3.3	Position-based force measurement	33
3.4	Displacement-based force measurement	36
3.5	Estimating forces in curved geometries	41
3.6	Summary and Conclusion	44
3.7	Appendices	46
II	Membrane mediated interactions	49
4	Surfactant-free colloidal particles with specific binding affinity	51
4.1	Introduction	52
4.2	Methods	53
4.3	Results and Discussion	58
4.4	Conclusion	66

5	Membrane-mediated attraction between curvature inducing objects	67
5.1	Introduction	68
5.2	Methods	69
5.3	Results and Discussion	73
5.4	Conclusion	80
6	Microparticle assembly pathways on lipid membranes	83
6.1	Introduction	84
6.2	Methods	84
6.3	Results and Discussion	88
6.4	Conclusion	97
III	Lipids for colloidal self-assembly	99
7	Colloidal organosilica spheres through spontaneous emulsification	101
7.1	Introduction	102
7.2	Methods	105
7.3	Results and Discussion	108
7.4	Conclusion	115
7.5	Supporting Figures	116
8	Lipid monolayers supported by TPM microemulsions	123
8.1	Introduction	124
8.2	Methods	124
8.3	Results and Discussion	128
8.4	Conclusion	134
	Samenvatting	135
	Publication List	137
	Curriculum Vitae	139
	Acknowledgement	141
	Bibliography	143

INTRODUCTION

The biological cell is the basic building block of life. Evolved from simple bacteria in the sea to the sophisticated humans, all organisms are built up from these carefully organized chemical factories. Despite the enormous variety of organisms, the chemical composition of the cell is remarkably conserved: the basic components DNA, proteins, sugars, and lipids can be found in each and every living cell.

An important structural component of the cell is the lipid bilayer, which constitutes a membrane that is impermeable to almost all molecules.¹ This nanometer thin lipid membrane acts as an effective barrier that compartmentalizes the cell into many types of organelles (see Fig. 1.1). Next to this, membranes provide a platform for proteins that drive biochemical processes, such as photosynthesis in chloroplasts, energy production in mitochondria, and signal transduction in the brain. Thus, lipid membranes fulfil a crucial structural roll in living cells.

This biological function is tightly related to the shape of the membrane, which varies strongly due to its flexible nature. For instance in the growth and migration of cells, or in more local processes such as vesicle budding (see Fig. 1.2a), membranes undergo dramatic shape changes.² This shape change is, among other things, guided by membrane deforming proteins.²⁻⁴ For instance, vesicle budding is initiated by membrane deforming proteins that create the initial dent in the membrane.^{5,6} Intriguingly, the opposite has also been observed: some proteins are sorted by the membrane, for example by spontaneously concentrating on the outside of membrane tubes.^{7,8} Thus, membrane-deforming proteins shape the membrane, and at the same time respond to the shape of the membrane.

A consequence of this two-way interaction is a force between membrane-deforming proteins that is mediated by the membrane. When one protein deforms the membrane, the other protein feels this deformation, leading to an effective attraction or repulsion between them. This membrane-mediated interaction has been predicted repeatedly, but has never been observed directly, mainly because proteins are too small to be resolved using conventional microscopy techniques. In this thesis, I address this open issue by employing micron-sized colloidal particles to experimentally measure forces between membrane deformations.

In Chapters 2 and 3, methods for extracting local forces from video images of colloidal particles are described. Then, in Chapter 4, the development of colloidal particles that strongly attach to specific lipid membranes is described. These are then used in Chapters 5 and 6, in which membrane mediated forces and assembly pathways between membrane attached colloidal particles are investigated and quantified. Finally, in Chapters 7 and 8, the preparation of micron-sized oil droplets is studied and their use as lipid monolayer support is demonstrated.

In the remaining sections of the Introduction, the necessary concepts and context for this thesis will be delineated. For a Dutch summary of the most important results and the main conclusions, see page 135.

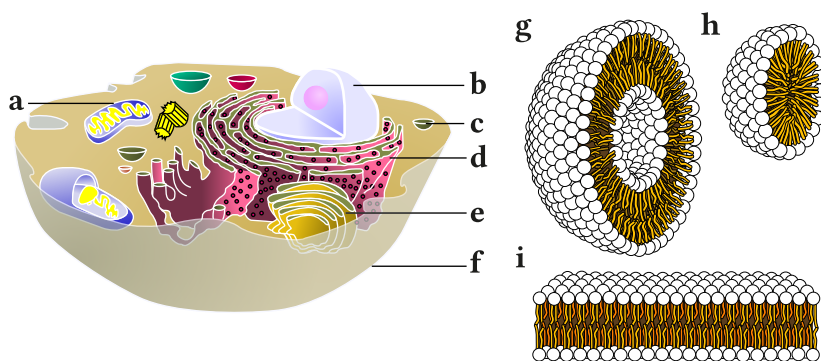


Figure 1.1. Cross-section of a eukaryotic cell (left) and self-assembled lipid structures (right). A selection of cellular organelles are denoted with letters, as follows: (a) mitochondria, (b) nucleus, (c) vesicle, (d) endoplasmic reticulum, (e) Golgi apparatus, and (f) the plasma membrane. In (g) to (i), lipids are denoted by a circle with two attached lines, which respectively denote the hydrophilic head, and the two hydrophobic fatty acid tails. (g) Lipids assemble into bilayers that close themselves into a vesicle. (h) Wedge-shaped lipids assemble into micelles. (i) Lipids with an aspect ratio near 1 assemble into planar bilayers. Images were reproduced from refs. [9, 10].

1.1 Lipid membranes: a biological view

Membrane structure Lipid molecules that form the lipid membrane are amphiphilic: their head group is hydrophilic, while their tail groups are hydrophobic.¹ Depending on their head-to-tail size ratio, they therefore self-assemble in water into structures with their head groups facing outwards. See Figure 1.1g–i. Cellular membranes mostly consist of phospholipids, which have a phosphate-based head group and two fatty acid tails. As lipids are not connected to one another, they behave like a fluid.¹¹ This makes most proteins that are associated with the membrane also mobile, which enables their biological function.

Membrane deforming proteins Cellular membranes are shaped by the interplay of different lipids and membrane proteins.² Many dynamic membrane processes are governed by proteins that attach to the membrane and induce local deformation. For example, the transport of nutrients and signalling molecules in and out of the cell requires the budding of vesicles from the plasma membrane. See Figure 1.2a–d. This important process involves the creation of negative and positive curvatures in the membrane, which is made possible by membrane-associated proteins.

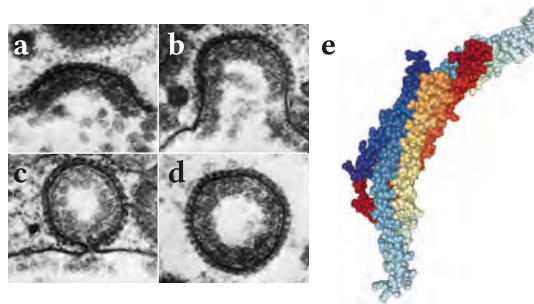


Figure 1.2. Membrane proteins shape the membrane. (a)–(d) Four different stages of vesicle invagination (endocytosis) in an immature chicken egg cell. In these electron micrographs, a cross-section of the membrane is visible with the cell inside on the top. The scale bar denotes 100 nm. Reprinted from ref. [12] with permission from The Company of Biologists. (e) Three-dimensional structure of another membrane-deforming protein: the Amphiphysin BAR domain. This structure was generated from the protein database¹³ with NGL Viewer.¹⁴

Perhaps the most pronounced example of membrane-deforming protein are the banana-shaped BAR domain containing proteins.^{13,15} See Figure 1.2b. These protein domains associate with lipid membranes and deform them locally due to their shape and specific binding characteristics. BAR domains are thought to play a role in the initiation of filopodia⁸ and in the stabilization of membrane tubes.¹⁶

In these examples, not one, but many proteins together result in membrane deformation. Computer simulations^{4,17–19} have predicted that through the membrane deformation of a single protein, other proteins are repositioned and membrane deformation increases, which eventually leads to a biological function such as vesicle budding. To understand this collective effect of local membrane deformations on the membrane shape, it is important to know how a pair of deformations interact with one another via the membrane. In Chapters 2 to 5, the development of an experimental model system that measures this membrane-mediated force is described.

Microparticles In this experimental model system, colloidal particles are used to deform the membrane and study the membrane-mediated interactions. These solid particles of micrometer size have been found to attach to lipid membranes, deform them, and aggregate on them, both on vesicles^{20,21} and on living cells^{22–24} (see Fig. 1.3). Due to

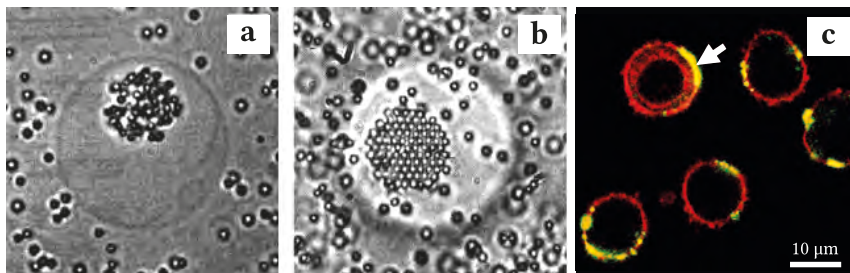


Figure 1.3. Aggregation of microparticles on lipid membranes. Bright field images of (a) disordered and (b) ordered aggregates of micron-sized latex particles adsorbed on bilayer vesicles. (c) Fluorescence images of polymeric particles (green) adsorbed on KG1a cells (red). The arrow indicates an aggregate of particles. (a) and (b) were reprinted from ref. [20] with permission from AAAS. (c) was reprinted from ref. [22] with permission from Elsevier.

their increased use in paints, cosmetics, and pharmacological applications, these microplastics are present more and more in the environment.²⁵ Therefore, studying the interaction between microparticles and lipid membranes is not only useful as model system for membrane-mediated forces, but also to address the question how microplastics influence lipid membranes. In Chapter 5 we will describe how microparticles attach to lipid membranes, and in Chapter 6, we will systematically investigate permanent assembly pathways that lead to aggregation of microparticles on lipid membranes.

1.2 Lipid membranes: a physical view

The physical model The lipid membrane can be seen as a two-dimensional fluid of lipid molecules with a certain surface viscosity and area compressibility modulus. In addition to that, membranes can curve in the third dimension. The compressibility modulus of both membrane monolayers gives bilayers a certain resistance against bending, which is expressed in the bending rigidity. This mix of liquid and elastic properties make lipid membranes unique physical objects that require a separate theoretical description. The generally accepted model for the energy of a symmetric lipid membrane was formulated by Canham and Helfrich in the 70s as follows:^{26,27}

$$U = \iint [\sigma + \kappa H^2 + \kappa_g K] dA, \quad (1.1)$$

with U the energy, σ the membrane tension, κ the bending rigidity, κ_g the Gaussian bending rigidity, H the mean curvature, and K the Gaussian curvature (see Fig. 1.4a). For

a closed surface like a vesicle (Fig. 1.1g), it follows from the Gauss-Bonnet theorem that the integral over the Gaussian curvature contributes a constant energy. As constant contributions to the energy are irrelevant, this term is typically left out.

Membrane tension Surface tension is defined as the free energy increase associated with the increase of surface area. For example in a water/air interface surface tension is always positive so that the surface tends to contract, minimizing its surface area. This process is driven by the transport of water molecules from the interface to the bulk. For lipid membranes, however, we do not have a bulk and therefore, transport of lipid molecules is only possible if there is a reservoir of lipids at the membrane edges. Lipid vesicles in general have no such reservoir and therefore they have a constant number of surface molecules, which is a situation that is uncommon for conventional interfaces.

Elastic extension then becomes the only mechanism through which the membrane surface area can change. This typically requires high tensions, which can be achieved through high osmotic pressure differences or by suction through a micropipette,²⁸ until the vesicle bursts. Outside of this stretched regime, vesicles essentially have a constant area, so that the Helfrich energy (Eq. 1.1) of a vesicle simplifies to:

$$U_{vesicle} = \iint \kappa H^2 dA. \quad (1.2)$$

Nevertheless, in literature there is often a membrane tension assigned to deflated vesicles. While the surface area of a vesicle cannot change, the projected surface area can, and through thermal fluctuations, this can be expressed in an effective membrane tension which is related directly to the (real) area-to-volume ratio of the vesicle.²⁹ This entropic surface tension is used throughout this thesis as the membrane tension.

Membrane-mediated forces A single membrane-deforming object introduces a deformation field in the membrane.³⁰ See for example Fig. 1.4b–c for two membrane-deforming objects. When two of these objects approach each other, the induced membrane deformation fields interact resulting in effective attractive or repulsive forces between the deformations. This membrane-mediated force stems from the minimization of the membrane free energy.

Since the 90s, there have been many predictions of membrane-mediated forces, including forces mediated by membrane thickness modulation,³¹ Casimir-type fluctuation mediated forces,³² and interactions driven by the phase separation of multicomponent membranes.³³ The main focus of previous work however involves a membrane-bending mediated force, that follows from the minimization of the Helfrich energy (Eq. 1.2). By linearising this equation, which is valid only for small membrane deformations, repulsive interaction forces have been predicted.¹⁷ For large deformations, this approach is however not valid and an effective field theory approach can be taken to describe the force between two membrane inclusions. However, this approach is not able to predict even the sign of the membrane-mediated force.³⁴

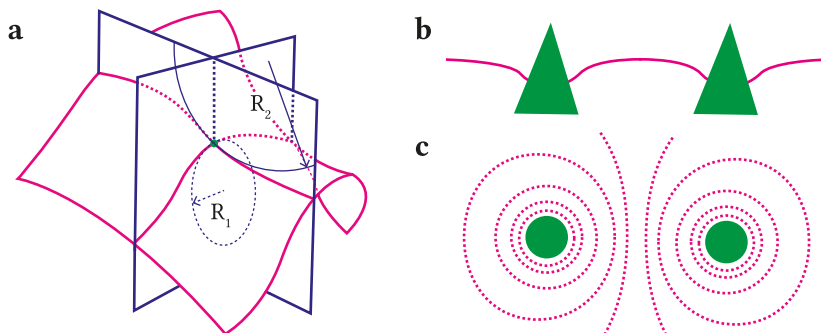


Figure 1.4. Illustrations of membrane deformations. (a) Sketch of an arbitrarily shaped membrane patch (magenta) with the radii of curvature in a point (green) drawn on planes perpendicular to the surface. The mean curvature H is defined as the average of $1/R_1$ and $1/R_2$ and the Gaussian curvature K as the product between $1/R_1$ and $1/R_2$. Curvature also has a sign. If the vesicle inside is below the sketch, R_1 is positive and R_2 is negative. (b) Cross section of a membrane with two inclusions (green) that induce local curvature (c) Top view with the contours of equal height as dashed lines, showing that the deformation fields interact with each other. These illustrations are sketches and not numerical results.

Computer simulations have extended the theoretical descriptions and have been able to quantitatively predict membrane bending mediated forces. The predicted forces between membrane-embedded objects can be repulsive or attractive, depending on the extent of the deformation and the distance between the objects.³⁵ Simulations involving many membrane-deforming objects have shown that these interactions can indeed lead to global deformation of the membrane, such as line formation, tubulation, and vesiculation.^{4,18,19,36} In Chapter 5, this membrane-mediated force is quantified experimentally and compared to these numerical predictions.

1.3 Lipids in self-assembly

Next to their presence in biological processes and in food science, lipids have also found their way into a variety of technological applications, such as targeted drug delivery,³⁷ surface passivation in microfluidics,³⁸ nanoporous materials, electronics, and photonics.³⁹ In this thesis we will focus on yet another application of lipids: the production of self-assembled colloidal materials.

Colloidal self-assembly is a promising tool for creating new materials from the bottom up. To engineer a self-assembled colloidal structure, building blocks with specific and directional bonding sites are required.⁴⁰ Important steps have been taken to create these controlled building blocks with specific linkers,⁴¹ however the self-assembly of complex materials remains a challenge because of kinetic arrest that occurs when

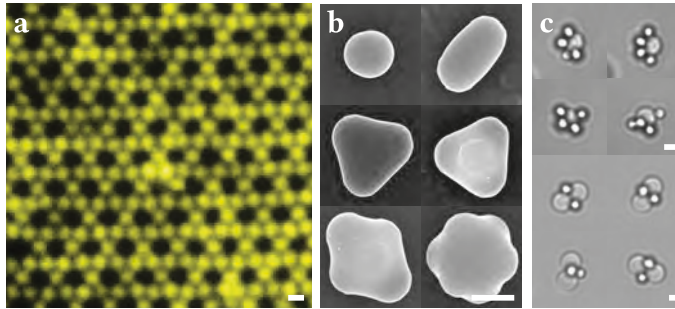


Figure 1.5. Examples of self-assembled colloidal structures. (a) Self-assembled colloidal Kagome lattice, which has useful optical properties. (b) Colloidal clusters with controlled shape, self-assembled from 1 to 6 spheres.⁴³ (c) Two examples of flexible self-assembled structures.⁴⁴ On the top, four snapshots of a colloidal ball joint is shown, and on the bottom a hinge joint. Scale bars denote 1 μm . (a) was adapted from ref. [45] with permission from Macmillan Publishers, copyright 2011.

building blocks bind together, yielding open random packings.⁴²

To controllably assemble structures such as displayed in Figure 1.5, building blocks need to be able to rearrange after connecting.^{46,47} One way to achieve this bond flexibility is the use of lipid-coated emulsions instead of solid particles as building blocks.^{48,49} Here, the lipids provide the specific linking capability, while they are mobile laterally on the emulsion surface. Oil-in-water emulsions however typically have a wide size distribution, and are therefore less useful to build regular structures.

In this thesis, lipid-coated 3-(trimethoxysilyl)propyl methacrylate (TPM) microdroplets were investigated as a possible material to produce dynamic colloidal assemblies. TPM has the advantage that it spontaneously forms emulsions in water with a narrow size distribution.^{50,51} In Chapter 7 we will investigate this spontaneous emulsification to be able to control the resulting droplet size. Then, in Chapter 8, we will study the mobility of lipids, DNA-linkers, and colloidal particles on the surface of these TPM emulsion droplets.

Part I

Methods of single particle tracking

TRACKING OF COLLOIDAL CLUSTERS WITH SUB-PIXEL ACCURACY AND PRECISION

This chapter is published as C. M. van der Wel and D. J. Kraft, 'Automated tracking of colloidal clusters with sub-pixel accuracy and precision', *J. Phys. Condens. Mat.* **29**, 044001 (2017) DOI: 10.1088/1361-648X/29/4/044001

Abstract

Quantitative tracking of features from video images is a basic technique employed in many areas of science. Here, we present a method for the tracking of features that partially overlap, in order to be able to track so-called colloidal molecules. Our approach implements two improvements into existing particle tracking algorithms. Firstly, we use the history of previously identified feature locations to successfully find their positions in consecutive frames. Secondly, we present a framework for non-linear least-squares fitting to summed radial model functions and analyse the accuracy (bias) and precision (random error) of the method on artificial data. We find that our tracking algorithm correctly identifies overlapping features with an accuracy below 0.2 % of the feature radius and a precision of 0.1 to 0.01 pixels for a typical image of a colloidal cluster. Finally, we use our method to extract the three-dimensional diffusion tensor from the Brownian motion of colloidal dimers.

2.1 Introduction

Extracting quantitative information about the position and motion of features in video images is often key to understanding fundamental problems in science. For example, the tracking of colloidal hard spheres in three-dimensional confocal images has provided important insights into phenomena such as melting, crystallization, and the glass transition.^{52–56} Biophysical experiments such as the investigation of cell mechanics by microrheology^{57,58} or the measurement of single biomolecule mechanics using optical or magnetic tweezers⁵⁹ rely on the precise positional measurement of single colloidal particles. Moreover, the tracking of single proteins in live cells provided a powerful tool for understanding biological processes,^{60,61} and eventually lead to the development of super-resolution microscopy techniques such as PALM and STORM.^{62–64} Crucial for these studies is a method to extract trajectories of features from video images, which has been described extensively in colloidal science^{65,66} as well as in single molecule tracking.^{67–70}

Most single particle tracking algorithms have been designed for spherical features, as it is the most common type of signal. Recent developments in colloidal synthesis^{43,71,72} provide means to create anisotropic particles, for example by assembling spheres in so-called colloidal molecules. Single particle tracking of these clusters of spheres is expected to provide insights into the role of anisotropy in for instance crystallization and diffusion.^{40,73,74} As the basic building blocks of these studies contain closely spaced or partially interpenetrating spherical particles, a robust automated method is required to perform accurate particle tracking on partially overlapping features.

Automated methods for single-particle tracking follow roughly the following pattern: an image with features of interest is first preprocessed to remove background and noise, then single features are identified in a process called “segmentation”, these feature coordinates are refined to sub-pixel accuracy, and finally the features are linked to the features in the previous image. Iteration of this algorithm over a sequence of images results in particle trajectories that can be used for further analysis. Although this method has proven itself as a robust and accurate method,^{75,76} issues arise when features become so closely spaced that their signals overlap. Commonly, these issues are avoided experimentally by studying dilute systems, repelling particles, or model systems with very specific characteristics such as index-matched and core-shell fluorescent particles.^{77,78} However, this is not always a possibility: therefore, issues from feature overlap persist in many measurements, especially involving colloidal clusters.

In particular, overlapping feature signals give rise to two complications: firstly, the segmentation step regularly recognizes two closely spaced features as one feature due to the overlap of signals. In order to identify the trajectories of closely spaced features completely, tedious frame-by-frame manual corrections are necessary, prohibiting the analysis of large data sets. In super-resolution microscopy methods, reported approaches to solve this issue are repeated subtraction of point-spread functions of detected features,⁷⁹ or advanced statistical models classifying merge and split events.⁸⁰ Notably, these tracking methods do not use all the available information: as the feature locations are known

in the previous frame, the segmentation of the image may be enhanced using the projected feature locations. This has been shown to improve segmentation significantly, for example in the tracking of biological cells.^{81,82} Here we will present a fast and simple method for image segmentation that makes use of this history of the feature locations. We will test this method on artificial images and experimental data of colloidal dimers.

A second issue that arises when two feature signals overlap is that their refined coordinates will underestimate the separation distance. Especially the commonly employed centre-of-mass centroiding suffers from this systematic “overlap bias”, leading to an apparent attraction between colloidal particles.^{76,83} For fluorescence images, this issue can be addressed by least-squares fitting to a sum of Gaussians, which has been reported as a way to measure the distance between overlapping diffraction limited features.^{84,85} Here, we will apply this method to images with features that are not diffraction limited. We will conduct systematic tests on the accuracy (bias) and precision (random error) of the obtained feature positions.

To demonstrate the automated segmentation and refinement methods, we will apply it to three-dimensional confocal images of a diffusing colloidal cluster consisting of two spheres and use the obtained trajectories to extract its diffusion tensor.

2.2 Methods

2.2.1 Segmentation

As our algorithm for single particle tracking is based on the widely employed algorithm by Crocker and Grier,⁶⁵ we will first introduce their algorithm and call it “CG algorithm”. Throughout this work a Python implementation of this algorithm, Trackpy,⁸⁶ was used for comparison. The CG algorithm consists of four subsequent steps: preprocessing, feature segmentation, refinement, and linking. See Figure 2.1a for a schematic overview.

The preprocessing consists of noise reduction by convolution with a 1 pixel (px) sized Gaussian kernel and background signal reduction by subtracting a rolling average from the image with kernel size $2R + 1$. The length scale R is chosen just larger than the feature radius. The subsequent segmentation step finds pixels that are above a given relative intensity threshold and are local maxima within a certain radius S . The length scale S is the minimum allowed separation between particles. After the refinement step (see next section) the linking connects the features in frame i with features in frame $i - 1$ by minimizing the total displacement between the frames. Between two frames, particles are allowed to move up to a maximum distance L .

In this process, each frame is treated individually: only during the final step (linking), features are connected into trajectories. We rearranged this process so that the information about the particle locations in the previous frame is used already in the segmentation. This allows us to project the expected feature locations in consecutive frames and therefore increases the success rate of segmentation. See Figure 2.1b for a schematic overview. We describe our segmentation algorithm here using a minimal example

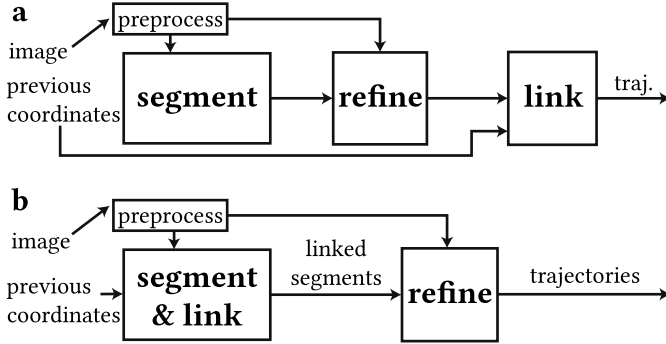


Figure 2.1. Schematic of the particle tracking of a single frame in (a) the CG algorithm and (b) the new algorithm. In the CG algorithm (a) the image is preprocessed and segmented. Starting from the segments and the preprocessed image, a refinement step is performed. Finally, consecutive coordinates are linked together with the coordinates in the previous frame. In our algorithm (b) the image is preprocessed and segmented, making use of the knowledge of the previous coordinates. The linked segments are refined afterwards to yield sub-pixel precision.

of two closely spaced features in two consecutive frames, which can be generalized to an arbitrary number of features in any number of frames. The technique is also valid in three dimensions, as demonstrated in section 2.3.3. See Figures 2.2a–c.

We will assume that feature finding and refinement was performed successfully on frame 1 (Figure 2.2d). Frame 2 is first subjected to grey dilation and thresholding step, just as in the CG algorithm. Because features are closely spaced in that frame, this leads to segmentation into only one single feature (Figure 2.2e).

Then a part of the linking step is executed: features are divided into so-called subnetworks. This is a necessary step in the CG algorithm to break the $\mathcal{O}(N!)$ sized combinatorial problem of linking two sets of N features into smaller parts. First, linking candidates are identified using a kd-tree.^{86,87} Linking candidates for features in frame 1 are features that are displaced up to a distance L in frame 2 and vice versa. Then subnetworks are created such that all features that share linking candidates are in the same subnetwork. For a sufficiently large distance L , all features in Figure 2.2f belong to the same subnet: the feature in frame 2 is a linking candidate for both features in frame 1.

From the subnetworks, the number and estimated location of missing features is obtained “for free”: if a subnetwork contains fewer particles in frame 2 than in frame 1, there must be missing features in its vicinity. To account for the possibility that a missing feature could connect two subnetworks, we combine subnetworks if they are less than a distance $2L$ apart in frame 1 whenever missing features are being located.

In order to estimate the location of the missing features, a region up to distance $L + S$ around the features in frame 1 is masked in frame 2 (dashed yellow line in Figures 2.2g–h). Subsequently, all already found features are masked up to a radius of S

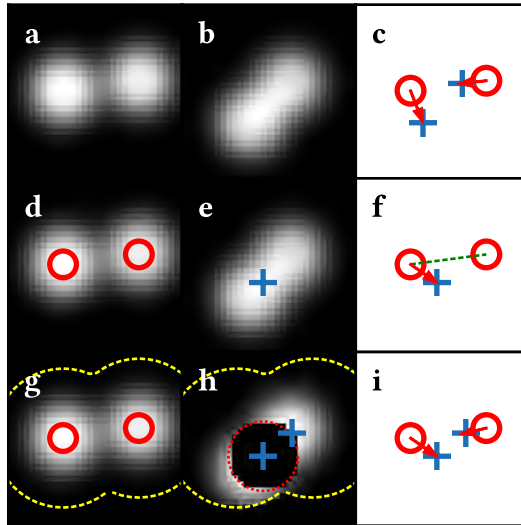


Figure 2.2. Artificial example to illustrate the integrated segmentation and linking step. In (a) and (b) two consecutive computer-generated frames are shown and in (c) the corresponding true feature locations, with the frame 1 features in red circles and the frame 2 features in blue crosses. Links are indicated by red arrows. In (d) frame 1 is shown again, overlaid with its feature coordinates in red circles and in (e) the result of the initial feature finding is indicated by a blue cross on top of frame 2. (f) The subnet is formed by the linking candidates. Additionally, the green dashed line denotes a distance between features that is less than $2L$. Therefore these features could belong to a single subnet via a missing feature. (g) Subsequently, a region of interest (dashed yellow line) is defined, comprising the pixels that are closer than $L + S$ to any feature in frame 1. This region is used to identify to which positions features in frame 1 could have moved in frame 2 (h). Also all features that were found already in frame 2 are masked out (dotted red line). These two operations enable the detection of the missing feature, which is then added to the subnet so that the linking can be completed (i).

(Figure 2.2h). This enables us to find local maxima that are further than distance S from all other features in frame 2 and closer than distance L from the features in frame 1. From the masked sub-image, local maxima are obtained again through grey dilation and thresholding. After this, feature selection filters can be inserted in order to select appropriate features, for example with a minimum amount of integrated intensity. Then the new feature is added to the subnetwork and linking is completed by minimizing the total feature displacement (Figure 2.2i).

By performing the linking during the segmentation process, additional information is taken into account: not only the present image is used to identify the features, but also the coordinates from the previous frame. Therefore, we expect a higher number of cor-

rectly identified feature positions for the combined linking and segmentation method. Because all the computationally intensive tasks were already present in the original algorithm, the execution time of our new algorithm was observed to be similar.

2.2.2 Refinement

Sub-pixel accuracy and precision are key features of single particle tracking. Although the size of a single pixel is diffraction limited to approximately 200 nm, localization precisions down to 1 nm have been reported.^{69,75} These sub-pixel feature locations are obtained by starting from an initial guess supplied by the segmentation step, which is then improved in the so-called “refinement” step. Here, we will describe a general-purpose framework for refinement of overlapping features using non-linear least squares fitting to summed radial model functions.

We will compare this method to the centre-of-mass centroiding that is present in the CG algorithm.⁶⁵ For radially symmetric features, the feature position is given by its centre-of-mass. Due to its simplicity and computational efficiency, this method is a preferred choice for many tracking applications. In the centre-of-mass refinement, the centre coordinate \vec{c} of the feature is obtained from the image $I(\vec{x})$, such that:

$$\sum_{\text{dist}(\vec{x}, \vec{c}) \leq R} I(\vec{x})(\vec{x} - \vec{c}) = 0. \quad (2.1)$$

In order to obtain the centre-of-mass, a region $\text{dist}(\vec{x}, \vec{c}) \leq R$ is selected using the initial coordinate guess from the segmentation. In general, this is not necessarily close to the actual feature position: see for example Fig. 2.2e. Therefore, commonly an iterative centre-of-mass algorithm is employed⁸⁶ to be able to shift the region on which the centre-of-mass is computed. Throughout this work we will employ this iterative algorithm to find the centre-of-mass position.

Non-linear least squares fitting to a model function is conceptually different, since it goes beyond assuming only feature symmetry and requires knowledge on the feature shape. If image noise is uncorrelated and normal distributed, this method gives the maximum likelihood estimate of the true centroid. Although this assumption is not strictly valid,^{66,69} the precision of this method is generally higher than the centre-of-mass method when the image is subject to noise.⁷⁵ By simultaneously fitting a sum of multiple model functions, this method can be extended to tracking multiple overlapping features.^{84,85} We employ this approach here and formulate the feature model function F in the following way:

$$F(\vec{x}, \vec{c}, A, \vec{\sigma}, \vec{p}) = \begin{cases} A \cdot f(r(\vec{x}, \vec{c}, \vec{\sigma}), \vec{p}) & \text{dist}(\vec{x}, \vec{c}) \leq R \\ 0 & \text{otherwise} \end{cases}, \quad (2.2)$$

$$r^2(\vec{x}, \vec{c}, \vec{\sigma}) = \sum_{j=1}^D \left(\frac{x_j - c_j}{\sigma_j} \right)^2. \quad (2.3)$$

Here, \vec{x} is the image coordinate, \vec{c} the feature centre, A its intensity, $\vec{\sigma}$ its radius, and f a model function of a single feature, which is a function of r and a list of parameters \vec{p} . The reduced radial coordinate r is defined for any number of dimensions D and allows for anisotropic pixel sizes through the vector nature of $\vec{\sigma}$. The feature model function is defined only up to distance R from the feature centre. With this definition, it is possible to use any function for f and apply it to images with different signal intensities and physical pixel sizes through the separate parameters A and $\vec{\sigma}$. In our tests, we keep $\vec{\sigma}$ constant and allow \vec{c} and A to be optimized.

The model image is constructed by the summation of the individual features, which are each only defined within a region with radius R . This additivity is a good assumption for fluorescence microscopy techniques.⁷⁶ We add a fixed background signal B , which we keep constant within each cluster of overlapping features, but we allow it to vary between clusters to account for spatially different background values. For an image or video consisting of N features, the following “objective function” is minimized:

$$\sum_{\vec{x}} \left(I(\vec{x}) - B - \sum_{i=1}^N F(\vec{x}, \vec{c}_i, A_i, \vec{\sigma}_i, \vec{p}_i) \right)^2. \quad (2.4)$$

The feature model function F is given in Eq. 2.2. In order to avoid discontinuities in f around $r = 0$, we omit points \vec{x} from the objective function that are closer than 1 pixel from any feature centre \vec{c} .

If all features are separated by more than $2R$, this minimization can be separated into N single feature problems. However, when features have overlapping regions, their objective functions cannot be separated and have to be minimized simultaneously. We separate the full image objective function (Eq. 2.4) into groups (“clusters”) using the kd-tree algorithm.⁸⁷ Each of the resulting cluster objective function is minimized using the sequential linear least squares programming (SLSQP) algorithm⁸⁸ interfaced through the open-source Python package SciPy.⁸⁹ This SLSQP algorithm allows for additional constraints and bounds on the parameters. We use bounds to suppress diverging solutions and constraints to, for example, fix the distance between two features to a known value. The optimizer is supplied with an analytic Jacobian of Eq. 2.4 to increase performance.

The here described framework of feature refinement in principle allows refinement of any feature that can be described by a radial function. Although less computationally efficient than the conventional refinement by centre-of-mass, it can take into account feature overlap and additionally allows for constraints on parameters.

2.2.3 Testing methods

The above described methods for single particle tracking were tested quantitatively on both artificial and experimental data. In order to model fluorescence images of colloidal particles, we chose three different artificial feature functions. Firstly we use the Gaussian function to describe diffraction-limited features:

$$f_{\text{gauss}}(r) = \exp[-r^2]. \quad (2.5)$$

Secondly, we describe colloidal particles that are larger than the diffraction limit by a hat-shaped function consisting of a solid disc with radius d surrounded with a Gaussian-decaying boundary:

$$f_{\text{disc}}(r, d) = \begin{cases} \exp\left[-\left(\frac{r-d}{1-d}\right)^2\right] & r \geq d \\ 1 & \text{otherwise.} \end{cases} \quad (2.6)$$

Thirdly, as a model for particles with fluorescent markers on their surface only, we define a ring shaped function with ring thickness t :

$$f_{\text{ring}}(r, t) = \exp\left[-\left(\frac{r-t-1}{t}\right)^2\right]. \quad (2.7)$$

See Figure 2.3 for model features of the hat- and ring-shaped functions. The artificial features are defined in such a way that their size σ equals the radius at which the feature signal has decayed by a factor $e^{-1} \approx 0.37$ from its maximum value. Note that σ is not the same as the previously defined refinement radius R . As R should be chosen larger than the feature radius, we took $R = 2\sigma$ in our tests.

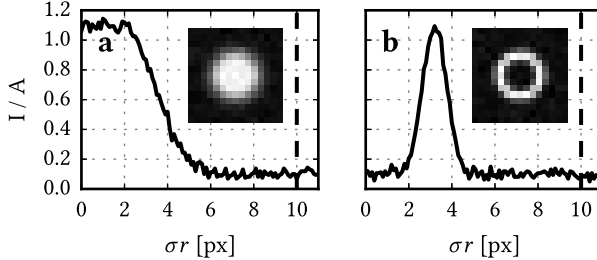


Figure 2.3. Radial intensity functions of (a) a hat-shaped and (b) a ring-shaped model feature in arbitrary units, generated with Equations 2.6 and 2.7 with parameters $\sigma = 4$ px, $d = 0.5$, and $t = 0.2$. The insets show the corresponding single-feature images. Poisson distributed noise was added to each feature.

The feature is generated on a pixel grid from a randomly generated sub-pixel location. Unless stated otherwise, we chose the feature size σ to be 4 px. Depending on the application, the physical size of a single pixel typically ranges from 100–500 nm. The feature maximum A is chosen at 160 and unless stated otherwise, $d = 0.5$ and $t = 0.2$. Images were discretized to integer values and a Poisson distributed, signal-independent

background noise with a mean intensity of $N = 16$ was added to each image. The corresponding signal-to-noise ratio S/N is defined as A/N . Each refinement test was performed on 100 images having two overlapping features with a given centre-to-centre distance and random orientations. In order to ensure that the choice of initial coordinates did not affect the refined coordinate, we generated the initial coordinates randomly within 0.5σ from the actual coordinate.

Experimental measurements on colloidal particles were performed with an inverted Nikon TiE microscope equipped with a Nikon A1R confocal scanhead. For the two-dimensional diffusion measurements, we used a $20\times$ objective ($NA = 0.75$), resulting in a physical pixel size of $0.399\ \mu\text{m}$ in x - and y -directions. The images were recorded with Galvano mirrors acquiring images of 64×64 pixels at $15.4\ \text{Hz}$. For the three-dimensional measurements, a $100\times$ ($NA = 1.45$) oil immersion objective was used, resulting in an xy pixel size of $0.166\ \mu\text{m}$. A calibrated MCL NanoDrive stage enabled fast z stack acquisition with a z step size of $0.300\ \mu\text{m}$. As the objective immersion liquid ($N_D = 1.515$) is closely matched with the sample solvent ($N_D = 1.49$), this step size equals the physical pixel size in z direction within an error of 5% .⁹⁰ We acquired 5.13 three-dimensional images per second with a size of $512 \times 64 \times 35$ pixels in xyz , respectively.

For two-dimensional diffusion measurements we used samples consisting of partially clustered TPM (3-(trimethoxysilyl)propyl methacrylate) colloids with a diameter of $1.94 \pm 0.09\ \mu\text{m}$ containing an RITC (rhodamine B isothiocyanate) fluorescent marker, as described in Chapter 7. Because of their density difference with water, the particles were confined to the coverslip by gravity, enabling two-dimensional tracking.

The samples for three-dimensional measurements consisted of core-shell RITC labelled PMMA (polymethylmethacrylate) colloidal clusters that were synthesized via an emulsification-evaporation method according to ref. [71]. The average distance between the two constituent spheres of diameter $1.87 \pm 0.06\ \mu\text{m}$ in a cluster is $1.58 \pm 0.12\ \mu\text{m}$, determined by scanning electron microscopy using an FEI NanoSEM at $15\ \text{kV}$. The clusters were both index and density matched using a mixture of cyclohexyl bromide and *cis*-decalin in a weight ratio of 72:28 and imaged in a rectangular capillary, similar to experiments described in ref. [91].

The Python code on which this work is based is available online in the package Trackpy,⁸⁶ that is available through Conda as well as through the Python Package Index. All tests described in this work are implemented as “unittests” that ensure the correct functioning of the code on each update.



2.3 Results and Discussion

2.3.1 Segmentation and Linking

As described in the Methods section, the integrated segmentation and linking step extends the frame-by-frame segmentation used in the CG algorithm in such a way that it makes use of the history of feature locations. In order to test the effect of our exten-

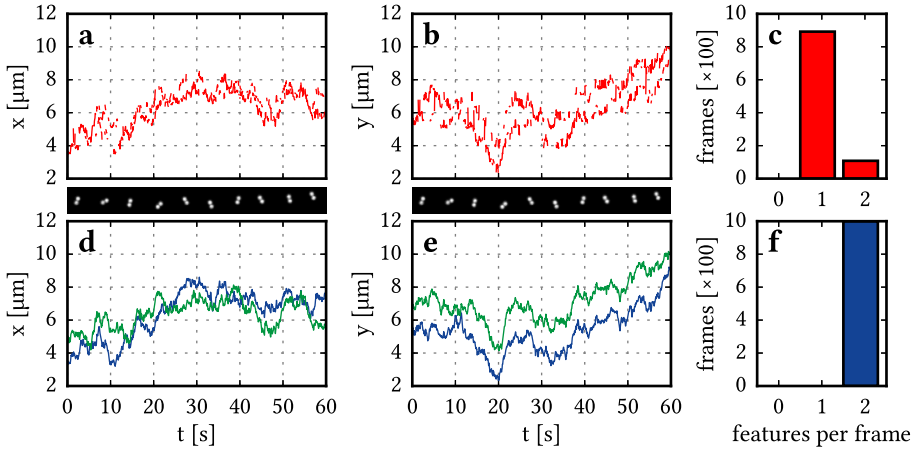


Figure 2.4. Segmentation of an experimental 2D video image of a colloidal dimer. In (a) and (b) the x and y coordinates obtained using the CG algorithm are shown. The corresponding histogram of features per frame is displayed in (c). As the two features were identified correctly in only 11% of the frames, trajectories could not be identified. In (d) and (e) the trajectories were obtained using the integrated segmentation and linking algorithm. As all frames had two features (see the histogram in (f)), trajectories were identified completely. In these plots, coordinates were refined using least-squares fitting to a sum of Gaussians. A video of this comparison is available online.

sion, we compared the segmentation in the CG algorithm with our integrated segmentation and linking on experimental video images. As a distinct example of overlapping features, we analysed a single colloidal dimer, which consists of two permanently connected spheres. The dimer exhibits Brownian motion in two dimensions. The identified trajectories for 1000 frames are displayed in Figure 2.4.

The CG algorithm identified two features in only 11% of the frames, resulting in short disconnected trajectories that appear to hop between two feature locations. Apart from that, the single features were often localized at a position in between the two features, which compromises the refinement step. The here described extension of segmentation improves the feature identification significantly: by taking into account the history of the feature positions, we detect two features in every frame.

As we have refined the feature positions using the described least-squares fitting method, we are also able to compute the average distance between the particles. We find $2.04 \pm 0.03 \mu\text{m}$. As the dimer consists of aggregated spheres, we can compare this directly to the average particle diameter ($1.94 \pm 0.09 \mu\text{m}$). Due to the size polydispersity of the sample, we cannot use this to quantify the bias in the feature positions. The precision can however be estimated using the spread in the measured separation lengths: we find 0.08 px. Part of this is stemming from a physical effect, as the dimer can slightly tilt in

the third dimension.

The here described extension of segmentation increases the number of correctly segmented features significantly. It has to be noted though that the segmentation of the first frame is not enhanced by our method because of the lack of information on the previous feature positions. Generally, there is a start-up period of a few frames in which the number of correctly segmented features increases. The length of this start-up period can be estimated from the probability of correctly identifying a dimer in absence of information about the previous positions: in our case, this probability is 11 %. This corresponds to a probability of 90 % of having at least one correctly segmented frame in the first 20 frames. These potentially incorrectly tracked frames can be ignored for most tracking applications. For cases where the first frames are relevant, the algorithm may be run backwards from the first correctly segmented frame.

2.3.2 Refinement

After the segmentation step the sub-pixel position is obtained in the refinement step. In this section we will analyse the effect of signal overlap on the accuracy and precision in the refined feature coordinates using both centre-of-mass and the here described least-squares fitting to sums of model functions. We define the accuracy or bias as the mean difference between the measured and the true value. The precision is the random deviation around the measured average, which we calculate with the sum of the root of squared deviations from the measured average.

Firstly, we took two Gaussian-shaped features (Eq. 2.5) with radius $\sigma = 4$ px and varied their spacing between 1.5σ and 5.5σ . See Figure 2.5. The deviations of the obtained positions are measured parallel and perpendicular to the line connecting the two actual feature positions. We observed no bias in the perpendicular coordinate for either refinement method. For the parallel coordinate, however, we found a clear difference between the two approaches: in centre-of-mass centroiding, the parallel coordinate was negatively biased because of feature overlap, meaning that the distance between the two overlapping features was systematically underestimated. In least-squares refinement, this bias was not present and the features were located with sub-pixel accuracy for all particle spacings.

The negative bias for centre-of-mass centroiding has been described before^{83,92} and is a consequence of the method: if two features overlap, each of the features obtains extra intensity on the inside of the dimer. This bias increases in magnitude with decreasing particle separation, until both features are detected precisely in between the two actual positions. The bias increases also with increasing mask radius R , as shown in Figure 2.5.

Apart from this negative bias, we observed a longer ranged positive bias. This effect has its origin in the preprocessing. For centre-of-mass centroiding, it is vital that any constant image background is subtracted. This is conventionally achieved by subtracting a rolling average of the image with box size of typically $D_{bg} = 2R + 1$.⁶⁵ Although this method has proven to be robust for background subtraction, it also introduces a skew in the feature signals when features are closer than $\ell + D_{bg}$ (see Figure 2.9 on page 29).

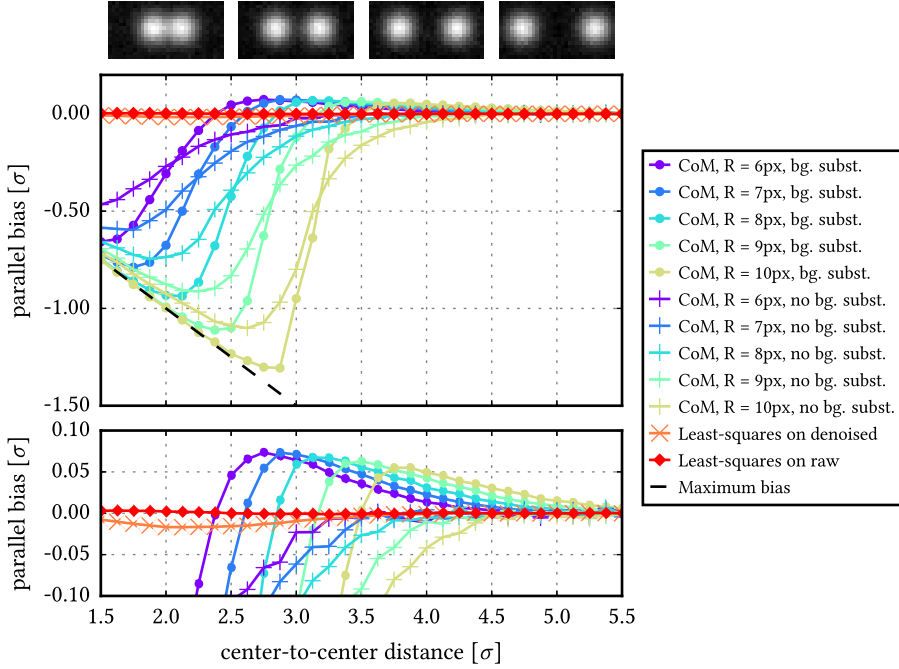


Figure 2.5. The effect of feature overlap on the bias in the parallel coordinate. The bias is negative when features appear too close together. In both graphs, the bias in the parallel coordinate as a function of the centre-to-centre distance is shown, for two Gaussian features with $\sigma = 4$ px and signal-to-noise ratio $S/N = 10$. The bias for the centre-of-mass (CoM) refinement is shown for mask radius R from 6 to 10, both with rolling average background subtraction (denoted with dots) and without (denoted with crosses). The bias for the least-squares fitting to a sum of Gaussians method is shown in orange tilted crosses for the case that the fitted image was denoised first. Direct least-squares fitting of the raw image is shown in red diamonds. The dashed black line denotes the bias at which features are detected precisely in between the two actual feature positions. The insets correspond to centre-to-centre distances of 2σ , 3σ , 4σ , and 5σ .

Here, ℓ is the typical feature diameter. From this we conclude that it is important not to use a rolling average background subtraction in order to accurately track features that are spaced closer than $\ell + D_{bg}$. If the background subtraction was omitted, the positive bias was indeed not observed, as can be seen in Figure 2.5. In order to account for the background signal in the least-squares fitting algorithm, we introduced a background variable B in the objective function (Eq. 2.4) instead.

The least-squares fitting to sums of model functions is clearly better able to provide an unbiased localization of the feature: the (absolute) bias stayed below 0.2% of the

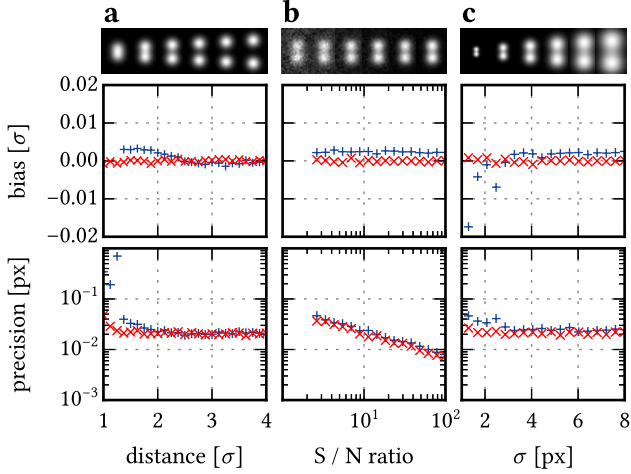


Figure 2.6. Localization errors of Gaussian-shaped features. The top row presents the computer generated model features, the middle and bottom row show the mean deviation (bias) and the root of the central variance of the deviations (precision), respectively. The data is separated into the error parallel (upright blue crosses) and perpendicular (tilted red crosses) to the line connecting the true feature positions. Unless stated otherwise, a feature size $\sigma = 4$ px, a feature centre-to-centre distance of 2σ , and signal-to-noise ratio $S/N = 10$ were employed. (a) Overlapping features were localized with bias below 0.004σ and sub-pixel precision, for a feature separation distances larger than 1.4σ . (b) Above a signal-to-noise ratio (S/N ratio) of 2, bias was independent of noise and precision improved with increasing S/N ratio. (c) Below a feature size of 2 px, the (absolute) bias increased steeply. The precision was independent of the feature size.

feature radius for all separation distances. We observed that denoising the image before least-squares fitting causes a bias of up to 0.02σ , depending on the feature separation. This is because denoising adds a correlation between neighbouring pixels, while least-squares assumes an absence of correlation between datapoints. Therefore we conclude that direct fitting of a raw image gives the most accurate results.

Secondly, we analysed the bias and precision in the coordinates of overlapping Gaussian features, while systematically varying the particle spacing, signal-to-noise ratio, and size. See Figure 2.6. In all cases, we observed no bias in the perpendicular coordinate, as is expected from the symmetry of the dimer. Also, the precision for the perpendicular and parallel directions were in close agreement. As shown in Figure 2.11 on page 30, the bias is proportional to the feature size σ , while the precision is independent of σ . Therefore, we report the bias in units of σ , and the precision in units of pixels (px).

We observed accurate and precise refinement down to particle separations of 1.4σ : at shorter separation distances, the algorithm was not able to separate the features (see Figure 2.6a). In Figure 2.6b, it can be seen that the signal-to-noise (S/N) ratio does not

influence the bias, while the precision improves with increasing S/N ratio. At $S/N < 2$, the optimizer sometimes diverged and yielded random results. This failure of least-squares fitting was reported already for $S/N < 4$ by Cheezum and co-workers.⁷⁵ As the SLSQP minimization allows for bounds on the feature parameters, we were able to suppress the diverging solutions by limiting the displacements of centre coordinates to the mask size R . This enhancement enabled us to also use the least-squares method for $2 \leq S/N < 4$.

In Figure 2.6c and Figure 2.11, it can be seen that the bias in the parallel coordinate is a constant fraction of the feature size (0.2%). Although this bias is negligibly small, it is still larger than the bias in the perpendicular coordinate, showing the influence of particle overlap. Below a feature radius σ of 2 px, we observed that the bias increased steeply. Presumably there is not enough information in these small features to accurately determine the two positions.

As colloidal molecules are often larger than the diffraction limit, their feature shape is typically not Gaussian. We assessed the effect of the mismatch between a non-Gaussian feature and a Gaussian fit function by gradually changing the non-Gaussianness of the model feature, using hat- and ring-shaped model features as described by Eqs. 2.6 and 2.7. See Figures 2.7a and 2.10a (page 29). The observed precision in the refined position of the overlapping hat- and ring-shaped features was roughly independent of the mismatch between feature and fit function, but deteriorated at solid disc size $d > 0.8$ or ring thickness $t < 0.5$. The bias increased for increasing mismatch between feature and fit function up to a maximum of 0.06σ . Although a Gaussian fit of a non-Gaussian feature may appear to be very precise, we conclude here that it is systematically biased due to the mismatch between feature and fit function.

In order to obtain more accurate positions for non-Gaussian shaped features, we exploit the ability of our algorithm to accept any fit function. In Figure 2.7b–d we fitted the hat-shaped features with hat-shaped functions, and in Figure 2.10b–d ring-shaped features with ring-shaped functions. In both cases, we observed a bias below 0.2% of the feature radius. The precision even increased for increasingly less Gaussian like features. We hypothesize that this is caused by the steeper gradients at the edges of hat- and ring-shaped features, which lead to a better definition of the position. The other trends in precision are similar to Gaussian-shaped features: the observed constraints are $S/N \geq 2$ and $\sigma \geq 1.8$ px for hat-shaped and $S/N \geq 2.5$ and $\sigma \geq 1.8$ px for ring shaped features.

To summarize, we observed that least-squares fitting to sums of model functions is able to accurately refine the location of overlapping features. The negative bias of multiple pixels present in centre-of-mass centroiding is reduced to less than 0.2% of the feature radius if the feature radius is above 2 px and S/N ratio above 2. The least-squares algorithm is robust against large deviations of the initial location guess, which we tested for deviations up to 50% of the feature radius. This makes fitting to sums of model functions an appropriate method for refining overlapping features, given that the size and noise constraints are met. Although the Gaussian fit function was able to fit hat-shaped and ring-shaped features with precisions compared to Gaussian-shaped

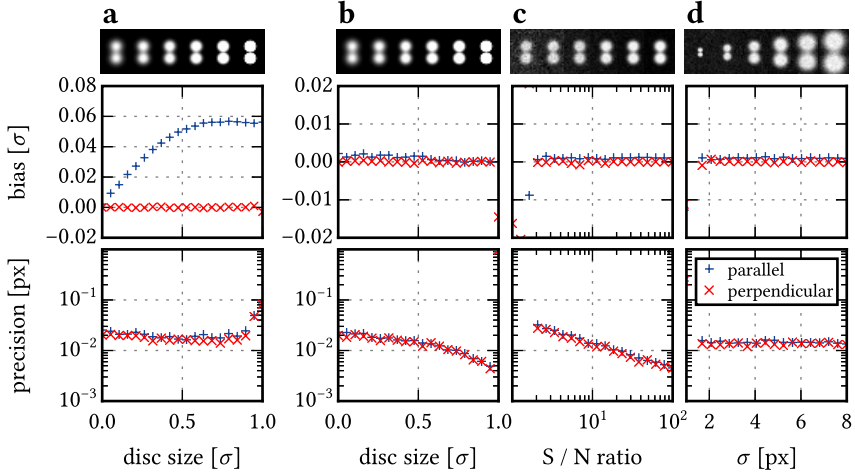


Figure 2.7. Localization errors of hat-shaped features (see Eq. 2.6), which are models for colloidal particles with a size larger than the diffraction limit. Tests were done using Gaussian-shaped (a) and hat-shaped (b)-(d) fit functions. (a) For an increasing solid disc size d , the bias increased up to 0.06σ due to an increasing mismatch between the feature and the (Gaussian) model function. The precision started to decrease above a relative disc size $d = 0.8\sigma$. (b) When a hat-shaped model function was used, the bias improved such that it stayed below 0.002σ for all d . It slightly decreased with increasing d . The precision increased with d . (c) The bias was independent of S/N, and the precision increased with increasing S/N ratio, for S/N values above 2. (d) The bias was proportional to σ , and the precision was independent of σ , for $\sigma \geq 1.8$ px.

features, we showed that the bias in fact increases up to 6 % of the feature radius. By using more appropriate fit functions, this bias can be reduced to 0.2 %, as we showed for hat- and ring-shaped features.

As described by Jenkins *et al.* [76], it is possible to experimentally obtain an average feature shape and successfully use this for feature refinement of single features. If a continuous function is available that describes the average feature, this could be used directly in our framework for least-squares minimization, extending their technique to any number of overlapping features. A different approach of tracking overlapping particles should also be mentioned. Tracking only the non-overlapping part of colloidal dimers has been reported using a mirroring technique⁹³ or cross-correlation.⁹⁴ These techniques rely on a significant fraction of the feature that is not influenced by feature overlap, and are therefore mainly applicable to colloidal dimers.

We note here that from the objective function (Eq. 2.4), not only the minimum, but also the uncertainty in the minimum could in principle be obtained. This computation would provide a per-particle measure for the positional uncertainty, which is important especially for inhomogeneous images. Such a computation would require mapping out

the multidimensional contour at which the objective function $\Delta\chi^2 = \min(\chi^2)$,^{76,95} which is beyond the scope of this chapter.

Although the reported accuracy of 0.002σ is sufficient for most applications, a further improvement could be reached by maximizing the log-likelihood corresponding to Eq. 2.4 instead of using the direct least-squares minimization. For single features, using a maximum likelihood estimator has been proven to give a more precise estimate of the true feature positions.^{70,96}

2.3.3 Constrained least-squares

If additional information about the tracked features is available, constraints can be applied to increase tracking accuracy. In our framework for least-squares optimization of summed radial model functions, any combination of parameters in the image model function (Eq. 2.2) can be constrained by equations of the following form:

$$g(P_n) = 0 \quad \text{or} \quad g(P_n) \geq 0. \quad (2.8)$$

Here, g is a function and P_n is an array consisting of all parameters of features that are in a cluster of size n . We demonstrate the use of constraints here using colloidal dimers with known distance between the two constituent spheres. Using our algorithm we automatically tracked 1006 out of 1170 recorded frames. A constraint was chosen such that the distance between the constituent spheres equals the average distance measured on SEM images ($1.58\ \mu\text{m}$). A video of the resulting tracked three-dimensional images is available online.

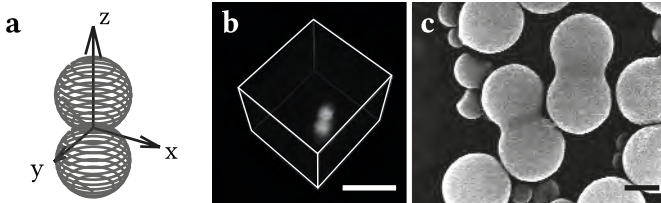


Figure 2.8. Images of colloidal PMMA dimers. (a) The coordinate system corresponding to the diffusion tensor originates from the point of highest symmetry. (b) A typical three-dimensional confocal image that is used for the particle tracking. (c) A representative Scanning Electron Micrograph of the employed colloidal dimers. The scalebars in (b) and (c) denote $5\ \mu\text{m}$ and $1\ \mu\text{m}$, respectively.

As the shape of a colloidal cluster is anisotropic, the short-term diffusion of such a particle is also anisotropic: for example, a dimer experiences a lower hydrodynamic friction when moving along its z -axis, compared to when moving along its x -axis. In general, the dynamics of any Brownian object is described by a symmetric second-rank tensor of diffusion coefficients, consisting of 21 independent elements.⁹¹ We chose the point of highest symmetry as the origin of the cluster based coordinate system and

Table 2.1. Tensor of dimer diffusion coefficients, averaged over time differences (lag times) of 0.2, 0.4, and 0.6 s. The coordinate system is defined in Figure 2.8. The translational coefficients are given in units of $10^{-3} \mu\text{m}^2 \text{s}^{-1}$, the rotational coefficients in units of 10^{-3}s^{-1} , and the rotation-translation cross terms in units of $10^{-3} \mu\text{m} \text{s}^{-1}$. Because rotation around the z-axis cannot be measured for a dimer, we omitted the corresponding elements. The error denotes the 95 % confidence interval estimated using a bootstrap algorithm.

	x	y	z	θ_x	θ_y
x	61.6±4.0	-0.9±2.8	-0.4±3.1	0.0±1.3	-0.4±1.3
y	-0.9±2.8	60.8±3.8	-0.7±3.0	-0.4±1.3	-0.2±1.4
z	-0.4±3.1	-0.7±3.0	65.2±4.2	-0.0±1.3	-0.4±1.4
θ_x	0.0±1.3	-0.4±1.3	-0.0±1.3	12.5±1.1	-0.2±0.7
θ_y	-0.4±1.3	-0.2±1.4	-0.4±1.4	-0.2±0.7	13.4±1.1

aligned the z-axis with the long axis of the dimer, so that all off-diagonal terms in the diffusion tensor are zero. See Figure 2.8a. In order to compute particle displacements for the diffusion tensor, any time difference can be used as long as it is short enough to preserve the orientational information of the cluster. We computed diffusion tensors for lag times of 0.2, 0.4, and 0.6 s. The resulting averaged diffusion tensor reflects the symmetry of the dimer and can be seen in Table 2.1.

In line with previous results from holographic microscopy measurements,⁹⁷ we observed that the translational diffusion constant along z is higher than the translational coefficient along x and y. These results illustrate that our new tracking algorithm is able to compute quantitative information from microscopy images of colloidal clusters without the need of manual corrections.

2.4 Conclusion

We have presented a new algorithm for single-particle tracking that enables automated tracking of overlapping features with high accuracy and precision. It is based on a the well-known algorithm developed by Crocker and Grier⁶⁵ and implements two improvements. First, by exploiting the information obtained from the linking already in the segmentation stage, we were able to use the history of the feature positions to obtain segmentation with significantly fewer mistakes. In a test on two-dimensional experimental data of dimers, all frames were segmented correctly, while the conventional algorithm correctly segmented only 11 % of the frames.

The second improvement consists of a method for sub-pixel accurate localization of overlapping features. The conventional centre-of-mass refinement is unable to find unbiased feature locations: signal overlap results in a negative bias if the feature separation distance is below the mask diameter, and the commonly used rolling average background subtraction imposes a positive bias already at separation distances below approximately 1.5 times the mask diameter. We reach sub-pixel accuracy and precision

by least-squares fitting the unprocessed images to sums of radial model functions.

Firstly, we tested Gaussian-shaped model features with varying separation distance, signal-to-noise ratio, and feature size and found an accuracy of less than 0.2 % of the feature radius, for separation distances above 1.4σ , S/N ratios above 2, and feature radii above 2 px. The precision depends on the S/N ratio only. Secondly, we showed that non-Gaussian features can be tracked with roughly similar precision as the Gaussian features, however the accuracy degrades to 6 % of the feature radius due to the mismatch between feature and fit functions. Thirdly, we showed that significantly better accuracies were obtained by using more appropriate feature models, such as hat- and ring-shaped functions.

We demonstrated the use of constraints in least squares fitting using experimental three-dimensional image sequences of colloidal dimers. Trajectories from 86 % of all frames were readily obtained without any manual refinement. From this, the diffusion tensor was reported and found to accurately reflect the particle symmetry.

With the described method, two problems are solved that are encountered when employing conventional tracking methods on overlapping features. Firstly, the need for case-to-case optimization or manual reparation of tracks is significantly reduced. Secondly, by employing least squares fitting to summed model functions we found that the bias of the centre-to-centre separation distance is 0.2 % of the feature radius in the worst case, which clearly outperforms the centre-of-mass centroiding. Our method provides accurate automated tracking of videos containing overlapping features with minimal need for manual adjustments.

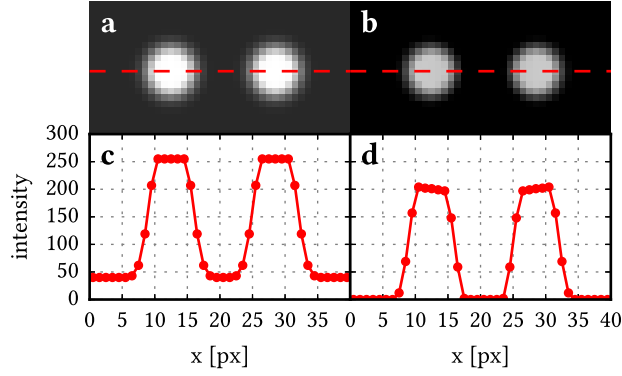


Figure 2.9. Illustration of the positive bias due to background subtraction. If the image background is non-zero (a), it can be subtracted using a rolling average resulting in a perfectly black background (b). However, in the image cross sections (c) and (d), it can be seen that the rolling average also results in a skew of the feature shapes, which gives an outwards directed bias when locating the feature positions.

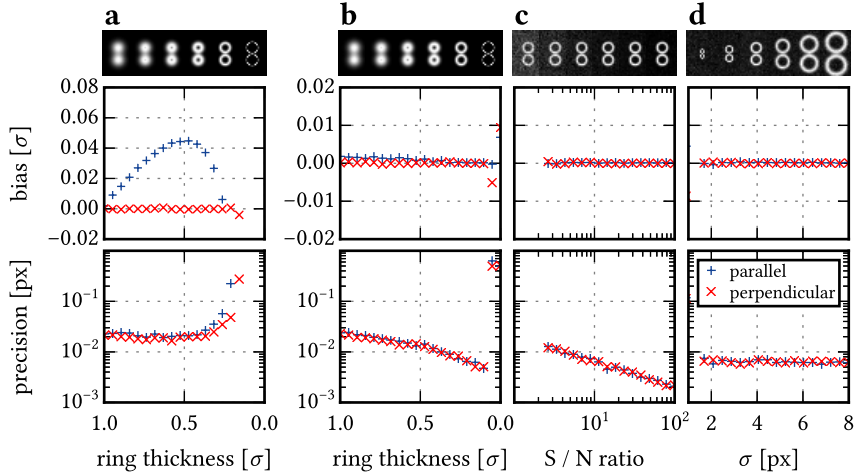


Figure 2.10. Localization errors of ring-shaped features (see Eq. 2.7). These features are models for colloidal particles with surface-bound fluorophores. Tests were done using Gaussian-shaped (a) and ring-shaped (b)-(d) fit functions. (a) Using a Gaussian fit function, the bias increased up to 0.05σ . Below a relative ring thickness t of 0.2σ , the refinement diverged. The precision started to decrease below $t = 0.5\sigma$. (b) When a ring-shaped model function was used, the bias stayed below 0.002σ for $t > 0.1\sigma$. The refinement diverged for too thin rings ($t \leq 0.1\sigma$). The precision increased with t . (c) The bias was independent of S/N , and the precision increased with increasing S/N ratio, for S/N values above 2. (d) The bias was proportional to σ , and the precision was independent of σ , for $\sigma \geq 1.8$ px.

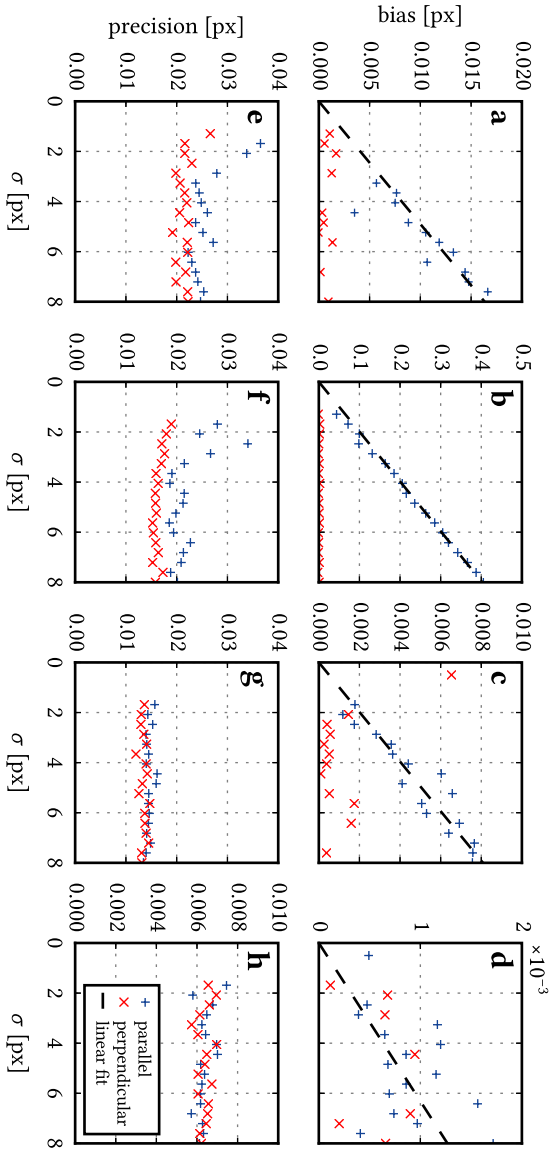


Figure 2.11. Trends of bias and precision with feature size σ . In all cases, the bias was proportional to σ , while the precision was independent of σ . We employed (a) a Gaussian feature to refine with a Gaussian fit function, and (b) a hat-shaped feature with a Gaussian fit function. In (c), a hat-shaped feature is refined with a hat-shaped fit function, and in (d) a ring-shaped feature with a ring-shaped function. In (e)-(h), the corresponding precisions are shown.

FORCE MEASUREMENT FROM SPARSE TRAJECTORIES IN CURVED GEOMETRIES

Abstract

The quantitative measurement of forces between microscopic particles is crucial for understanding soft materials. Here, we describe three methods to extract a potential energy landscape from the trajectories of thermally excited particles. We study the measurement accuracy of these methods using simulated data and we describe how to apply them to arbitrarily curved geometries. The first method uses direct position sampling, for which we establish what determines the optimum sampling time. The second uses displacement sampling. We devise selection rules that allow us to for instance isolate two-body interactions. Then we study the accuracy of maximum likelihood estimation of a piecewise interpolated interaction force using an approximate analytical form for the transition probability. The accuracy of this second method improves with increasing sampling time up to a limiting value that is set by the gradient of the force. The third method is derived from a master equation. This approach does not involve an approximate analytical model for the transition probability, but instead finds a stationary solution from binned transition probabilities. With this chapter, we provide a reference for how to extract forces from the trajectories of thermally activated particles in arbitrary geometries.

3.1 Introduction

Soft materials such as food, ceramics, cosmetics, pharmaceuticals, paints, and even living organisms typically contain particles in the micrometer range. The properties of these complex materials depend sensitively on the interaction forces between these micrometer-sized constituents. Therefore, knowledge of the microscopic interaction forces is crucial for understanding soft material properties. For example, the phase behaviour of colloidal suspensions is governed by the forces between individual particles, which is described by DLVO theory*. This theory has been established experimentally using video microscopy: by following the thermal fluctuations in the positions of individual particles, interaction forces were directly observed.^{65,98,99} This approach has also been successful for measuring forces between colloidal particles and a wall,¹⁰⁰ forces mediated by oil-water interfaces,¹⁰¹ by lipid membranes (see Chapter 5), and even forces acting on single proteins in nerve cells.¹⁰²

Throughout these works, several techniques have been employed to extract interaction forces from particle trajectories. Here, we will summarize these methods and evaluate which is most accurate, using a Brownian dynamics simulation. We will extend these methods for use in curved geometries, to be able to interpret particle movements on the surface of curved lipid membranes. We restrict ourselves to Brownian motion at low Reynolds number, which means that particle inertia does not play a role and particle dynamics are completely described by the overdamped Langevin equation.

The problem is stated as follows: given N particle trajectories of length M and sampling interval τ , what is the interaction energy $U(\vec{x})$? The meaning of the independent coordinate \vec{x} can vary from experiment to experiment: for instance, in the case of particle-wall interaction,¹⁰⁰ \vec{x} is the distance between particle and wall, and for particles that interact via a radial force, \vec{x} is the distance between two particles.^{99,103} As the force measurement methods remain conceptually the same for all these cases, we will first discuss the methods in one dimension only, and afterwards extend them to arbitrary number of dimensions and curved geometries.

First we will describe the direct position sampling method, in which independent observations of \vec{x} are counted and $U(\vec{x})$ is induced by assuming the Boltzmann equilibrium distribution.⁹⁸ Second, we will discuss how to sample displacements instead of positions and use these to induce local forces via either an analytic model of the transition probabilities^{103,104} or via a master equation.^{65,99} Finally, we will discuss how to apply these methods in arbitrary geometries.

3.2 Methods

Particle trajectories were generated using a Brownian dynamics simulation implemented in Python 3.4 and Numpy 1.11. Displacements of single particles in each dimension i

*DLVO is an acronym for Derjaguin, Landau, Verweij, and Overbeek, who formulated the theory that combines the Van der Waals and electrostatic interactions between liquid-immersed charged surfaces.

were drawn from a normal distribution with width $\sigma = \sqrt{2D\tau_S}$ and mean $\mu_i = \beta F_i D \tau_S$, where the diffusion coefficient D was fixed at 0.5, the simulation time step τ_S at 0.001, and the inverse thermal energy β at 1. The force F_i was given by $-\nabla_i U$. We chose the energy U as follows:

$$\beta U(r) = \frac{5\epsilon}{4} \left[5 \left(\frac{r}{\ell} \right)^4 - 4 \left(\frac{r}{\ell} \right)^2 \right].$$

Here, r denotes the distance to the origin, ϵ the energy well depth, and ℓ the extent of the potential field. If not stated otherwise, we used $\epsilon = 2$ and $\ell = 5$. See Fig. 3.1c for the shape of $U(r)$.

3.3 Position-based force measurement

The most straightforward way to induce forces from particle trajectories involves direct sampling of particle positions.⁹⁸ For measuring interactions between particles, the result of this technique is better known as the radial distribution function, which is typically denoted as $g(r)$. Starting from N independent observations, the number of occurrences N_i inside bin i with centre x_i and size δx are counted to estimate the probability density $\rho(x)$:

$$\frac{N_i}{N} = \int_{x_i - \frac{\delta x}{2}}^{x_i + \frac{\delta x}{2}} \rho(x) dx \approx \rho(x_i) \delta x. \quad (3.1)$$

Assuming that the observations of x are sampled at equilibrium, $\rho(x)$ can be related directly to the interaction energy $U(x)$ via the Boltzmann distribution:

$$U(x_i) = U_0 - k_B T \ln \rho(x_i), \quad (3.2)$$

in which the energy U is determined with respect to a reference value U_0 .

To analyse the accuracy of this technique, we sampled $N = 2000$ non-interacting particles in a radial potential field.[†] In Figures 3.1a–b two of these simulations are shown, along with the employed radial potential wells $U(r)$ in solid lines in Fig. 3.1c. From these 2000 particle positions we straightforwardly recovered the energy landscape $U(r)$ that we used in the simulation (see points in Fig. 3.1c). The precision of this measurement is computed directly from the number of observations per bin: it can be shown that the absolute standard error in energy equals $N_i^{-1/2}$, in units of $k_B T$ (see Appendix 1 on page 46).

To assess the accuracy of this method for determining the potential energy, we define the squared deviation of the measured $U(r_i)$ with respect to the model U , averaged over all bins: $\langle \sigma_U^2 \rangle$. We will use this quantity throughout this chapter and call it “the average accuracy”. In Fig. 3.1d it can be seen that this $\langle \sigma_U^2 \rangle$ is inversely proportional to the

[†]Two-dimensional radial coordinates are not directly described by Eq. 3.1. The Jacobian determinant of this coordinate system needs to be incorporated, which in this case amounts to $\delta \vec{x} = r \delta r$. See Section 3.5.

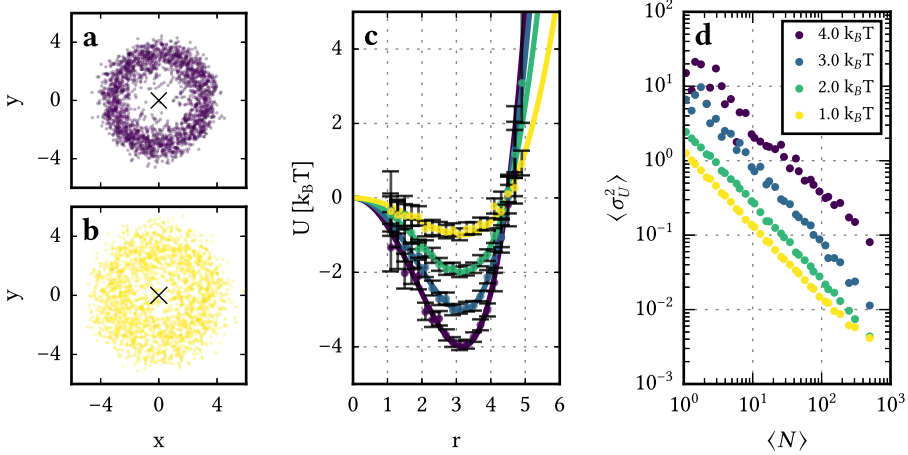


Figure 3.1. Interaction energy measurement of particles in a radial potential field at $\ell = 5$. (a, b) Simulations of $N = 2000$ particles equilibrated in a radial potential field with a well depth ϵ of (a) $4 k_B T$ and (b) $1 k_B T$. The potential energy $U(r)$ for four different well depths (see legend in d) are shown in (c) as solid lines. The energy was measured from the simulations and plotted as dots in (c), with error bars that denote the 2σ confidence intervals. (d) The mean squared deviation of the measured energy with respect to the model function, averaged over 200 independent simulations and over all bins. We varied the number of positions in a single simulation N between 10 and 10000, and the bin width δx between 0.05 and 0.2. On the horizontal axis, the average number of particles per bin is plotted, so that the measurements at different δx collapse onto a single curve. The observed precision follows the expected $\langle \sigma_U^2 \rangle \propto 1/\langle N \rangle$ relation.

average number of particles per bin. The absolute value of this accuracy depends on how the particles are distributed over the bins. Because the number of measurements inside a particular bin scales with the Boltzmann factor, high values of U become exponentially less frequent and therefore, the average accuracy deteriorates rapidly for increasing well depths ϵ . This is demonstrated in Fig. 3.1d: for $\epsilon = 1 k_B T$ we need 140 independent observations per bin to reach an accuracy of $0.1 k_B T$, while for $\epsilon = 4 k_B T$, we already require several thousands. Thus, direct position sampling is only viable when the involved energy differences do not exceed a few units of $k_B T$.

Up to now, we have considered independent observations of particle positions. If we however use positions on the same particle trajectory, these are only independent at considerably long sample times, as positions only change with the square root of time. We here ask the question: what is the average accuracy when coordinates are sampled from a single trajectory with time difference τ between measurements?

Theoretically, the correlation in particle positions is governed by the transition probability $P(x, \tau|x', 0)$, which depends on $U(x)$ that is not known analytically. Therefore,

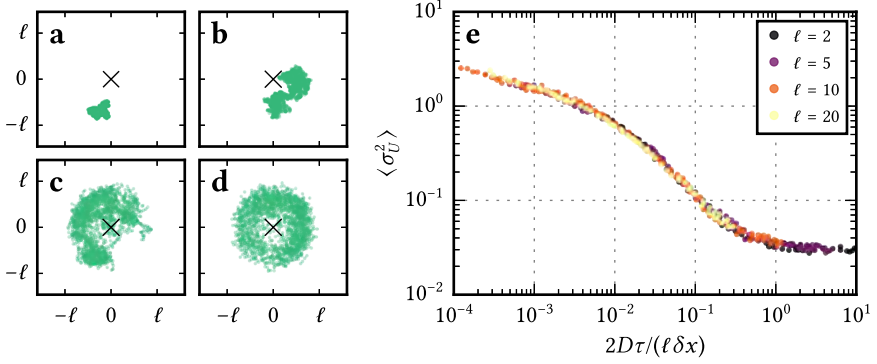


Figure 3.2. Direct sampling method applied to a single trajectory in a radial potential field. (a) to (d) show simulations of $N = 2000$ time steps with different sampling times τ of 0.001, 0.01, 0.1, and 1, respectively. The extent of correlation in position can be observed by eye from these trajectories. (e) We computed the corresponding U and averaged the deviations from the model potential over 200 independent trajectories, at a fixed $\langle N \rangle$ of 100, and for three bin widths δx ranging from 0.05 to 0.2 (plotted in the same colour). If we plot this against the dimensionless parameter $2D\tau/(\ell\delta x)$, we observe a collapse of the data onto a single curve.

we approach this question numerically: for a range of sampling times τ , we simulated 200 independent trajectories of length 2000 in a radial potential field. See Figures 3.2a–d of example trajectories with increasing sampling times. To probe the dependence of the average accuracy on τ , we fixed the average number of particles per bin $\langle N \rangle$ and simulated trajectories for different values of sampling time τ , bin width δx , and potential range ℓ . As can be seen in Figure 3.2e, we observe a data collapse when we plot the average accuracy against $2D\tau/(\ell\delta x)$. Naturally, this rescaling includes $2D\tau$, which is the squared typical distance that a particle displaces in time τ . This is then divided by two length scales: the range of the potential field ℓ , and the bin width δx , yielding a dimensionless number. From these observations we conclude that measurements are uncorrelated if $2D\tau/(\ell\delta x) \gg 1$. Such a dimensional analysis giving the minimum value of τ has been reported before,¹⁰⁰ however they compared $2D\tau$ with a different length scale. With our simulations, we have proven that the optimum sampling time depends on both the bin width and range of the interaction force.

When multiple particles are present in the measurement box, many-body effects have to be taken into account. Extracting two-body forces from many-particle radial distribution functions requires molecular dynamic simulations, and functions only under assumption of pairwise force additivity.^{98,105} In the next section, we will show that displacement-sampling based force measurement does not have this limitation.

To summarize, direct position sampling is a straightforward method that provides interaction energies directly from independent equilibrium positions. However, the

method is only applicable for energy differences of up to a few $k_B T$ and particle trajectories need to be sampled at sampling times $\tau \gg \ell \delta x / (2D)$ in order to ensure independent measurements.

3.4 Displacement-based force measurement

An entirely different approach to induce local forces from particle trajectories makes use of the fundamental Markov property of Brownian motion: as Brownian particles have no memory, their displacements are uncorrelated in time. Therefore, particles can act as local probes of the force field. As long as the sampling interval is above the Brownian timescale of the particles, the measured displacements are uncorrelated. The advantage of this approach is clear: the minimum sampling time is now set by the Brownian timescale, so that many independent measurements can be acquired within a limited time. Also, we need not to assume equilibrium, which allows for the measurement of larger energy differences.

3.4.1 Sampling

In literature, displacement sampling has been employed exclusively in combination with optical tweezers.^{99,103} In these type of experiments, trajectories are typically of high quality, meaning that particles are observed continuously and do not disappear. If we however use displacement sampling to extract forces from particle trajectories in a limited field-of-view and with out-of-focus movement, we have to take care not to introduce a bias in the measured forces. Here, we will describe sampling selection rules that effectively remove this “sampling bias”. These selection rules allow the use of displacement sampling techniques for analysing sparse trajectories.

Starting from observed particle trajectories, positions are rearranged into displacement pairs (x_0, x_1) with a given lag time. If a particle is positioned initially in the middle of the field of view, it will always be observed in the next frame (see triangle in Fig. 3.3). This allows for complete sampling of the particle displacements. However, for a particle that is positioned close to a field of view edge, we cannot sample all displacements, because we do not observe the particle if it steps outside (see diamond in Fig. 3.3). In this case, the mean of this distribution will be biased away from the field of view edge, so that there appears to exist an inwards force that acts on particles near a boundary.

To overcome this “sampling bias”, we include only displacement pairs in which the initial position x_0 is such that we are certain of observing it in the next frame. In this example, we would not include x_0 that is closer than L_τ to a boundary, in which L_τ is the maximum distance a particle can move in the sampling interval. In this way, we remove the sampling bias at the expense of ignoring part of the displacement data. This displacement pair selection is crucial to employ displacement-based sampling methods to sparse trajectories.

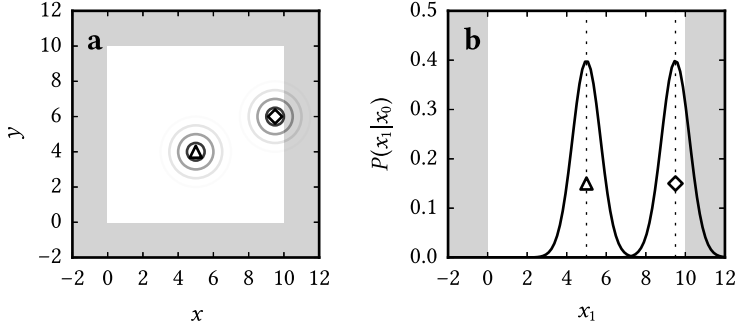


Figure 3.3. Displacement sampling near an edge. (a) A measurement box (white) with two Brownian particles. The circles denote 1, 2, and 3 σ contours of the probability to find particles in the next frame. (b) Transition probability densities $P(x_1|x_0)$ of the x coordinate of the two particles, with their initial positions x_0 shown in dashed lines. The particle in the centre (triangle) will remain visible in the next frame, while the particle at the edge (diamond) can step outside of the field of view, in which case its mean displacement will be biased away from the edge. Therefore, transitions starting close to the edge should be omitted to obtain unbiased displacement samples.

As long as we do not involve the final position x_1 in the selection of displacement pairs, we do not bias the measured distribution $P(x_1|x_0)$. In other words: as long as we base the selection on x_0 only, we can apply any selection rule. This is for instance useful in the case in which particles interact via forces that are not pairwise additive, in which case we look at $P(r_1|r_0)$, with r is the distance between two particles. To isolate the two-body interaction, do not want to incorporate displacement pairs in which the two particles between which r is measured have a third particle closer by than ℓ , the length scale of the interaction. The selection rule that excludes many-body interaction is then formulated as follows: ignore displacement pairs in which r_0 has more than one particle closer than $\ell + 2L_\tau$. Thus, displacement sampling can effectively isolate two-body interactions by adopting an appropriate data selection rule, which poses a clear advantage over the direct position sampling method.

3.4.2 Maximum likelihood estimation

To extract a local force from the sampled particle displacements, a model is required that describes the probability of observing a particle at position x_1 at time $t + \tau$, given a certain initial position x_0 at time t . This so-called *transition probability* $P(x_1, t + \tau|x_0, t)$ can be approximated analytically for sufficiently small times τ , as follows [106, p. 73]:

$$P_\tau(x_1|x_0) = \frac{1}{2\sqrt{\pi D(x)\tau}} \exp \left[-\frac{(x_1 - x_0 - \beta F(x)D(x)\tau)^2}{4D(x)\tau} \right]. \quad (3.3)$$

Here, we introduced $P_\tau(x_1|x_0)$ as a shorthand for $P(x_1, t + \tau|x_0, t)$. $F(x)$ and $D(x)$ are both allowed to vary as function of x , as long as they do not vary significantly within a single displacement.

To obtain the local force and diffusivity, we can straightforwardly compute a two-dimensional histogram of the displacement pairs $\{x_j, x_{j+1}\}$ and evaluate the mean and spread of the distributions for each initial displacement.¹⁰³ A more direct approach was reported recently in ref. [104] and directly fits a model for $F(x)$ and $D(x)$ to the displacements. Here, we employ the latter approach using a constant D and a piecewise interpolated force $F_i = F(x_i)$ on points x_i spaced δx from each other. Given this model, the maximum likelihood of the parameters can then be found by maximizing the log-likelihood \mathcal{L} , which is the logarithm of the probability of observing all the displacements $\{x_j, x_{j+1}\}$ given model parameters D and F_i :

$$\mathcal{L}(\{x_j, x_{j+1}\}|D, F_i) = \sum_{j=1}^N \log P_\tau(x_{j+1}|x_j, D, F_i), \quad (3.4)$$

where P_τ is given by Eq. 3.3. By maximizing this log-likelihood, the maximum likelihood estimate (*mle*) of D and F_i can be found. In Appendix 2 it is shown that the thus obtained F_{mle} indeed equals the force, but that D_{mle} slightly underestimates the true D . Therefore, we chose to fix D to the known value that we used in the simulation and only optimize for F_i . Using Eq. 3.4, a Bayesian approach was adopted to sample the piecewise interpolated force. After numerical integration, the energy was obtained up to an arbitrary choice of a reference energy. In Fig. 3.4a an example of this analysis is shown, obtained from $N = 10000$ uniformly sampled displacement pairs in a radial potential field.

We observed that the average accuracy of this method is inversely proportional to the number of observed displacements N , while it does not depend on the distance between points on the piecewise interpolated force (δx). See Figure 3.4b. Below $N = 1000$, we found that the numerical minimization of the log-likelihood has a high probability to diverge.

The average accuracy is also inversely proportional to τ , which can be understood by comparing the diffusive displacement $\sqrt{2D\tau}$ with the force-induced displacement $\beta FD\tau$. For low values of τ , the diffusive displacements dominate which makes the force measurement less precise. This measurement precision in the estimated force can be derived more precisely in the form of the Cramér-Rao lower bound (see Appendix 2). The energy is obtained through numerical integration of this force, so that this fundamental precision limit propagates into the energy.

We numerically evaluated the average accuracy in the energy by changing the sampling time τ at fixed number of measurements, and found that the accuracy is indeed inversely proportional to τ . See Fig. 3.4c. The numerical integration introduced a dependence on the length scale of the potential field, as displayed in Fig. 3.4c. Here we note that the analytical model for P_τ (Eq. 3.3) becomes inaccurate when the force changes during a single particle displacement, e.g. due to a large gradient in the force. Approximately, the corresponding condition is $\tau \ll (\beta D|F'(x_i)|)^{-1}$ (see Appendix 2). Because of

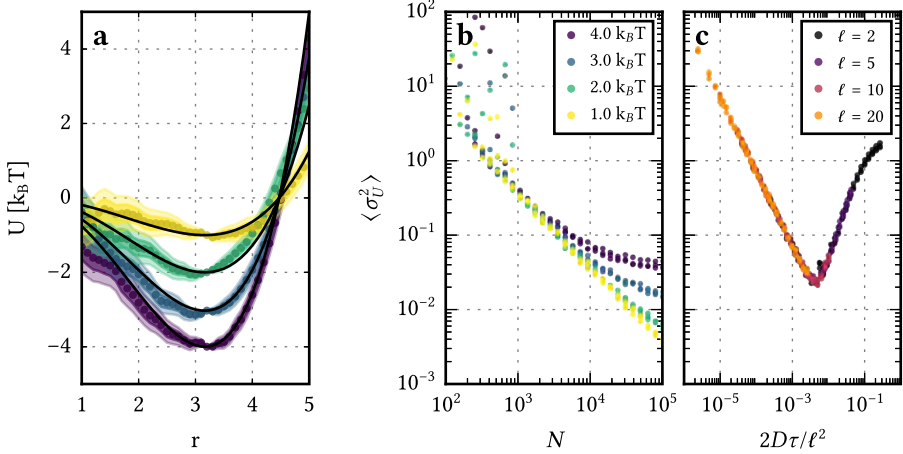


Figure 3.4. Maximum likelihood estimation of the energy applied to a single trajectory in a radial potential field. (a) Real (black line) and measured (points) potential energy curves for different well depths (see legend in b), each with $N = 10000$ measured displacements at $2D\tau = 0.05$. The dark and light shaded regions denote the 1σ and 2σ confidence intervals, respectively. The reference value of U was chosen at the potential minimum, therefore the confidence interval has zero width at that point. (b) The average accuracy of the measured energy $\langle \sigma_U^2 \rangle$, averaged over 200 independent simulations. We varied the number of displacements in a single simulation N between 100 and 100000, and the distance between the points in the piecewise interpolated force (δx) between 0.05 and 0.2, at a sampling time of $2D\tau = 0.05$. We found that the accuracy does not depend on δx and above a minimum sample size of $N = 1000$, the variance is inversely proportional to N , until it levels off due to the inaccuracy of the analytical model for P_r . For increasing well depths, this latter issue becomes increasingly more pronounced. (c) We varied the sampling time τ for different potential length scales ℓ and for δx between 0.05 and 0.2, at fixed $N = 10000$. The average accuracy $\langle \sigma_U^2 \rangle$ was inversely proportional to $2D\tau/\ell^2$, up to a critical value of τ after which it degrades due to inaccuracy of the analytical model for the transition probability.

this effect, we observed in Fig. 3.4c that the average accuracy increases proportionally to τ for larger values of τ .

Summarizing, we have shown that the maximum likelihood estimation is capable of inducing accurate energy profiles from particle displacement data. For optimal precision, sampling time as well as the number of observations should be chosen as high as possible. There however exists an upper limit for τ , which is due to the assumption that F is constant during a displacement. Further refinement of this model may be possible by adapting the chosen model of the transition probability. For instance, the transition probability in a parabolic potential can be derived analytically (the so-called Ornstein-Uhlenbeck process¹⁰⁶), which provides an analytical description up to the second derivative of the energy. Additionally, a means of combining analyses at dif-

ferent lag times into a single log-likelihood function might further improve the precision of this method.¹⁰³

3.4.3 Master equation method

When the previously discussed conditions for the approximate model of the transition probability does not hold, the maximum likelihood estimation becomes inaccurate. To address this issue we will here discuss another approach that makes use of the master equation of ρ . This approach to measuring interaction forces has been reported by Crocker and Grier [65, 99], although not in combination with the here described sampling selection rules, which make this method more widely applicable. Here, we will shortly summarize the method and evaluate its accuracy.

In general, the evolution of a probability density can be described with a master equation, as follows:

$$\rho(x, t + \tau) = \int P_\tau(x|x')\rho(x', t)dx', \quad (3.5)$$

in which the transition probability $P_\tau(x|x')$ is related to $U(x)$, which we want to measure. To find $U(x)$, we do not need to know this relation analytically, as we can use the stationary solution of the master equation:

$$\rho_s(x) = \int P_\tau(x|x')\rho_s(x')dx'. \quad (3.6)$$

If this solution exists, then ρ_s is also a stationary solution of the Smoluchowski equation, which for constant D is equivalent to the Boltzmann distribution in Eq. 3.2. See Appendix 3 for the corresponding derivation. Thus, we can obtain $U(x)$ by sampling the transition probability matrix $P_\tau(x_1|x_0)$ from the measured displacement pairs $\{x_0, x_1\}$ and finding the eigenvector of P_τ with eigenvalue 1.

Using our simulated data, we indeed recovered an accurate $U(x)$ through this method. See Figure 3.5a. The average accuracy $\langle \sigma_U^2 \rangle$ is again inversely proportional to the number of measurements, as can be seen in Fig. 3.5b. The lower boundary of the number of observations N is determined by how the observed displacements pairs $\{x_0, x_1\}$ are distributed over the bins: every initial position bin must contain at least 1 observation to be able to compute the energy. We observed that the accuracy is inversely proportional to $\langle N \rangle$, up to a certain point after which the spatial binning starts to play a role.

In Figure 3.5c it can be seen that for low sampling time τ , the average accuracy improves for increasing $2D\tau/(\ell\delta x)$. The reason for this is the same as for the maximum likelihood method: for low τ , random displacements dominate over the force-induced displacements and therefore the force measurement is less precise. For very large τ , we observed that the accuracy converges to a constant value. In that case, the master equation method is equivalent to the direct position sampling method, because $P_\tau(x_1|x_0)$ then directly equals $\rho(x_1)$, independent of x_0 .

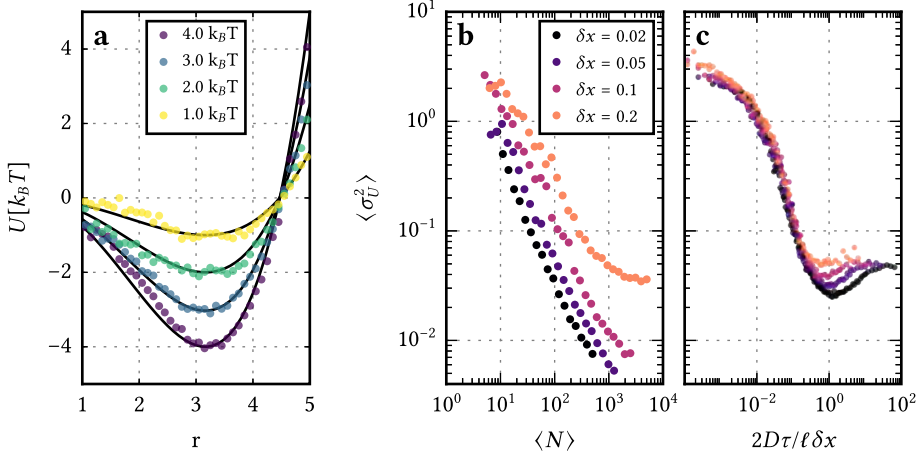


Figure 3.5. The master equation method applied to a single trajectory in a radial potential field. (a) Four examples with $N = 10000$ measured displacements, with the model potential in a black solid line and the measurement potential in coloured dots. (b) The average accuracy $\langle \sigma_U^2 \rangle$ was quantified by averaging the squared deviations of 200 independent simulations with the model function. The sampling time was fixed at $2D\tau = 0.05$, the length scale at $\ell = 5$, and the well depth at $\epsilon = 2k_B T$. The bin width was varied in between 0.02 and 0.2. The average accuracy is inversely proportional to the number of measurements. (c) We measured the average accuracy for four bin widths δx ranging from 0.02 to 0.2 (see legend in b) and four length scales ℓ (plotted in the same colour), at fixed $\langle N \rangle = 100$ and well depth $\epsilon = 2k_B T$. The accuracy improves with increasing $2D\tau/(\ell\delta x)$. Contrary to the maximum likelihood method, it does not deteriorate at larger values of τ . This is because the master equation method does not use an approximation for the transition probability.

3.5 Estimating forces in curved geometries

We have discussed three approaches for force measurement from trajectories in one dimension. Most experiments are, however, performed in multiple dimensions. For example, in sections 3.3 and 3.4, we analysed particle trajectories in a two-dimensional potential field, in which the force was dependent on the distance to the origin r . Therefore, it was useful to describe this system with radial coordinates r and θ (see Figure 3.6a). As a radial force does not depend on the angle θ , the dimensionality of the problem conveniently reduced to one.

However, it is important to note that in this curvilinear coordinate system, the infinitesimal area element dA depends on the coordinates: $dA = r dr d\theta$. This has the consequence that a particle has greater probability to move away from the origin, leading to an apparent force that is merely caused by the choice of coordinate system. In this section, we will describe how to accurately extract forces present in such coordin-

ate system for the three discussed force measurement methods. Also, we will show how to extend this to case that not only the coordinates are curvilinear, but also the geometry itself is curved, for example when a particle is confined to a spherical surface (see Figure 3.6b).

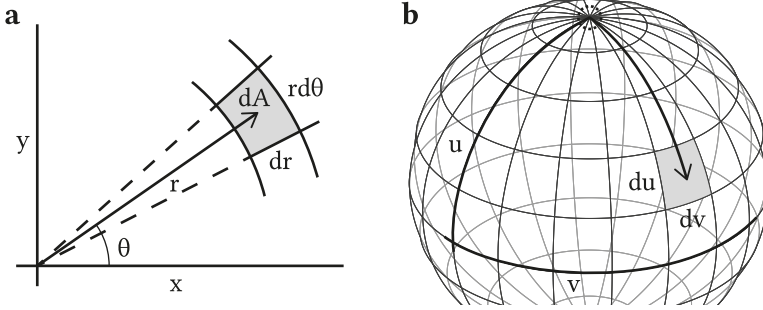


Figure 3.6. Two examples of integration in a non-Euclidean coordinate system. (a) Two-dimensional Euclidean space with a radial coordinate system $\vec{y} = \{r, \theta\}$. The infinitesimal area element dA (shaded region) is given in radial coordinates by $rd\theta dr$. (b) An intrinsically curved coordinate system $\vec{y} = \{u, v\}$ on the surface of a sphere with radius R . The origin of the coordinate system is denoted with a dotted circle. The infinitesimal area element (shaded region) at coordinates $\{u, v\}$ is given by $R^2 \sin(u) du dv$.

Position sampling When determining the probability density from the number of observations, we need to take into account the proper area element. This can be seen through substitution of variables when integrating the probability density:

$$\frac{N_i}{N} = \iint_{\delta A_i} \rho(\vec{x}) d\vec{x} = \iint_{\delta A_i} \rho(\vec{y}) J(\vec{y}) d\vec{y}, \quad (3.7)$$

where N_i is the number of observations in the two-dimensional bin δA_i and $J(\vec{y}) = |d\vec{x}/d\vec{y}|$ the determinant of the Jacobian matrix. $J(\vec{y}) = r$ in two-dimensional radial coordinates (see Figure 3.6a). For sufficiently small bins we can approximate the probability density and obtain:

$$\frac{N_i}{N} \approx \rho(\vec{y}) J(\vec{y}) \delta A, \quad (3.8)$$

where δA denotes the multiplication of the bin sizes in all dimensions. We can use this expression to extract $\rho(\vec{y})$ from a series of observations. From this perspective, the Jacobian determinant acts as a weighing function, as follows:

$$\rho(\vec{y}_i) \approx \frac{1}{N \delta A} \sum_{j=1}^{N_i} \frac{1}{J(\vec{y}_j)}, \quad (3.9)$$

where the summation sign sums over the N_i observations inside bin i . For Euclidean coordinate systems, $J = 1$, and this equation indeed reduces to Eq. 3.1.

Maximum likelihood estimation The extension of the maximum likelihood method into multiple dimensions requires an analytical form of the multidimensional transition probability. In an Euclidean geometry, this is achieved simply by multiplying the transition probabilities of the separate coordinates (Eq. 3.3). In curvilinear coordinate systems, however, we have to use a more complex expression instead, because the diffusion constant becomes a matrix. As a reference, we here provide this expression which was obtained from ref. [106, pp. 81–95].

$$P_\tau(\vec{y}|\vec{y}') = \frac{1}{2^M \sqrt{(\pi\tau)^M \det[\tilde{D}(\vec{y})]}} \times \exp \left[-\frac{1}{4\tau} [\tilde{D}(\vec{y})]_{ij}^{-1} (\Delta y_i - \tilde{F}_i(\vec{y})\tau)(\Delta y_j - \tilde{F}_j(\vec{y})\tau) \right], \quad (3.10)$$

in which repeated indices are summed and M denotes the number of dimensions. $\tilde{F}_i(\vec{y})$ and $\tilde{D}_{ij}(\vec{y})$ are obtained from the diffusion constant $D(\vec{x})$ and force vectors $F_i(\vec{x})$ in a Euclidean metric, as follows:

$$\tilde{F}_i(\vec{y}) = \sum_j \frac{\partial y_i}{\partial x_j} \beta F_j(\vec{x}) D(\vec{x}) + \sum_j \frac{\partial^2 y_i}{\partial x_j^2} D(\vec{x}), \quad (3.11)$$

$$\tilde{D}_{ij}(\vec{y}) = \sum_k \frac{\partial y_i}{\partial x_k} \frac{\partial y_j}{\partial x_k} D(\vec{x}). \quad (3.12)$$

In the example of a two-dimensional radial force, it follows that $\tilde{D}_{rr} = D$, $\tilde{D}_{\theta\theta} = D/r^2$, $\tilde{F}_r = D(\beta F_r + 1/r)$, and $\tilde{D}_{\theta r} = \tilde{D}_{r\theta} = \tilde{F}_\theta = 0$. In the corresponding analysis of trajectories in a two-dimensional radial potential (Fig. 3.4) we observed that this approach provided the same results as when performing the analysis in Euclidean coordinates.

Master equation The transition probabilities in a curved geometry can be sampled in a fashion similar to the direct position sampling method, as is shown conveniently from the master equation (Eq. 3.5). If we transform from an Euclidean coordinate system (\vec{x}) to another (\vec{y}), we obtain the following master equation:

$$\rho(\vec{y}, t + \tau) J(\vec{y}) = \int P_\tau(\vec{y}|\vec{y}') \rho(\vec{y}', t) J(\vec{y}') d\vec{y}' \quad (3.13)$$

$$\rho(\vec{y}, t + \tau) = \int \left[P_\tau(\vec{y}|\vec{y}') \frac{J(\vec{y}')}{J(\vec{y})} \right] \rho(\vec{y}', t) d\vec{y}'. \quad (3.14)$$

Therefore, $\rho_s(\vec{y})$ is not an eigenvector of the probability matrix $P_\tau(\vec{y}|\vec{y}')$, but of the rescaled probability matrix shown between brackets in Eq. 3.14. In our example of 2D radial coordinates, we thus have to weigh a displacement from r_0 to r_1 with r_0/r_1 when estimating the transition probability matrix. This approach is reminiscent of the projection method that is described in ref. [99], however by expressing this in the Jacobian determinant, we extended the method into arbitrarily curved geometries.

Curved geometry Some processes not only require a curvilinear coordinate system, but also take place on a geometry that has an intrinsic curvature. For example in Chapter 5, we extract a two-body interaction force from particle trajectories that are confined to a spherical surface. See Figure 3.6b for the corresponding coordinate system, in which we fixed one of the particles in the origin. In this case the intrinsic curvature of the geometry should be accounted for, which is possible through the embedding of the curved surface into three-dimensional flat space. In the example of a spherical surface, this embedding is formulated as follows:

$$\begin{cases} x_1 = R \cos v \sin u \\ x_2 = R \sin v \sin u \\ x_3 = R \cos u \end{cases} \quad (3.15)$$

Here, $\{x_1, x_2, x_3\}$ denote the three-dimensional Euclidean coordinates, R the curvature of the sphere, and $\{u, v\}$ the internal coordinates of the surface. An analytical model for the transition probability on the curved geometry can be acquired directly from these equations by evaluating the partial derivatives and substituting them in equations 3.10–3.12.

For the direct position sampling (Eq. 3.9) and the master equation (Eq. 3.14) methods, the infinitesimal area element J on the surface needs to be evaluated. This can be done through the metric tensor $g_{\mu\nu}$ as follows [107, pp. 88-90]:

$$g_{\mu\nu} = \sum_i \frac{\partial x_i}{\partial y_\mu} \frac{\partial x_i}{\partial y_\nu}, \quad (3.16)$$

$$J = \sqrt{\det g_{\mu\nu}}. \quad (3.17)$$

In the example of a spherical surface parametrized by $\vec{y} = \{u, v\}$, it follows that $g_{\mu\nu} = \{\{R^2, 0\}, \{0, R^2 \sin^2 u\}\}$, so that $J = R^2 \sin u$.

3.6 Summary and Conclusion

We have discussed three different techniques of measuring forces from the trajectories of Brownian particles in arbitrary geometries.

The first approach samples the equilibrium positions and computes the energy profile directly through the Boltzmann factor. We found that this approach requires that

particle positions are uncorrelated in time, with the condition $2D\tau \gg \ell\delta x$, with τ the sampling time, D the diffusion coefficient, ℓ the length scale of the potential, and δx the bin width. Provided that particle positions are uncorrelated, the measurement precision can be estimated directly from N_i , the number of particles per bin: $\sigma_{U,i} = k_B T / \sqrt{N_i}$. If enough independent samples from an equilibrium distribution are available, this straightforward approach is the method of choice.

A fundamentally different method uses displacement pairs instead of positions. This does not require the particle positions to be equilibrated, and as displacements are uncorrelated in time, higher sampling times are possible. This allows for force measurement from sparse data sets as well as selection of particular parts of the trajectory if necessary. Here presented data selection rules are able to remove artefacts such as three-body interactions without introducing a bias.

Displacements can be fitted directly to an analytical model of the transition probability. As this maximum likelihood approach is based on a log-likelihood maximization, we can use Bayesian methods to estimate the confidence intervals for the force. We found that the accuracy of the method improves with increasing sampling time τ , as long as forces are constant during each observed displacement. The corresponding condition for τ was found to be $\tau \ll (\beta D |F'(x_i)|)^{-1}$, with β the reciprocal thermal energy, and F' the gradient of the force.

If this condition cannot be met, a master equation approach can be used. This method is also based on the measurement of particle displacements, however it does not assume a model for the transition probability. Although this is less constrained than the direct fit to an analytical model of the transition probability, it does not provide a straightforward way to estimate the measurement precision. Therefore, when the sampling can be performed sufficiently fast, the transition probability method is preferred.

Appendix 1: Uncertainty in position sampling

The variance in the number of occurrences N_i inside a single bin is given by the Poisson distribution. For sufficiently large N_i , this is approximated by $\sigma_N^2 = N_i$. As ρ is proportional to N_i , the relative standard deviation in ρ is given by:

$$\frac{\sigma_\rho}{\rho} = \frac{\sigma_N}{N_i} = \frac{1}{\sqrt{N_i}}. \quad (3.18)$$

Using a Taylor series and Eq. 3.2, the standard deviation in U is then given as follows:

$$\sigma_U \approx \sigma_\rho \left| \frac{d}{d\rho} \left[k_B T \ln \left(\frac{\rho}{\rho_0} \right) \right] \right| = k_B T \frac{\sigma_\rho}{\rho} = \frac{k_B T}{\sqrt{N_i}}. \quad (3.19)$$

The average accuracy $\langle \sigma_u^2 \rangle$ is then directly given by Eq. 3.19 and depends on how the particles are distributed over the bins:

$$\langle \sigma_u^2 \rangle_{bins} = k_B T \langle N_i^{-1} \rangle_{bins}. \quad (3.20)$$

Appendix 2: Uncertainty in maximum likelihood estimation

The log-likelihood given by Equations 3.3 and 3.4 provides a maximum likelihood estimation of the parameters D and F . As Eq. 3.3 is a normal distribution with mean $\mu = \beta F D \tau$ and variance $\sigma^2 = 2D\tau$, the expected values of the maximum likelihood estimates of μ and σ^2 are given as follows:¹⁰⁸

$$E[\mu_{mle}] = \mu, \quad (3.21)$$

$$E[\sigma_{mle}^2] = \frac{N-1}{N} \sigma^2, \quad (3.22)$$

where N denotes the number of measurements. The expected value of μ_{mle} is unbiased, in contrary to the expected value of σ_{mle}^2 . Therefore, we prefer to determine the diffusion constant D separately and use this as a fixed constant in the maximum likelihood estimation. In that case, the fundamental limit in the measurement precision of μ_{mle} is given by the Cramér-Rao lower bound:¹⁰⁸

$$\text{var}[\mu_{mle}] = \frac{\sigma^2}{N}, \quad (3.23)$$

from which the expected variance in the measured force is readily obtained:

$$\text{var}[\beta F_{mle}] = 2(ND\tau)^{-1}. \quad (3.24)$$

Using Eq. 3.24, we can estimate the precision in each point of the piecewise approximation for $F(x)$. The observed accuracies and precisions are plotted against the expected precision $2(N_i D \tau)^{-1}$ in Figure 3.7. We observed that this expression systematically underestimated the precision by a factor of 1.7.

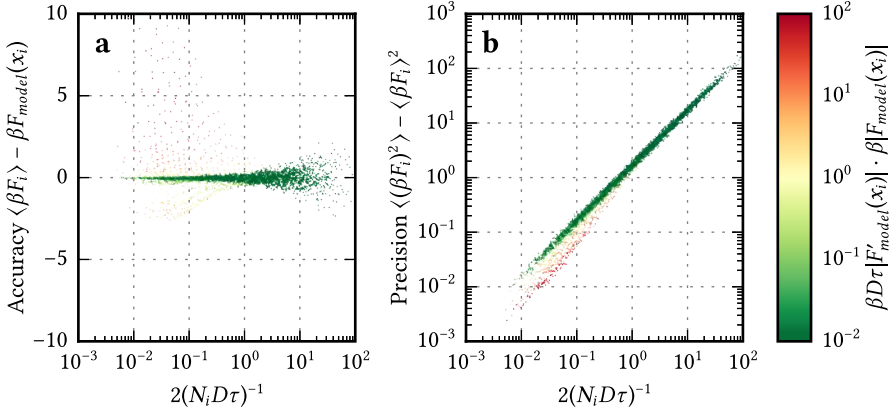


Figure 3.7. Accuracy and precision the maximum likelihood estimate of the piecewise interpolated force, for each $F_i = F_{mle}(x_i)$ separately. These were obtained from 200 independent simulations with ℓ ranging from 2 to 20, δx from 0.05 to 0.2, and τ from 0.001 to 1. N_i is the number of observations within δx of x_i . On average, the observed precision was 1.7 times the expected precision. The observations are coloured based on the force gradient in x_i , multiplied with the root mean squared expected displacement in that point. For large force gradients, the accuracy clearly degrades.

In this figure, it is also shown that this method becomes inaccurate if the local force gradients become too large. From a Taylor expansion of F around x_i , we estimate that the inaccuracy due to a gradient is given by:

$$|\langle F_i \rangle - F_{model}| \approx |\Delta x F'(x_i)| = \sqrt{2D\tau + (\beta F(x_i)D\tau)^2} |F'(x_i)|. \quad (3.25)$$

To find a useful expression for the upper limit of τ , we take the approximation $(\beta F)^2 \gg 2/(D\tau)$. When looking for an upper limit for τ , this approximation is often valid in at least one point on the interaction curve. We then obtain the following expression for the accuracy in F_i :

$$\left| \frac{\langle F_i \rangle - F_{model}}{F_{model}} \right| \approx |\beta F(x_i) D \tau F'(x_i)|, \quad (3.26)$$

which provides an upper limit for the sampling time: $\tau \ll (\beta D |F'(x_i)|)^{-1}$.

Appendix 3: Stationary solution of the Smoluchowski equation

We start with the Smoluchowski equation in a curved geometry:

$$\partial_t \rho = \nabla_\mu (D_{ij} \partial_\nu - \beta D_{ij} F_\nu) \rho. \quad (3.27)$$

Here, ∂_i denotes the partial derivative with respect to i , ∇_μ the covariant derivative, D_{ij} the diffusion matrix, and β the inverse of the thermal energy. As the diffusion matrix is a contravariant tensor,¹⁰⁶ we can replace D_{ij} with $Dg^{\mu\nu}$ if diffusion is isotropic in an Euclidean coordinate system. Here $g^{\mu\nu}$ is the inverse of the metric tensor. Therefore, using the Einstein notation:

$$\partial_t \rho = D \nabla_\mu (g^{\mu\nu} \partial_\nu - \beta g^{\mu\nu} F_\nu) \rho. \quad (3.28)$$

The force is related to the energy through differentiation, $F_\nu = -\partial_\nu U$. We now find a stationary solution, using the identity $\nabla_\mu g^{\mu\nu} = 0$ [107, p. 99]:

$$\begin{aligned} 0 &= \nabla_\mu (g^{\mu\nu} \partial_\nu - \beta g^{\mu\nu} F_\nu) \rho \\ &= (\partial_\nu \nabla_\mu g^{\mu\nu} + g^{\mu\nu} \nabla_\mu \partial_\nu - \beta F_\nu \nabla_\mu g^{\mu\nu} - \beta g^{\mu\nu} \nabla_\mu F_\nu) \rho \\ &= (g^{\mu\nu} \nabla_\mu \partial_\nu - \beta g^{\mu\nu} \nabla_\mu F_\nu) \rho \\ &= g^{\mu\nu} \nabla_\mu (\partial_\nu \rho + \beta \rho \partial_\nu U) \\ \rho &= \rho_0 \exp(-\beta U). \end{aligned}$$

Part II

Membrane mediated interactions

SURFACTANT-FREE COLLOIDAL PARTICLES WITH SPECIFIC BINDING AFFINITY

This chapter is being considered by Langmuir as C. M. van der Wel, N. Bossert, R. W. Verweij, Q. C. Mank, M. G. T. Winter, D. Heinrich and D. J. Kraft, 'Surfactant-free colloidal particles with specific binding affinity'. Reproduced with permission, unpublished work copyright 2017 American Chemical Society.

Abstract

Highly specific coatings are essential for techniques such as in vivo and in vitro biosensing, targeted drug delivery, and micrometer-scale self-assembly. Key to these techniques are typically colloidal particles with a coating that provides a high affinity to a specific molecule. Current particle coating methods require adsorbed surfactants, which typically influence lipid membranes. To address this issue and employ these particles for targeting molecules in lipid membranes, we have developed a completely surfactant-free coating method that provides target-specific colloidal particles. After activating charge-stabilized polystyrene microparticles with EDC/Sulfo-NHS, we first coat the particles with a specific protein and subsequently with a dense layer of poly(ethylene) glycol. This polymer layer provides colloidal stability at physiological conditions as well as anti-adhesive properties, while the protein coating provides the specific affinity to a targeted molecule. We show that NeutrAvidin coated particles bind specifically to biotinylated membranes, and that Concanavalin A coated particles bind specifically to the glycocortex of *Dictyostelium discoideum* cells. The affinity of the particles changes with the protein density, which can be tuned during the coating procedure. The here reported generic and surfactant-free coating method transfers the high affinity and specificity of a protein onto colloidal polystyrene microparticles.

4.1 Introduction

Surfaces with a high affinity to specific molecules are crucial in biological applications such as biosensing^{109,110} and drug targeting.^{111,112} Central to these applications is a particle coating that provides a high affinity and specificity to certain target molecules of interest. For example, colloidal particles can be functionalized with an affinity to particular proteins that are over-expressed on the cellular membrane of a tumour cell,¹¹³ which enables local drug release at targeted cells. We here focus on polystyrene microparticles that especially target molecules that are embedded in lipid membranes. Such particles are required in fundamental membrane studies such as membrane tether pulling,^{114,115} membrane viscosity measurements,^{116,117} and the quantification of membrane mediated forces.^{21,104,118} Also, it has recently been shown that a specific linkage between particles and lipid membranes can be adopted for the self-assembly of particles into mobile structures such as colloidal clusters, polymers, and dynamic networks.^{44,46,119,120}

A controllable affinity and specificity of colloidal particles requires a careful design of the surface coating process.^{47,109,110,121–123} Next to moieties that provide the actual affinity, hydrophilic polymers are typically attached to the particle surface, which are necessary to prevent the undesirable aggregation of particles at physiological salt concentrations. These seemingly contradicting requirements—specifically attracting moieties next to generically repelling polymers—are usually met by adsorbing a polymer surfactant onto the colloidal particles before or during the coating process. These polymers provide steric stabilisation against aggregation, while the functional binding sites of the particles are still accessible. However, amphiphilic polymers are known to interact with lipid membranes.^{124–127} If these colloidal particles are used in lipid membrane studies, desorbing surfactants may disrupt the lipid membranes and compromise the accuracy of the corresponding measurements. Therefore, a surfactant-free coating is required for studies involving lipid membranes.

To meet this requirement, we have developed a two-step method yielding stable and specific polystyrene microparticles that can be applied to lipid membrane studies. First, we created colloidal particles with a high affinity through immobilization of proteins that specifically bind to the desired target molecules.^{128–130} We focus mostly on the use of NeutrAvidin, as its affinity to biotin is used in many practical applications. This protocol can readily be used to prepare particles with other target-specificity, as we demonstrate by also employing the sugar-binding Concanavalin A. Second, we do not stabilize the colloidal particles by using adsorbed surfactants, but instead by covalent grafting of methoxypoly(ethylene) glycol (mPEG) to the particle surface, in such a way that it preserves the affinity and specificity of the tested proteins. At sufficiently high surface densities, mPEG is known to suppress particle aggregation.¹³¹ Also, a dense mPEG coating has been proven to suppress non-specific protein adsorption on the particles, thus providing “stealth” properties necessary for drug targeting in living organisms.^{109,111} These properties make mPEG an ideal choice as a stabilizer for colloidal particles at physiological conditions.

In this chapter, we will first describe the synthesis method and study the effect of

various parameters on the resulting surface density of avidin. Then we will assess the binding affinity of avidin-functionalized colloidal particles on biotinylated Giant Unilamellar Vesicles (GUVs). Finally, we show that avidin-functionalized particles bind specifically to biotinylated lipid membranes, and Concanavalin A-functionalized particles to the cellular membrane of *Dictyostelium discoideum* cells.

4.2 Methods

Materials Styrene (99%), itaconic acid (99%), 4,4'-azobis(4-cyanovaleric acid) (98%, ACVA), hydrochloric acid (HCl), D-glucose (99%), sodium phosphate (99%, Na₂HPO₄), deuterium oxide (70%, D₂O), Pluronic F-127, N-hydroxysulfosuccinimide sodium salt (98%, Sulfo-NHS), 1,3,5,7-tetramethyl-8-phenyl-4,4-difluoroboradiazaindacene (97%, BODIPY), and Newborn Bovine Serum (NBS) were acquired from Sigma-Aldrich; methoxypoly(ethylene) glycol amine (mPEG, M_w = 5000) from Alfa Aesar; sodium hydroxide (NaOH, 98.5%), sodium chloride (NaCl, 99%) and sodium azide (NaN₃, 99%) from Acros Organics; 1-ethyl-3-(3-dimethylaminopropyl) carbodiimide hydrochloride (99%, EDC) from Carl Roth; NeutrAvidin (avidin) and biotin-4-fluorescein from Molecular Probes; biotin-5'-TTTAATATTA-3'-Cy3 DNA oligonucleotides (btn-DNA-Cy3) from Integrated DNA Technologies; Δ9-cis 1,2-dioleoyl-*sn*-glycero-3-phosphocholine (DOPC), 1,2-dioleoyl-*sn*-glycero-3-phosphoethanolamine-N-[biotinyl-(polyethylene glycol)2000] (DOPE-PEG-biotin), 1,2-dioleoyl-*sn*-glycero-3-phosphoethanolamine-N-[methoxy(polyethylene glycol)2000] (DOPE-PEG), and 1,2-dioleoyl-*sn*-glycero-3-phosphoethanolamine-N-(lissaminerhodamine B sulfonyl) (DOPE-rhodamine) from Avanti Polar Lipids; OptiMEM (without phenol red), Dulbecco's modified minimal essential media (without phenol red, DMEM), Geneticin, Blasticidin-S HCl, GlutaMAX, and Trypsin from Life Technologies; Fetal Calf Serum (FCS) from Biowest; Penicillin-Streptomycin (P/S) from Duchefa Biochemie. All chemicals were used as received. Deionized water with 18.2 MΩcm resistivity was used, obtained using a Millipore Filtration System (Milli-Q Gradient A10). HL5 medium consisted of 5 g L⁻¹ protease peptone, 5 g L⁻¹ thiotone E peptone, 10 g L⁻¹ glucose, 5 g L⁻¹ yeast extract, 0.35 g L⁻¹ Na₂HPO₄ · 7 H₂O, 0.35 g L⁻¹ KH₂PO₄, and 0.05 g L⁻¹ dihydrostreptomycin sulphate, with a pH of 6.4-6.7. A549 cell imaging medium consisted of OptiMEM, 2.5 vol% FCS, 0.2 g L⁻¹ P/S, and 1.8 mM Glutamine-S. 3T3 cell imaging medium consisted of DMEM, 10 vol% NBS, 0.2 g L⁻¹ P/S, and 2 mM GlutaMAX.

Particle preparation Carboxylic acid functionalized polystyrene spheres were prepared using a surfactant-free dispersion polymerization protocol.¹³² To a solution of 500 mg itaconic acid in 125 mL water, 25 g styrene was added in a magnetically stirred round bottom flask. The mixture was purged four times with nitrogen and heated to 85 °C in an oil bath. Separately, 250 mg ACVA was dissolved in 9 mL of 0.2 M NaOH. This initiator was injected into the reaction mixture while stirring at 500 rpm. The reaction was allowed to proceed overnight, after which the dispersion was cooled down to

room temperature. Macroscopic polystyrene aggregates were filtered out through glass wool, after which the sample was washed three times with water. In order to obtain fluorescent particles, the synthesis procedure was repeated with additionally dissolving 10 mg of BODIPY (ex. 488 nm, em. 515 nm) in the styrene before addition to the reaction mixture. The size distribution was determined using a FEI nanoSEM 200 scanning electron microscope (see for example Fig. 4.1e). The non-fluorescent particles employed in this chapter were $1.06 \pm 0.02 \mu\text{m}$ in diameter, and the fluorescent particles $0.98 \pm 0.03 \mu\text{m}$. Their respective ζ -potentials in water (pH 5.7) were determined to be $-54 \pm 4 \text{ mV}$ and $-55 \pm 4 \text{ mV}$ using a Zetasizer Nano ZS from Malvern Instruments. These strongly negative values reflect the high density of carboxylic acid groups ($1\text{--}10 \text{ nm}^{-2}$) on the particle surface.¹³²

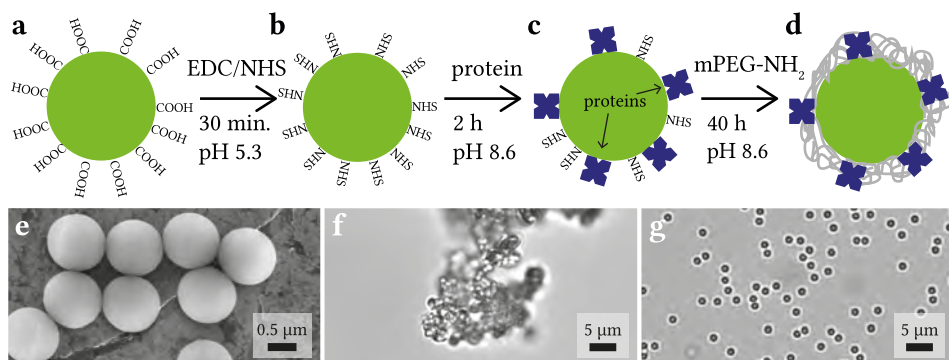


Figure 4.1. Illustration of the particle coating procedure. (a) Highly carboxylated (COOH) polystyrene particles were first activated using EDC/NHS so that the carboxylic acid groups form NHS esters. (b) The activated particles were then mixed with a precise quantity of protein at pH 8.6. (c) After a delay time of typically 2 hours, an excess of amine-functionalized methoxypoly(ethylene) glycol (mPEG-NH₂) was added to stabilize the particles. (d) The resulting particle coating contains the added proteins as well as a dense PEG layer that provides colloidal stability. (e) A Scanning Electron Micrograph of the uncoated particles. Light microscopy images after 1 h in 1 M NaCl show that (f) the uncoated polystyrene particles aggregated strongly and (g) the mPEG coated particles remained dispersed.

Coating and stabilization The particle coating procedure was extended from a covalent mPEG grafting protocol from literature¹³¹ (see Figure 4.1). All reactions were performed on a vortex mixer at 4 °C. The poly(styrene) particles with carboxylic acid groups were activated by adding 8 mM EDC and 2.5 mM Sulfo-NHS to the particles, which were suspended at 20 g/L. The EDC and Sulfo-NHS were dissolved immediately before use. At this concentration, the hydrochloric acid in the EDC ensures a pH of 5.3, which was confirmed using a calibrated Hach PH17-SS ISFET pH probe. After 30 min of mixing, the pH was brought to 8.6 using 0.2 M NaOH. At this pH, NHS hydrolysis starts, which

is reduced by performing the reactions at 4 °C. Then 5–500 µg of protein (NeutrAvidin or Concanavalin A) was added to 750 µL (15 mg) of the activated particles. After a delay time of 2 h, 4.0 mg mPEG5000-NH₂ dissolved in 200 µL water was added. The reaction was allowed to proceed for at least 40 h. To remove the remaining NHS groups, the pH was increased to 12 for 5 min using 1 M NaOH. For some proteins this high pH is undesirable, in which case pH 9 may be used for a longer time period to hydrolyse the NHS esters at room temperature.¹³³ The particles were washed one time with 10 mM HCl to neutralize the pH and three times with water. Finally, sodium azide was added to a concentration of 3 mM to prevent bacterial growth. The colloidal stability of each sample was assessed as follows: 50 µg particles were dispersed in 10 µL 1 M NaCl. After 1 h of mixing, the sample was diluted 20 times with 1 M NaCl and imaged using bright field microscopy (Fig. 4.1g). Resulting particle suspensions can be stored for at least two months at 4 °C. For longer shelf life, the particle suspensions should be frozen at -20 °C.

Avidin titration assay The number of biotin binding sites on the particles was measured using a titration assay, based on the binding of biotin-4-fluorescein to the particle-attached avidin. Because of the strong scattering of the particles, we could not measure the fluorescence of the avidin-bound biotin-4-fluorescein directly as described elsewhere.¹³⁴ Instead, we determined the remaining fluorescence of the supernatant for different amounts of added biotin-4-fluorescein. From a single particle batch, precisely known aliquots of 0.3–0.6 mg particles were dispersed into 1.00 mL PBS buffer (12.5 mM Na₂HPO₄, 50 mM NaCl, 3 mM NaN₃, with a pH of 7.5). Subsequently, quantities of 0–10 µL of 1.8–7.3 µM biotin-4-fluorescein were incubated with the particles for 20 min at 55 °C. After this, the particles were removed by centrifugation. Then, 750 µL supernatant was diluted with 750 µL PBS and the fluorescence of each aliquot was determined using a Varian Cary Eclipse fluorescence spectrophotometer (ex. 494 nm, em. 524 nm). From the intersection of the baseline fluorescence and the final slope of the titration curve, the amount of biotin binding sites in the sample was determined. Together with the separately determined dry weight and diameter of the particles, the amount of biotin binding sites per particle was computed.

Avidin fluorescence assay In order to measure the distribution of biotin binding sites on avidin-functionalized particles within a single batch, we added a fluorescent marker for use in fluorescence microscopy. The employed fluorescent marker was a biotin- and Cy3-functionalized DNA oligonucleotide, as DNA is well soluble in water and shows no aspecific adsorption to the particle surface. To stain the particle-attached avidin, we incubated 50 µg particles with 60 pmol btn-DNA-Cy3 in 310 µL PBS buffer for 30 min at 55 °C in a nuclease-free plastic microtube. To be able to use the same protocol for unstable particles, we added 0.5 wt% of the steric stabilizer Pluronic F-127 to the PBS buffer (see previous subsection for the contents). After cooling down to room temperature, the samples were washed three times with water and one time with PBS. Finally, the samples were inserted into a rectangular capillary and imaged on a Nikon

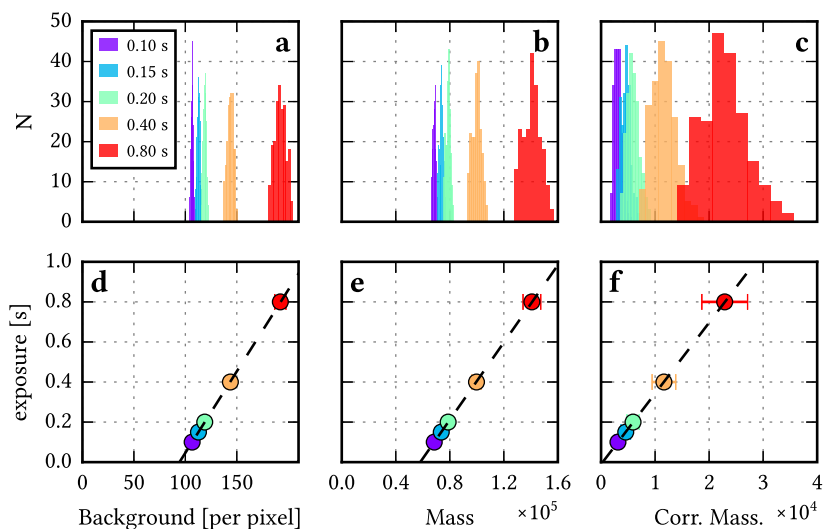


Figure 4.2. Emission intensity of the same particle batch at different camera exposure times. (a) Histograms of the background emission around each particle for different exposure times. (d) The corresponding fit shows a linear relation, but nonzero intercept. (b) Histograms of the integrated intensity of each particle. (e) The corresponding fit shows a linear relation. (c, f) The background-corrected mass is proportional to the camera exposure time.

Ti-E microscope equipped with a Nikon $100\times$ CFI Apo TIRF oil-immersion objective ($NA = 1.49$), Intensilight fluorescent lamp (ex. 540 ± 25 nm, em. 605 ± 55 nm), and a DS-Qi1 monochrome CCD camera with an exposure time that was set such that all particles had a fluorescence signal in between the camera background and saturation levels (100–800 ms). In a separate experiment, the background-corrected emission intensity per feature was confirmed to be proportional to the exposure time (see Fig. 4.2). The resulting images were ensured to be in the same focal plane and the integrated intensity per particle was computed using Trackpy.⁸⁶

Giant unilamellar vesicles GUVs of 10–100 μm diameter were prepared by electroformation.¹³⁵ Lipid mixtures consisting of 97.5 wt% DOPC, 0.5 wt% DOPE- rhodamine and 2 wt% DOPE-PEG-biotin (or DOPE-PEG) were prepared in chloroform at 2 g L^{-1} . 10 μL of this lipid solution was dried on each of two 6 cm^2 ITO-coated glass slides ($15\text{--}25\ \Omega/\text{sq}$, Sigma-Aldrich). The two electrodes were placed in 1.8 mL of 100 mM glucose solution (with 0.3 mM NaN_3) and subjected to 1.1 V (rms) at 10 Hz for 2 h, with a gradual increase during the first 2 min. The vesicles were stored in a BSA-coated vial at room temperature.

Dictyostelium discoideum cell preparation *Dictyostelium discoideum* SadA-GFP Lim-RFP cells were cultured in HL5 medium at 21 °C and supplemented with 10 mg L⁻¹ Geneticin and 10 mg L⁻¹ Blasticidin-S. For the experiments the cells were harvested and washed three times with phosphate buffer (PB; 2.00 g L⁻¹ KH₂PO₄ with 0.36 g L⁻¹ Na₂HPO₄ · H₂O, with a pH of 6.0) by centrifugation at 400 rcf for 5 min.

Imaging Samples were prepared on a hydrophobic coverslip that was incubated for 15 min in Pluronic F-127 (5 wt% in water). Subsequently, the excess Pluronic F-127 was removed by washing three times with the appropriate buffer. GUV samples were prepared by consecutive addition of 50 µL phosphate buffered saline solution (with a total osmotic content of 100 mM), 0.5 µL 3 wt% particles, and 2 µL GUVs. *D. discoideum* samples were prepared by subsequent addition of 50 µL PB (see previous subsection), 0.5 µL 1.5 wt% particles, and 10 µL cells. All microscopy images were taken 30–45 min after mixing. Microscopy images were acquired with a Nikon Ti-E microscope equipped with a A1R confocal scanhead and a 60× water immersion objective ($NA = 1.2$). The sample was mounted on a MCL Nanodrive to enable fast z-stack acquisition.

4.3 Results and Discussion

We here describe a surfactant-free preparation method of colloidal particles that specifically bind to target molecules. In this method, polystyrene microparticles are first coated with a protein that provides the specific affinity, and subsequently with a layer of mPEG that provides stability against aggregation under physiological conditions (see Fig. 4.1). As protein we primarily use avidin, which has a high affinity to biotin, and further show that the method is readily transferable to the sugar-binding Concanavalin A. In the following, we will characterize the particle coating and show its affinity and specificity on vesicles as well as on living cells. Firstly, we study the colloidal stability of the particles at various physiological conditions. Secondly, we quantify how the number of biotin binding sites on the avidin-coated particles depends on the synthesis parameters. Thirdly, we measure the binding affinity of the avidin-coated particles to biotinylated membranes. Finally, we demonstrate that avidin-coated particles bind specifically to biotinylated membranes, and that Concanavalin A-coated particles bind specifically to the glycocortex of *D. discoideum* cells.

4.3.1 Colloidal stability

One of the most important requirements of a colloidal dispersion is its stability. Without a polymer coating, colloidal stability relies on Coulomb repulsion: the surface charge of the particles prevents aggregation in deionized water. At a physiological salt concentration, however, the Coulomb force is screened by counter-ions so that the short ranged Van der Waals force induces permanent particle aggregation (see Fig. 4.1e). Therefore, steric stabilization is necessary to use colloidal particles at physiological conditions. This involves adsorbing or grafting a layer of well-soluble polymers to the particle surface. When particles approach each other, the layers on neighbouring particles will interpenetrate, which costs free energy as the polymers can occupy less volume.¹³⁶ For a sufficiently dense and thick polymer layer, this yields a repulsive force that counteracts the Van der Waals attraction and protects the particles from aggregating at arbitrary salt concentrations.¹³⁷

We here achieve this steric stabilization by covalently grafting methoxypoly(ethylene) glycol (mPEG5000) to the particles by an NHS/Sulfo-NHS linking procedure.¹³¹ mPEG is an excellent candidate for stabilizing colloidal particles as it is uncharged and hydrophilic. Furthermore, mPEG coatings have been shown to reduce the non-specific adhesion of particles to proteins, cells, and tissues.¹²² As these properties make the particles less visible to the immune system, mPEG coatings are particularly interesting for drug delivery applications.¹¹¹

Indeed, we found that after 1 h in 1 M NaCl, the here employed mPEG5000 coated particles showed excellent stability against aggregation. We observed that performing the mPEG coating at 4 °C for a minimum of 24 h is essential for obtaining the required colloidal stability, which is in agreement with earlier reports on mPEG-coated particles.¹³¹ The ζ -potential before particle coating (-55 ± 4 mV) clearly becomes less negative after

the mPEG coating (see Table 4.1), which additional further evidence for the presence of a dense PEG layer.¹³¹ The remaining negative charge is likely caused by unreacted carboxylic acid groups.

Furthermore, we assessed the stability of the mPEG-coated particles in a standard PBS buffer and in three typical cell culture media. After 1 h of mixing, we did not observe any aggregation of the particles inside any of these solvents. In HL5 medium, the ζ -potential was similar to that in the PBS buffer, while we observed a significant change in both the mammalian cell media A549 and 3T3 (see Table 4.1). While HL5 contains mostly salts, sugars, and amino acids, the A549 and 3T3 cell media contain significant amounts of proteins from bovine serum. Protein adsorption has been shown to be suppressed, but not completely prevented by a dense mPEG coating such as employed here.^{138,139} Therefore, we attribute the less negative ζ -potential in the A549 and 3T3 cell media to non-specific protein adsorption.

Table 4.1. The ζ -potential of mPEG-coated particles after 1 h incubation in water, phosphate buffered saline (PBS), the *D. discoideum* medium HL5, and mammalian cell media A549 and 3T3 (see Materials section for the contents of the media).

Solvent	pH	ζ -potential [mV]
Water	5.7	-24 ± 4
PBS	7.3	-18 ± 4
HL5	6.6	-15 ± 5
A549	7.6	-7 ± 5
3T3	8.1	-7 ± 5

To summarize, the here described particles with a dense layer of mPEG on their surface do not show aggregation at high salt concentration, as well as in several cell culture media. To now provide these particles with an affinity to a specific molecule, we introduce an additional step in the procedure: we first coat the EDC/Sulfo-NHS activated particles with a functional protein before saturating the surface with an excess of mPEG (see Fig. 4.1). The resulting particles possess functional proteins as well as mPEG polymers on their surface. We still observed that these particles were stable in 1 M NaCl after 1 h, for protein densities of up to 67 μg per mg particles. Although the proteins occupy significant space on the particles (see next section), we conclude that the density and size of mPEG5000 is still sufficiently high to protect the particles from aggregating. This combination of covalent colloidal stability with a specific-binding protein is key to targeting specific molecules on lipid membranes.

4.3.2 Accessible binding sites

In general, a specific binding affinity of a colloidal particle is provided by a finite number of binding sites on the particle surface. The number of sites will directly influence the binding affinity of the particle and therefore we quantified this parameter for the here

described particles. In the coating method, we immobilized the protein via NHS groups on the particles, which are known to form a covalent amine bond with random lysine residues that are typically present in the protein exterior.^{128,129} As an example, we coated particles with avidin, which is a protein that binds to biotin with high affinity (approx. $17 \text{ k}_B\text{T}$ per bond¹⁴⁰). Because of this high affinity, and the versatility of avidin, it has been widely applied as a connector in biochemistry, for instance as a binding site for attaching biotinylated monoclonal antibodies.^{141,142} We here use NeutrAvidin, which is a neutral and non-glycosylated avidin, and quantify the number of biotin binding sites using a combined titration and fluorescence assay for several synthesis conditions.

To rule out non-covalent adsorption of the avidin on the particles during the preparation,¹⁴³ we performed the synthesis without the EDC/NHS activation (Fig. 4.1a). The absence of NHS esters resulted in particles without biotin binding sites, while at the same time the particles were unstable in 1 M NaCl. This shows that the NHS activation is necessary for avidin and mPEG binding: we conclude that all biotin binding sites that we observed in this section are caused by avidin that is covalently linked to particles via amine bonds through the EDC/NHS chemistry.

The number of biotin binding sites on the particles is controlled by the amount of avidin that is added during synthesis. To probe this relation, we changed the quantity of added avidin between 0–7 μg per mg particles and measured the resulting average number of biotin binding sites per particle with a titration assay (Fig. 4.3a). Clearly, the amount of added avidin allows for continuously changing the average number of biotin binding sites per particle up to at least 2.9×10^4 . Assuming a typical protein size of 5 nm, we estimate that at this value approximately 1% of the particle surface is covered with protein. The slope of the linear regression in Fig. 4.3a provides information on the synthesis yield: the biotin binding capacity corresponds to 0.71 accessible biotin binding site per added avidin protein, which has a total of 4 binding sites. Apart from the chemical yield of the avidin immobilization, we presume that part of the biotin binding sites are actually present on the particles, but not accessible because of the random orientations of the avidin proteins,¹²⁸ steric hindrance by the covalently grafted mPEG polymers, or unfolding of the proteins during the pH 12 synthesis step.

Additionally, we measured the distribution of the number of biotin binding sites per particle using quantitative fluorescence microscopy. By incubating the particles with btm-DNA-Cy3, we visualized the accessible biotin binding sites for individual particles. As can be seen in Fig. 4.3b, the resulting distributions are broad and skewed towards lower values of fluorescence. The relatively large spread is a consequence of the random immobilization of the avidin on the particle surfaces. To mitigate this effect, it is important that the added protein is well mixed with the particles during the coating procedure. Here, we achieved this by vortexing the mixture directly after the addition of protein to the particles.

By combining the distributions from the fluorescence assay with the quantitative results from the titration assay, we obtained the most frequently occurring numbers of biotin binding sites, which are shown in Figure 4.3c together with the one-standard

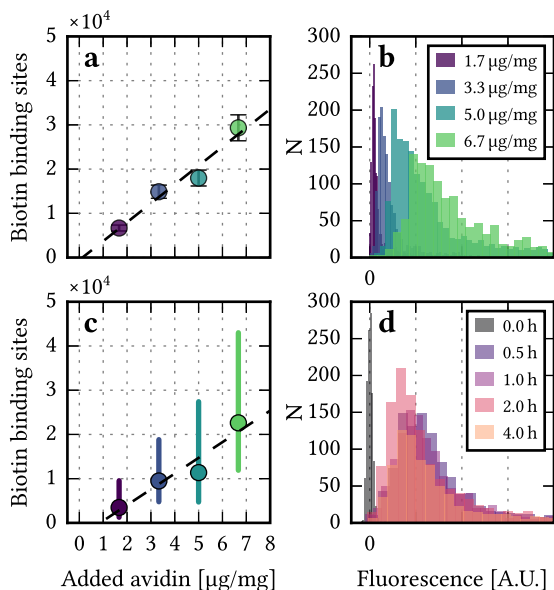


Figure 4.3. The amount of biotin binding sites on avidin-coated particles. (a) The average number of binding sites per particle, measured by titration. Four particle batches with varying amounts of avidin were analysed. Error bars denote the measurement precision. (b) Histograms of the btn-DNA-Cy3 fluorescence of same particle batches (see legend) show a skewed distribution for all samples. Combining the averages from the titration assay (a) with the relative spreads from the fluorescence assay (b), the spread in the number of binding sites within particles of a single batch could be recovered, which is displayed in (c). Here, error bars denote the one standard deviation spread of biotin binding sites per particle in a single batch, and the discs mark the most frequently occurring value. Lines in (a) and (c) are linear regressions. (d) Histograms of the btn-DNA-Cy3 fluorescence of five particle batches with varying delay time between avidin and mPEG addition (see legend), at a fixed avidin concentration of 3.3 $\mu\text{g}/\text{mg}$. As the distributions did not change after 0.5 h, we concluded that the avidin coating was completed within 0.5 h after avidin addition.

deviation spread. Due to the skewed distributions, the average number of biotin binding sites is higher than the most frequently occurring number of biotin binding sites. Still, this quantity is linear with the amount of added avidin and therefore it can be tuned readily by varying the avidin concentration.

After activating the carboxylic acid particles with NHS, avidin and mPEG are added sequentially. As the two reactions compete with one another for the NHS esters, we used a delay time between avidin and mPEG addition, so that the avidin immobilization is allowed to complete before mPEG starts to occupy particle surface area. The duration of this delay may affect the final avidin density on the particles. In order to find the

minimum delay time between the addition of avidin and mPEG, we varied the delay between 0–4 h at a fixed amount of avidin of $3.3 \mu\text{g}$ per mg particles. See Fig. 4.3d for the corresponding distributions of the btm-DNA-Cy3 fluorescence. As the distributions do not change significantly between 0.5–4 h, we conclude that the distribution of linker densities already reached a steady state within the first 0.5 h. Throughout this chapter, we fixed the delay time at 2 h to ensure the complete grafting of proteins.

To summarize, we have shown that the reported particle coating method allows for tuning the average number of accessible biotin binding sites up to 2.9×10^4 per particle, which is sufficient to achieve high binding affinity and specificity, as will be demonstrated in the next sections.

4.3.3 Binding affinity

In the previous section, we have shown that the avidin-coated particles bind fluorescently labelled biotin molecules. Next, we investigated whether this binding affinity also holds for lipid membranes that feature biotin target groups. As a model membrane, we used Giant Unilamellar Vesicles ($10\text{--}50 \mu\text{m}$ in diameter) that contain biotinylated lipids. After 30 min incubation of these vesicles in a 0.02 vol% particle suspension, we imaged the vesicles with confocal microscopy. See Fig. 4.4a for a GUV that was incubated with

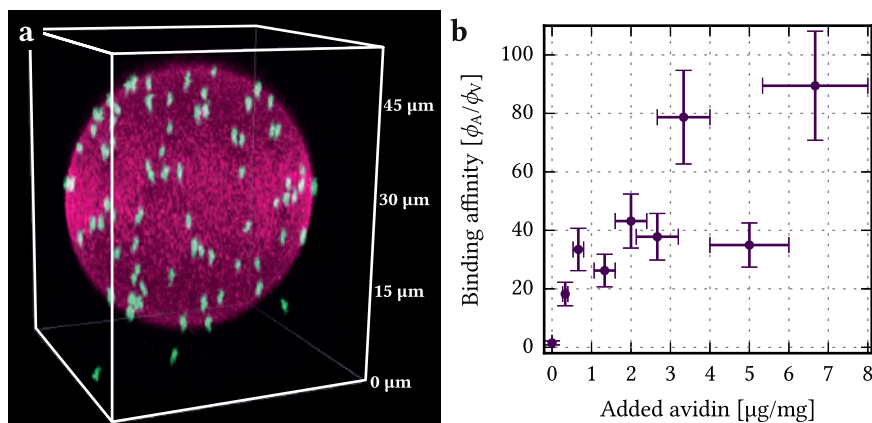


Figure 4.4. Binding affinity of avidin-coated particles on biotinylated lipid membranes. (a) A three-dimensional confocal image showing a biotinylated GUV (magenta) that has been incubated for 30 min with avidin-coated particles (green). (b) The membrane area coverage ϕ_A was measured and averaged over 10 randomly selected GUVs, for varying amount of avidin on the particles. The particle volume fraction ϕ_V was 0.021 ± 0.004 vol %. The vertical error bars denote the uncertainty in binding affinity due to the imprecision in particle volume fraction; the horizontal error bars denote the uncertainty in the amount of added avidin. The confocal image in (a) corresponds to the point at $3.3 \mu\text{g}/\text{mg}$ avidin.

3.3 $\mu\text{g}/\text{mg}$ avidin-coated particles, which clearly adhered to the biotin-containing membranes.

As the surrounding liquid is stationary, a diffusion-limited adsorption model seems applicable.¹⁴⁴ To explain the dependence of particle adsorption on avidin density, we presume that the avidin concentration on the particles determines a certain binding probability to biotin-containing membranes. For low membrane coverage, the covered membrane area fraction is proportional to the particle concentration in the surrounding liquid and therefore it is reasonable to define a (non-equilibrium) binding affinity with the membrane area that is covered by particles ϕ_A , divided by the bulk particle volume fraction ϕ_V , at fixed incubation time. We measured this membrane area fraction ϕ_A using tracking methods described in Chapter 5 on the three-dimensional confocal images.^{86,145}

The observed binding affinities (ϕ_A/ϕ_V) after 30 min incubation are shown in Fig. 4.4b. The effect of avidin on the binding affinity to biotin-containing GUVs is clear: between 0 and 0.3 $\mu\text{g}/\text{mg}$, the binding affinity increased more than tenfold from 1.5 ± 0.7 to 18 ± 4 . After that, binding affinity increased for increasing avidin densities, until a membrane area coverage of 1.9% after 30 min in a 0.02 vol % particle suspension was achieved. At amounts of added avidin larger than 3 $\mu\text{g}/\text{mg}$, we observed large fluctuations in the binding affinities. A possible reason for these is a large spread in the number of binding sites per particle: as mentioned before, it is important that the proteins are well mixed with the activated particles in order to obtain homogeneous coatings throughout the sample. From this we conclude that the binding probability of avidin-coated particles increases with increasing avidin density on the particles.

4.3.4 Binding specificity

We have shown that by immobilizing a protein on the surface of colloidal particles, the affinity to its target molecule is transferred from the protein to the particle surface. Now, we investigate whether also the binding specificity is conserved. For this, we assessed the binding affinity of three types of functionalized particles to different lipid membranes. As a control experiment, we first tested the binding affinity of particles with only mPEG on their surface. Then, in order to show the specific targeting to biotinylated surfaces, we used the avidin-coated particles that we investigated in detail in the previous sections (3.3 μg avidin per mg particles). Finally, to show the generality of the coating protocol, we also assessed particles functionalized with 33 $\mu\text{g}/\text{mg}$ of the sugar-binding protein Concanavalin A (ConA).

The specific binding affinity of these three types of particles was tested first on model lipid membranes (GUVs) of known composition (see Method section). In Figures 4.5a–c, we show that none of the investigated particles bound to lipid membranes without exposed biotin molecules: the dense mPEG coating clearly suppressed aspecific binding to the GUVs, irrespective of the immobilized proteins that are also present on the particles. On biotinylated membranes, however, we observed binding of avidin-coated particles with high affinity, while the control and ConA coated particles did not show significant

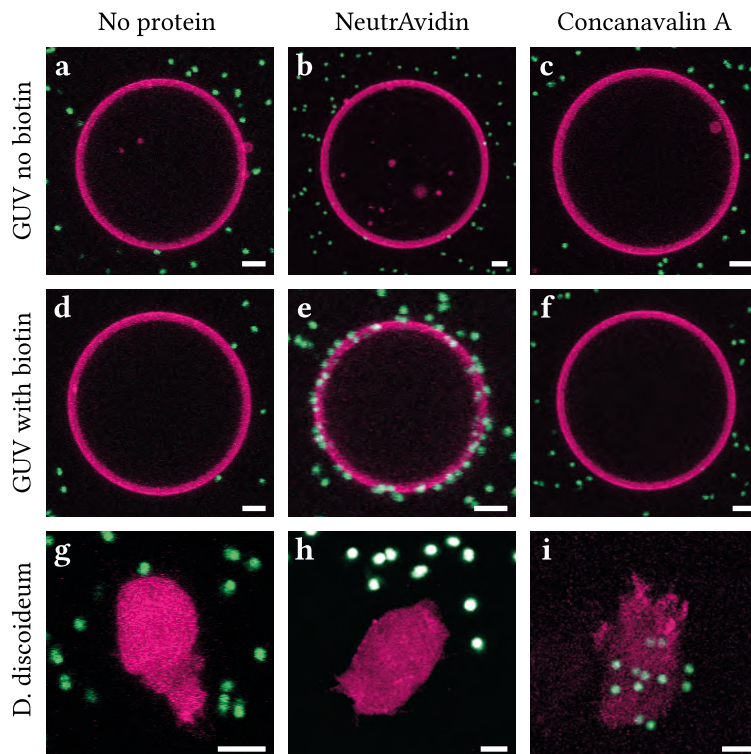


Figure 4.5. Binding specificity of non-functionalized particles, NeutrAvidin-coated particles, and Concanavalin A-coated particles. The specific adhesion is shown on (a)-(c) GUVs with only PEG on their surface, (d)-(f) GUVs with an excess of biotinylated PEG on their surface, and (g)-(i) *D. discoideum* cells. All images are maximum intensity projections of three-dimensional confocal images. For the GUVs in (a)-(f), the particles are displayed in green and the membrane in magenta. For the cells in (g)-(i), the magenta denotes the filamentous actin, which visualizes the cell contour. These pictures were chosen such that there were no particles floating in front or behind, otherwise the cells are representative of the samples. The scale bars denote 5 μm .

binding (Figs. 4.5d-f). Therefore, we conclude that the here described coating protocol successfully transfers the specificity of the avidin to colloidal particles.

Additionally, we also investigated the specificity of these particles to living cells. For *D. discoideum* cells, we found that the mPEG coating successfully prohibited adhesion to the cells: without mPEG coating, 50% of the particles were internalized by the cells, while with mPEG coating, we observed none out of over 200 observed particles to be stuck to the cellular membrane (see Fig. 4.5g). At the other hand, on two types of mammalian cells (A549 human lung carcinoma and 3T3 mouse fibroblasts), we found that the mPEG-

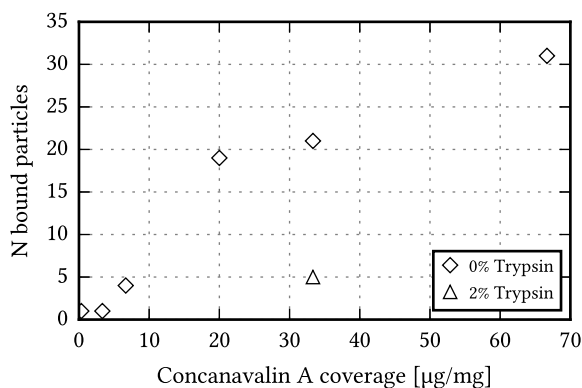


Figure 4.6. Number of ConA-coated particles that bound to the *D. discoideum* cells. We varied the amount of ConA per particle and observed the total number of particles that bound to two selected cells in the sample (diamonds). This provides a qualitative measure of the affinity of the particles to the cells. We also treated the cells with Trypsin (cells treated for 10 min in 2 wt% Trypsin at 30 °C), which removed glycoproteins, and indeed we observed a decrease in the number of adsorbed particles (triangle).

coated particles stuck non-specifically to the cellular membranes. As these cells are cultured in protein-rich media, we presume that the observed adhesion was caused by a protein corona that formed around the particles, which is supported by the ζ -potential measurements inside these media (see Table 4.1). Therefore, we conclude that protein-rich media may induce aspecific binding of mPEG-coated particles.

The particles that were functionalized with avidin also did not bind to the *D. discoideum* cells (Fig. 4.5h). These results are in line with the previous results on GUVs: the presence of the immobilized protein does not change the aspecific binding of the particles. The ConA-coated particles did however show significant binding (Fig. 4.5i). ConA binds selectively to glucose and mannose residues¹⁴⁶ which are present in the glycocortex of the *D. discoideum* cells. The ConA functionalization indeed resulted in particles that bound specifically to the *D. discoideum* cells, while the ConA did not cause any binding to the GUVs (Figs. 4.5c and f). As with the avidin-coated particles to biotinylated membranes, binding affinity of the ConA particles to the *D. discoideum* cells seems to depend on the amount of ConA on the particles (see Fig. 4.6). Also, we observed that after cleaving glycoproteins from the cellular membranes by addition of Trypsin,¹⁴⁷ the binding affinity decreased significantly.

These observations confirm that the here described surfactant-free coating protocol readily transfers the specificity of a certain protein to a colloidal particle. As long as non-specific binding is suppressed, which we showed on GUVs without biotin, GUVs with biotin, and on *D. discoideum* cells, our method provides a means to design colloidal

particles that ‘target’ specific molecules in lipid membranes, which has useful applications in fundamental membrane studies, micrometer-sized self-assembly, and directed drug release.

4.4 Conclusion

To direct colloidal particles to specific molecules in lipid membranes, we have developed a surfactant-free coating procedure that produces particles with a high affinity to specific molecules. A coating with proteins provides the binding affinity, while at the same time a dense layer of covalently coupled mPEG gives stability at physiological conditions. As the method is surfactant-free, the particles are especially useful for surfactant-sensitive applications, such as studying lipid membrane properties, also in living environments.

The protein density on the particles can be tuned in order to adapt the binding affinity, which we have shown for the biotin-binding protein NeutrAvidin using a combined titration and fluorescence assay. The yield of the coating method is such that 18 % of the biotin binding sites is accessible after the coating procedure, which is presumably caused by the random protein orientations and the high mPEG coverage that potentially obstructs the binding sites. The largest observed number of biotin binding sites was 2.9×10^4 per $1.06 \mu\text{m}$ diameter particle.

These avidin-coated particles spontaneously bind to biotinylated membranes. We have shown that the amount of NeutrAvidin on these particles directly influences the binding affinity. While particles without avidin did not exhibit any significant binding to these membranes, avidin coated particles reached up to 1.9% membrane coverage after 0.5 h in a 0.02 vol % particle suspension.

Additionally, we have shown that the coating procedure can be readily transferred to the sugar-binding protein Concanavalin A. Functionalized with this protein, particles become specific to the outside of *D. discoideum* cells, while they do not bind to biotinylated membranes. On the other hand, while the avidin-coated particles bind to biotinylated GUVs, they do not bind to these cells. This shows that the specificity of a protein can be transferred successfully to the surface of the colloidal particles.

Our surfactant-free coating method makes colloidal particles selectively adhesive to certain targeted molecules at physiological conditions. The fact that the coating procedure only applies covalently linked mPEG as stabilizer makes it applicable to cases in which surfactants are undesirable. The procedure is readily adjustable to include different proteins, which will provide custom colloidal particles for use in future lipid membrane measurements, micrometer-scale self-assembly, drug targeting, and biosensing applications.

MEMBRANE-MEDIATED ATTRACTION BETWEEN CURVATURE INDUCING OBJECTS

This chapter is published as C. M. van der Wel, A. Vahid, A. Šarić, T. Idema, D. Heinrich and D. J. Kraft, 'Lipid membrane-mediated attractions between curvature inducing objects', *Sci. Rep.* **6**, 32825 (2016) DOI:10.1038/srep32825

Abstract

The interplay of membrane proteins is vital for many biological processes, such as cellular transport, cell division, and signal transduction between nerve cells. Theoretical considerations have led to the idea that the membrane itself mediates protein self-organization in these processes through minimization of membrane curvature energy. Here, we present a combined experimental and numerical study in which we quantify these interactions directly for the first time. In our experimental model system we control the deformation of a lipid membrane by adhering colloidal particles. Using confocal microscopy, we establish that these membrane deformations cause an attractive interaction force leading to reversible binding. The attraction extends over 2.5 times the particle diameter and has a strength of three times the thermal energy ($-3.3 k_B T$). Coarse-grained Monte-Carlo simulations of the system are in excellent agreement with the experimental results and prove that the measured interaction is independent of length scale. Our combined experimental and numerical results reveal membrane curvature as a common physical origin for interactions between any membrane-deforming objects, from nanometre-sized proteins to micrometre-sized particles.

5.1 Introduction

Interactions between membrane proteins are of key importance for the survival of cells as they are involved in many dynamical processes. The organization of membrane proteins into complexes and their effect on membrane shape enables for instance intracellular transport, cell division, cell migration, and signal transduction.² Understanding the underlying principles of protein organization is therefore crucial to unravel processes such as cell-cell signalling in the brain¹⁴⁸ or disease mechanisms like membrane-associated protein aggregation in Parkinson's disease.¹⁴⁹

Besides specific protein-protein interactions and interactions with the cytoskeleton, protein organization in membranes is thought to be driven by a universal interaction force arising from membrane deformations. Theoretical models^{17,32,150–152} and simulations^{4,19,153–156} predict that by deforming the membrane locally, membrane proteins can self-assemble into complex structures such as lines, rings, and ordered packings. Observations in living cells^{13,149} support the existence of such membrane-mediated interactions, but have yet to provide conclusive experimental proof of their common physical origin: separation of contributions arising from specific protein-protein interactions and interactions with the cytoskeleton is extremely challenging.

Further experimental indications for a universal membrane-mediated interaction stem from simplified model systems: phase-separated membrane domains are known to repel each other¹⁵⁷ while colloidal particles have been observed to irreversibly stick together when attached to lipid vesicles.^{20,21} However, the hypothesized connection between curvature and interaction force has not been quantified to date.

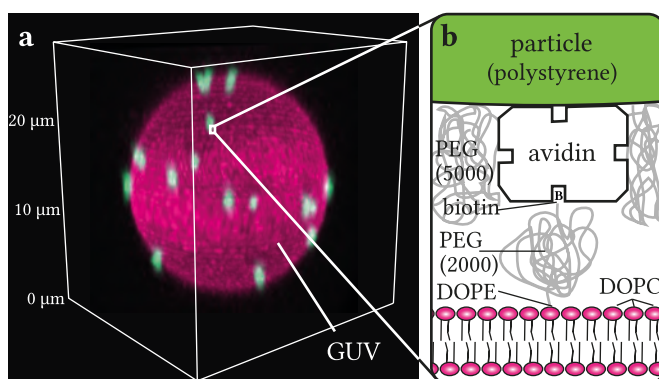


Figure 5.1. Experimental model system for studying membrane-mediated interactions. (a) Three-dimensional confocal image of a typical Giant Unilamellar Vesicle (GUV, in magenta) with attached colloidal particles (in green). A typical 3D video is available online. (b) Schematic of the avidin-biotin linkage between membrane and particle. By varying the avidin concentration on the particles we control the adhesion strength. Polyethylene glycol (PEG) suppresses electrostatic interactions between membrane and particles, as well as non-specific adhesion between particles.

Existing model systems for studying surface-mediated interactions are typically based on deformations of liquid-liquid or liquid-air interfaces.^{158–160} In these systems, interactions are governed by surface tension, while in lipid vesicles elastic *surface bending* is expected to be the dominant factor. In addition, lipid vesicles are bilayers of molecules that cannot exchange molecules with the surrounding medium, which makes them profoundly different from other liquid interfaces. The experimental quantification of interface-mediated interactions in lipid membranes thus requires a clean and dedicated model system.

In this chapter, we describe such a specialized model system consisting of membrane-adhering colloidal particles on Giant Unilamellar Vesicles (GUVs). We characterize for the first time the effect of a single adhesive colloidal particle on the local membrane shape using confocal microscopy. We find that the particle is either fully wrapped by the membrane or not wrapped at all, depending on the adhesion strength. Next, we measure the interaction potential for particles in these two states and we find that only wrapped particles show a reversible attraction, which implies that the attraction is purely caused by the membrane deformation. Monte Carlo simulations of the bending-mediated interaction between wrapped particles result in an interaction potential that quantitatively agrees with the experimental result. Since these simulations do not contain any absolute length scale, we conclude that the measured attraction caused by lipid membrane deformations is scale-independent. Our combined model system and simulations therefore quantitatively describe the interactions of any membrane-deforming object, ranging from nanometre-sized proteins to micrometre-sized colloidal particles.

5.2 Methods

Chemicals Styrene, itaconic acid, 4,4'-azobis(4-cyanovaleric acid) (ACVA), 1,3,5,7-tetramethyl-8-phenyl-4,4-difluoroboradiazaindacene (BODIPY), methoxypoly(ethylene glycol) amine (mPEG-NH₂, M_w = 5000), N-hydroxysulfosuccinimide sodium salt (Sulfo-NHS), sodium phosphate, D-glucose, methanol, ethanol, acetic acid, ammonium hydroxide 28–30% (NH₄OH), Hellmanex III, Pluronic F-127, deuterium oxide 70% (D₂O), 3-(trimethoxysilyl)propyl methacrylate (TPM), and bovine serum albumin (BSA) were purchased from Sigma-Aldrich; sodium chloride, sodium azide, hydrogen peroxide 35% (H₂O₂), acrylamide, N,N,N',N'-tetramethylethylenediamine (TEMED), and ammonium persulfate (APS) from Acros Organics; 1-ethyl-3-(3-dimethylaminopropyl)carbodiimide hydrochloride (EDC) from Carl Roth; NeutrAvidin from Thermo Scientific; DNA oligonucleotides (biotin-5'-TTTAATATTA-3'-Cy3) from Integrated DNA Technologies; Δ9-cis 1,2-dioleoyl-*sn*-glycero-3-phosphocholine (DOPC), 1,2-dioleoyl-*sn*-glycero-3-phosphoethanolamineN-(lissaminerhodamine B sulfonyl) (DOPE-rhodamine), and 1,2-dioleoyl-*sn*-glycero-3-phosphoethanolamine-N-[biotinyl(polyethylene glycol)-2000] (DOPE-PEG-biotin) from Avanti Polar Lipids. Unless stated otherwise, chemicals were used as received. Deionized water is used with 18.2 MΩcm resistivity, obtained using a Millipore Filtration System (Milli-Q Gradient A10).

Probe particles Polystyrene particles are synthesized from styrene, itaconic acid, ACVA, and BODIPY in water using a surfactant-free radical polymerization described in ref. [132], resulting in monodisperse spheres with a diameter of $0.98 \pm 0.03 \mu\text{m}$. Resulting particles are coated with NeutrAvidin and mPEG-NH₂ using an a protocol adjusted from ref. [131]. All subsequent reactions are done at 4 °C to slow down NHS hydrolysis. 1 mL 20 wt% particles are mixed with 80 μmol EDC and 25 μmol Sulfo-NHS in 10 mL water at pH = 5.3 and stirred for 30 min. The pH of the resulting NHS-activated particles is brought to 8.6 using 0.2 M NaOH. 750 μL of the 2 wt% activated particles is then mixed with 0.5–50 μg NeutrAvidin. After 30 min, 4 mg mPEG-NH₂ is added and the reaction proceeds for 40 h. Then the pH is brought to 12 with 1 M NaOH, the particles are ultrasonicated for 5 min and then washed 1 time with 0.01 M HCl and 3 times with water. Finally, sodium azide is added to a concentration of 3 mM to prevent bacterial growth.

Biotin binding sites assay In order to quantify the number of biotin binding sites (the ‘linker density’) on each particle, we measure fluorescence of biotin- and dye-functionalized DNA strands. DNA strands have the advantage that they are well soluble in water, so that there is no non-specific adhesion to the particle surface. 10 μL 6 μM DNA (in water) is mixed with 10 μL 0.5 wt% particles in a total volume of 310 μL 50 mM PBS buffer with 0.5 wt% Pluronic F-127. The mixture is heated to 55 °C for 30 min and washed 3 times with water. The sample is diluted 10 times in a PBS buffer inserted into an untreated rectangular glass capillary, which immobilizes the particles. The fluorescence intensity is quantified using fluorescence microscopy (Nikon Intensilight) with reproducible settings and using a reference value obtained from commercial particles with a known amount of avidin (Spherotech PC-S-1.0) we can obtain a distribution of avidin linkers per particle.

GUV preparation Vesicles are prepared using a standard electrosweeling technique.¹³⁵ A lipid mixture of DOPC, DOPE-PEG-biotin, and DOPE-rhodamine in a 97.5:2:0.5 weight ratio is used, ensuring a liquid bilayer at room temperature. 2 times 20 μg of the lipids in chloroform are dried on two 25 × 25 mm ITO-coated glass slides (15–25 Ω , Sigma-Aldrich), placed in 1.8 mL of a solution with 100 mM glucose and 0.3 mM sodium azide in 49:51 (mass) D₂O:H₂O. The cell is subjected to 1.1 V (rms) at 10 Hz for 2 h, with the first 2 min a linear increase from 0 V. GUVs are stored in a BSA-coated glass vial at room temperature. In order to remove small lipid structures,¹⁶¹ 100 μL GUV solution is pipetted on a Whatmann 5.0 μm pore size cellulosenitrate filter and slowly flushed with 5.0 mL of glucose solution. 100 μL purified GUVs are harvested from the filter and used the same day. All handling is done with care not to mechanically shock the solution.

Coverglass treatment We employed a polymerization of acrylamide onto TPM-coated glasses,¹⁶² as follows: coverglasses are cleaned for 30 min in a 2 vol% Hellmanex solution, rinsed 3 times with water, immersed in 5:1:1 H₂O:NH₄OH:H₂O₂ for 30 min at 70 °C, rinsed 3 times with water, and 2 times with ethanol. TPM functionalization is done by immersing 15 min in ethanol with 1 vol% acetic acid and 0.5 vol% TPM, rins-

ing 3 times with ethanol and incubating for 1 h at 80 °C. Polymerization is done in a 2 wt% solution of acrylamide (evacuated in vacuum for 30 min to remove oxygen), with 0.035 vol% TEMED and 0.070 wt% APS for 2 h. Resulting coverglasses were kept inside the polymerization solution at 4 °C until use. Directly before use, a coverglass is rinsed with water and blow-dried with nitrogen.

Density matching A density-matched PBS stock buffer of 200 mOsm is prepared containing 10.0 mM sodium phosphate, 82.0 mM sodium chloride, and 3.0 mM sodium azide. Density-matching with the probe particles was achieved by gradually adding D₂O until no sedimentation or creaming occurred at 10 000 g for 1 h. The mass ratio D₂O:H₂O for water is roughly 51:49; for the buffer it is roughly 45:55 because the solutes increase the density. Using ratios between the stock buffer and density-matched water, buffers at different osmolarities are obtained. Density matching is confirmed for each mixture separately.

Sample preparation Samples are prepared on polyacrylamide-coated coverglasses and density matched with D₂O. 2 µL 2 wt% particles, 4 µL 150 mOsm PBS buffer, and 20 µL filtered GUVs are incubated for 10 min in a plastic microtube. Then 10 µL of this mixture is slowly distributed into the sample holder with 50 µL 100 mOsm PBS buffer already inside. The sample holder consists of a Teflon ring clamped on a pretreated coverglass. For tense GUVs, the sample holder is closed with vacuum grease and a second coverglass; for floppy GUVs, the sample holder is kept open to air for 30 min so that evaporation leads to an increase in osmotic pressure, and consequentially a decrease of membrane tension. All experiments were performed at a room temperature of 19–22 °C.

Imaging Imaging is done with an inverted Nikon TiE microscope equipped with a Nikon A1R confocal scanhead with both galvano and resonant scanning mirrors. High-speed trajectory imaging is achieved with a horizontal resonant mirror scanning lines at 15 kHz; single-particle close-ups are done with the galvano mirrors. We use a 60× water immersion objective (NA = 1.2) to reduce axial aberration due to index of refraction mismatch. The excitation laser is passed through a quarter wave plate to mitigate polarization effects of bilayer-attached dye molecules. Excitation (at 488 nm and 561 nm) and detection are performed simultaneously (for trajectory imaging) or sequentially (for close-ups) using a dichroic mirror splitting the emission signal onto 500–550 nm and 565–625 nm filters. The sample is mounted on an MCL NanoDrive stage to enable fast z-stack acquisition.

Image analysis The raw images of the interaction measurements are high speed (29–57 Hz) confocal images containing two separate colours, being the vesicle fluorescence and the particle fluorescence. Images are convolved with a Gaussian kernel with an rms width of 1 pixel to reduce random noise.

The particle fluorescence signals are tracked using a widely employed centre-of-mass based particle tracking algorithm in a Python implementation, which is available online.^{65,163} All particle trajectories are checked manually for missing coordinates and corrected if necessary. Because the used centre-of-mass refinement technique systematically finds coordinates of overlapping features too close together, we refine overlapping signals additionally by least-squares fitting to a sum of Gaussians (see Chapter 2).

The three-dimensional coordinates of the particles relative to the vesicle (x_{rel} , y_{rel} , z_{rel}) are determined as follows: $x_{rel} = x - x_c$; $y_{rel} = y - y_c$; $z_{rel}^2 = (R+h)^2 - x_{rel}^2 - y_{rel}^2$. The vesicle radius R is obtained in a separate three-dimensional confocal measurement; the particle-vesicle distance h is known from the wrapping state of the particle; the vesicle centre (x_c , y_c) is measured simultaneously with the particle tracking (x , y) from the high-speed 2D confocal images.

For the vesicle tracking, we interpolate the image on lines that are drawn outwards from a rough estimate of the vesicle centre. The maximum value on each of these lines provides an estimate of the vesicle perimeter. Around each maximum, a fit region of 5 pixels is defined for further refinement: linear regression on the discrete derivative provides the position of the vesicle perimeter with sub-pixel resolution. Finally, we perform a least-squares fit to a circle (for two dimensions) or ellipsoid (for three dimensions) to obtain the refined vesicle centre and radius. This algorithm is available online.¹⁴⁵

Modelling Details The curvature energy of a biological membrane is described by the Helfrich energy functional²⁷ as:

$$u_{\text{Curv}} = \frac{\kappa}{2} \int_A (2H)^2 dA, \quad (5.1)$$

where H is the mean curvature of the membrane, which is defined as the divergence of the surface normal vector, $H = -\frac{1}{2}\nabla \cdot \mathbf{n}$. We model the vesicle by a network of vertices with the minimum length of l that are connected in a triangular network. The curvature energy of our discretized membrane is given by:

$$u_{\text{Curv}} = \sqrt{3}\kappa \sum_{\langle ij \rangle} 1 - \mathbf{n}_i \cdot \mathbf{n}_j, \quad (5.2)$$

where \mathbf{n}_i and \mathbf{n}_j are the normal vectors to any pair of adjacent triangles i and j , respectively. The summation runs over all pairs of such triangles. To simulate the fluidity of the membrane, we change the connectivity of the network: we cut and reattach connections between the four vertices of any two neighbouring triangles. The surface area A and volume V of the vesicle, are maintained by constraints $u_A = K_A(A - A_t)^2/A_t$ and $u_V = K_V(V - V_t)^2/V_t$ with $K_A = 10^3 k_B T/l^2$ and $K_V = 4 \times 10^3 k_B T/D_p l^2$, where $k_B T$, D_p , A_t and V_t are the thermal energy, the diameter of the particles, the target surface area and the target volume of the vesicle, respectively. In each simulation we set the target

values of surface area and volume of the vesicle with diameter $D_v = 50l$ as $A_t = 1.05A_0$ and $V_t = V_0$, respectively. These parameters cause the final volume and surface area to deviate less than 0.01% from the target values. To let the vertices of the membrane wrap around the particles, we introduce an attraction potential between them:

$$u_{\text{Ad}} = \begin{cases} -\varepsilon(l_m/r)^6 & \text{if } \theta \leq \theta_{\text{Wr}}, \\ 0 & \text{otherwise,} \end{cases} \quad (5.3)$$

where ε is the particles' adhesion energy and r is the centre-to-centre distance between particles and vertices. θ is the angle between the vector normal to the active area of the particles and the vectors that connect the particles to vertices. The maximum angle θ_{Wr} is defined to control the area that is forced to be wrapped by the membrane, preventing very sharp membrane bends. $l_m = (l + D_p)/2$ is the shortest distance between particles and vertices, where the diameter of the particles is set to $D_p = 8l$. We set a cut-off radius for the attraction potential at $1.2l$ to make sure that other than forming a layer of membrane on the surface of the particles, it has no extra effects. The total energy u_{T} of the system is the sum of the curvature energy (Eq. 5.2) and the adhesion energy (Eq. 5.3).

To analyse the equilibrium shape of the membrane, we implement the Monte Carlo simulated annealing in order to minimize the total energy of the system. For our Monte Carlo simulations, we use the Metropolis algorithm to move vertices and particles, and flip the edges of the membrane triangulation, in order to change the configuration of the system (shape of the membrane). The temperature of the system is also slowly decreased so that we suppress the fluctuation of the membrane and identify the minimum-energy configuration.

5.3 Results and Discussion

5.3.1 Particle-induced membrane deformation

As a dedicated model system for membrane-deforming proteins we use micrometre-sized colloidal particles (polystyrene, $0.98 \pm 0.03 \mu\text{m}$ in diameter) adhered to single-component Giant Unilamellar Vesicles (GUVs, diameters ranging from 5–100 μm), allowing us to study membrane-mediated interactions with confocal microscopy (see Figure 5.1). The GUVs consists of DOPC lipids, which is above its melting point at room temperature, ensuring a single-phase liquid membrane. The connection between membrane and particle is realized by coating the particles with varying amounts of avidin, a protein that binds strongly and specifically to biotin,¹⁴⁰ which we attach to the membrane through a functionalized lipid. The concentration of avidin linkers on the particle surface allows us to effectively tune the adhesion strength of the particle to the membrane.

By choosing different fluorescent markers for the particles and lipid membranes, we are able to visualize the effect of a single particle on a lipid membrane (see Figure 5.2).

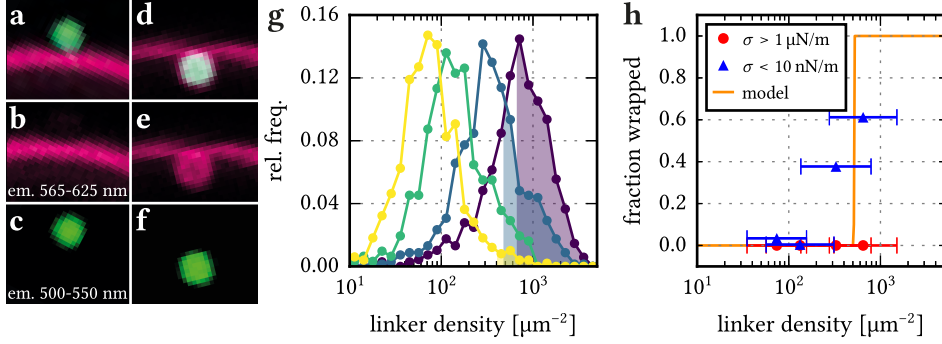


Figure 5.2. The effect of particle linker density on the membrane wrapping state. (a) Fluorescence signal of a non-wrapped particle (green) and a membrane (magenta). The separate fluorescence signals of the membrane and particle are displayed in (b) and (c), respectively. In (d)-(f) the wrapped state is displayed analogously. The scale bar is $1 \mu\text{m}$. (g) Distribution of particle linker densities for four particle batches coated with different amounts of linker protein avidin (5, 20, 25, and $50 \mu\text{g}$ per mg particles, respectively shown in yellow, green, blue, and purple). In order to relate the fraction of wrapped particles to these distributions, the right tail of each distribution is shaded up to the measured fraction of wrapped particles. From this, we estimate the critical linker density to be $513 \pm 77 \mu\text{m}^{-2}$. (h) Fraction of wrapped particles as a function of linker density on floppy membranes (blue triangles, membrane tension $\sigma < 10 \text{ nN/m}$) and tense membranes (red circles, $\sigma > 1 \mu\text{N/m}$). The width of the distributions displayed in (g) is shown with horizontal error bars in (h). The solid line is the analytic model at $\sigma = 0$ derived from Equation 5.4 via the Boltzmann factor. Horizontal error bars show the spread (one standard deviation) in linker density.

We find that particles exist in either a completely wrapped state or a completely non-wrapped state: partial wrapping is only observed as a transient situation. Non-wrapped particles are located on the outside of the vesicle without deforming the membrane (Figure 5.2a-c), while wrapped particles are protruding into the interior of the vesicle (Figure 5.2d-f). Co-localization of the membrane fluorescence with the particle fluorescence further corroborates the fully wrapped state.

This two-state behaviour is in agreement with theoretical predictions.¹⁶⁴ Using a similar approach, we express the total energy of particle wrapping derived from the Canham-Helfrich energy functional:²⁷

$$E = \left(\frac{2\kappa}{R^2} + \sigma - u_{ad} \right) A. \quad (5.4)$$

Here, κ denotes the membrane bending rigidity, R the particle radius, σ the membrane tension, A the contact area, and u_{ad} the adhesion energy per unit area. This equation states that the energy is minimized by either minimizing or maximizing the contact area, depending only on the sign of the prefactor between brackets. The value of this prefactor in turn depends on the tunable parameters membrane tension and adhesion energy.

We vary the membrane tension σ by adjusting the salt concentration in the vesicle exterior. For this we discern two extreme situations: *tense* vesicles with a (non-fluctuating) spherical shape ($\sigma > 1 \mu\text{N/m}$) and *floppy* vesicles that exhibit clear fluctuations around a spherical shape ($\sigma < 10 \text{ nN/m}$). The values of the surface tension have been derived from the spectral analysis of the fluctuating vesicle contour according to ref. [165].

To vary the adhesion energy u_{ad} , we coat particles with different amounts of linker protein avidin. We measure the distribution of linker densities in a fluorescence assay (see Methods section) and relate this to the fraction of particles that are wrapped by floppy membranes (see Figure 5.2g and h). We find that wrapping occurs above a critical linker density of $513 \pm 77 \mu\text{m}^{-2}$. On tense membranes we never observe wrapping of particles.

Our DOPC membranes have membrane bending rigidity $\kappa = 21 \text{ k}_B\text{T}$.¹⁶⁶ In the case of floppy membranes ($\sigma \ll 2\kappa R^{-2}$), Equation 5.4 yields a corresponding adhesion energy per unit area of $168 \text{ k}_B\text{T}/\mu\text{m}^2$. Comparing this adhesion energy to the literature value of the binding energy per avidin-biotin bond ($17 \text{ k}_B\text{T}$),¹⁴⁰ we conclude that effectively only 2% of the surface linkers are binding. This is probably due to the presence of the polymer between biotin and lipids: the bulky polymer may reduce the binding energy per linker, prevent access to some avidin binding sites, and cause an additional non-specific steric repulsion because of overlap with polymers on the particles.

Note that while wrapping requires floppy membranes, it is irreversible and affects the membrane tension: an initially floppy membrane gradually increases its surface tension upon wrapping particles, due to the effective removal of membrane surface area. In this way, a tense membrane with wrapped particles can be obtained as well.

The observed “all or nothing” wrapping behaviour provides a means to control local membrane deformations through easily accessible experimental parameters. We will use this experimental control in the next section to investigate the forces between local membrane deformations.

5.3.2 Membrane shape mediated interactions

When two wrapped particles approach within a distance of several particle diameters, we observe a reversible, long-ranged attraction between them (see supporting video). Excitingly, this interaction is absent for particles that are adhered to but not wrapped by the membrane (see supporting video). This implies that the interaction observed between wrapped particles is purely caused by the local deformation arising from particle wrapping.

To be able to single out the membrane-mediated force, we exclude all other relevant forces on the particles. Firstly, electrostatic interactions are screened up to a Debye-Hückel screening length of 1 nm by adding 50 mM of salt to the vesicle exterior. Secondly, gravity is compensated with buoyancy by carefully increasing the water density with heavy water (D_2O). Thirdly, wall interactions are suppressed by coating the coverglass with polymer.¹⁶² Finally, we ensure that particles do not attract via Van der Waals forces



by grafting a high density of poly(ethylene) glycol (PEG) to the particle surface, which acts as a steric stabilizer.¹³⁷ We confirm with particle tracking in three-dimensional confocal images that the particles indeed do not interact or sediment (see Fig. 5.3).

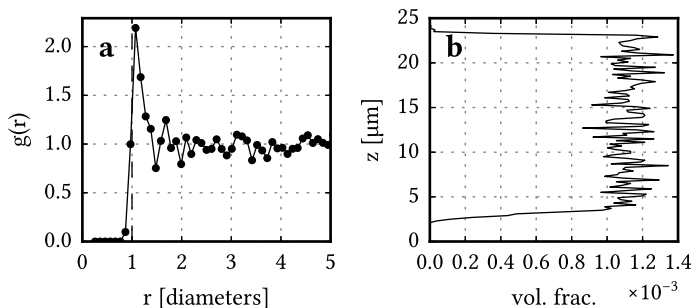


Figure 5.3. Three-dimensional radial distribution function and sedimentation profile of particles suspended at a volume fraction of 0.0011 in a 50 mM density matched PBS solution. (a) The radial distribution $g(r)$ shows no interaction between particles. The dashed vertical line indicates particle contact. The sharp peak at a distance of 1 diameter is due to the presence of a few dimers originating from the particle synthesis. (b) The density profile shows that there is no gradient in concentration due to gravity.

In order to quantify the membrane shape mediated interaction, we track the membrane-adhered particles using confocal microscopy at a frame rate of 29–57 Hz. We are able to extract the 3D particle coordinates from these 2D image sequences by simultaneously tracking the vesicle to which the particles are confined (see Methods section). The pair interaction energy is inferred from direct measurement of the transition probability matrix P_{ij} , describing the probability for particles to move from separation distance s_i to separation distance s_j (see Chapter 3). Here, the distance s is the geodesic distance between the points where the particles connect to the membrane. From P_{ij} a stationary probability distribution for s is obtained. This is equal to the equilibrium distribution, assuming that the hydrodynamic drag forces on the particle do not depend on their separation. From the Boltzmann distribution we then determine the energy of two interacting particles, $u(s)$.

Using this method, we infer the pair interaction energy $u(s)$ between wrapped particles and between non-wrapped particles. Clearly, non-wrapped particles do not interact, while wrapped particles show a long-ranged attraction (Figure 5.4d–e). The shape of the interaction potential for wrapped particles does not depend on the membrane tension, although the interaction strength is lower on tense membranes. We find that the interaction strength for floppy membranes is $-3.3 k_B T$ and that the attraction extends over a range of $2.5 \mu\text{m}$, which is equivalent to 2.5 particle diameters. As the interaction energy is larger than $k_B T$, this attraction can be observed by eye from the relative movement of membrane-wrapped particles. The interaction force is only present for particles that

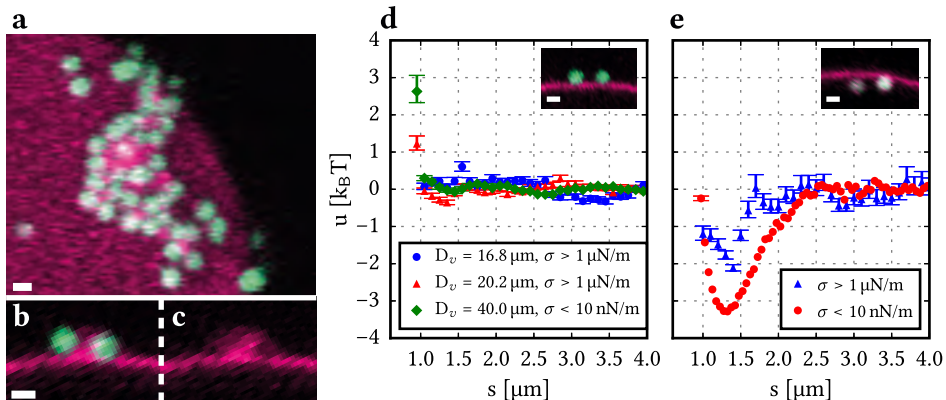


Figure 5.4. Interactions between membrane-attached particles. (a)–(c) Confocal images of non-wrapped particles that stick irreversibly together via lipid structures. The membrane fluorescence from the image in (b) is shown separately in (c). (d)–(e) Interaction energy $u(s)$ as a function of geodesic particle separation distance s for (d) two non-wrapped particles and (e) two wrapped particles. For non-wrapped particles (d) there is no significant interaction on both tense ($\sigma > 1 \mu\text{N/m}$) and floppy ($\sigma < 10 \text{ nN/m}$) membranes in a vesicle diameter range of $D_v = 16.8\text{--}40 \mu\text{m}$. For wrapped particles (e) the interaction potential shows a long-ranged attraction. The data for tense vesicles is obtained from particle trajectories on a single tense membrane with $D_v = 36 \mu\text{m}$, while the interaction energy for floppy vesicles is obtained from an average transition probability matrix of particle trajectories on 3 floppy membranes with $D_v = 14\text{--}40 \mu\text{m}$. Every measurement point is based on 20–1400 independent pair measurements. Error bars denote one standard deviation. Scale bars are $1 \mu\text{m}$.

deform the membrane: therefore we conclude that the reason for the interaction is the membrane deformation only and that the membrane mediates this force.

In earlier work by Koltover *et al.* [21] and Ramos *et al.* [20], an attraction between membrane-bound particles was observed that lead to irreversible aggregation. Strikingly, in our experiments the interaction potential does not feature this short-ranged permanent binding, but a long-ranged reversible attraction. We explain this as follows: similar to the referenced work,^{20,21} our initial experiments also contained particle aggregates on the membrane (see Figure 5.4a–c). However, confocal microscopy revealed that these aggregates are mediated by small ($< 1 \mu\text{m}$) lipid vesicles always present in GUV solutions.¹⁶¹ As their membrane composition is equal to that of the GUVs, they contain biotin linkers as well and thereby irreversibly bind to the adhered particles. This “bridging” process gives rise to a short ranged irreversible attraction. Previously, these lipid structures could not be identified because they are invisible in bright field microscopy due to their small size, while they are detected easily in the confocal microscopy experiments presented here. We deliberately remove the small lipid structures in our experiments by filtration (see Methods section) enabling us to single out the membrane-

mediated interaction.

We note again that lipid membranes are profoundly different from liquid/air and liquid/liquid interfaces where surface bending is negligible and surface tension effects such as capillary forces dominate. In the absence of gravity, two ideal spheres bound to a liquid/air or liquid/liquid interface do not interact, because on these types of surfaces, a sphere will adjust its height until it accommodates the wetting angle and therefore does not induce any surface deformation.^{167,168} Capillary forces due to interface deformations are only observed for particles with an anisotropy in their shape or roughness of the particle-interface contact line.^{158,159,167,168} In the case of lipid membranes, however, this consideration is only valid in the limit of high membrane tension, as hypothesized recently by Sarfati and Dufresne [104]. For our low tension membranes, curvature energy is the most significant energy contribution, as will be corroborated further in the next section.

Analytic approximations for a membrane-bending mediated interaction in the weakly curved limit predict a fluctuation mediated attraction as well as a bending mediated repulsion,^{17,32} at least in the case of isotropic deformations. Our attractive interaction, however, cannot be caused by fluctuations since such an attraction is negligible compared to $k_B T$ at this length scale.¹⁶⁹ The repulsion due to membrane curvature should thus be dominant, but clearly cannot explain the attraction we observe. Therefore, we conclude that the deformations induced by the wrapped colloidal particles cannot be described by linearised theory.

With non-linear field theory it is possible to calculate the interaction force from the exact membrane shape, even in the highly curved limit.¹⁵¹ Without this information, however, it is not even clear whether the particles repel or attract. In the limit of asymptotically flat membranes, Reynwar *et al.* [35] computed the interaction energy explicitly by numerically solving the membrane shape equation. They found an attraction with a well depth of the interaction potential on the same order of magnitude as in our experiments, $-3 k_B T$, albeit with an additional energy barrier at longer ranges. To more closely resemble our experimental system, we therefore performed computer simulations on spherical membranes with fixed area.

5.3.3 Simulations of membrane-mediated interactions

To investigate the origin of the observed membrane-mediated interaction, we simulate the interaction between two particles adhered to a spherical fluid membrane. This numerical work was performed by Afshin Vahid and Dr. Timon Idema (*TU Delft*). Their approach is based on earlier work by Šarić and Cacciuto [19, 36, 154] and is explained in detail in the Methods section. In short, we describe the vesicle using a dynamically triangulated network consisting of 5882 vertices. Between the vertices we apply hard-core repulsion such that the minimum edge length of the network is l . The fluid nature of the membrane is taken into account by allowing the edges of this network to flip. The vesicle itself, in equilibrium, forms a sphere of diameter $D_v = 50l$. We introduce two colloidal particles with diameter $D_p = 8l$, chosen such that the D_p/D_v ratio is similar

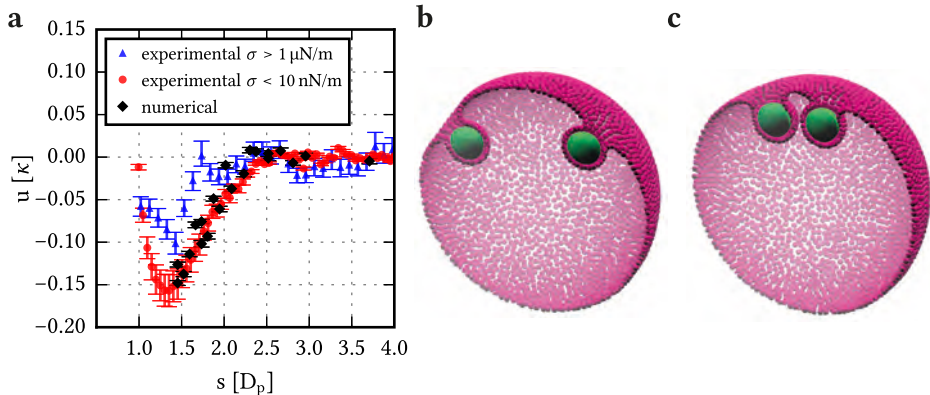


Figure 5.5. Computer simulation of the interaction between two membrane-wrapped particles. (a) The numerical results are displayed together with the experimental results, which are rescaled by the bending rigidity $\kappa = 20.9 \pm 2.5 k_B T$ [166] and the particle diameter $D_p = 0.98 \pm 0.03 \mu\text{m}$. (b)-(c) show cross-sections of the simulations of two particles (green) adhered to a coarse-grained membrane (magenta), at separation $s = 3.7 D_p$ (b) and $1.5 D_p$ (c). The membrane vertices are denoted by small spheres with diameter l .

to the experimental value. Having set the volume and surface area of the vesicle to the target values, we apply an adhesion potential between the attractive part of the particles (which in our system is about 90% of the particles' total area) and the vertices in the vesicle to let the membrane wrap around the particles. We use a Monte Carlo annealing algorithm to identify the equilibrium shape of the membrane for different positions of the particles. Note that there is no absolute length scale involved in these simulations.

Once the particles are wrapped by the membrane, the adhesion energy and degree of wrapping remain constant, but the curvature energy depends on the separation between the particles. The excess energy of the membrane for different separations s is shown in Figure 5.5, together with the experimental data. We find that the curvature energy of the membrane favours attraction between the particles for distances $1.5 D_p \lesssim s \lesssim 2.2 D_p$, in excellent agreement with the experimental results. For larger distances the energy of the vesicle is barely affected by a change of the separation between the particles. The minimum distance is set by the resolution of our coarse grained description of the membrane: at $1.5 D_p$ we can be sure to always have two layers of vertices between the particles. Because of this limitation our simulations cannot capture the short-range effects observed in the experiment as well as in the higher resolution simulations of Reynwar *et al.* [4, 35]. In contrast to earlier work, however, our simulations do take the overall curved shape of the vesicle into account, as well as the fact that it is a closed surface with fixed area and enclosed volume. For these conditions, we find that there is no long-range repulsion between the particles, in contrast to some earlier numerical predictions on asymptotically flat membranes.³⁵ The observed attraction is entirely due to

a decrease in the bending energy of the membrane upon approach of the particles and is quantitatively agreeing with our experimental results on vesicles.

5.4 Conclusion

We established an experimental system of particles adhering to Giant Unilamellar Vesicles that enables quantitative measurement of interactions mediated by lipid membrane curvature. For individual membrane-adhering particles, we showed that there are only two states of membrane deformation: a non-wrapped and a fully wrapped state. This “all-or-nothing” behaviour is controlled by the particle-membrane adhesion strength and membrane tension, which agrees with a simple model based on bending, tension and adhesion energies.

The two-state particle wrapping allows us to selectively measure the effect of local membrane deformations on the pair interaction. For two membrane-wrapped particles, we observed a reversible attraction of three times the thermal energy over a distance of several microns. As the interaction is absent for non-wrapped particles, we conclude that it is mediated by the lipid membrane and originates solely from the particle-induced membrane deformation.

To further probe the underlying physical cause of this attraction, we used a coarse-grained numerical model and Monte Carlo methods from which we determined the interaction energy between two wrapped particles. Apart from the geometry and bending modulus of the membrane, which we respectively set to the experimental and literature values, the model requires no adjustable parameters. The energy profile we obtained from our simulations is in excellent quantitative agreement with the experiments. In particular, we find a long-ranged attraction between the wrapped particles, which is entirely due to a decrease in the bending energy of the membrane as the two particles approach each other.

As the observed interaction is determined by bending energy only, there is no absolute length scale involved in the simulations. This implies that the membrane curvature mediated force equally applies to the described colloidal particles as well as to membrane proteins such as proteins containing a BAR domain.¹³ In fact, our experimental measurements quantitatively model protein interactions on closed membranes, as long as the Helfrich energy description holds. More local membrane deformations induced by for instance transmembrane proteins² might also deform the membrane in a similar fashion, but on a length scale comparable to the membrane thickness. In this case the membrane can no longer be described by a two-dimensional surface, and consequently other effects such as membrane thickness modulations³¹ could lead to interactions. On the other hand, aggregates of transmembrane proteins may again act as larger membrane-deforming objects that are described by our model.

To more closely mimic biological systems, lipid membranes with multiple components and colloidal particles with anisotropic shapes or adhesion patches may be employed in the future. Multi-component membranes may locally phase-separate and af-

fect the measured interaction potential through an intricate process: the object-induced curvature may influence the local membrane composition¹⁷⁰ and thus spatially modulate the elastic constants of the membrane. A preference of the particle for a particular phase may further induce a local phase-separation that adds an additional force driven by the line tension of the phase boundaries³³. Besides multi-component membranes, colloidal particles with anisotropic shapes or site-specific adhesion patches may be used to mimic the complicated deformation profiles of proteins. These additional complexities will enable quantitative modelling of the interaction profile between membrane proteins of various geometries and thus further improve our understanding of cellular processes that involve membrane-shaping proteins.

MICROPARTICLE ASSEMBLY PATHWAYS ON LIPID MEMBRANES

This chapter is published as C. M. van der Wel, D. Heinrich and D. J. Kraft, 'Microparticle assembly pathways on lipid membranes', *Biophys. J.* **113**, in press (2017)
DOI:10.1016/j.bpj.2017.07.019

Abstract

Understanding interactions between microparticles and lipid membranes is of increasing importance, especially for unravelling the influence of microplastics on our health and environment. Here, we study how a short-ranged adhesive force between microparticles and model lipid membranes causes membrane-mediated particle assembly. Using confocal microscopy, we observe the initial particle attachment to the membrane, then particle wrapping, and in rare cases spontaneous membrane tubulation. In the attached state, we measure that the particle mobility decreases by 26 %. If multiple particles adhere to the same vesicle, their initial single-particle state determines their interactions and subsequent assembly pathways: 1) attached particles only aggregate when small adhesive vesicles are present in solution, 2) wrapped particles reversibly attract one another by membrane deformation, and 3) a combination of wrapped and attached particles form membrane-mediated dimers, which further assemble into a variety of complex structures. The experimental observation of distinct assembly pathways induced only by a short ranged membrane-particle adhesion, shows that a cytoskeleton or other active components are not required for microparticle aggregation. We suggest that this membrane-mediated microparticle aggregation is a reason behind reported long retention times of polymer microparticles in organisms.

6.1 Introduction

Artificial microparticles are increasingly applied in ceramics, paints, cosmetics, drug delivery,¹⁷¹ and microbiological techniques such as microrheology.⁵⁸ However, the negative environmental effects of polymer based microparticles, for example through uptake by and high retention in marine organisms, are becoming increasingly clear.²⁵ In order to be able to unravel the implications of microparticles on health and environment, it is crucial to understand their impact on cellular processes and especially their interactions with the cellular membrane, which is the most important protective barrier of the cell.

The first step in the interaction of microparticles with living cells is their adhesion to the membrane. This adhesion can be caused by a variety of mechanisms such as Van der Waals, Coulomb or hydrophobic forces, or complementary protein interactions.^{111,112,172} Subsequent internalization into the cell depends on the cell type, the particle size, and the particle surface moieties.^{22,23,111,173} Particularly micrometer-sized particles have been observed to not be internalized, but to form aggregates that remain irreversibly attached to the cellular membrane.^{22,23} Intriguingly, this membrane-mediated particle aggregation has also been reported on lipid vesicles,^{20,21,104} suggesting that a physical property of the lipid membrane drives the observed particle aggregation on living cells.

Here, we investigate this membrane-mediated particle assembly using a well-controlled model system that is described in Chapter 5. In this membrane-microparticle system, we use confocal microscopy to visualize both the membrane and particles through their fluorescence. Previously, we established that a single membrane adhesive particle is either completely wrapped by the membrane, or only attaches without inducing visible deformation. Here, we first quantify the mobilities of these two types of membrane-associated particles and find that the membrane significantly reduces the particle diffusivity.

This particle mobility enables membrane-mediated processes that assemble particles into aggregates. Previously, we have quantified an attraction between membrane-wrapped particles and noticed a short ranged irreversible force leading to particle aggregates (see Chapter 5). Here, we investigate the mechanisms that lead to the formation of these aggregates. We establish that the initial state of individual particles determines which assembly pathways they take: wrapped particles only interact via a membrane bending mediated force, attached particles stick together via small adhesive vesicles, and wrapped and attached particles form dimers driven by the strong membrane-particle adhesion. Finally, we describe and discuss the case in which a wrapped particle induces spontaneous membrane tubulation.

6.2 Methods

Chemicals Styrene (99%), itaconic acid (99%), 4,4'-azobis(4-cyanovaleric acid) (98%, ACVA), D-glucose (99%), bovine serum albumin (98%, BSA), methanol (99.9%), chloroform (99%), sodium phosphate (99%), deuterium oxide (70%), N-hydroxysulfosuccinimide

sodium salt (98%, Sulfo-NHS), and 1,3,5,7-tetramethyl-8-phenyl-4,4-difluoroboradiazaindacene (97%, BODIPY) were acquired from Sigma-Aldrich; methoxypoly(ethylene)glycol amine (mPEG, $M_w = 5000$) from Alfa Aesar; sodium chloride (99%), and sodium azide (99%) from Acros Organics; 1-ethyl-3-(3-dimethylaminopropyl) carbodiimide hydrochloride (99%, EDC) from Carl Roth; NeutrAvidin (avidin) and cholera toxin (subunit B) Alexa Fluor 488 conjugate (cholera toxin 488) from Thermo Scientific; DNA oligonucleotides (biotin-5'-TTTAATATTA-3'-Cy3) from Integrated DNA Technologies; $\Delta 9$ -cis 1,2-dioleoyl-*sn*-glycero-3-phosphocholine (DOPC), 1,2-dioleoyl-*sn*-glycero-3-phosphoethanolamine-N-[biotinyl(polyethylene glycol)2000] (DOPE-PEG-biotin), 1,2-dioleoyl-*sn*-glycero-3-phosphoethanolamineN-(lissaminerhodamine B sulfonyl) (DOPE-rhodamine), and G_{M1} ganglioside (GM1) from Avanti Polar Lipids. All chemicals were used as received. Deionized water with 18.2 M Ω cm resistivity, obtained using a Millipore Filtration System (Milli-Q Gradient A10), was used in all experiments.

Membrane preparation Giant Unilamellar Vesicles (GUVs) with diameters ranging from 5 to 20 μm were produced using the standard electrosweeling technique.¹³⁵ A lipid mixture was prepared in chloroform at 2 g/L consisting of DOPC, DOPE-PEG-biotin, and DOPE-rhodamine in a 97.5:2:0.5 weight ratio. 10 μL of this solution was dried on each of two 6 cm^2 ITO-coated glass slides (15–25 Ω , Sigma-Aldrich) and subsequently submersed in a solution containing 100 mM glucose and 0.3 mM sodium azide in 49:51 $\text{D}_2\text{O}:\text{H}_2\text{O}$. To induce vesicle formation, the electrodes were subjected to 1.1 V (rms) at 10 Hz for 2 hour. The thus obtained vesicles were stored in a BSA-coated vial at room temperature. To suppress the amount of smaller lipid vesicles, we filtered the GUV solution using a Whatmann 5.0 μm pore size cellulosenitrate filter directly before use. For the membrane tubulation experiments, the outer membrane leaflet was stained using the ganglioside GM1 and the dye cholera toxin 488, as follows: the above lipid mixture in chloroform was transferred to methanol, adding 0.2 wt% GM1. The electrosweeling then proceeded as described above. Before sample preparation, cholera toxin 488 (50 mg/L) was added to the PBS to stain the outer leaflet of the vesicles only.

Microparticle preparation Carboxylated polystyrene microparticles with a diameter of $0.98 \pm 0.03 \mu\text{m}$ were synthesized in a surfactant-free radical polymerization from 25.0 g styrene, 500 mg itaconic acid, 250 mg ACVA, and 125 mL water.¹³² 10 mg of the fluorescent dye BODIPY was included during synthesis. The size distribution of the particles was measured from electron micrographs taken by an FEI NanoSEM 200. To ensure a specific and strong adhesion between the microparticles and the lipid membrane we coated the microparticles with avidin and mPEG, using an EDC/Sulfo-NHS coating procedure.¹³¹ Per 15 mg particles, 15–50 μg NeutrAvidin and 4.0 mg mPEG were used. Sodium azide was added to a concentration of 3 mM to prevent bacterial growth. The density of biotin binding sites ($5 \times 10^1 - 1.5 \times 10^3 \mu\text{m}^{-2}$) was quantified using a fluorescence assay with DNA oligonucleotides having a biotin and a fluorescent marker. The particle coating and the quantification of biotin binding sites are described in Ch. 4.

Sample preparation To attach the microparticles to the model membranes, we gently mixed 20 μL of the GUVs with 0.04 μg microparticles dispersed in 6 μL phosphate buffered saline solution (PBS, $\text{pH}=7.4$). The PBS was density-matched with the microparticles (using D_2O) and had the same osmolarity as the glucose inside the GUV. After an incubation time of 10 min, the GUV-particle mixture was distributed into a microscope sample holder containing 50 μL of PBS. Due to the small density difference between PBS and glucose solutions, the particle-covered GUVs sediment to the bottom and could be visualized with an inverted microscope.

To control the tension of the vesicles, we change the osmotic pressure outside of the vesicles as follows: If the sample holder is sealed directly after preparation, there is no water evaporation and the osmotic pressure is preserved. In this case, no fluctuations of the membrane are observed and the vesicles are denoted “tense”, which for the here employed DOPC membranes corresponds to a membrane tension that is above $1 \mu\text{N m}^{-1}$. If the sample is imaged while leaving the sample holder open for a period of 30–60 min, water evaporates, the osmolarity of the outside solution increases, and the membrane tension of the vesicles decreases. During this process, we are able to image so-called “floppy” vesicles that exhibit membrane undulations with an amplitude greater than $1 \mu\text{m}$. The corresponding membrane tension that follows from the fluctuation analysis described in ref. [165] lays below $0.2 \mu\text{N m}^{-1}$. Figure 6.1 shows such a floppy vesicle together with its fluctuation spectrum.

As described in Chapter 5, the microparticles attach spontaneously to the model membranes due to the strong non-covalent binding between NeutrAvidin and the biotinylated lipids. If the particle-membrane adhesion is larger than the membrane bending energy, and the vesicle is floppy, particles will be wrapped by the membrane, which is observed by the colocalization of membrane and particle fluorescence. As the membrane-particle linkage is irreversible, tense membranes with wrapped particles can be obtained by increasing the tension of an initially floppy membrane, for instance by wrapping of additional particles.

Diffusion measurements Diffusion measurements of membrane-attached particles were performed by imaging the top part of a tense GUV with attached particles (see supporting video online). The particles were tracked in the recorded video images with sub-pixel precision using Trackpy.⁸⁶ Simultaneously, the fluorescence signal of the top part of the vesicle was recorded. We extract the centre of the vesicle from a two-dimensional Gaussian fit of this fluorescence. Using a separate measurement of the vesicle size, the full three-dimensional coordinates of the particles could be reconstructed.

Diffusion measurements of wrapped particles were performed on sequences of confocal slices of particle-covered GUVs (see supporting video online). Wrapped particles were identified by colocalization of membrane and particle fluorescence. The particles were tracked in the same way as with the attached particles. The vesicle position was determined by fitting circles to the vesicle contour.¹⁴⁵ The particle displacements were then measured in one dimension along the vesicle contour.

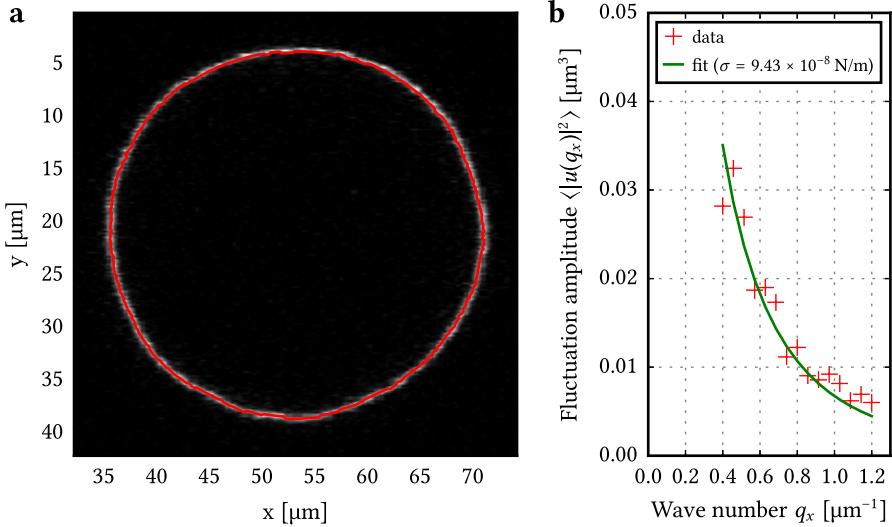


Figure 6.1. Fluctuation analysis of a GUV. (a) A cross-section of the vesicle with its tracked profile indicated using a red line. The corresponding video is available online. (b) The absolute value of the Fourier transform of the tracked membrane profile is shown in red crosses as a function of wavenumber. The green solid line denotes a least-squares one-parameter fit to the theoretical power spectrum.¹⁶⁵ The experimental power spectrum was averaged over 75 frames. The first five modes were discarded (corresponding to $q_x < 0.4 \mu\text{m}^{-1}$) as the fit model is erroneous for these modes due to the closed topology of the vesicle. Also, wave numbers larger than $1.2 \mu\text{m}^{-1}$ were omitted so that the correlation time of the fluctuations was at least four times larger than 6 ms, which is the time difference in the line scanning confocal microscope between acquiring the upper and lower vesicle boundaries. The fit was performed with a fixed membrane bending rigidity κ of $21 k_B T$. This yielded a membrane tension σ of 94 ± 7 nN/m. The analysis was done according to Pécrcéaux et al. [165].



Drifting vesicles were not analysed to rule out particle drift due to vesicle rotation. Particles that were closer than $2.5 \mu\text{m}$ to other particles were also omitted to rule out the long-ranged interparticle forces caused by membrane deformation described in Chapter 5. The diffusion coefficient was measured for each particle separately with linear regression of the mean squared displacements. As particles were confined to a spherical surface, the mean squared displacement only grows linearly in time if the squared curvature R^2 is much larger than the measured mean squared displacement.¹⁷⁴ To meet this condition, we limited the displacement measurements to short time intervals of up to 4 frames, corresponding to maximum lag times of 35–70 ms.

The measurement precision of each single-particle diffusion coefficient depends on the measured trajectory length.^{175,176} We computed these uncertainties and omitted

measurements with an imprecision larger than $0.04\mu\text{m}^2\text{s}^{-1}$ from the histograms of single-particle diffusion coefficients. This resulted in 39 trajectories (8 different GUVs) of attached particles and 25 trajectories of wrapped particles (on 14 different GUVs).

Imaging Samples were imaged with a Nikon Ti-E A1R confocal microscope equipped with a $60\times$ water immersion objective (NA = 1.2). The BODIPY and cholera toxin 488 (ex. 488 nm, em. 525 ± 25 nm) and DOPE-rhodamine (ex. 561 nm, em. 595 ± 30 nm) emissions were recorded simultaneously with a dichroic mirror separating the emission signal onto two detectors. The coverslips were pretreated with a layer of polyacrylamide to prevent particle and GUV adhesion, using a method described in Chapter 5. High-speed images used in the diffusion measurements were recorded at 57–110 Hz using a horizontal resonant scanning mirror, while high-resolution close-ups were recorded with a set of Galvano scanning mirrors.

6.3 Results and Discussion

Polymer microparticles adhere to lipid membranes by various kinds of (bio)chemical interactions, such as Van der Waals forces, electrostatic forces, or complementary protein interactions.^{111,112,172} In our experiments, we realized particle adhesion in a controlled manner by coating polystyrene particles ($1\mu\text{m}$ diameter) with the protein avidin and including a biotinylated lipid in the membranes. Once connected to the membrane, the particles do not detach due to the high energy gain associated with the non-covalent linkage between biotin and avidin (approx. $17k_{\text{B}}T$,¹⁴⁰ with $k_{\text{B}}T$ being the thermal energy), and the possibility of forming multiple avidin-biotin connections. An individual membrane-associated sphere usually occupies only one of two equilibrium states: either the membrane fully wraps around the microparticle or it does not deform at all.^{177–180} This can be tuned by changing the membrane tension and the membrane-particle adhesion energy (see Chapter 5).

In this chapter, we investigated the dynamics of particles in the attached and the wrapped state as well as their assembly behaviour over time. We first probed the membrane association of isolated particles by measuring the influence of the membrane on the particle mobility. Then, we mapped out the assembly pathways of multiple particles that interact through membrane deformations and eventually lead to membrane-mediated aggregates. Finally, we investigated a spontaneous tubulation process that occurs at particle inclusions.

6.3.1 Mobility of membrane-associated particles

While a particle retains its lateral mobility when it adheres to a liquid lipid membrane, the Brownian motion of the particle changes from three-dimensional to two-dimensional. Therefore its mean squared displacement changes from $\langle x^2 \rangle = 6Dt$ in the freely dispersed case to $4Dt$ in the bound case, where D is the diffusion coefficient and t

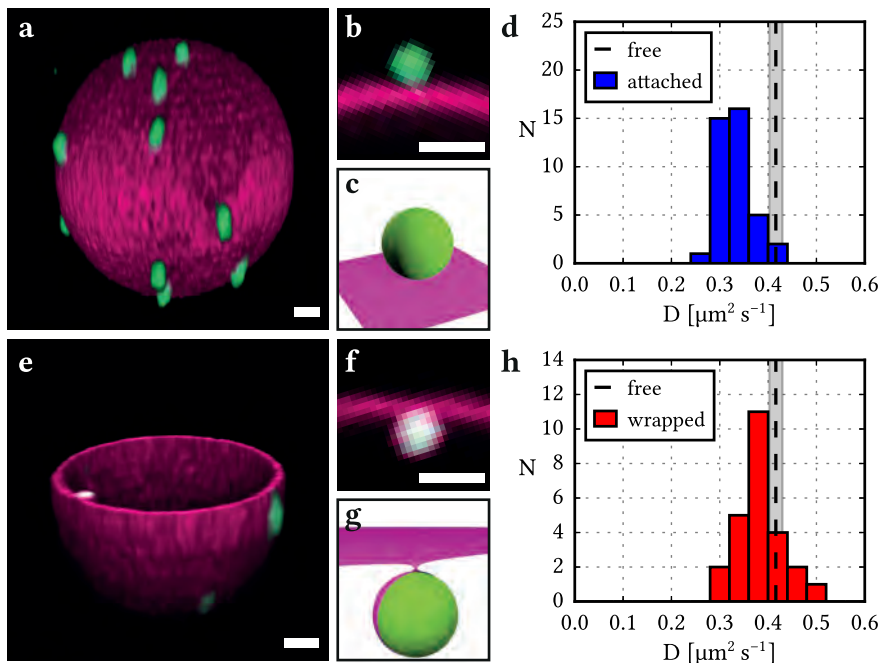


Figure 6.2. Diffusion coefficients of membrane adhered particles. In (a), a three-dimensional reconstruction of a confocal image with particles attached to a vesicle is shown (scalebar $2 \mu\text{m}$), with the corresponding close-up in (b) and illustration in (c). A histogram of single-particle diffusion coefficients of these attached particles is shown in (d). In (e), one hemisphere of a membrane with one wrapped and two attached particles is displayed (scalebar $2 \mu\text{m}$), with (f) the corresponding close-up, (g) an illustration, and (h) the histogram of single-particle diffusion coefficients. In the histograms, only coefficients with a standard error below $0.04 \mu\text{m}^2 \text{s}^{-1}$ were included. The binning width equals this value. For reference, the diffusion coefficient of freely dispersed particles is displayed by a dashed black line, with a shaded area that denotes the corresponding spread.

denotes the lag time over which $\langle x^2 \rangle$ is measured. Additionally, upon particle adhesion we expect that its diffusion coefficient is lowered significantly due to an additional drag force caused by the relatively high viscosity of the membrane.

To quantify the diffusion of attached particles, we used particles with biotin binding site densities ranging from 5×10^1 to $1.5 \times 10^3 \mu\text{m}^{-2}$ adhered to GUVs with diameters above $15 \mu\text{m}$ and with a surface tension above $1 \mu\text{N m}^{-1}$. This choice of membrane tension and biotin binding site density ensured that particles remained not wrapped (see Figure 6.2a). As a reference, we first measured the diffusion constant of freely suspended particles and found it to be $0.416 \mu\text{m}^2 \text{s}^{-1}$, which is in agreement with the Stokes-Einstein relation. The distribution of the single-particle diffusion coefficients after membrane attachment is shown in Figure 6.2d. Compared to freely suspended particles, the average

diffusion coefficient decreased significantly to $0.334 \pm 0.006 \mu\text{m}^2 \text{s}^{-1}$. The corresponding increase in drag coefficient $\zeta = k_B T/D$ due to the proximity of the membrane is 26%. The observed $0.04 \mu\text{m}^2 \text{s}^{-1}$ spread of single-particle diffusion coefficients is caused by measurement imprecision, the 3% spread in particle diameters, and possibly different avidin coating densities yielding different particle-membrane adhesion shapes.

The diffusion measurements of wrapped particles were performed using a single particle batch with a higher biotin binding site density ranging between 1.3×10^2 and $1.5 \times 10^3 \mu\text{m}^{-2}$. To ensure a wrapped fraction of particles of 60%, we increased the available membrane surface area by lowering the tension of the GUVs temporarily below 10 nN m^{-1} , as described in Chapter 5. The resulting histogram of single-particle diffusion coefficients is shown in Figure 6.2h. Again, the membrane association lowered the diffusivity of the particles, albeit less than for simple membrane attachment: we found $0.381 \pm 0.010 \mu\text{m}^2 \text{s}^{-1}$ as the average diffusion coefficient of wrapped particles. The corresponding increase in drag is only 9%. Apparently, the membrane has less effect on the particle's mobility if it wraps around the particle. The difference between the diffusion coefficients of the wrapped and attached particles is significant with a certainty of 99%, as determined by Student's t -test ($t = 2.57$). We hypothesize that this is due to distance between the particle and the bulk membrane (see Figs. 6.2c and g). Particle wrapping involves membrane bending,³⁰ which increases the distance between membrane and particle compared to the attached case. The farther the particle is from the membrane, the lower the influence of the membrane on the particle,¹¹⁶ which might explain the higher mobility of wrapped particles.

To quantitatively explain the excess drag exerted by a membrane on a Brownian particle, several models have been proposed relating the membrane surface viscosity to the particle's drag coefficient. As the employed spheres of $1 \mu\text{m}$ diameter are much larger than the membrane thickness, we cannot use models based on the Saffman-Delbrück description,¹⁸¹⁻¹⁸³ which only consider the drag experienced by a circular membrane patch, and not by the full sphere that is attached to it. This is seen conveniently by evaluating the dimensionless Boussinesq number $B = \eta_S/(\eta R)$, with η_S the membrane surface viscosity, η the bulk viscosity, and R the sphere radius. For the Saffman-Delbrück model to be applicable, bulk viscous effects on the sphere have to be negligible and $B \gg 1$. We estimate $B = 10$ for our system and therefore employ the analysis by Dimowa et al, which is a numerical solution to the full hydrodynamic model for spheres embedded in a viscous membrane.¹⁸⁴ As they found the counter-intuitive result that the drag coefficient only slightly depends on the inclusion height of the particle relative to the membrane, we may invoke their numerical relation without precisely knowing the particle-membrane adhesion patch size. From our measured excess drag coefficient we thereby obtain $\eta_S = 1.2 \pm 0.1 \times 10^{-9} \text{ Pa s m}$. This DOPC membrane viscosity lies in between previously reported values of $5.9 \pm 0.2 \times 10^{-10} \text{ Pa s m}$ [185] and $15.9 \pm 2.3 \times 10^{-9} \text{ Pa s m}$ [117].

To summarize, we observed that membrane-attached particles experience an excess drag of 26% due to the membrane. Using the model by Dimowa and Danov, and

neglecting differences due to inclusion height, we obtained a membrane viscosity of $1.2 \pm 0.1 \times 10^{-9}$ Pa s m. Furthermore, we observed that membrane-wrapped particles only experience an excess drag of 9%, which we explain by a finite distance between membrane and particle which decreases the influence of the membrane viscosity. The here described diffusion measurements have direct consequences for the timescales of the diffusion-limited aggregation processes that are described in the next section.

6.3.2 Microparticle assembly pathways

When particles were incubated with floppy vesicles for more than 30 min, we observed the formation of large particle aggregates on the membrane. For example, in Figure 6.3, snapshots of the same vesicle at different points in time are shown, which demonstrates the gradual appearance of particle clusters through membrane-mediated aggregation. The same particles were observed to not aggregate in the absence of vesicles: the assembly pathways described here only occur after adhesion to the membrane. We found that the two states of particle-membrane adhesion, attached to and wrapped by the membrane (Figures 6.4a and b), induce distinct assembly pathways, leading to the observed aggregation of particles on GUVs. In this section, we will categorize and discuss their interactions and assembly pathways, starting from all combinations of single-particle adhesion states: (1) wrapped-wrapped, (2) attached-attached, and (3) wrapped-attached.

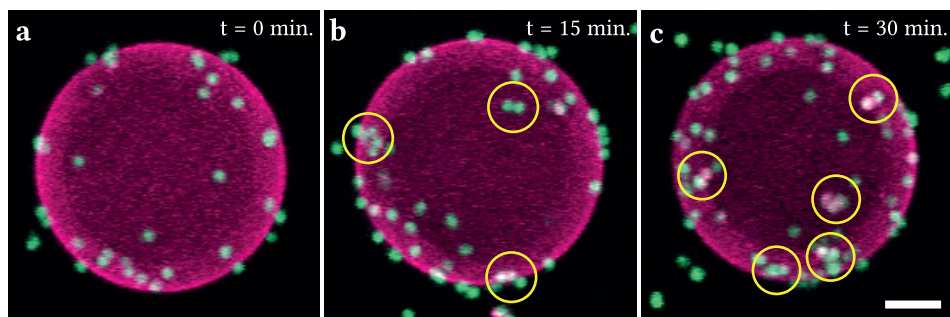


Figure 6.3. Microparticles that aggregate on a lipid vesicle. A vesicle (in magenta) with associated particles (in green) is shown (a) directly after sample preparation, (b) after 15 min, and (c) after 30 min. The images are maximum intensity projections. Formed aggregates, which were identified from the full three-dimensional images, are denoted by yellow circles. These aggregates formed after adhesion of the particles to the vesicles, which we observed by following the clustering of single particles. The scale bar denotes 5 μ m.

The first assembly pathway is due to the long ranged attraction exhibited by two membrane-wrapped particles (Figure 6.4f). This interaction force has been described extensively in theory and simulation,^{35,36,152,186} but only recently in experiment (see Chapter 5). In the experimental system employed here, the attractive potential was found

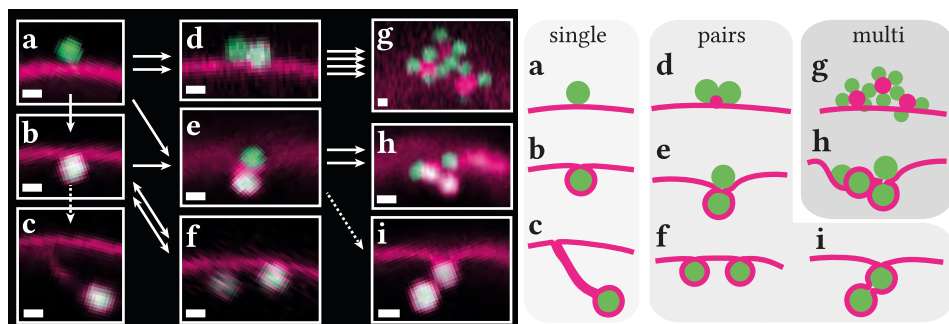


Figure 6.4. Membrane-mediated irreversible assembly pathways of microparticles, displayed in confocal images (left, scale bars: 1 μm) and sketches (right). Solid arrows denote irreversible particle assembly pathways, two-sided arrows denote a reversible pathway, and dotted arrows denote pathways that were observed less than 1% of the cases. (a) A membrane attached particle is (b) wrapped at large membrane-particle adhesion energy and low membrane tension. (c) A wrapped particle can induce the formation of a membrane tube. Subsequently, (d) two attached particles stick together via secondary lipid vesicles. (e) An attached particle assembles with a wrapped particle forming a membrane-mediated dimer (see video online), while (f) two wrapped particles interact reversibly. (g) Multiple particles form an aggregate via secondary lipid vesicles. (h) The dimers aggregate into tetramers and larger structures (see video online). (i) The membrane-mediated dimer (e) can be fully wrapped by the membrane. The wrapped half of the dimer can be identified by the white colour which is caused by the overlap of the membrane and particle fluorescence.

to range over 2.5 μm with a strength of three times the thermal energy. For sparse coverage with microparticles, both assembly into a dimer state and subsequent disassembly were observed indicating reversibility of this assembly pathway. For a more dense coverage with wrapped particles, simulations predict the formation of linear and crystalline structures.^{17,19,187}

Second, membrane-attached particles (Figure 6.4a) do not interact with each other. However, in the presence of small ($R < 1 \mu\text{m}$) lipid vesicles, aggregation of these particles can be observed. This leads to particle aggregates mediated by small lipid structures, as shown in Figures 6.4d and g. Filtration of the GUVs reduces the amount of free small lipid vesicles, and consequently the amount of particle aggregates (see Chapter 5). However, we note that many GUVs have small lipid structures associated on them, even after filtration (see Figure 6.5). We presume that these originate from the preparation or from mechanic shocks during sample handling. Contrary to the attached particles, fully wrapped particles cannot aggregate via small lipid vesicles, for the reason that their surface is already occupied by the GUV membrane.

A third and most complex pathway occurs for a combination of wrapped and attached particles and starts with a well-defined assembly step; the local deformation of the membrane induced by the wrapped particles can serve as a binding site for attached

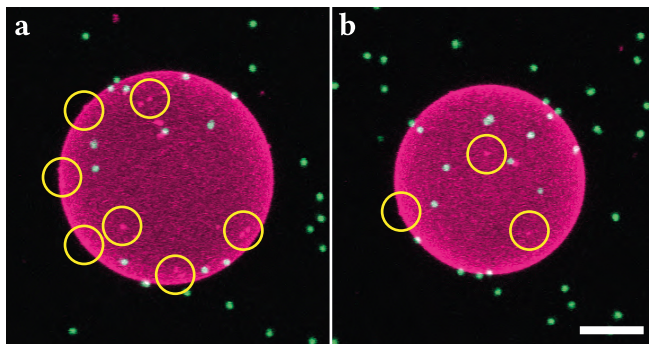


Figure 6.5. Maximum intensity projections of two GUVs (magenta) with attached particles (green). Bright fluorescent spots on the GUVs are denoted with yellow circles. These spots originate from small lipid structures, that are attached to the GUV membrane. Unlike the freely suspended lipid structures, these cannot be removed using filtration. We observed that these structures cause the assembly of membrane-attached particles into membrane-attached aggregates. The scale bar denotes 10 μm .

particles (Figure 6.4e). We observed this membrane-mediated dimerization only when an attached particle came into contact with a wrapped particle, and the resulting dimer structure occurs frequently on membranes that initially had both attached and wrapped particles present. The dimers remain stable over the course of the experiment, unless they assemble further into larger aggregates (for example, Figure 6.4h). We hypothesize that the attached particles are captured irreversibly on top of the wrapped particle due to the increased contact area, as illustrated in Figure 6.6. Although the membrane-particle linkages are mobile in the membrane, the attached particle cannot escape once sufficient linkages have been formed in this ring-shaped region. This is because the formed ring of bound linkers would need to cross the central non-binding patch, which requires the breakage of linkages. In this way, the attached particle is topologically protected from detaching from the wrapped particle and they diffuse together as a membrane-mediated dimer.

Rarely, we observed a two-step hierarchical wrapping: after formation of the membrane-mediated dimer, the previously only attached particle becomes wrapped as well, resulting in a tube-like structure containing two wrapped spheres (see Figure 6.4i). This indicates that the biotin binding site density on this particle is large enough to ultimately become wrapped but, coincidentally, this only occurred after it had been captured by the earlier wrapped particle. Although similar configurations of multiple particles wrapped in membrane tubes have been observed in simulations,^{36,179,186} it is important to note here that membrane-particle binding in our experiments is an irreversible process due to the strong avidin-biotin bonds. Therefore, equilibrium considerations do not necessarily apply to our adhesion-driven interaction pathways. Also, this implies that the tubularly wrapped spheres cannot be formed by the combination of two wrapped

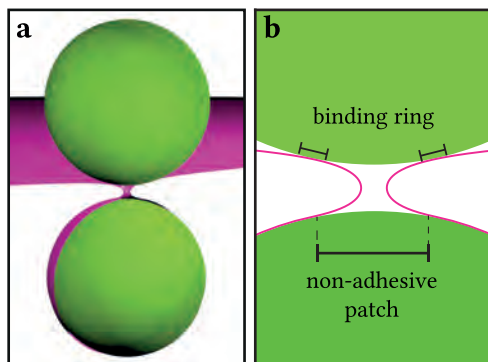


Figure 6.6. Membrane-mediated dimer of microparticles. A three-dimensional illustration of the dimer is shown in (a). In (b) a cross-section is depicted, showing the binding ring between the membrane and the top particle, which irreversibly connects the particles. The non-adhesive patch size was chosen arbitrarily for the purpose of this illustration; the membrane thickness is to scale with the particle diameter. See also Figure 6.4e.

particles, as this would require partial unwrapping and thus breakage of membrane-particle linkages. Yet, the presence of membrane deformation induced by the initially wrapped particle may promote wrapping of the second particle by lowering a kinetic barrier towards the energetically more favourable wrapped state.

The relative frequencies of the three described dimerization pathways are fully determined by the initial particle wrapping state: we exclusively observe small-vesicle mediated interaction for attached particles, long ranged attraction for wrapped particles, and irreversible dimerization for the combination attached-wrapped. Thus, the short-ranged membrane-particle adhesion mechanism drives the lipid vesicle mediated interactions that result in aggregation of attached particles (Figure 6.4d) as well as in the dimerization of attached and wrapped particles (Figure 6.4e).

These adhesion-driven interactions continue to play a role as long as there is area on the particle left that is not covered by membrane, such as is the case for the attached particles (Figure 6.4a and d) or for the membrane-mediated dimer (Figure 6.4e). Indeed, two dimers can assemble into larger structures such as tetramers (Figure 6.4h), and multiple attached particles aggregate via secondary lipid vesicles (Figure 6.4g). Depending on the particle concentration and waiting time after mixing, particles were observed to assemble on floppy membranes into permanent aggregates of 5-50 particles (see for example Figure 5.4a). On tense membranes, however, particles do not become wrapped and therefore only the small lipid vesicle mediated aggregation can be observed (Figures 6.4d and g).

In summary, by using confocal microscopy we were able to distinguish a variety of assembled microparticle structures mediated purely by a lipid membrane, either through membrane deformations or the short-ranged adhesive forces between membrane and

particles. We correlated the different observed structures with the initial state of wrapping of the individual particles and formulated an aggregation model containing three mechanisms for membrane-mediated interactions. Apart from the secondary lipid structure interactions, which can be suppressed, we can categorize collective particle interactions on membranes into three different types: First, membrane-attached particles exhibit only diffusive motion and do not interact with each other. Second, membrane-wrapped particles interact with each other via membrane deformation forces. Multiple wrapped particles are expected to form linear and crystalline structures.^{17,19,187} However, we did not observe this behaviour because of the third regime: a mixture of attached and wrapped particles starts with the formation of permanent dimers and eventually leads to permanent particle aggregates. This observation of microparticle aggregation on GUVs proves that for the formation of membrane-mediated aggregates, no cytoskeleton or other active components are necessary: the adhesion between particle and membrane is sufficient for aggregation.

When considering the impact of microparticles on living organisms, internalization into the cell has been the major focus in literature, although aggregation on cellular membranes has been reported.^{22,23,173} Here, we showed that this aggregation is driven by the membrane itself and therefore is a generic property of microparticles that adhere to cellular membranes. This has the following important consequence on the particle retention timescales: whereas a single microparticle may be bound reversibly to the membrane, aggregates will form multiple bonds with the membrane which take exponentially longer times to break.¹⁸⁸ Therefore, the here described membrane-mediated aggregation of microparticles might be an important factor contributing to the high retention times of polymer microparticles in organisms.

6.3.3 Spontaneous membrane tubulation

After a particle had been wrapped by the lipid membrane, we occasionally observed ($N = 20$) spontaneous formation of a membrane tube starting from the neck of the wrapped particle onwards (see Figure 6.7a). This tubulation process occurred for less than 1% of all wrapped particles. The particles remained wrapped by and connected to the vesicle membrane, but could freely diffuse in the vesicle interior. The membrane tubes elongated rapidly and exhibited large thermal fluctuations. In addition, we never observed reversal of the tubulation, which underlines the surprising absence of retracting tensile forces.

To prove that the observed structure is in fact a membrane tube, and not a rod-like micelle, we enable distinction between the inner and outer leaflet of the membrane through inclusion of a fluorescent dye. By adding cholera toxin 488 after formation of GUVs that contained 0.2 wt% GM1, we achieved exclusive staining of the outer leaflet. This is confirmed by the absence of green fluorescence in other membrane structures inside the GUV (see Figure 6.7b–d). If the particle would have induced hemifusion of the membrane thereby creating a tubular micelle that connected the wrapped particle to the membrane, the tube would consist of the inner leaflet only. Conversely, the membrane would be made up of both the inner and outer leaflet if the particle had truly produced

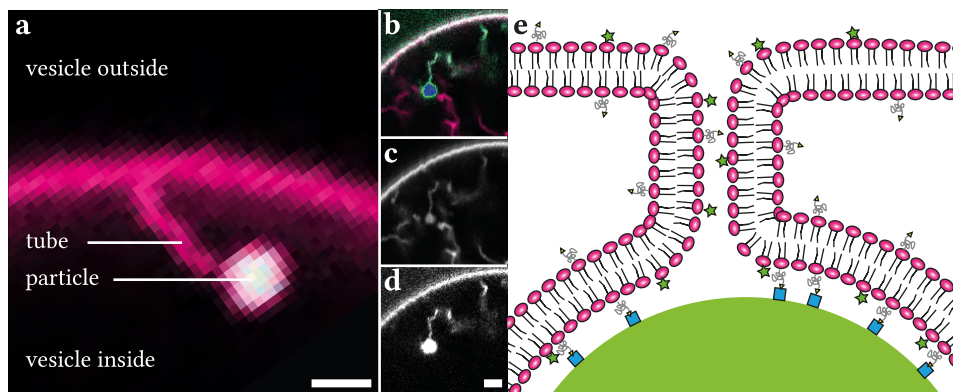


Figure 6.7. Spontaneous membrane tubulation at wrapped microparticles. The corresponding video is available online. (a) A confocal close-up of a particle (green) that is connected to the membrane (magenta) via a tube. To stain only the outer membrane leaflet, we included GM1 lipids into the GUVs and added cholera toxin 488 after GUV formation. (b) A channel overlay with the membrane in magenta, cholera toxin 488 in green, and the particle fluorescence in blue. A single channel image in the wavelength range 500–550 nm (c) shows only the DOPE-rhodamine, and 565–625 nm (d) shows the cholera toxin 488 together with the microparticle. As the particle-induced tube clearly exhibited green fluorescence, we conclude that the outer leaflet is present and therefore the structure must be a membrane tube. The absence of green fluorescence in the other membrane structures inside the GUV confirms that the cholera toxin 488 only stains the vesicle outside. (e) An illustration of the membrane tube. Here, green stars denote the cholera toxin 488 which is attached to GM1, yellow triangles the biotin which is connected via a PEG2000 spacer to DOPE lipids, and blue squares the NeutrAvidin which is connected to the particle. Scalebars denote 2 μm .

a tubular structure. The fluorescence of cholera toxin 488 in the tube observed in the experiment clearly indicated that the outer leaflet is present. Thus, we can conclude that the observed structure in between the particle and the GUV in fact consists of a strongly curved tubular membrane.

Why do membrane tubes spontaneously nucleate at wrapped particles? While this process is ubiquitous in living cells,^{189–191} it is typically not observed in (symmetric) model bilayers. In the absence of preferred curvature, it has been established both theoretically and experimentally that a supporting force $F = 2\pi\sqrt{2\sigma\kappa}$ is necessary to stabilize a tube against retraction, and that its radius is given by $R = \sqrt{\kappa/(2\sigma)}$.^{115,192,193} Here, σ denotes the membrane tension and κ its bending rigidity. Taken together, this yields $F = 2\pi\kappa/R$. Since the membrane diameter of our observed tubes is below the diffraction limit, $R < 100$ nm, a tube-supporting tensile force would need to be larger than 5 pN (given $\kappa = 21$ k_BT [166]). Clearly, such a force is absent in our experiments, as the particle diffuses freely after tube-formation for the duration of the experiment. A force of 1 pN on a freely suspended colloidal particle would already result in a particle drift

velocity of $100 \mu\text{m s}^{-1}$. Thus, we conclude that only a preferred curvature of the bilayer could explain the observed membrane tubes.¹⁹⁴ Also in the presence of a pressure difference across the membrane, a more complex analysis shows that preferred curvature is necessary for stable force-free membrane tubes.¹⁹⁵

The bulky DOPE-PEG-biotin lipids could indeed generate such a preferred curvature, if they would be distributed unevenly across the bilayer leaflets.¹⁹⁵ Depletion of these lipids by adhesion to the particles seems however unlikely: the here employed DOPE-PEG-biotin molar fraction of 0.5% is well above the number of biotin binding sites on the particles of linkers on the particles. Therefore, an initial bilayer asymmetry due to an uneven distribution of lipids or due to solvent asymmetry¹⁹⁶ are likely causes of the observed preferred bilayer curvature.

Given the presence of a preferred curvature, the neck that is induced by the wrapped particles logically serves as a starting point for the formation of a tube, which would otherwise have to cross a significant energy barrier.¹¹⁵ In this way, membrane-wrapped microparticles act as nucleation sites for membrane tubes.

6.4 Conclusion

We have shown that microparticles aggregate on lipid membranes. After adhesion to the membrane, particles remain laterally mobile on the membrane. We have quantified the particles' mobility and found that their diffusion coefficients of $0.416 \pm 0.014 \mu\text{m}^2 \text{s}^{-1}$ in dispersion are reduced to $0.33 \pm 0.04 \mu\text{m}^2 \text{s}^{-1}$ after membrane attachment. Using the numerical model by Dimowa et al. [116, 184, 197], we computed the membrane surface viscosity and found $1.2 \pm 0.7 \times 10^{-9} \text{ Pa s m}$. This value falls in between two previously determined values for a pure DOPC membrane.^{117,185} For wrapped particles, we observed diffusion coefficients of $0.38 \pm 0.05 \mu\text{m}^2 \text{s}^{-1}$. We hypothesize that the higher diffusivity is due to an increased distance between membrane and particle.

We have established a complete picture of the onset of aggregation of microparticles associated with lipid membranes. Particles can interact with each other in the following three ways. Firstly, membrane-wrapped particles interact with each other through a membrane deformation mediated force that ranges over several particle diameters, as has been shown in refs. [21], [104], and Chapter 5. Secondly, this interaction is not present for attached particles that do not deform the membrane. However, these can irreversibly aggregate via smaller secondary vesicles. Thirdly, we have shown here that attached particles can become trapped in the deformation sites created by a wrapped particle, forming membrane-mediated dimers. The last two adhesion-mediated mechanisms ultimately result in complex random aggregates of multiple particles. In the case in which the membrane has a preferred curvature, wrapped microparticles can also serve as a nucleation site for membrane tubes.

The observed aggregation of colloidal particles mediated by lipid membranes shows that even in the absence of proteins or active components, particles aggregate in order to optimize their contact area with the lipid membrane, or to minimize the membrane de-

formation. This has important consequences: whereas in general single microparticles may easily adsorb and desorb on the membrane, aggregates of particles desorb exponentially slower, which might explain the reported high retention times in organisms. This systematic description of the assembly pathways of microparticles on model lipid membranes will enable a better understanding of microparticle aggregation in biological systems, and especially the accumulation of microplastics.

Part III

Lipids for colloidal self-assembly

COLLOIDAL ORGANOSILICA SPHERES THROUGH SPONTANEOUS EMULSIFICATION

This chapter is published as C. M. van der Wel, R. K. Bhan, R. W. Verweij, H. C. Frijters, Z. Gong, A. D. Hollingsworth, S. Sacanna, and D. J. Kraft, 'Preparation of colloidal organosilica spheres through spontaneous emulsification', *Langmuir* **33**, in press (2017) DOI:10.1021/acs.langmuir.7b01398 Reproduced with permission, copyright 2017 American Chemical Society.

Abstract

Colloidal particles of controlled size are promising building blocks for self-assembly of functional materials. Here, we systematically study a method to synthesize monodisperse, micrometer-sized spheres from 3-(trimethoxysilyl)propyl methacrylate (TPM) in a bench-top experiment. Their ease of preparation, smoothness, and physical properties provide distinct advantages over other widely employed materials such as silica, polystyrene, and poly(methyl methacrylate). We describe that the spontaneous emulsification of TPM droplets in water is caused by base-catalysed hydrolysis, self-condensation, and deprotonation of TPM. By studying the time-dependent size evolution, we find that the droplet size increases without any detectable secondary nucleation. Resulting TPM droplets are polymerized to form solid particles. The particle diameter can be controlled in the range of 0.4–2.8 μm by adjusting the volume fraction of added monomer and the pH of the solution. Droplets can be grown to diameters of up to 4 μm by adding TPM monomer after the initial emulsification. Additionally, we characterize various physical parameters of the TPM particles and we describe methods to incorporate several fluorescent dyes.

7.1 Introduction

Colloidal particles are widely used in industrial applications and also serve as model systems for fundamental studies, such as crystallization,^{47,198} the packing of small clusters,⁷¹ and the glass transition.⁵³ Many of these applications rely on the availability of spherical particles that have an accurately controlled size: for instance, crystallization requires spheres with a polydispersity below 6%.¹⁹⁹ Monodisperse colloidal spheres can also be employed as basic building blocks for fabricating more complex anisotropic structures, such as lock-and-key particles, colloidal molecules, and Janus particles.^{43,45,50,200}

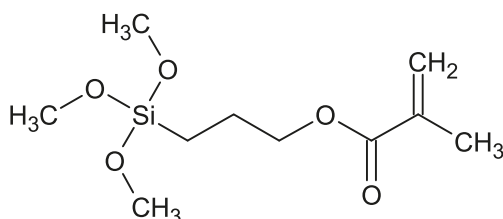


Figure 7.1. Structural formula of 3-(trimethoxysilyl)propyl methacrylate (TPM).

Therefore, the synthesis of micrometer-sized monodisperse spheres has become an indispensable technique in colloidal science. Synthesis protocols for a select range of widely used materials are well established, in particular for silica,²⁰¹ polystyrene,²⁰² and poly(methyl methacrylate).²⁰³ Each of these materials has its own advantages: for example, silane chemistry allows for a wide range of possible surface coatings, polystyrene particles can be density matched with water in order to exclude gravitational effects, and poly(methyl methacrylate) particles can be refractive index and density matched in an organic solvent, enabling accurate three-dimensional confocal imaging.

Despite the well-documented and mostly straightforward synthesis methods, many scientists refrain from synthesizing these particles themselves due to the basic chemistry infrastructure that is required. Here, we study a bench-top preparation of monodisperse colloidal particles that can be implemented with as little as a stirred beaker and thus is readily accessible to a wide range of scientists. This synthesis method employs the alkoxy silane 3-(trimethoxysilyl)propyl methacrylate (TPM, see Figure 7.1). The advantage of this material is threefold: First, the preparation can be performed without extensive chemical equipment and can be completed within four hours. Second, we show that tuning the available synthesis parameters allows control over the particle size from 0.45–1.70 μm . Third, the organosilica material of the resulting colloidal spheres has the chemical versatility of silica, while the material is stable in water, its density is lower than that of silica, and its refractive index is similar to that of poly(methyl methacrylate). This combination of features opens up new experimental possibilities, for instance the manipulation and three-dimensional tracking of dense suspensions²⁰⁴.

The preparation of TPM spheres begins with the spontaneous formation of TPM emulsion droplets in water. This phenomenon has been described previously for different alkoxy silanes in water under alkaline conditions.²⁰⁵ Since TPM can be polymerized at its methacrylate moiety, these emulsion droplets can also be used to fabricate solid colloidal particles, which has been used in the past to image Pickering emulsions^{51,206} as well as to make complex and anisotropic particles.^{50,200,204} However, the preparation method of TPM spheres has not been studied systematically to date. In order to provide a reference for the TPM microparticle preparation, we here first review previous studies on the emulsification of trialkoxy silanes. Then we summarize the preparation method and several ways of including fluorescent dyes, measurements of material properties, a time-resolved measurement of the synthesis, and a study of the effect of various synthesis parameters. Finally, we describe and characterize a seeded growth method for creating TPM droplets with sizes of up to 4 μm .

7.1.1 Review of Previous Work

Obey and Vincent [205] first showed that a monodisperse emulsion can be formed spontaneously by mixing an alkoxy silane, dimethyldiethoxy silane, with water or ethanol mixtures at alkaline conditions. They proposed a mechanism that required the base-catalysed nucleation and growth of poly-alkoxy silane in water from an initial single-phase system. The emulsions formed were thought to be kinetically stabilized against aggregation by negative charges on the droplet interface.

The same method was adapted to create emulsions of TPM stabilized by various inorganic nanoparticles and tetramethylammonium hydroxide (TMAH) ions, so-called Pickering emulsions.^{206,207} Stable emulsion droplets of diameters ranging from 10–100 nm were observed in the presence of these nanoparticles. For Pickering emulsions stabilized by magnetite particles,²⁰⁶ the droplet size increased with increasing TPM volume fraction and decreased when more of the magnetite particles were added at constant TPM volume fraction. The emulsion is also formed when the TPM is mixed with other monomers such as methyl methacrylate and styrene, indicating that only relatively small amounts of TPM are needed to stabilize the droplets.²⁰⁸

Later it was found that TPM emulsions can also be obtained in the absence of nanoparticles.^{50,51} These emulsions had diameters of approximately 1 μm , which is much larger than the Pickering emulsions. The initially polydisperse emulsions were formed after 1 day using a mixture of TPM, water, and various quaternary ammonium salts at pH 9 to 10.⁵¹ By adding pre-hydrolysed TPM drop-wise to an ammonia solution until the droplets reached their target size, Sacanna et al. [50] succeeded in making these TPM-in-water emulsions monodisperse. The advantage of using TPM is that these droplets could then be polymerized using a radical initiator, which resulted in solid dimpled spheres if the polymerization was initiated from the water phase. Furthermore, the droplets could be fluorescently labelled by the addition of a rhodamine dye covalently linked to the alkoxy silane APS (3-aminopropyl triethoxy silane) after droplet formation.²⁰⁰

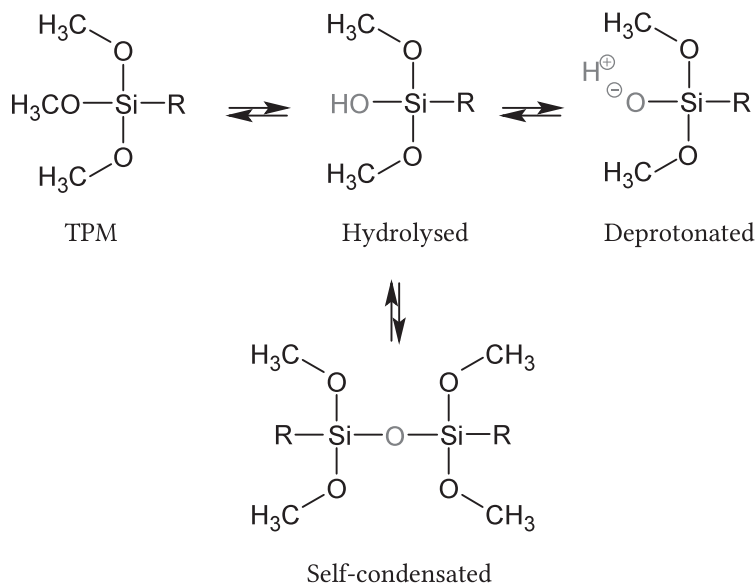


Figure 7.2. Hydrolysis, deprotonation and self-condensation reactions of TPM. “R” stands for the propylmethacrylate group. The scheme is far from complete: reaction products can hydrolyse, deprotonate and self-condensate again giving an extensive network of possible reaction pathways and products.

Because TPM will hydrolyse and subsequently self-condensate in water,^{209,210} hydrolysis and self-condensation reactions are believed to be the driving forces for the formation of a TPM emulsion.^{51,205} An overview of these reactions is given in Fig. 7.2. The rates of these processes increase strongly with the pH of the solution: at neutral pH, only 1–5 % of TPM monomers have reacted after 12 h,^{211–213} while the reported first order rate constant for hydrolysis at pH 9 is 1.2 h^{-1} ,²¹² which means that 90 % of the TPM monomers have hydrolysed after 2 h. Condensation reactions eventually lead to TPM oligomers that are built up from octamers.^{209,211} Indeed, Sacanna et al. [214] confirmed the release of methanol during TPM emulsion formation by ^1H NMR, which indicates that the TPM is at least partially hydrolysed in the emulsification process. The same TPM oligomers were found regardless of the type of base added, indicating that the oligomers grow by the same mechanism.²¹¹ This implies that, while only ammonia has been employed so far, any base could in principle be used to form a monodisperse TPM emulsion.

In addition to hydrolysis and self-condensation, deprotonation is known to happen for silicates and alkyl substituted silanols.^{215,216} Although there is no study available on the deprotonation of TPM, there is evidence that at pH 9.2 TPM oligomers become

negatively charged.²¹⁷ Sacanna et al. [214] proposed a mechanism where the TPM will produce its own charged surfactant consisting of deprotonated TPM at the TPM/water interface which could contribute to the stabilization of the emulsion droplets. By analysing bulk TPM/water surface tensions, Kraft et al. [218] found that emulsions are formed if the bulk surface tension is below 10 mN m^{-1} . Below this surface tension, an increasingly larger droplet surface area is created with decreasing surface tension. Increasing the concentration of hydrolysed TPM lowers the interfacial tension, pointing again toward the stabilizing properties of deprotonated TPM molecules.

In this study, we describe a preparation method of micrometer-sized TPM spheres as well as methods of including several fluorescent dyes. Then we characterize the material properties of TPM spheres. To further understand the spontaneous emulsification of TPM, we then study the time evolution of the TPM droplets during a synthesis as well as the effects of various synthesis parameters on the particle size distribution. Finally, we describe a seeded growth method to obtain particles with diameters of up to $4 \mu\text{m}$.

7.2 Methods

Materials 3-(Trimethoxysilyl)propyl methacrylate (TPM, 98 %), ammonium hydroxide (28 % NH_3 in water), tetramethylammonium hydroxide (TMAH, 25 % in water), azobis(isobutyronitrile) (AIBN, ≥ 98 %), potassium peroxydisulfate (KPS, ≥ 99 %), 2-hydroxy-2-methylpropiophenone (≥ 97 %), rhodamine B isothiocyanate (RITC, mixed isomers), fluorescein isothiocyanate isomer I (FITC, ≥ 90 %), 3-(aminopropyl)triethoxysilane (APS, ≥ 98 %), dimethyl sulfoxide (DMSO, ≥ 99.9 %), 1,3,5,7-tetramethyl-8-phenyl-4,4-difluoroboradiazaindacene (BODIPY, 97 %), perylene (≥ 99.5 %), pyridine (≥ 99.9 %), and 2-ethylhexyl 4-methoxycinnamate (98 %) were purchased from Sigma-Aldrich and used as received. Sodium hydroxide (NaOH, 98.5 %) was obtained from Acros Organics. All solutions were prepared from deionized water with $18.2 \text{ M}\Omega \text{ cm}$ resistivity, using a Millipore Filtration System (Milli-Q Gradient A10).

Emulsification To prepare TPM emulsions in water, we used ammonium hydroxide as a catalyst. 15 mL of ammonia solution of 1–1000 mM was added to a 100 mL plastic (polypropylene) beaker with a PTFE coated stir bar. The use of glassware was avoided as TPM reacts with the glass surface²¹⁰ and leaves visible patches that cannot be cleaned easily (see Fig. 7.3). The pH of the ammonia solution was measured using a HACH HQ40d pH meter with a calibrated IntelliCAL PHC101 standard gel filled pH electrode. pH measurements were not performed after the addition of TPM because we suspect TPM reacts with the glass surface of the pH probe. Throughout, the beaker was covered with Parafilm to prevent pH change due to ammonia evaporation. While the solution was stirred at 350 rpm (medium-sized vortex), an accurate volume of TPM monomer was injected with a plastic pipette. During the first 20 min of the reaction, the solution gradually becomes more turbid and the TPM droplets observed at the start of the reaction

disappear. At this point, the stirring speed was lowered and stirring continued at 200 rpm until a total stirring time of 2.5 h.

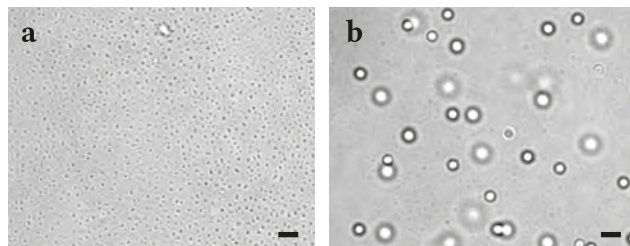


Figure 7.3. Bright field images of a glass cover slide containing the reaction mixture 10 min (a) and 45 min (b) after TPM injection. TPM reacts to glass cover slides, resulting in a visible speckle pattern. In (b), the TPM emulsion itself is also visible. Samples that were taken after 60 min of reaction did not develop this pattern.

Radical polymerization After the spontaneous emulsification of TPM, the emulsion droplets can be polymerized in a radical polymerization reaction. During this process, the methacrylate moieties of the TPM polymerize, yielding a rigid particle that can be stored at room temperature for years.

To polymerize a TPM emulsion, we transferred the emulsion to a capped vial and added 10 mg of the radical initiator AIBN per 15 mL of the emulsion. To initiate polymerization, the solution was heated to 80 °C for 2 h. To prevent sedimentation, the vial was tumbled by hand at 30 min intervals. In the case in which droplets sedimented too quickly, leading to coalescence and a polydisperse dispersion, polymerization in an oil bath under continuous tumbling was employed.

Alternatively, 0.5 mM potassium persulfate (KPS) can be used to initiate polymerization. Similar to AIBN, polymerization of the TPM droplets with KPS at 80 °C for 2 h yields spherical and solid colloids. Here we note that KPS can also yield dimpled spheres through shell buckling.²¹⁹ If heating the sample during polymerization is undesirable, then a photo-initiator (0.1 vol % 2-hydroxy-2-methylpropiophenone) can be employed. After illumination with ultraviolet light (a Rayonet photochemical reactor operating at 350 nm wavelength) for 1.5 h, rigid particles are obtained. See Figure 7.9 on page 116 for SEM pictures of colloidal particles prepared with these alternative initiators.

To corroborate the radical polymerization mechanism, we monitored the change in the FTIR spectrum in samples of emulsified TPM droplets and polymerized TPM spheres (see Fig. 7.11 on page 117). We found that the carbon-carbon double-bond vibration decreased by 63 % after polymerization. Therefore, we estimate the unreacted monomer fraction of methacrylate moieties at 37 %.

Fluorescent dyes To enable fluorescence microscopy of the TPM particles, several fluorophores are available for integration into the particles. All dyes were added after droplet formation. The dispersion was stirred for an additional 15 min to ensure a good distribution throughout the droplets. Then the emulsion was polymerized as described in the previous section.

Silane chemistry was used to covalently link the dyes to the organosilica network of TPM.^{220,221} For example, RITC (576 nm emission) and FITC (525 nm emission) can be covalently attached to the amino group in 3-(aminopropyl)triethoxysilane (APS), as follows: 10.2 mg RITC and 8.6 μL of APS were dissolved in 10 mL of DMSO and stirred overnight. Typically, 10 μL of this RITC-APS solution was added per 1 mL of TPM emulsion. The dye solution can be stored at room temperature under light exclusion for months without degradation.

FITC is linked to APS as follows: 3 mg FITC and 22.5 μL APS were dissolved in 250 μL ethanol and stirred overnight. Typically, 2.3 μL of this FITC-APS solution was added per 1 mL of TPM emulsion. For long-term storage, water must be excluded to prevent hydrolysis and self-condensation of the APS molecules.²²⁰

Because of the hydrophobic nature of TPM, it is possible to also include hydrophobic dyes: both BODIPY (508 nm emission, also available in other colours) and perylene (447 nm emission) were dissolved at 1 g L^{-1} in DMSO. Typically, 10 μL of one of these dye solutions is added per 1 mL of TPM emulsion in order to obtain fluorescent particles. These non-covalently incorporated dyes migrate from the particles when they are transferred to a hydrophobic solvent.

Imaging methods TPM emulsions were imaged using a Nikon Eclipse Ti microscope with a 100 \times oil-immersion objective (NA=1.4). Dried samples of polymerized particles were sputter coated with Pt/Pd and imaged using a FEI nanoSEM 200 scanning electron microscope (SEM) using an acceleration voltage of 15 kV. The particles obtained through the seeded growth process were imaged on a Zeiss Merlin field emission SEM using an acceleration voltage of 1 kV. The SEM images were analysed using ImageJ software and a Python algorithm²²² to determine the particle size distribution.

7.3 Results and Discussion

7.3.1 Physical properties

This section summarizes some physical properties of TPM. The density and refractive index measurements were performed by our collaborators at *New York University*, and the dielectric measurements by Dr. Rob Kortschot at *Utrecht University*.

The supplier-reported density of TPM monomer is 1.045 g cm^{-3} . We measured the density of TPM in dispersion with an Anton-Paar DMA 4500M density meter. From the total dispersion density at four different particle mass fractions, the density of self-emulsified TPM was determined to be $1.235 \pm 0.010 \text{ g cm}^{-3}$. After polymerization, the density increased by approximately 7% to $1.314 \pm 0.004 \text{ g cm}^{-3}$. Polymerized particles that were calcined for 2 h at $700 \text{ }^\circ\text{C}$ further increased in density to $2.094 \pm 0.016 \text{ g cm}^{-3}$. All density measurements were performed at $20.0 \text{ }^\circ\text{C}$.

The refractive index of polymerized TPM particles was measured by a refractive index matching process. TPM particles were dispersed in a mixture of pyridine ($n_D = 1.509$) and 2-ethylhexyl 4-methoxycinnamate ($n_D = 1.545$) and the scattering intensity of the dispersion was measured at angles 60° , 120° , and 150° with a static light scattering instrument (Scitech Instruments ST-100). The refractive index of TPM particles was estimated to be between 1.512 and 1.513, assuming that the fluids are non-solvents for the particles. Refractive index measurements were performed with a standard Abbe refractometer (Edmund Optics) at room temperature ($22.5 \text{ }^\circ\text{C}$).

The dielectric constant of liquid TPM was measured using a calibrated parallel plate capacitor and an HP4192A impedance analyzer (Hewlett-Packard) in the frequency range of 10–100 kHz. The dielectric constant of liquid TPM was found to be 6.58 ± 0.04 at $22.3 \text{ }^\circ\text{C}$.

The zeta potential of the polymerized TPM particles was measured using a Zetasizer Nano ZS (Malvern Instruments) on dilute aqueous samples (pH 5.6) at $25.0 \text{ }^\circ\text{C}$. We determined that the TPM particles were negatively charged for all synthesis parameters, with a zeta potential of $-36 \pm 3 \text{ mV}$.

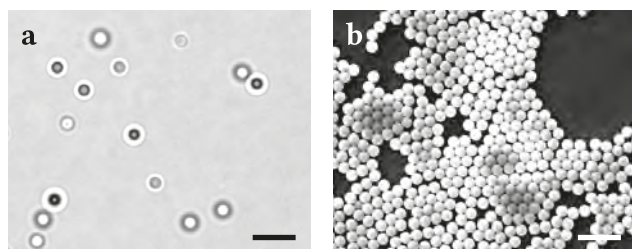


Figure 7.4. Microscopy images of TPM droplets. (a) Optical microscopy image of unpolymerized TPM droplets. (b) SEM micrograph of the same dispersion after polymerization. The scalebars denote $5 \mu\text{m}$.

7.3.2 Emulsification

In order to gain insight into the spontaneous emulsification of TPM in water, we studied the evolution of the droplet size during synthesis. At given intervals following the TPM monomer injection, we sampled 100 μL of the reacting dispersion and imaged a 10 μL aliquot with light microscopy. In order to freeze the emulsification process so that the size distribution could be determined accurately, we polymerized each sample directly as follows: 1 min before sampling, a vial with 1 mg of AIBN and 1 mL of water at 80 $^{\circ}\text{C}$ was prepared. Then, a 90 μL aliquot of the sample was added to the vial and polymerized for at least 2 h in an 80 $^{\circ}\text{C}$ oven.

With SEM, we observed that the particles remained spherical during polymerization (see Figure 7.4). Next to these TPM spheres, sub-200 nm objects were visible that decreased in number throughout the process. As we did not detect these before polymerization, we concluded that they are an artefact of the employed SEM sample preparation. Possibly, the incompletely reacted TPM species polymerize from solution. As these objects tended to precipitate on the growing droplets, the smoothness of the particles could be confirmed only at the end of the process. For the size measurements, we therefore washed the polymerized samples two times with water. Note that we measure the diameter of the polymerized TPM particles: as the density of polymerized TPM is 7 % higher with respect to the emulsion droplets, we expect the particles to be smaller accordingly.

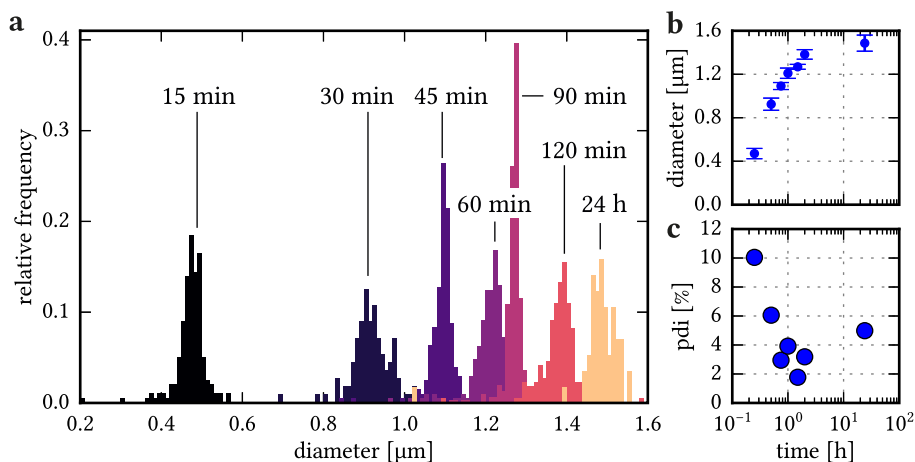


Figure 7.5. Temporal evolution of the size distribution of polymerized TPM droplets in a typical synthesis. The corresponding SEM images are shown in Fig. 7.12 and bright field microscopy videos are available online. (a) Size distributions at different time points in the synthesis. (b) The distributions show a strongly decreasing growth speed. (c) The polydispersity index (PDI) decreases initially and then slowly increases.



The temporal evolution of the size distribution during a synthesis in ammonia solution at initial pH 10.4 and TPM volume fraction $\phi = 0.005$ is shown in Figure 7.5. Corresponding SEM images can be found in Figure 7.12 on page 118. We define $t = 0$ at the time of TPM monomer injection. At $t = 10$ min, ca. 200 nm TPM droplets were observed by light microscopy. At $t = 15$ min, spherical particles with a unimodal diameter distribution of $0.47 \pm 0.05 \mu\text{m}$ were identified using SEM. After this initially fast nucleation step, droplets grow with a decreasing growth rate (see Figure 7.5b). As can be seen in Figure 7.5c, the polydispersity index decreases before plateauing to 2-4% at $t = 90$ min. After that period, the size distribution broadens slightly until the droplets reach a stable size of $1.49 \pm 0.07 \mu\text{m}$.

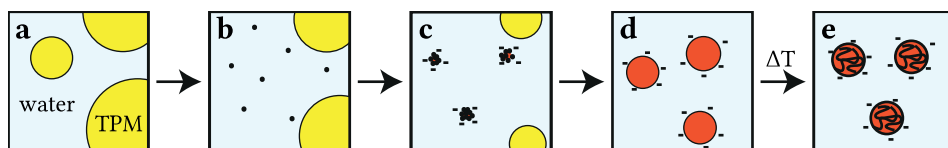


Figure 7.6. Schematic representation of the spontaneous emulsification and subsequent polymerization of TPM. (a) The process starts with TPM monomer injection with a two-phase system consisting of liquid TPM monomer (yellow) and water. (b) Hydrolysis and self-condensation of TPM result in oligomers of several monomer units (black dots). (c) Oligomers nucleate emulsion droplets (red) that are eventually stabilized by charge. The dispersion becomes turbid. (d) The droplets grow by acquiring more TPM-species. In this stage, additional TPM monomer or dye solutions can be added that also transfer to the emulsion droplets. (e) In a second synthesis step, the methacrylate moiety of the TPM is polymerized by adding a radical initiator at elevated temperature.

On the basis of these observations, we propose the following mechanism for the spontaneous emulsification of TPM droplets (see Figure 7.6). Although our mechanism does not capture the details of the nucleation process, it provides a qualitative description of the particle synthesis. Directly after monomer injection, TPM starts to hydrolyse and self-condensate (see Fig. 7.2 on page 104) into oligomers of several monomer units due to a well-established cascade of base-catalysed reactions.^{209,211,212} The gradual shrinkage of bulk monomer droplets has also been observed directly in the preparation of magnetite-covered TPM droplets.²⁰⁷ Because the oligomers become increasingly less soluble in water, they may self-nucleate or aggregatively nucleate (or both) to form the initial emulsion droplets. The accumulation of surface charge on the droplets due to silanol deprotonation prevents or limits the agglomeration of the small particles from forming larger ones.^{205,215,216} The influence of deprotonation will be further investigated in the next section by varying the pH.

At this point, the number of droplets does not appear to change appreciably: we hypothesize that any insoluble oligomeric species with insufficient charge is taken up by the droplets. The dispersion gradually becomes turbid, and we observed the formation of an emulsion with an average droplet diameter of approximately $0.5 \mu\text{m}$. Particles

grow with decreasing growth rate by taking up TPM species in hydrolysed, condensed and/or coagulated form. The macroscopic monomer reservoirs are ultimately consumed during the growth of the droplets. Droplet growth is faster for smaller particles so that the size distribution of emulsion droplets will narrow with time. At a later stage the polydispersity increases slightly, possibly due to Ostwald ripening.

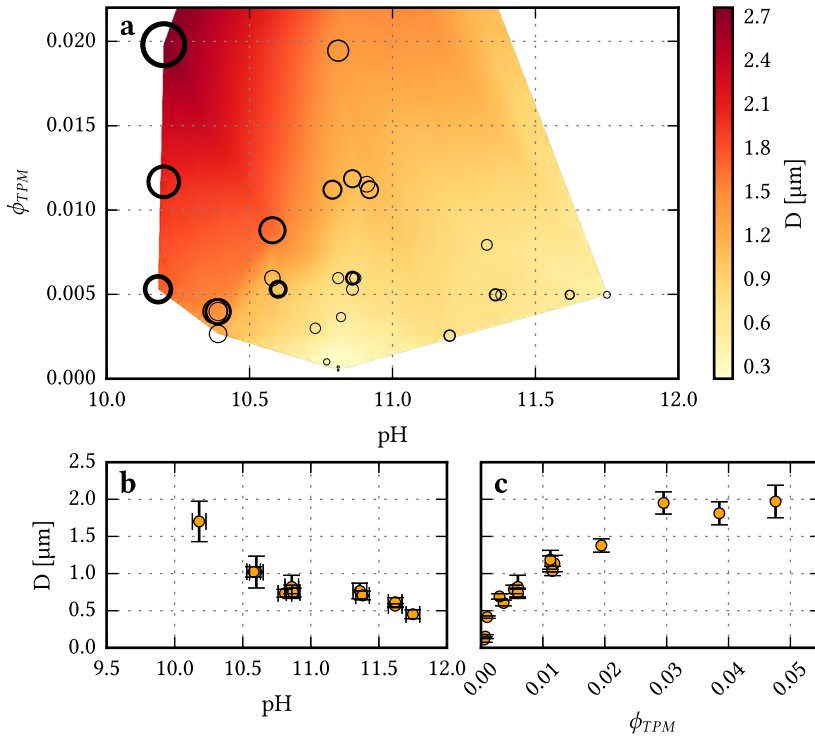


Figure 7.7. Plots of the influence of pH and TPM volume fraction on the diameter of TPM particles. (a) The diameter and line thickness of the plotted circles represent the diameter and polydispersity of the polymerized particles, respectively. The colours are linear interpolations between the measured points. (b) Particle diameter D as function of pH at a fixed TPM monomer fraction of 0.005 to 0.006. The particle size decreases as the pH increases. (c) Particle diameter as function of TPM monomer fraction ϕ at a fixed initial pH of 10.80 ± 0.05 . The particle size increases as the TPM monomer fraction increases.

7.3.3 Change of pH and monomer fraction

The synthesis of TPM particles, as described in the preceding section, has only a few parameters, of which the most important ones are the pH and TPM monomer fraction. We demonstrate their effect on the resulting particle size and polydispersity by a systematic variation and polymerization after 2.5 h of emulsification. See Figure 7.7. Monodisperse emulsions formed only when the pH exceeded 9.7; below that value, highly polydisperse emulsions with sizes ranging from 2–20 μm after 24 h of stirring were observed (see Fig. 7.10 on page 116). Apparently, the hydrolysis and self-condensation reactions proceed too slowly below pH 9.7. Also, colloidal stability is compromised under this condition due to insufficient deprotonation of the TPM species. Above pH 12, we observed the formation of emulsions with a large spread of diameters ranging from 0.2 to 0.5 μm , which limits the synthesis conditions at the other end of the pH range.

For reaction conditions with initial pH values between 10.2 and 11.8, we found that the particle diameter decreased monotonically for increasing pH (see Figure 7.7b). The observed trend is supported by our proposed particle formation mechanism: at higher pH, TPM oligomerization occurs more rapidly.^{211,212,217} Silanol deprotonation is enhanced under these conditions as well,²¹⁶ resulting in a larger number of primary droplets. Therefore, if the TPM volume fraction is kept constant, then smaller particles are produced as we observed. A shorter nucleation period is further supported by the observed narrowing of the size distribution with increasing pH.

Similarly to previous experiments on magnetite-covered TPM emulsions,²⁰⁷ we found that the particle diameter increased with increasing monomer volume fraction. For a fixed pH of 10.8 (see Figure 7.7c) the diameter of the emulsion droplets could be continuously tuned from 0.1 to 2.0 μm by simply adjusting the TPM volume fraction from 0.05 to 5 vol %. Below a volume fraction of 0.1 vol %, the relative polydispersity increased to 20 %. This effectively sets a lower limit of the TPM monomer fraction at 0.1 vol %, which corresponds to a droplet diameter of 0.4 μm . Above a monomer volume fraction of 3 vol %, the droplets did not grow significantly, while the droplet polydispersity increased. Therefore, we conclude that at pH 10.8 the practical range for the TPM volume fraction is 0.1 to 3 vol %.

7.3.4 TPM monomer storage

To investigate the importance of the TPM monomer storage conditions, we also performed the synthesis using a TPM stock that was exposed periodically to air during a period of roughly six months. It is known²¹¹ that TPM slowly forms oligomers when contacted with small amounts of moisture such as is present in the air. Using the air-exposed TPM, we synthesized particles and measured their average size as a function of monomer volume fraction and pH, see Fig. 7.13 on page 119. We found the particle size to depend non-linearly on the pH. Above pH 9.7 a stable emulsion was formed, comparable to the synthesis with fresh TPM. Similarly, from pH 9.7 to 10.7, the particle size decreases monotonically. However, from pH 10.7 to 12, the particle size was found

to increase again to a diameter of $1.47 \pm 0.14 \mu\text{m}$ (pH 12.0, $\phi = 0.005$), which contrasts sharply with the monotonous decrease to $0.45 \pm 0.06 \mu\text{m}$ (pH 11.8, $\phi = 0.005$) observed for fresh TPM. The particle size polydispersity did not increase significantly due to the uncontrolled moisture exposure. These results indicate that the initial droplet formation, but not the droplet growth, is affected by the ageing of TPM. Therefore, to ensure batch to batch reproducibility, we recommend handling the TPM monomer as a moisture-sensitive compound, taking care to exclude or minimize exposure to air, for example by storing under a nitrogen atmosphere.

7.3.5 Influence of base species

To evaluate other base catalysts, we performed the particle synthesis using three different basic compounds: ammonia, sodium hydroxide (NaOH) and tetramethylammonium hydroxide (TMAH). If the emulsification process were dependent on the base-catalysed processes alone, then the type of base used to adjust the pH should not be important.^{211,216} Indeed, we observed that for all three bases a monodisperse emulsion was formed under appropriate conditions, confirming that pH is the control parameter for stable emulsion formation.

The results for the particle size as a function of pH and TPM volume fraction are presented in Figure 7.14 (TMAH) and Figure 7.15 (NaOH) on page 120. For fixed monomer volume fraction ($\phi = 0.005$), the resulting particles were $0.61 \pm 0.06 \mu\text{m}$ when using ammonia at pH 11.6, $0.72 \pm 0.03 \mu\text{m}$ when using TMAH at pH 11.7, and $0.78 \pm 0.08 \mu\text{m}$ when using NaOH at pH 11.8. Because of the differences in base dissociation constants, the respective concentrations of these solutions were 0.9 M ammonia ($\text{p}K_{\text{b}} = 4.75$), 0.4 M TMAH ($\text{p}K_{\text{b}} = 4.2$), and 6.3 mM NaOH ($\text{p}K_{\text{b}} = 0.20$). Although there is a large difference in base concentration, the resulting particle sizes are very similar. This observation supports our claim that the synthesis process and resulting particle size depend mainly on pH and less on the type of base employed.

The fact that TMAH can be used to form monodisperse emulsions of TPM in water also sheds new light on previous experiments performed with TPM droplets that were stabilized by various inorganic colloids in the presence of TMAH.^{206–208,214,218,223} It was proposed that the formed TPM emulsions were stabilized by inorganic colloids at the interface, deprotonated TPM molecules, and TMAH that functions as a peptizing agent. Our study shows that the TMAH-induced deprotonation of TPM might be more important than the stabilization by TMAH itself. This suggests that TPM droplet formation is governed primarily by the volume fraction of TPM monomer and the pH of the solution.

7.3.6 Seeded growth

TPM droplets can be grown to larger sizes through a seeded growth process. This work was performed by Rohit Bhan, Dr. Andrew Hollingsworth, and Dr. Stefano Sacanna (*New York University*). After the initial emulsification of the droplets, additional TPM monomer is added to the stirred system to increase the diameter of the particles. A period

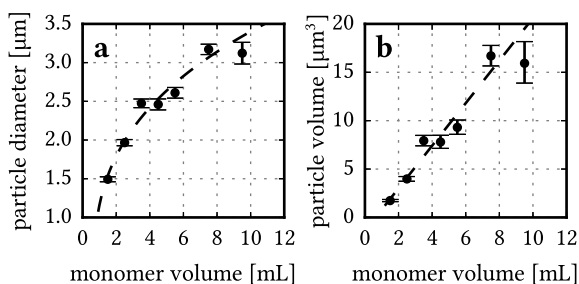


Figure 7.8. Dependence of TPM particle size on added monomer in a seeded growth process. (a) Particle diameter as a function of total added monomer volume. (b) Particle volume as function of total added monomer volume. The dashed line in (b) is obtained with linear regression. The same line is also displayed in (a). Corresponding SEM images can be found in Figure 7.16 on page 121.

of 1 h is necessary for complete hydrolysis and condensation of the first addition of oil-monomer, resulting in visibly larger emulsions. This process can be repeated multiple times, allowing growth to a desired particle size.

In a typical procedure, we add 500 μL TPM monomer ($\geq 98\%$) to 100 mL of ammonia solution at pH 11 (1 mL of 2.8% ammonia and of 99 mL water in a stirred and covered glass beaker). Every hour, we added an additional 1 mL of TPM monomer to the emulsion. When using this technique to grow large droplets (above 2.5 μm), both the ratio of water-to-oil and interparticle spacing decrease. At low water-to-oil ratios, a phase separation can occur, driving emulsion droplets back into the oil phase. This situation can be avoided easily by increasing the volume of the solution. Adding 100 mL of ammonia solution every fifth addition of monomer sustained particle growth. Larger particles can be grown in fewer intervals by increasing the amount of monomer added. We recommend adding no more than four times the original amount of monomer (2 mL in our procedure). The addition of too much monomer can cause a phase separation between water and TPM monomer and thus a loss of particles.

This process results in very low particle polydispersity, as can be seen from the crystal lattice formation in the SEM images (see Figure 7.16 on page 121). The resulting particle diameters are shown in Figure 7.8. Clearly, the particle volume increases linearly with the added monomer volume, indicating a pure growth process. This behaviour is unlike the behaviour for the initial emulsification step. The absence of secondary nucleation further corroborates the conclusion that the added TPM is distributed evenly over the TPM droplets.

7.4 Conclusion

We have systematically studied a straightforward particle synthesis to prepare monodisperse colloids based on the spontaneous emulsification of a polymerizable trialkoxysilane. Also, we characterized the density, refractive index, dielectric constant, and zeta potential of the particles as well as several ways to include dyes for use in fluorescence microscopy. We found that the TPM particle size can be controlled via the pH and the volume fraction of added monomer to produce particles of 0.4–2.8 μm in diameter. The particle size was observed to increase with increasing monomer volume fraction while the particle size decreased with increasing pH. Furthermore, we showed that these trends hold regardless of which base is used as a catalyst.

We proposed a mechanism for the spontaneous emulsification of TPM droplets. First, the hydrolysis and self-condensation of TPM produce oligomers that subsequently nucleate ca. 200 nm primary droplets. Deprotonation of the TPM species provides charge to these droplets. When the droplet charge is sufficiently large to ensure colloidal stability, the process enters a growth step in which the particle size increases without secondary nucleation. The relative polydispersity decreases in this growth step, although at longer times the particle size distribution broadened slightly.

For increasing synthesis pH, we obtain smaller droplets. As a higher pH induces more charges in the droplet surface, deprotonation suppresses TPM oligomer coagulation at an earlier stage by means of electrostatic repulsion between droplets, so that a (colloidally) stable emulsion with more droplets is obtained. Because the available TPM monomer is distributed over the droplets, a smaller size is obtained. After the initial emulsification step, particles can be grown to sizes of up to 4 μm by repeated addition of monomeric TPM. In this way, particles with a narrow size distribution can be obtained over a large size range from 0.4–4 μm .

TPM particles have already been proven to be a versatile template for the bulk synthesis of more complex particles.^{47,50,200,204} The organosilica nature of the TPM particles provides handles for many chemical functionalizations, and the fact that the size of the particles can be tuned by changing easily accessible parameters such as the pH or the amount of added monomer provides flexibility. In this method, no extensive chemical equipment is required: if for instance a dilute sodium hydroxide stock is used, then the synthesis can be performed as a tabletop experiment. The simplicity of this colloidal synthesis makes it easily accessible to a wide range of applications.

7.5 Supporting Figures

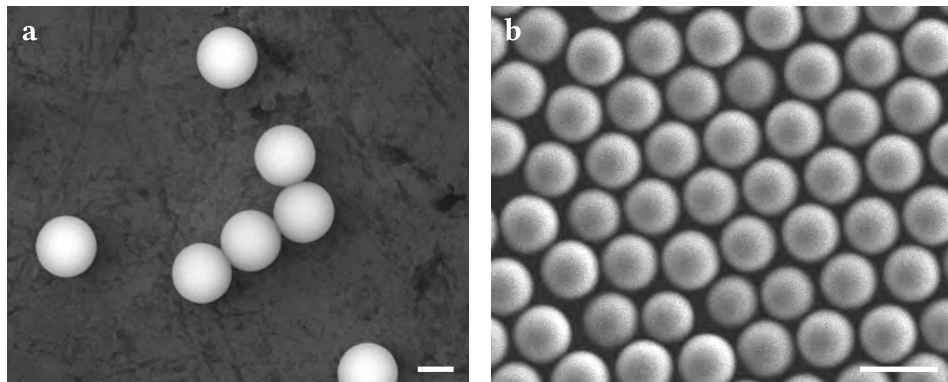


Figure 7.9. SEM pictures of TPM particles with two alternative radical initiators. Different batches of emulsion droplets were polymerized (a) thermally with potassium persulfate (KPS) or (b) photochemically with 2-hydroxy-2-methylpropiophenone. The scalebars denote 1 μm .

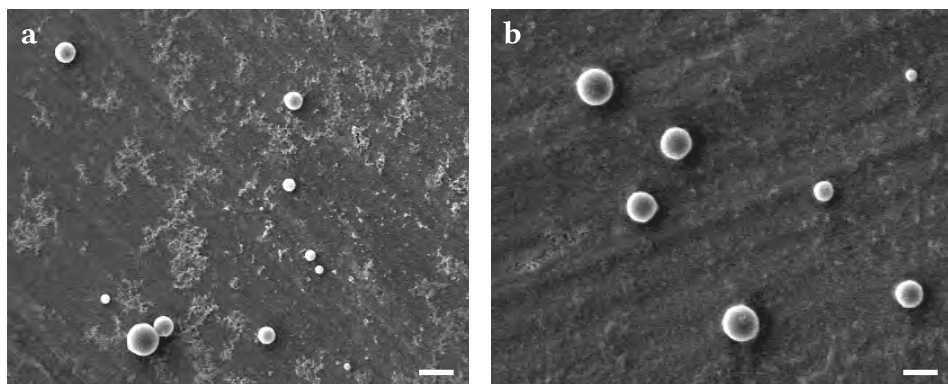


Figure 7.10. SEM micrographs showing TPM droplets that were stirred for 24 h at (a) pH 8.7 and (b) pH 9.4. Both samples contain highly polydisperse TPM droplets with diameters ranging from 2–20 μm . The scalebars denote 5 μm .

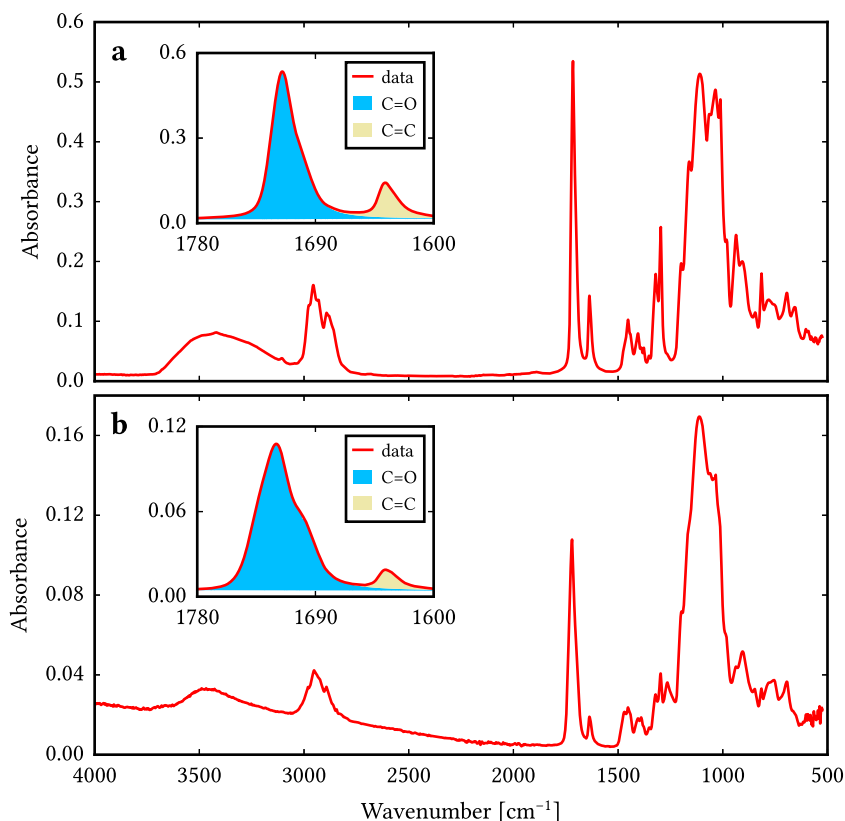


Figure 7.11. Infrared spectra of (a) unpolymerized TPM droplets and (b) polymerized TPM particles. The emulsification was performed in 12.4 mM ammonia (pH 10.7) at a TPM monomer volume fraction $\phi = 0.005$. After emulsification, an aliquot the droplets was first washed with water to remove the excess of ammonia. Then the droplets were coalesced by centrifugation at 3500 rcf and the spectrum (top) was recorded. Another aliquot of the emulsion droplets was polymerized with 0.67 g L⁻¹ AIBN at 80 °C for 2 h. The polymerized particles were washed two times with water, dried overnight at 90 °C and then the FTIR spectrum was recorded. To estimate the degree of polymerization, we compared the area under the peaks at 1636 cm⁻¹ and 1720 cm⁻¹, which respectively are the C=C and C=O stretch vibrations. As shown in the inset graphs, we numerically integrated the baseline-corrected absorbance, separating the two peaks by a local fit of two Lorentzians. As the C=O bonds are unaffected during polymerization, we may use the ratio between these areas to compute the decrease in the number of C=C bonds. We found that this area ratio (C=C:C=O) decreased from 0.195 to 0.072, corresponding to a polymerization degree of 63%. This corroborates that the TPM droplets have polymerized through a radical polymerization in the second step. These data were acquired by Zhe Gong and Dr. Stefano Sacanna at *New York University*.

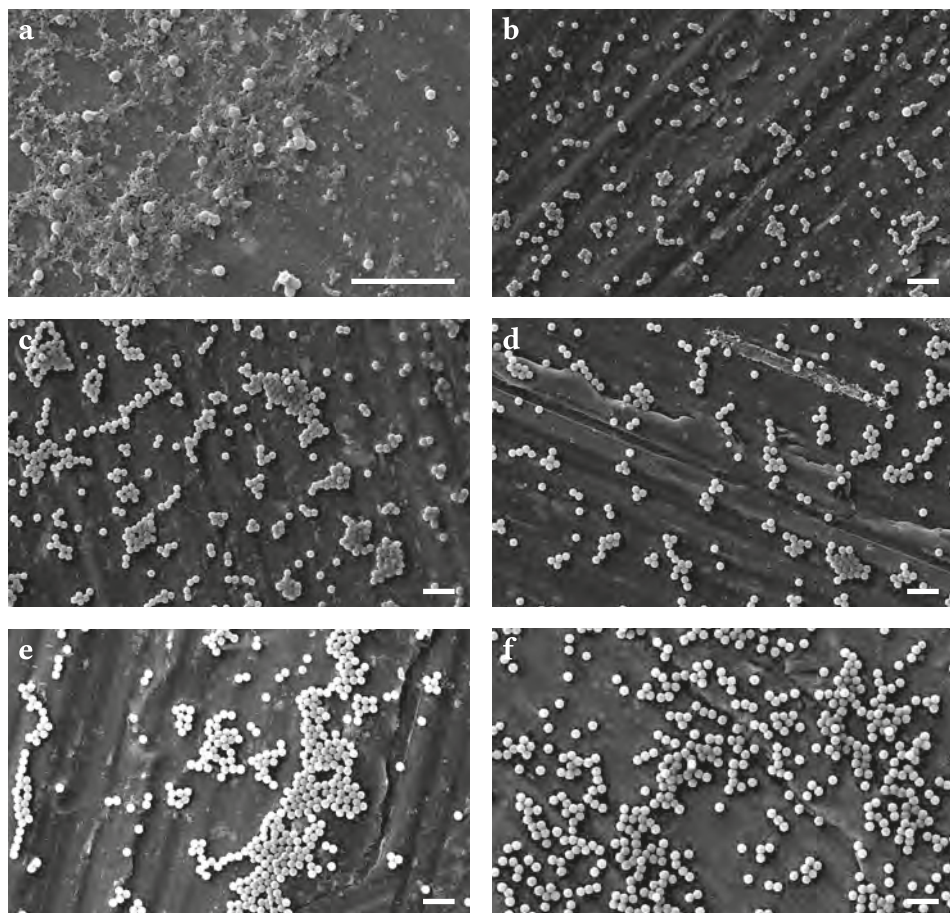


Figure 7.12. Representative SEM micrographs showing the time evolution of polymerized TPM droplets in a single synthesis. The shown pictures were obtained from the polymerized samples that were taken at 15 min (a), 30 min (b), 45 min (c), 60 min (d), 90 min (e), and 120 min (f) after TPM monomer injection. There are sub-200 nm objects visible that decrease in number throughout the process. We also observed these objects by light microscopy in the polymerized samples, but not in the unpolymerized samples. Therefore we concluded that they are an artefact of the employed sample preparation. Note that the samples were washed for measuring the particle diameters; these images are not shown. Scalebars denote 5 μm .

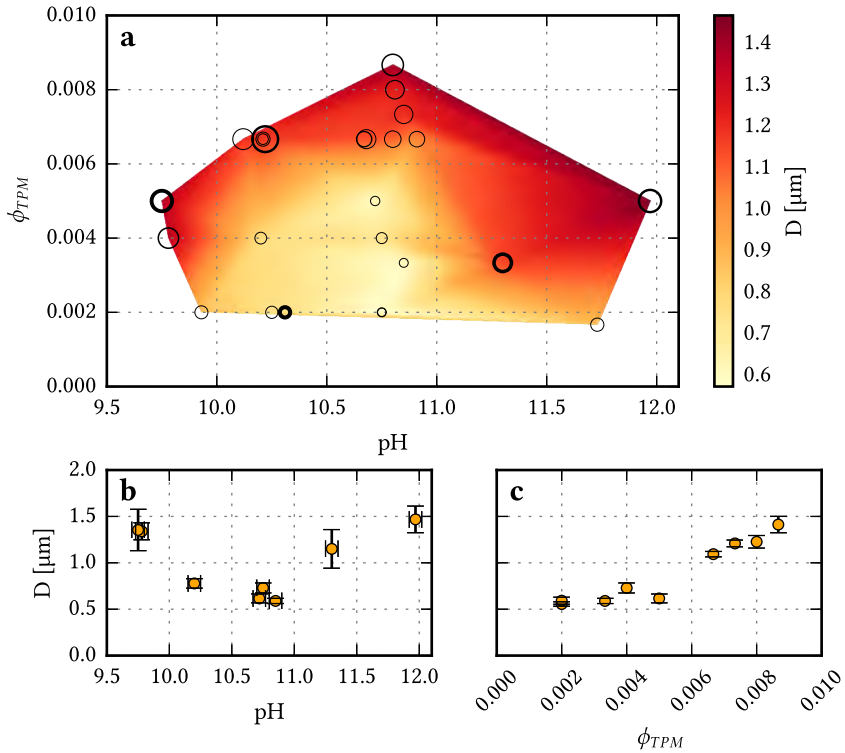


Figure 7.13. Plots of the influence of pH and TPM volume fraction on the particle diameter, in the case TPM is used that was subject to ambient conditions for approximately 6 months. Ammonia was used to adjust the pH. (a) The diameter and line thickness of the plotted circles represent the diameter and polydispersity of the polymerized particles, respectively. The colours are linear interpolations between the measured points. (b) Particle diameter D as function of pH at a fixed TPM monomer fraction of 0.003 to 0.005. The particle size decreases as the pH increases and at high pH increases again. The minimum particle size occurs at pH 10.75. The size polydispersity has a minimum between pH 10 and 11. (c) Particle diameter as function of TPM monomer fraction ϕ at a fixed pH of 10.7 to 10.9. The particle diameter increases with increasing monomer volume fraction.

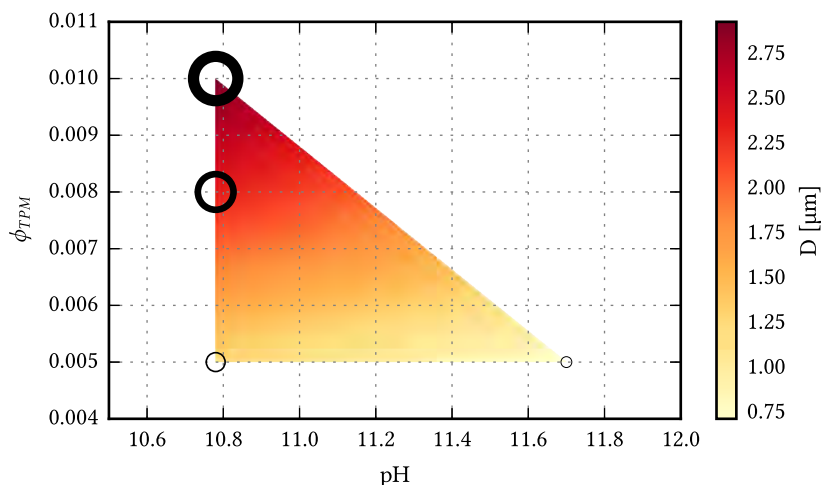


Figure 7.14. Plots of the influence of pH and TPM volume fraction on the particle diameter, using tetramethyl ammonium hydroxide (TMAH) to adjust the pH. The diameter and line thickness of the plotted circles represent the diameter and polydispersity of the polymerized particles, respectively. The particle diameter increases with increasing monomer volume fractions and decreases as the pH increases.

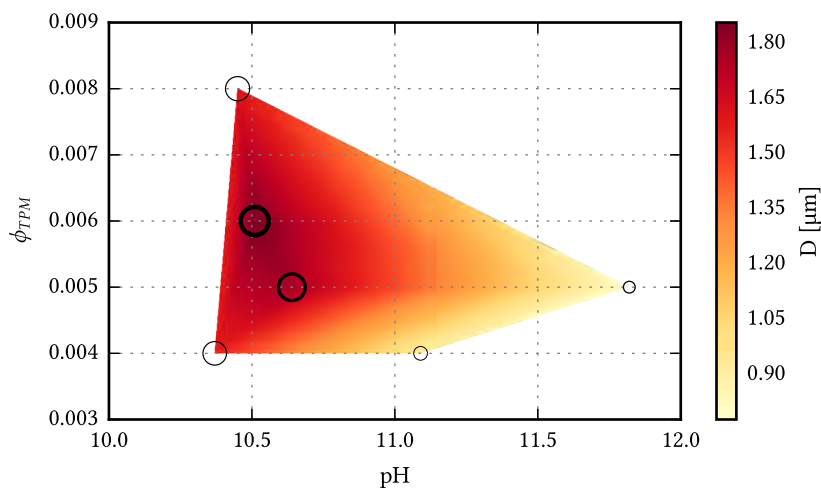


Figure 7.15. Plots of the influence of pH and TPM volume fraction on the particle diameter, using sodium hydroxide (NaOH) to adjust the pH. The diameter and line thickness of the plotted circles represent the diameter and polydispersity of the polymerized particles, respectively. The particle diameter increases with increasing monomer volume fractions, but less than when TMAH or ammonia are used as base catalyst. The particle size decreases as the pH increases.

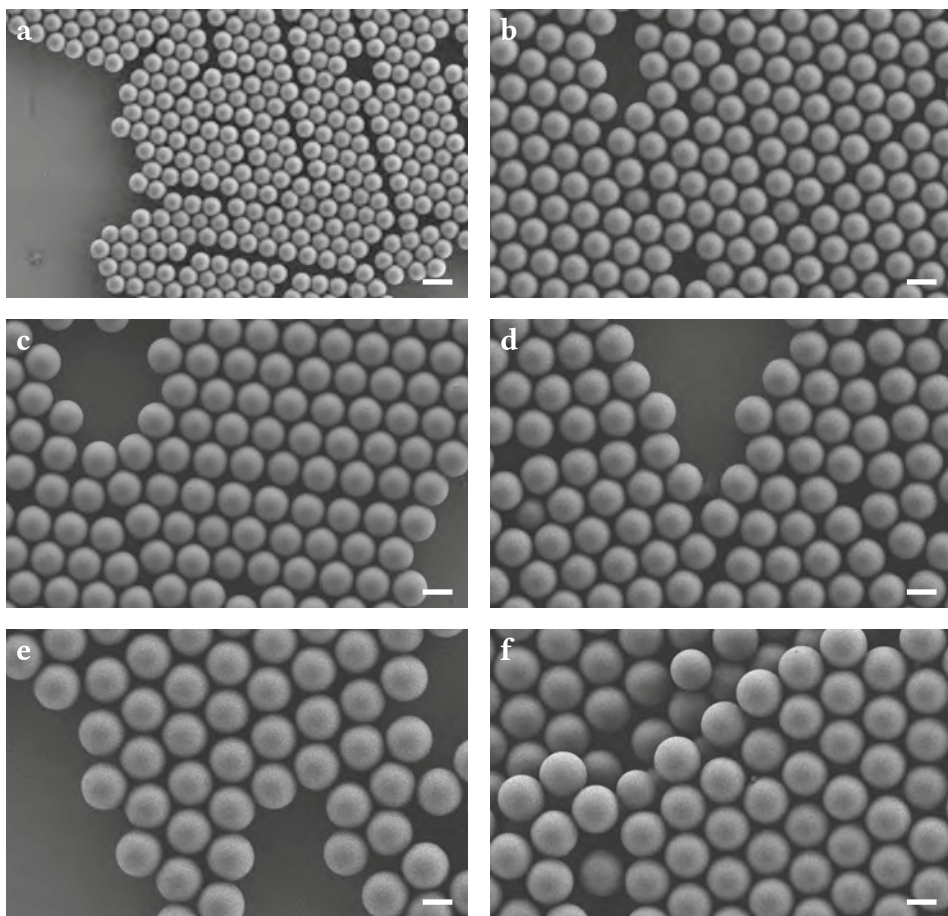


Figure 7.16. SEM micrographs of TPM particles obtained through a single seeded growth process. After nucleation with 500 μL TPM monomer in 100 mL diluted ammonia, samples were made after (a) a single addition of 1 mL monomer, (b) a second addition of 1 mL monomer, (c) a third addition of 1 mL monomer. Then a fourth addition of 1 mL monomer was done, the reaction volume was doubled by adding 100 mL diluted ammonia, and (d) the fifth addition of 1 mL monomer, (e) the sixth addition of 2 mL monomer and (f) the seventh addition of 2 mL monomer were done. Scalebars denote 2 μm .

LIPID MONOLAYERS SUPPORTED BY TPM MICROEMULSIONS

This chapter is based on H. C. Frijters, ‘Directed self-assembly of tetrahedral particles’, Bachelor thesis (2015); R. W. Verweij, ‘Using polymerizable microemulsions for reconfigurable colloidal clusters’, Master thesis (2016); and G. L. van de Stolpe, ‘The mobility of micron-sized TPM clusters’, Bachelor thesis (2017).

Abstract

Supported lipid membranes are important for studying fundamental lipid membrane processes as well as for biotechnological applications. Here, we investigate microemulsions from TPM (3-(trimethoxysilyl)propyl methacrylate) as a platform for lipid monolayers. TPM droplets can be produced with a narrow size distribution, thus providing model lipid membranes with controlled size and curvature. With fluorescence recovery after photobleaching (FRAP), we observed that droplet-attached lipids, NeutrAvidin proteins, and DNA oligonucleotides all show lateral mobility. A potential application of these droplets with surface-mobile lipids is the self-assembly of colloidal clusters of defined shape. We assembled micron-sized particles on TPM-droplets by either the specific avidin-biotin interaction or by double-stranded short DNA strands, and we conclude that although single linker molecules are mobile, particles that are attached to them are not. We speculate that this is caused by the heterogeneous nature of emulsified TPM, forming an entangled network that limits the collective motion of linkers, but allows mobility of individual TPM-attached molecules.

8.1 Introduction

Interfacial mobility is a distinct property of lipid membranes that is crucial for biological processes in every organism.¹¹ This property is often isolated in the form of supported lipid monolayers or bilayers, thereby enabling controlled study of processes that involve lipid membranes or membrane proteins.^{39,224–226} For example, a recent study has shown that the mobility of antibodies on lipid-coated droplets results in an up to ten times faster uptake by macrophages compared to particles with immobilized antibodies.²²⁷ Next to this, micrometer-sized self-assembly has been inspired by the inherent mobility of lipid monolayers: lipid-coated emulsion droplets have lead to for instance force measurements on cell-cell adhesion,²²⁸ and lipid-coated silica particles to flexible colloidal joints.⁴⁴

We here focus on so-called droplet interface monolayers, which are oil droplets with lipids on their surface.²²⁹ Control over the size of the droplets is important for the involved applications and therefore we here investigate membranes that are supported on 3-(trimethoxysilyl)propyl methacrylate (TPM), which is a polymerizable oil that spontaneously forms emulsions of accurate sizes in between 0.45–4 μm (see Chapter 7). First, we will investigate the mobility of TPM-attached lipids, proteins, and DNA oligonucleotides, which is a key property for both biological studies and self-assembly applications. The resulting lipid-coated droplets mimic biological lipid membranes with controlled size and curvature. Then, we will investigate the use of these TPM-droplet supported lipid monolayers for the bulk production of colloidal clusters.

Clusters of micron-sized spheres are important building blocks in the area of micron-sized self-assembly.^{40,230} In order to access their self-assembled structures, multiple methods to prepare colloidal clusters have been developed in the past.^{41,43,71} One approach to prepare colloidal clusters is through the assembly of colloidal particles around a central particle. For small cluster sizes, the cluster size and shape is then determined uniquely by the ratio of the particle diameters.²³¹ Assembly of these optimally packed clusters, however, requires the particles to be able to rearrange over the surface of the central particle.²³² Because the liquid nature of TPM droplets presumably allows for this rearrangement, and the droplet size can be accurately controlled (see Chapter 7), lipid-coated TPM droplets are promising candidates for this application. Therefore, we here investigate the mobility of colloidal particles linked to the surface of TPM droplets via lipid molecules.

8.2 Methods

Materials 3-(Trimethoxysilyl)propyl methacrylate (TPM, 98%), ammonium hydroxide (28%), azobisisobutyronitrile (AIBN, $\geq 98\%$), ethanol (99.8%), and sodium phosphate dibasic were purchased from Sigma-Aldrich; Sodium chloride (NaCl) and sodium

azide (NaN_3 , 99%) from Acros Organics; DNA oligonucleotides from Integrated DNA Technologies; NeutrAvidin and NeutrAvidin–Oregon 488 from Thermo Scientific; $\Delta 9$ -cis 1,2-dioleoyl-*sn*-glycero-3-phosphocholine (DOPC), 1,2-dioleoyl-*sn*-glycero-3-phosphoethanolamine-N-[methoxy(polyethylene glycol)-3000] (DOPE-PEG3000), DOPE-PEG2000, DOPE-PEG5000, 1,2-distearyl-*sn*-glycero-3-phosphoethanolamineN[biotinyl-(polyethylene glycol)-2000] (DSPE-PEG-btn), and 1,2-dioleoyl-*sn*-glycero-3-phosphoethanolamine-N-(7-nitro-2-1,3-benzoxadiazol-4-yl) (DOPE-NBD) from Avanti Polar Lipids. All chemicals were used as received. All solutions were prepared from deionized water with 18.2 M Ω cm resistivity, using a Millipore Filtration System (Milli-Q Gradient A10). Phosphate buffered saline (PBS) solution consisted of 25 mM sodium phosphate, 100 mM sodium chloride, and 3 mM sodium azide, in water with the pH brought to 7.5.

DNA oligonucleotides The following DNA oligonucleotides were used:

- Biotin-TEG-3'-TTT TAG CGA TGG GAA GCG TGT CAG TTA GAT CTC TCG GGA CGG AAT GC-5' (btn-B)
- Cy3-5'-TTT ATC GCT ACC CTT CGC ACA GTC AAT CTA GAG AGC CCT GCC TTA CGA CCT ACT TCT AC-3' (Cy3-B'-S)
- 6FAM-5'-TTT ATC GCT ACC CTT CGC ACA GTC AAT CTA GAG AGC CCT GCC TTA CGA GTA GAA GTA GG-3' (6FAM-B'-S')

Here, A stands for Adenine, C for Cytosine, G for Guanine, T for Thymine, B for base strand, S for sticky end (corresponding bases are printed in italics), TEG for tetraethyleneglycol, Cy3 for a cyanine dye (exc. 550 nm em. 570 nm) and 6FAM for 6-carboxyfluorescein (exc. 495 nm em. 517 nm). These DNA strands were hybridized into double-stranded (ds) DNA, by heating 0.4 nmol Cy3-B'-S/6FAM-B'-S' and 0.8 nmol btn-B to 90 °C in 200 μL PBS. This solution was cooled down to room temperature over the course of 2 h after which the resulting hybridized DNA was stored at 4 °C. In the remainder of this chapter, we use dsDNA-Cy3 as a shorthand for the combination of btn-B and Cy3-B'-S, and dsDNA-6FAM for the combination of btn-B and 6FAM-B'-S'.

TPM emulsification TPM oil was emulsified following the protocol in Chapter 7. In short, 250 μL of 2.8 vol % ammonia was added to 15 mL water in a plastic (PP) beaker covered with Parafilm. The pH was confirmed to be in the range 10.4–10.6 with a Hach H270G ISFET pH probe. While magnetically stirring at 350 rpm, 75–100 μL TPM was injected. After 15 min, the stirring speed was reduced to 200 rpm, and after 2.5 h, the stirring was stopped and the resulting emulsion was stored in a glass vial. For each reaction batch, the dry weight and droplet radius were determined. Using the density of TPM emulsion droplets ($1.235 \pm 0.010 \text{ g cm}^{-3}$, see Chapter 7), the total TPM/water interfacial area could be computed per volume, which we did for every TPM emulsion. This was then used to compute the 'maximum surface coverage' (MSC), which we here define as the the number of added molecules per TPM/water surface area.

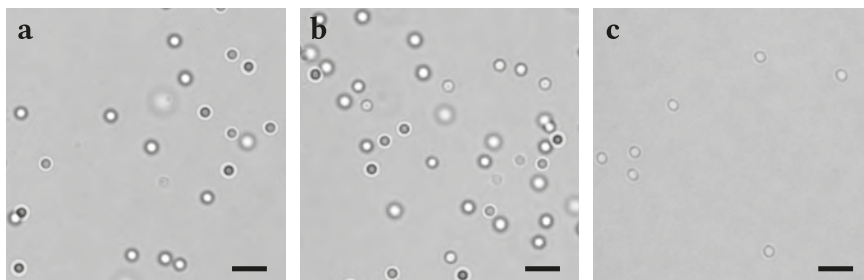


Figure 8.1. Light microscopy images of the same TPM droplets in (a) water, (b) 10 vol % ethanol, and (c) 0.2 vol % isopropanol. The ethanol had no observable effect on the droplets, while the isopropanol clearly reduced the total number of droplets through droplet coalescence and droplet loss at the container walls. Scalebars denote 5 μm .

Lipid transfer Lipids were transferred to the TPM droplets by dissolving the DOPC, DOPE-PEG, and DSPE-PEG-btn in ethanol at 1 g L^{-1} , and then adding them to the TPM droplets in the desired quantity (see Table 8.1). In a separate experiment, we confirmed that the added ethanol did not influence the size of the TPM droplets, while for instance the addition of isopropanol did lead to droplet coalescence and droplet loss at the container walls (see Fig. 8.1). The samples were rotated for at least 3 h in a Stuart Rotator SB3, and then washed two times with water by centrifugation at 43 rcf for 30 min. The lipid-coated emulsion droplets were stored at 4°C .

Droplet functionalization We functionalized the TPM droplets with NeutrAvidin by adding the desired MSC of NeutrAvidin (dissolved at 1 g L^{-1} in PBS buffer) to lipid-coated TPM droplets. The DNA-functionalization was done by adding a pre-assembled dsDNA-NeutrAvidin construct, which was prepared as follows: NeutrAvidin and dsDNA-Cy3 were mixed in the desired molar ratio (see Table 8.1) in the rotator for a minimum of 3 h. The resulting dsDNA-NeutrAvidin constructs were stored at 4°C . Then, a lipid-coated TPM emulsion was transferred to PBS and the dsDNA-NeutrAvidin constructs were added up to the desired MSC. The functionalized emulsion was washed three times with PBS. We noted that the presence of the polymer surfactant Pluronic F-127 removed the DNA oligonucleotides from the droplet surface, therefore we recommend avoiding the use of amphiphilic polymers.

We also noted that centrifugation of the coated droplets in PBS lead to partial droplet coalescence and loss at the walls of the sample container. This was solved by avoiding the centrifugation of TPM droplets in PBS. Although we did not use this protocol for the results in this chapter, we provide it here for future reference. First, we added an excess of NeutrAvidin to the emulsion droplets (MSC of $1 \times 10^5 \mu\text{m}^{-1}$). After rotating for 3 h, we washed the emulsion two times with water, and re-suspended it in PBS in the last step. Finally, we added the desired amount of DNA.

Table 8.1. Employed TPM droplet functionalization concentrations. All numbers are max surface coverage (MSC) values, given in number of added molecules per μm^2 of water/TPM interfacial area.

#	DOPE-PEG3000 [μm^{-2}]	DSPE-PEG-btn [μm^{-2}]	NeutrAvidin [μm^{-2}]	dsDNA-Cy3 [μm^{-2}]
1	3×10^5	3×10^4	$4 \times 10^{4*}$	-
2	1×10^5	1×10^4	1×10^4	3×10^4
3	-	1×10^6	-	-
4	-	2×10^6	-	-
5	$3 \times 10^{6\dagger}$	-	-	-
6	2×10^5	3×10^4	4×10^4	4×10^3
7	7×10^5	8×10^4	8×10^3	2×10^4
8	2×10^5	3×10^4	8×10^2	8×10^2
9	$8 \times 10^{5‡}$	9×10^4	5×10^3	2×10^3

* NeutrAvidin-Oregon 488 was used instead of NeutrAvidin.

† DOPE-PEG2000 was used instead of DOPE-PEG3000.

‡ DOPE-PEG5000 was used instead of DOPE-PEG3000.

Particle preparation NeutrAvidin and poly(ethylene)glycol coated polystyrene particles with a diameter of $0.98 \pm 0.03 \mu\text{m}$ were prepared using $3.3 \mu\text{g}$ NeutrAvidin per mg particles following a method described in Chapter 4. For the dsDNA-functionalized particles, these NeutrAvidin-coated particles were incubated for 30 min at 55°C with the desired amount of dsDNA-6FAM (typically $4 \times 10^3 \mu\text{m}^{-2}$) in a PBS buffer, and washed three times with PBS afterwards.

Cluster preparation For the preparation of particle-droplet clusters, particles and droplets were mixed in an estimated 4:1 number ratio at a TPM droplet number density of 10^8cm^{-3} . The resulting sample was left overnight in the tumbler. For the polymerized sample in Figure 8.3c, clusters were polymerized for 2.5 h at 80°C with 1 g/L AIBN. In this process, a large fraction of the clusters disassembled, likely due to the unbinding of biotin-NeutrAvidin at elevated temperatures. This might be improved in the future by using a photo-initiator instead of a thermal initiator (see Chapter 7).

Imaging Imaging was done using a Nikon Ti-E A1R confocal microscope equipped with a $100\times$ NA 1.49 oil immersion objective. The Cy3 dye was excited by a 561 nm laser, and the Oregon 488 and 6FAM dyes with a 488 nm laser. Emissions were recorded respectively through $525 \pm 25 \text{nm}$ and $595 \pm 30 \text{nm}$ filters. The imaging coverslips were pre-treated with a layer of polyacrylamide to prevent droplet adhesion, using the method described in Chapter 5.

FRAP Fluorescence recovery after photobleaching (FRAP) experiments were performed on untreated glass coverslips to fixate the droplets. Using a focussed laser and a set of Galvano mirrors, dye molecules in a region on a single emulsion droplet were bleached, after which we observed the recovery with confocal microscopy. The recovery of fluorescence is caused by the diffusive exchange of molecules from the bleached patch with the rest of the droplet. Following ref. [233], we define the bleaching-corrected relative intensity $I_r(t) = I(t)/I(t = 0)$, with I the bleaching-corrected intensity $I = I_{FRAP}/I_{ref}$. I_{ref} is the fluorescence in a reference area, that captures the global bleaching due to imaging. We then fit $I_r(t)$ to an exponential recovery curve: $I_r = \alpha(1 - \exp[-(t - t_0)/\tau])$, with t the time, t_0 the starting time, τ the recovery time, and α the extent of recovery.

8.3 Results and Discussion

8.3.1 Mobility

The most important property of a droplet-supported lipid monolayer is its mobility. We studied the mobility of single TPM-droplet attached molecules using FRAP. First, we prepared TPM droplets with attached DOPE lipids that have a covalently attached fluorescent dye (DOPE-NBD with an MSC of $1 \times 10^5 \mu\text{m}^{-2}$). The corresponding FRAP experiment (see Figs. 8.2a–d) showed a complete recovery with a recovery time of 0.6 s. The small bleaching area and spherical particle geometry prohibited the quantitative comparison of the timescale with the lipid diffusion coefficients, such as usual for planar supported bilayers.²³³ Qualitatively, the order of magnitude of the recovery time in a patch size of approximately $1 \mu\text{m}$ is comparable to typical diffusion coefficients of DOPE lipids ($10 \mu\text{m}^2 \text{s}^{-1}$, see ref. [234]). From this, we conclude that lipids on TPM microemulsion droplets have a mobility comparable to lipids in a lipid bilayer.

Next, we prepared DOPE-PEG3000/DSPE-PEG2000-btn stabilised TPM emulsion droplets (experiment #1 in Table 8.1) and attached an excess of NeutrAvidin functionalized with the fluorescent dye Oregon 488. See Figs. 8.2e–h for the corresponding FRAP experiment. The observed recovery time of 0.4 s was comparable to the lipid recovery time, so we conclude that TPM microemulsions can be coated with NeutrAvidin proteins that are mobile on the droplet surface. These NeutrAvidin proteins are widely employed to link molecules non-covalently together, which could be used to for instance attach monoclonal antibodies^{142,227} or DNA oligonucleotides^{48,235} to the liquid droplet surface.

To prove the lateral mobility of NeutrAvidin-attached molecules, we linked double-stranded DNA oligonucleotides to the DSPE-PEG2000-btn-NeutrAvidin construct (experiment #2 in Table 8.1). The here employed dsDNA-Cy3 was functionalized with a fluorescent dye, so that we could use FRAP to quantify the mobility on six particles distributed over two TPM emulsion batches. See Figs. 8.2j–m for a representative result. All droplets showed mobility, with an extent of recovery of $93 \pm 2\%$ and a recovery time of 1.8 ± 0.2 s, which is significantly slower than the recovery of the NeutrAvidin proteins. We presume this is related to the size of the double-stranded DNA.

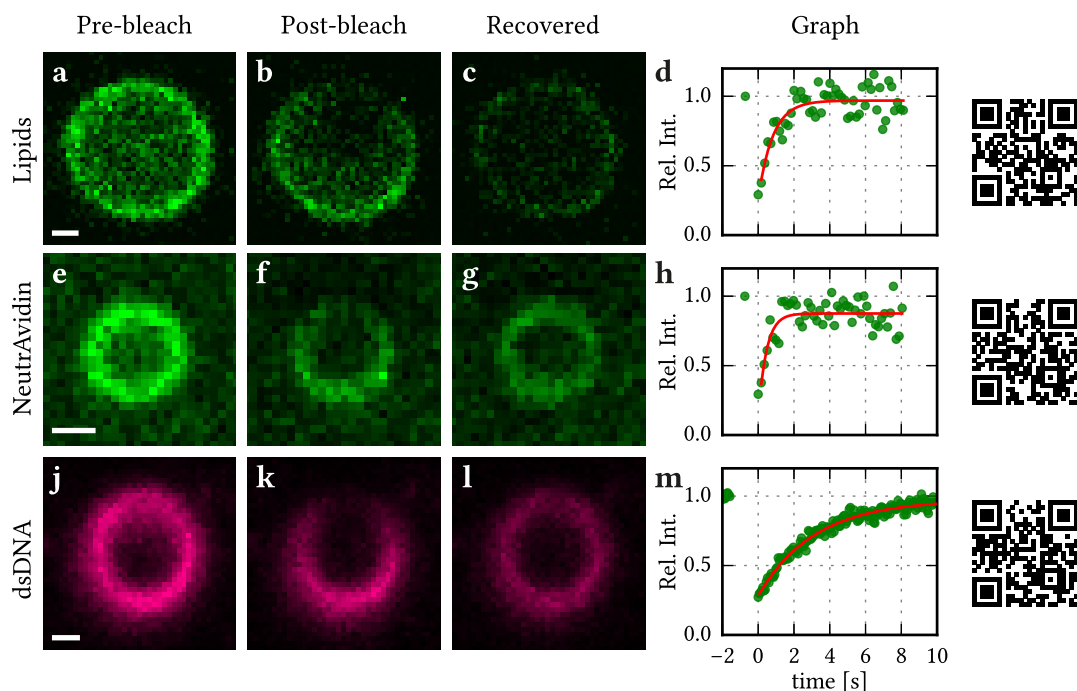


Figure 8.2. FRAP experiment showing the mobility of molecules attached to TPM emulsion droplets. In (a) to (d), confocal images of DOPE–NBD (experiment #1 in Table 8.1) on the surface of a TPM droplet are shown (a) before bleaching, (b) directly after bleaching, and (c) after recovery. In (d), the bleaching-corrected relative intensity is shown, together with a least squares fit with recovery time 0.6 s. The relative intensity is subject to error in the first (pre-bleach) data point. Within this error, the observed recovery was complete. Similarly, in (e) to (h) the recovery of NeutrAvidin–Oregon 488 (experiment #2 in Table 8.1) is shown with recovery time 0.4 s. In (j)–(m) the recovery of dsDNA–Cy3 (experiment #3 in Table 8.1) is shown with recovery time 1.8 ± 0.2 s and relative recovery of $93 \pm 2\%$. The videos corresponding to these three FRAP experiments are available online.

These results show that lipid-coated TPM droplets can be functionalized with surface-mobile macromolecules, which provides a versatile platform for in vitro biological studies such as phagocytosis.²²⁷

8.3.2 Cluster self-assembly

As alluded to in the introduction, droplets with surface-mobile molecules are promising candidates for applications in micron-scale self-assembly. The preparation of TPM droplets with linked colloidal particles that are able to rearrange on the TPM surface

would open up a way to bulk synthesize colloidal clusters of well defined shape.^{231,232} Also, these flexible TPM-based clusters could be used as microscopic equivalents to hinges and joints, as has been shown recently using lipid bilayer-coated silica microparticles.⁴⁴ We here investigate two types of linkages between lipid-coated TPM droplets and particles to obtain these flexible clusters: biotin-NeutrAvidin (as described in Chapters 4–6) and complementary DNA oligonucleotides.^{41,44,119}

Starting from DSPE-PEG-btn coated TPM droplets, we created colloidal clusters by mixing the TPM droplets with NeutrAvidin-coated polystyrene particles (experiment #3 in Table 8.1). Through the specific biotin-NeutrAvidin linkage, the particles accumulate on the TPM droplets and colloidal clusters formed within minutes, as can be seen in Figure 8.3. The NeutrAvidin-coated polystyrene particles attached specifically to the biotin-coated TPM droplets: we did not observe clustering of polystyrene particles or TPM droplets at these conditions. Indeed, in the absence of biotin on the TPM particles (experiment #5 in Table 8.1), NeutrAvidin-coated polystyrene particles did not attach to the TPM droplets. The formed clusters can be fixated by polymerizing the TPM droplet (experiment #4 in Table 8.1), which enables the use of these clusters as building blocks for self-assembly. See Figure 8.3c for a SEM image of a polymerized cluster.

The resulting colloidal clusters were however not of uniform shape. This is caused by the immobility of the particles on the TPM droplet surface, which was confirmed separately by following the relative orientations of the particles in a single cluster. Because we presume that the TPM droplet is liquid, this result is surprising. There is apparently sufficient friction between the TPM and particle to fixate most of the clusters, at least during a single cluster observation of a few minutes. Unlike experiments on a similar system,⁴⁴ we here observed that lowering the number of biotin linkers on the TPM droplets did not result in a reproducible cluster flexibility. A probable explanation for this is that the PEG2000 polymers on the TPM droplet have insufficient length (Flory radius of 3.5 nm¹³⁶) to prevent Van der Waals interactions between the TPM oil and polystyrene particles. Therefore, we took another approach and investigated the use of double-stranded DNA ‘linkers’ (dsDNA) that protrude approx. 14 nm from the TPM droplets. The dsDNA terminates with a single-stranded ‘sticky end’ that protrudes from the particle, which allows binding with its complementary strand¹¹⁹ while keeping the bound particle sufficiently far from the TPM surface to prevent Van der Waals forces to fixate the cluster.

The specific interactions between DNA oligonucleotides only function in the presence of salt. As the salt screens the electrostatic repulsions between TPM droplets, additional stabilization of the TPM droplets is necessary to prevent droplet coalescence. We achieve this by coating the particles with an excess of DOPE-PEG3000. With a concentration series, we observed that a minimum MSC of $6 \times 10^4 \mu\text{m}^{-2}$ is necessary to prevent droplet coalescence in 0.1 M NaCl. Note that this MSC is the number of added lipids to the TPM emulsion, and not the actual number of lipids per unit area, which presumably is lower. The thus stabilised TPM-droplets can be easily centrifuged and are stable for weeks in the tumbler.

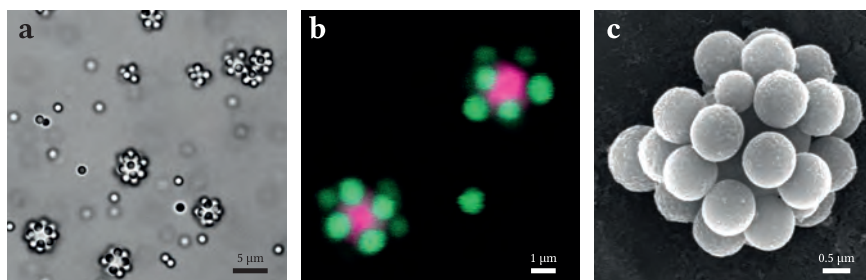


Figure 8.3. Colloidal clusters from DSPE-PEG2000-btn coated TPM droplets and NeutrAvidin-coated polystyrene, in water. (a) Bright field image of several colloidal clusters and free polystyrene (experiment #3 in Table 8.1). (b) Confocal image of the same sample with two TPM droplets (magenta) each surrounded by multiple attached polystyrene particles (green). (c) Scanning electron micrograph (taken by an FEI NanoSEM) of a TPM droplet with attached polystyrene particles, that was polymerized after cluster assembly (experiment #4 in Table 8.1).

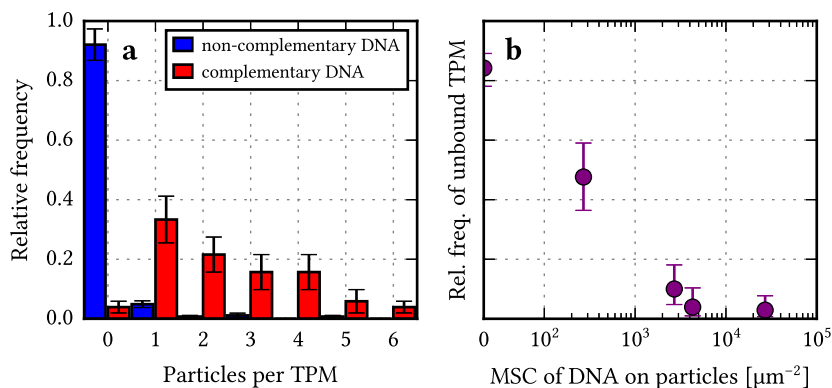


Figure 8.4. DNA-mediated cluster formation of TPM droplets with polystyrene particles (see experiment #6 in Table 8.1). (a) Distribution of cluster sizes for dsDNA-Cy3 coated TPM droplets with complementary particles (dsDNA-6FAM coated) and non-complementary particles (dsDNA-Cy3 coated). After 3 h, 98% of the TPM droplets have bound to at least one complementary particle, while only 8% of the droplets bound to the non-complementary particles. The droplet:particle number ratio in these experiments were 1:2.3 and 1:0.7, respectively, and the MSC of DNA on the particles was $4.3 \times 10^3 \mu\text{m}^{-2}$. (b) The probability of observing unbound TPM droplets increased with decreasing DNA coverage on the particles. This provides additional evidence that DNA is causing the droplet-particle binding.

On these stabilised TPM droplets, we assembled NeutrAvidin–dsDNA–Cy3 constructs, which can be visualised through the fluorescent dye Cy3 on the DNA, see Fig. 8.2j. To prove the specific assembly of particles on these TPM droplets, we then added particles with the complementary (dsDNA–6FAM) DNA strands and particles with the non-complementary (dsDNA–Cy3) DNA strands (see experiment #6 in Table 8.1). After 3 h we counted the formed clusters and observed that in the first case, 98% of the TPM droplets was indeed bound to at least one particle, as opposed to 8% in the control experiment (see Fig. 8.4a). The probability of binding increased with increasing DNA density on the polystyrene particles, as displayed in Fig. 8.4b. We therefore concluded that the observed binding is due to the complementary DNA strands.

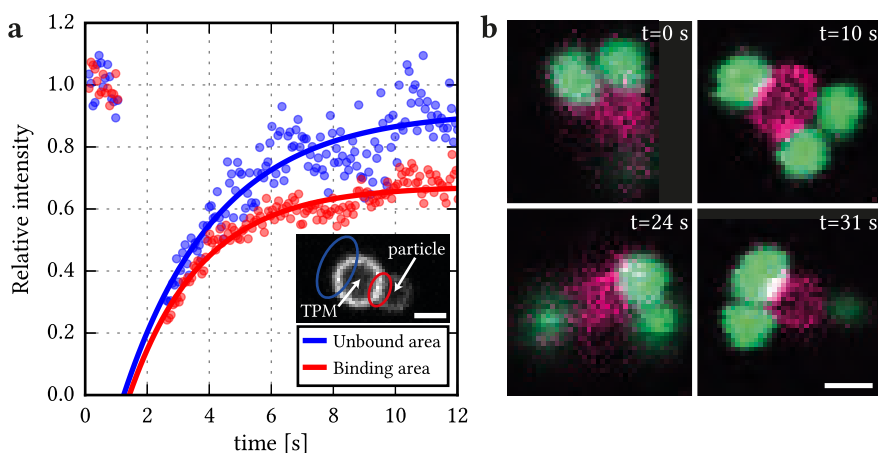


Figure 8.5. The mobility of DNA-mediated TPM clusters. (a) The FRAP recovery of dsDNA linkers in the binding area is only 67% (red), as opposed to the 92% recovery in an unbound area (blue). The corresponding confocal image is displayed in the inset, together with the approximate FRAP areas of the binding patch (red) and unbound area (blue) (experiment #7 in Table 8.1). (b) Four confocal images of the same DNA-mediated TPM cluster (experiment #8 in Table 8.1). The cluster rotation is visible, however the relative orientation of particles remains fixed. Clusters with fixed conformations were observed throughout all samples. The corresponding video is available online. Scalebars denote 1 μm.

The DNA-mediated linkage between TPM droplets and polystyrene particles can also be observed in a FRAP experiment (experiment #7 in Table 8.1). In Figure 8.5a, the recovery of DNA fluorescence in a binding area is compared to the recovery outside the binding area. The bleaching-corrected fluorescence in the binding area was observed to recover to only 67% after photobleaching, while the unbound area recovered to 92%. This incomplete recovery shows that part of the DNA linkers are confined inside the linking patch between the TPM droplet and polystyrene particle, which is a logical consequence of the DNA-mediated linkage between droplet and particle.

Although we concluded that the DNA linkages were mobile on the TPM surface with the droplet-particle linkage caused by the DNA, we did not observe mobility of the particles on the TPM droplets. This is illustrated in Figure 8.5b, in which the relative orientation of the polystyrene particles on the central TPM droplet does not change over the course of the experiment (1 min). One factor that may influence the cluster flexibility is the number of particle-droplet linkages. In similar work⁴⁴ that uses lipid bilayer-coated silica particles to form colloidal clusters, it was found that mobile clusters are found only below a DNA surface concentration of $1 \times 10^4 \mu\text{m}^{-2}$. However, we observed that at a DNA maximum surface coverage (MSC) of $2.7 \times 10^2 \mu\text{m}^{-2}$ on the particles, the clusters were still not flexible. Because at this coverage, almost half of the TPM droplets does not bind any particle (see Fig. 8.4b), we conclude that we cannot achieve mobile clusters by reducing the number of DNA linkages.

We here propose two possible reasons for the lack of cluster mobility. Firstly, the steric stabilization of the TPM droplets might be insufficient. We attempted to improve the thickness of the steric stabilization layer by using DOPE-PEG5000 lipids instead of DOPE-PEG3000 (see Table 8.1, experiment #9), however this also did not lead to mobile clusters. Therefore, we suggest a second reason for the absence of cluster flexibility, which is connected to the heterogeneous nature of TPM. The TPM microemulsion droplets are formed by hydrolysis and subsequent oligomerization of TPM monomers (see Chapter 7). It is likely that TPM oligomers are predominantly present on the TPM droplet surface and form a network of crosslinked TPM molecules. Single molecules that are embedded in this interface are able to move on this heterogeneous surface, while collective motion of multiple linkages is prohibited. See Figure 8.6 for an illustration of this hypothesis. This would explain the almost complete recovery of dsDNA on the TPM

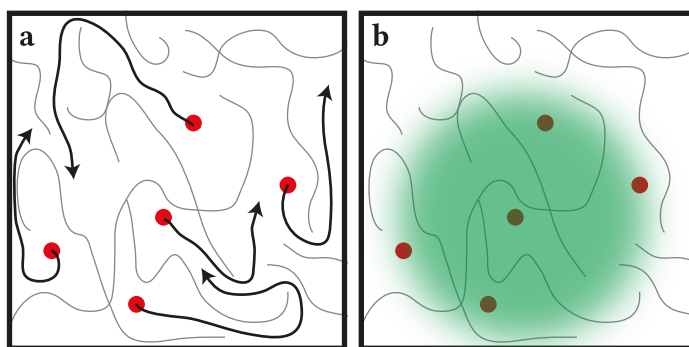


Figure 8.6. Sketch illustrating the hypothesized effect of TPM heterogeneity on the collective mobility of attached lipid molecules. (a) Single lipid molecules (red discs) can freely move through the network of TPM oligomers (grey lines), as denoted with the black arrows. (b) If the same lipids would be interconnected by a linked particle (green shaded area), they move collectively, and their movement becomes inhibited by the TPM oligomer network.

droplet surface (see Fig. 8.2), and at the same time the immobility of clusters that are formed exclusively through dsDNA linkages.

8.4 Conclusion

We have shown that TPM droplet surfaces can be used as a lipid monolayer support. Using fluorescence recovery after photobleaching, we have proven that the fluorescence provided by DOPE-NBD lipids on the interface of TPM droplets fully recovers within seconds after photobleaching, which is comparable to lipid diffusion in bilayers. Also, when the protein NeutrAvidin is attached to a DOPE-PEG2000-btn lipid, an equally high mobility was observed. Using remaining binding sites on the NeutrAvidin, we attached double-stranded DNA oligomers, which also showed lateral mobility, albeit with a longer recovery time of 1.8 ± 0.2 s and with a recovery after photobleaching of 93 ± 2 %. TPM microemulsions therefore provide a model of cells with surface-mobile moieties, which will be useful in the future for controlled phagocytosis experiments.²²⁷

Because TPM droplets can be produced with a narrow size distribution, these are interesting candidates for the self-assembly of micron-sized colloidal clusters. We showed that NeutrAvidin-coated particles attach to biotin-coated TPM-droplets, and also that the resulting clusters could be fixated by polymerizing the TPM droplets, enabling their use in further self-assembly steps. Using a different approach with double-stranded DNA oligomers, we were also able to specifically assemble particles on the surface of TPM droplets.

Surprisingly, the resulting clusters were not flexible, while we established that the single molecules that link the droplet and particles together are mobile on the TPM surface. We hypothesize that the mobility of a collection of TPM-attached molecules is inhibited because of the oligomeric TPM structures that are present in the TPM droplets. While most of the single linkers are able to diffuse through this network of TPM oligomers, a collection of linkers is effectively stuck at a fixed position on the TPM droplet. TPM droplets thus provide an interesting mixture of single lipid mobility and collective immobility, which will be interesting for further research.

Samenvatting

Ons lichaam is opgebouwd uit vele cellen van een honderdste millimeter groot. Elk van deze cellen is omringd door een membraan van vetmoleculen: de *lipide bilaag*. Het is uitermate belangrijk dat deze dunne laag de celeiwitten en het DNA binnen de cel houdt, terwijl het zaken die het leven bedreigen buiten houdt. Niet alleen de buitenkant van de cel bestaat uit een membraan: ook de verschillende compartimenten in de cel worden omringd door een lipide bilaag. Zie figuur 1.1 op pagina 2 voor een illustratie.

Niet alleen de biologie, maar ook de mechanica van een celmembraan blijkt uniek te zijn. Natuurkundig gezien ligt een celmembraan namelijk in het midden tussen een plastic tas en een zeepbel: aan de ene kant heeft het elastische eigenschappen, maar aan de andere kant is het membraan vloeibaar en kan het zich aan alle vormen aanpassen. In de laatste decennia zijn er verschillende theoretische studies gedaan naar mogelijke gevolgen van deze bijzondere eigenschappen, wat onder andere heeft geleid tot de voorspelling dat membraan-eiwitten het membraan gebruiken om zich in grotere structuren te organiseren. Dit zou een drijvende kracht zijn achter bijvoorbeeld het afsnoeren van kleine transportblaasjes (endocytose, zie figuur 1.2 op pagina 3).

Het is echter nog niet mogelijk gebleken om deze voorspelling experimenteel te toetsen. Een deel van deze uitdaging is dat eiwitten zo klein zijn dat ze niet met een lichtmicroscop van elkaar te onderscheiden zijn. In mijn proefschrift heb ik dit probleem benaderd door in plaats van eiwitten, duizend maal grotere objecten op celmembranen te zetten: plastic deeltjes van een micrometer (0.001 millimeter). Deze zijn goed te bestuderen met een microscoop, terwijl ze klein genoeg zijn om geen zwaartekracht te voelen en de willekeurige bewegingen te vertonen waar eiwitten ook aan onderhevig zijn. Een voorbeeld hiervan is te zien op de omslag van dit proefschrift: hier bewegen twee deeltjes zich willekeurig over het oppervlak van een bolvormig membraan.

De vraag die ik in mijn proefschrift tracht te beantwoorden is: kan een lipide membraan krachten veroorzaken tussen objecten die het membraan lokaal vervormen? Om deze vraag te beantwoorden heb ik microdeeltjes ontwikkeld die zich specifiek en met hoge affiniteit aan membranen met biotine hechten. Dit soort deeltjes zijn ook te koop, echter bevatten deze dan altijd oppervlakte-actieve stoffen (zeep) die membranen destabiliseren. In hoofdstuk 4 wordt een zeepvrije methode beschreven die microdeeltjes specifiek aan bepaalde moleculen laat binden (zie figuur 4.5 op pagina 64). Naast

toepassing in dit proefschrift, zijn dit soort deeltjes-coatings ook interessant voor lokale toediening van medicijnen.

Om nu uit microscoop-opnames van deze microdeeltjes iets te kunnen zeggen over welke krachten ze op elkaar uitoefenen, waren analyse-methoden nodig. In hoofdstuk 2 beschrijf ik een nieuwe beeldanalysetechniek om de deeltjes te volgen. Naast dat deze techniek de locatie van een deeltje in een foto kan bepalen met een meetnauwkeurigheid onder de 0.1 pixel, kan het ook deeltjes van elkaar onderscheiden in 100% van de geteste beelden, terwijl de conventionele methode slechts in 11% van de beelden de deeltjes juist onderscheidt (zie figuur 2.4 op pagina 20). In hoofdstuk 3 vergelijk ik vervolgens drie methodes om krachten af te leiden uit de de geobserveerde deeltjes-trajecten.

Deze methodes komen bij elkaar in hoofdstuk 5, waar ik het gedrag van microdeeltjes op lipide membranen bestudeer. Verassend genoeg blijken deze deeltjes ofwel aan het membraan vast te gaan zitten zonder het membraan te vervormen, ofwel ze wikkelen zichzelf helemaal in in het membraan en veroorzaken een vervorming (zie figuur 5.2 op pagina 74). Dit ‘alles of niets’ gedrag is te beïnvloeden door de affiniteit van de deeltjes voor de membranen te veranderen. Alleen de deeltjes die het membraan vervormen, oefenen een kracht op elkaar uit. Dit bewijst de voorspelling dat celmembranen krachten tussen membraan-vervormende objecten kunnen overbrengen. Computer-simulaties (zie figuur 5.5 op pagina 79) laten zien dat de gemeten kracht voortkomt uit de buigstijfheid van het membraan.

In hoofdstuk 6 gebruik ik dezelfde experimenten om een heel andere vraag te beantwoorden: hoe gedragen plastic microdeeltjes zich op celmembranen? Deze vraag wordt steeds urgenter nu microplastics zich via de zee verspreiden in de voedselketen. Ik beschrijf dat wanneer meerdere deeltjes blijven plakken aan een celmembraan, deze via verschillende mechanismen op het membraan kan samenklonteren (zie figuur 6.4 op pagina 92). Dit is een mogelijke verklaring voor de onverwacht hoge retentietijden van microplastics in levende organismen: omdat de microplastics samenklonteren, raakt een organisme ze veel minder snel weer kwijt.

In de laatste twee hoofdstukken van mijn proefschrift beschrijf ik een mogelijke toepassing van lipiden. Eerst, in hoofdstuk 7, bestudeer ik een olie (TPM) die in een basische oplossing emulsiedruppels vormt van één bepaalde grootte. Vervolgens zet ik in hoofdstuk 8 lipiden op het oppervlak van deze druppels. Omdat de druppels vloeibaar zijn, zijn de lipiden mobiel over het oppervlak. Ik laat zien dat eiwitten en DNA-moleculen die aan deze lipiden worden vastgemaakt ook mobiel zijn over het oppervlak van de druppels (zie figuur 8.2 op pagina 129). Dit maakt deze lipide monolagen een model voor celmembranen met gecontroleerde krommingsstraal. Alhoewel individuele moleculen mobiel zijn, zijn microdeeltjes die aan het druppeloppervlak zitten dat niet. TPM-druppels zijn dus niet volledig vloeibaar.

Met dit proefschrift hoop ik een bijdrage te leveren aan het begrip over krachten die membranen overbrengen. Enerzijds is dit begrip fundamenteel celbiologisch en zegt het iets over krachten tussen membraan-eiwitten, anderzijds draagt het bij aan het begrip over de toxiciteit van microplastics.

Publication List

Published work presented in this thesis

- C. M. van der Wel and D. J. Kraft. 'Automated tracking of colloidal clusters with sub-pixel accuracy and precision', *J. Phys. Condens. Mat.* **29**, 44001 (2017) DOI:10.1088/1361-648X/29/4/044001 (Chapter 2).
- C. M. van der Wel, N. Bossert, Q. C. Mank, M. G. T. Winter, D. Heinrich and D. J. Kraft, 'Surfactant-free colloidal particles with specific binding affinity', submitted (Chapter 4).
- C. M. van der Wel, A. Vahid, A. Šarić, T. Idema, D. Heinrich and D. J. Kraft. 'Lipid membrane-mediated attractions between curvature inducing objects', *Sci. Rep.* **6**, 32825 (2016) DOI:10.1038/srep32825 (Chapter 5).
- C. M. van der Wel, D. Heinrich and D. J. Kraft, 'Microparticle assembly pathways on lipid membranes', *Biophys. J.* **113**, in press (2017) DOI:10.1016/j.bpj.2017.07.019 (Chapter 6).
- C. M. van der Wel, R. K. Bhan, R. W. Verweij, H. C. Frijters, Z. Gong, A. D. Hollingsworth, S. Sacanna and D. J. Kraft, 'Preparation of colloidal organosilica spheres through spontaneous emulsification', *Langmuir* **33**, in press (2017) DOI:10.1021/acs.langmuir.7b01398 (Chapter 7).

Other published work

- I. Chakraborty, V. Meester, C. M. van der Wel and D. J. Kraft, 'Colloidal joints with designed motion range and tunable joint flexibility', *Nanoscale* **9**, 7814 (2017) DOI:10.1039/C6NR08069C
- V. Meester, R. W. Verweij, C. M. van der Wel and D. J. Kraft. 'Colloidal recycling: reconfiguration of random aggregates into patchy particles', *ACS Nano* **10**, 4322 (2016) DOI:10.1021/acsnano.5b07901

- A. Mohan, C. M. van der Wel, R. E. I. Schropp and J. K. Rath, 'Probing periodic oscillations in a silane dusty plasma in a very high-frequency plasma enhanced chemical vapor deposition', *Can. J. Phys.* **92**, 744 (2014)
doi:10.1139/cjp-2013-0611
- C. M. van der Wel, R. J. Kortschot, I. A. Bakelaar, B. H. Ern e and B. W. M. Kuipers, 'Rapid offset reduction of impedance bridges taking into account instrumental damping and phase shifting', *Rev. Sci. Instrum.* **84**, 36109 (2013)
doi:10.1063/1.4795554

Published software

Authors are listed alphabetically

- C. M. van der Wel, 'Circletracking v1.0', Zenodo 47216 (2016)
doi:10.5281/zenodo.47216
- C. M. van der Wel, 'PIMSviewer v1.0',
<https://pypi.python.org/pypi/pimsviewer/1.0> (2017)
- D. B. Allan, T. A. Caswell, N. C. Keim, C. M. van der Wel and others, 'Python Image Sequence (PIMS) v0.3.3', <https://pypi.python.org/pypi/PIMS/0.3.3> (2016).
- D. B. Allan, T. A. Caswell, N. C. Keim, C. M. van der Wel and others, 'Python Image Sequence (PIMS) v0.4', <https://pypi.python.org/pypi/PIMS/0.4> (2017).
- R. W. Verweij and C. M. van der Wel, 'Semtracking v1.0.3', Zenodo 45575 (2016)
doi:10.5281/zenodo.45575
- D. B. Allan, T. A. Caswell, N. C. Keim, C. M. van der Wel and others, 'Trackpy v0.3.0', Zenodo 34028 (2015) doi:10.5281/zenodo.34028
- D. B. Allan, T. A. Caswell, N. C. Keim, C. M. van der Wel and others, 'Trackpy v0.3.1', Zenodo 55143 (2016) doi:10.5281/zenodo.55143
- D. B. Allan, T. A. Caswell, N. C. Keim, C. M. van der Wel and others, 'Trackpy v0.4', in preparation.

Curriculum Vitae

I was born in Hilversum, where I grew up and received my secondary education at *Ge-meentelijk Gymnasium*. During the exam year in 2006, I won the National Chemistry Olympiad and received the silver medal at the International Chemistry Olympiad in Gyeongsan, South Korea.

Directly after my secondary education, I enrolled to the BSc program Chemistry at *Utrecht University*. Starting from my second year, I took extra classes in physics, which continued until 2011 when I finished both bachelors cum laude with a thesis on high sensitivity dielectric spectroscopy measurements. After that, I continued in the master programme *Nanomaterials: Chemistry and Physics* at the same university. I spent one year in the *Physics of Devices* group, studying fluctuations in dusty plasmas for the preparation of thin-film solar cells, and six months at Philips Research, where I studied water electrochemistry. In April 2013, I received my MSc diploma cum laude. During these seven years at *Utrecht University*, I spent one year full-time as financial manager of the Dutch Student Orchestra (NSO), and two years part-time as board member of USConcert. From 2011, I founded and co-organised the opera project *Rheingold on the Rhine*, which took place in a converted Rhine barge in July 2013.

In September 2013, I started as a PhD candidate at *Leiden University* under supervision of Dr. Daniela Kraft and Dr. Doris Heinrich. I studied lipid mediated interactions between colloidal particles, the results of which are presented in this thesis. Part of the work has been performed in close collaboration with Afshin Vahid and Dr. Timon Idema at *Delft University of Technology*, and another part with Dr. Stefano Sacanna and Dr. Andrew Hollingsworth at *New York University*.

During my PhD, I (co-)supervised 10 undergraduate students and I was a teaching assistant of the undergraduate courses *Experimental Physics* and *Diffusion*. I attended schools in Han-sur-Lesse (Belgium) and Varenna (Italy), and presented my work at the APS March meeting 2015 (San Antonio, USA), CHAINS 2015 (Veldhoven), the International Soft Matter Conference 2016 (Grenoble, France), Biophysics@Veldhoven 2016, and Physics@Veldhoven 2017.

After my PhD, I aim to use my knowledge of the natural sciences to solve current problems in applied science, in a research position in industry or a governmental institute.

Acknowledgement

The work performed for this thesis could not have taken place without the support of many people. Firstly, I express my gratitude to Dr. Daniela Kraft for the thoughtful supervision providing the confidence necessary to conduct my own research. Secondly, I thank Dr. Doris Heinrich for the inspiring discussions and the scientific freedom. I thank Prof. Thomas Schmidt for acting as promotor.

I am thankful for the discussions with our collaborators Afshin Vahid and Dr. Timon Idema (*TU Delft*), who together with Dr. Anđela Šarić (*UC London*) provided the numerical work in Chapter 5. Also, I thank Rohit Bhan, Zhe Gong, Dr. Andrew Hollingsworth, and Dr. Stefano Sacanna (*New York University*) for their contributions to Chapter 7. I thank Benny van Zuiden for the discussions and explanations about Brownian motion in curved geometry (Chapter 3). Finally, I thank Nelli Bossert and Marcel Winter for their work that is included in Chapter 4.

Part of the work in this thesis was conducted by undergraduate students. I enjoyed coaching Alex Blokhuis, Hans Frijters, Willem Hekman, Jelle Hockx, Quinten Mank, Sergio Rus Moreno, Joseph Salaris, and Guido van de Stolpe, each of whom provided valuable results. I especially thank Ernst Jan Vegter for his persevering work on supported lipid bilayers, a project that is still ongoing, and Ruben Verweij for his significant contributions to the TPM-supported lipid monolayers described in Chapters 7 and 8.

The technical support by the fine mechanical and electronic departments were indispensable: I especially thank Raphaël Zwier and Jeroen Mesman. I thank Daniëlle Jansen and Ernst van Duijvendijk (*Nikon Instruments*) for their support on the microscopes. I thank Daniëlle Duijn and Yvonne van Rooij for the secretary work.

I am grateful to my dear colleague Vera Meester for support and feedback during my PhD, as well as for sharing the responsibility of managing the Soft Matter Physics laboratory. I also thank my colleagues Indrani Chakraborty, Melissa Rinaldin, Nemanja Markešević, Ruben Verweij, Marcel Winter, Dominique Donato, Joeri Wondergem, Nelli Bossert, Elena Beletkaia, and Maria Mytiliniou for the careful feedback and useful discussions. I also thank the people who created a friendly and fruitful scientific environment: Martin, Geert, Bastiaan, Merlijn, Luuk, Peter, Anne, Scott, Coentin, Rachel, Stefania, Luca, Dan, Koen, Piermarco, Ireth, Benny, Anton, Yujie, Saptaswa, Biswajit, Wim, and others I omitted unintentionally. Finally, I express my gratitude to my family and especially to Runa for the love and constant positive support during all these years.

Bibliography

1. B. Alberts, A. Johnson, J. Lewis, M. Raff, K. Roberts and P. Walter, 'Membrane Structure', in *Molecular biology of the cell*, 4th ed. (Garland Science, 2002) Chap. 10, p. 583, ISBN: 0-8153-4072-9 (pp. 1, 2).
2. H. T. McMahon and J. L. Gallop, 'Membrane curvature and mechanisms of dynamic cell membrane remodelling', *Nature* **438**, 590 (2005) DOI: 10.1038/nature04396 (pp. 1, 3, 68, 80).
3. J. Zimmerberg and M. M. Kozlov, 'How proteins produce cellular membrane curvature', *Nat. Rev. Microbiol.* **7**, 9 (2006) DOI: 10.1038/nrm1784 (p. 1).
4. B. J. Reynwar, G. Illya, V. A. Harmandaris, M. M. Müller, K. Kremer and M. Deserno, 'Aggregation and vesiculation of membrane proteins by curvature-mediated interactions', *Nature* **447**, 461 (2007) DOI: 10.1038/nature05840 (pp. 1, 3, 6, 68, 79).
5. W. M. Henne, E. Boucrot, M. Meinecke, E. Evergren, Y. Vallis, R. Mittal and H. T. McMahon, 'FCHo proteins are nucleators of clathrin-mediated endocytosis', *Science* **328**, 1281 (2010) DOI: 10.1126/science.1188462 (p. 1).
6. H. T. McMahon and E. Boucrot, 'Molecular mechanism and physiological functions of clathrin-mediated endocytosis', *Nat. Rev. Mol. Cell Bio.* **12**, 517 (2011) DOI: 10.1038/nrm3151 (p. 1).
7. C. Zhu, S. L. Das and T. Baumgart, 'Nonlinear sorting, curvature generation, and crowding of endophilin N-BAR on tubular membranes', *Biophys. J.* **102**, 1837 (2012) DOI: 10.1016/j.bpj.2012.03.039 (p. 1).
8. C. Prévost, H. Zhao, J. Manzi, E. Lemichez, P. Lappalainen, A. Callan-Jones and P. Bassereau, 'IRSp53 senses negative membrane curvature and phase separates along membrane tubules', *Nat. Commun.* **6**, 8529 (2015) DOI: 10.1038/ncomms9529 (pp. 1, 3).
9. https://commons.wikimedia.org/wiki/File:Biological_cell.svg, 2006 (p. 2).
10. https://commons.wikimedia.org/wiki/File:Phospholipids_aqueous_solution_structures.svg, 2007 (p. 2).
11. S. J. Singer and G. L. Nicolson, 'The fluid mosaic model of the structure of cell membranes', *Science* **175**, 720 (1972) DOI: 10.1126/science.175.4023.720 (pp. 2, 124).

12. M. M. Perry and A. B. Gilbert, 'Yolk transport in the ovarian follicle of the hen (*Gallus domesticus*): lipoprotein-like particles at the periphery of the oocyte in the rapid growth phase', *J. Cell Sci.* **39**, 257, ISSN: 0021-9533 (1979) (p. 3).
13. B. J. Peter, H. M. Kent, I. G. Mills, Y. Vallis, P. J. G. Butler, P. R. Evans and H. T. McMahon, 'BAR domains as sensors of membrane curvature: the amphiphysin BAR structure', *Science* **303**, 495 (2004) DOI: 10.1126/science.1092586 (pp. 3, 68, 80).
14. A. S. Rose and P. W. Hildebrand, 'NGL Viewer: a web application for molecular visualization', *Nucleic Acids Res.* **43**, W576 (2015) DOI: 10.1093/nar/gkv402 (p. 3).
15. A. Frost, V. M. Unger and P. De Camilli, 'The BAR domain superfamily: Membrane-molding macromolecules', *Cell* **137**, 191 (2009) DOI: 10.1016/j.cell.2009.04.010 (p. 3).
16. M. Simunovic et al., 'How curvature-generating proteins build scaffolds on membrane nanotubes', *P. Natl. Acad. Sci. USA* **113**, 11226 (2016) DOI: 10.1073/pnas.1606943113 (p. 3).
17. P. G. Dommersnes and J.-B. Fournier, 'The many-body problem for anisotropic membrane inclusions and the self-assembly of "saddle" defects into an "egg carton"', *Biophys. J.* **83**, 2898 (2002) DOI: 10.1016/S0006-3495(02)75299-5 (pp. 3, 5, 68, 78, 92, 95).
18. T. Auth and G. Gompper, 'Budding and vesiculation induced by conical membrane inclusions', *Phys. Rev. E* **80**, 031901 (2009) DOI: 10.1103/PhysRevE.80.031901 (pp. 3, 6).
19. A. Šarić and A. Cacciuto, 'Fluid membranes can drive linear aggregation of adsorbed spherical nanoparticles', *Phys. Rev. Lett.* **108**, 118101 (2012) DOI: 10.1103/PhysRevLett.108.118101 (pp. 3, 6, 68, 78, 92, 95).
20. L. Ramos, T. Lubensky, N. Dan, P. Nelson and D. A. Weitz, 'Surfactant-mediated two-dimensional crystallization of colloidal crystals', *Science* **286**, 2325 (1999) DOI: 10.1126/science.286.5448.2325 (pp. 3, 4, 68, 77, 84).
21. I. Koltover, J. O. Rädler and C. R. Safinya, 'Membrane mediated attraction and ordered aggregation of colloidal particles bound to giant phospholipid vesicles', *Phys. Rev. Lett.* **82**, 1991 (1999) DOI: 10.1103/PhysRevLett.82.1991 (pp. 3, 52, 68, 77, 84, 97).
22. M. R. Lorenz, V. Holzapfel, A. Musyanovych, K. Nothelfer, P. Walther, H. Frank, K. Landfester, H. Schrezenmeier and V. Mailänder, 'Uptake of functionalized, fluorescent-labeled polymeric particles in different cell lines and stem cells', *Biomaterials* **27**, 2820 (2006) DOI: 10.1016/j.biomaterials.2005.12.022 (pp. 3, 4, 84, 95).
23. M. Gaumet, R. Gurny and F. Delie, 'Localization and quantification of biodegradable particles in an intestinal cell model: the influence of particle size', *Eur. J. Pharm. Sci.* **36**, 465 (2009) DOI: 10.1016/j.ejps.2008.11.015 (pp. 3, 84, 95).

-
24. Y. Yu and S. Granick, 'Pearling of lipid vesicles induced by nanoparticles', *J. Am. Chem. Soc.* **131**, 14158 (2009) DOI: 10.1021/ja905900h (p. 3).
 25. M. Cole, P. Lindeque, C. Halsband and T. S. Galloway, 'Microplastics as contaminants in the marine environment: a review', *Mar. Pollut. Bull.* **62**, 2588 (2011) DOI: 10.1016/j.marpolbul.2011.09.025 (pp. 4, 84).
 26. P. B. Canham, 'The minimum energy of bending as a possible explanation of the biconcave shape of the human red blood cell', *J. Theor. Biol.* **26**, 61 (1970) DOI: 10.1016/S0022-5193(70)80032-7 (p. 4).
 27. W. Helfrich, 'Elastic properties of lipid bilayers: theory and possible experiments', *Z. Naturforsch. C* **28**, 693 (1973) DOI: 10.1515/znc-1973-11-1209 (pp. 4, 72, 74).
 28. P. Bassereau, B. Sorre and A. Lévy, 'Bending lipid membranes: experiments after W. Helfrich's model', *Adv. Colloid Interfac.* **208**, 47 (2014) DOI: 10.1016/j.cis.2014.02.002 (p. 5).
 29. E. Evans and W. Rawicz, 'Entropy-driven tension and bending elasticity in condensed-fluid membranes', *Phys. Rev. Lett.* **64**, 2094 (1990) DOI: 10.1103/PhysRevLett.64.2094 (p. 5).
 30. M. Deserno, 'Elastic deformation of a fluid membrane upon colloid binding', *Phys. Rev. E* **69**, 031903 (2004) DOI: 10.1103/PhysRevE.69.031903 (pp. 5, 90).
 31. N. Dan, P. Pincus and S. A. Safran, 'Membrane-induced interactions between inclusions', *Langmuir* **9**, 2768 (1993) DOI: 10.1051/jp2:1994227 (pp. 5, 80).
 32. M. Goulian, R. Bruinsma and P. Pincus, 'Long-range forces in heterogeneous fluid membranes', *Europhys. Lett.* **22**, 145 (1993) DOI: 10.1209/0295-5075/22/2/012 (pp. 5, 68, 78).
 33. S. Katira, K. K. Mandadapu, S. Vaikuntanathan, B. Smit and D. Chandler, 'Pre-transition effects mediate forces of assembly between transmembrane proteins', *Elife* **5**, e13150 (2016) DOI: 10.7554/eLife.13150 (pp. 5, 81).
 34. M. Deserno, 'Fluid lipid membranes: From differential geometry to curvature stresses', *Chem. Phys. Lipids* **185**, 11 (2015) DOI: 10.1016/j.chemphyslip.2014.05.001 (p. 5).
 35. B. J. Reynwar and M. Deserno, 'Membrane-mediated interactions between circular particles in the strongly curved regime', *Soft Matter* **7**, 8567 (2011) DOI: 10.1039/c1sm05358b (pp. 6, 78, 79, 91).
 36. A. Šarić and A. Cacciuto, 'Mechanism of membrane tube formation induced by adhesive nanocomponents', *Phys. Rev. Lett.* **109**, 188101 (2012) DOI: 10.1103/PhysRevLett.109.188101 (pp. 6, 78, 91, 93).
 37. C. E. Ashley et al., 'The targeted delivery of multicomponent cargos to cancer cells by nanoporous particle-supported lipid bilayers', *Nat. Mater.* **10**, 389 (2011) DOI: 10.1038/nmat3042 (p. 6).

38. F. Persson, J. Fritzsche, K. U. Mir, M. Modesti, F. Westerlund and J. O. Tegenfeldt, 'Lipid-based passivation in nanofluidics', *Nano Lett.* **12**, 2260 (2012) DOI: 10.1021/nl204535h (p. 6).
39. S. Mashaghi, T. Jadidi, G. Koenderink and A. Mashaghi, 'Lipid nanotechnology', *Int. J. Mol. Sci.* **14**, 4242 (2013) DOI: 10.3390/ijms14024242 (pp. 6, 124).
40. S. C. Glotzer and M. J. Solomon, 'Anisotropy of building blocks and their assembly into complex structures', *Nat. Mater.* **6**, 557 (2007) DOI: 10.1038/nmat1949 (pp. 6, 12, 124).
41. Y. Wang, Y. Wang, D. R. Breed, V. N. Manoharan, L. Feng, A. D. Hollingsworth, M. Weck and D. J. Pine, 'Colloids with valence and specific directional bonding', *Nature* **491**, 51 (2012) DOI: 10.1038/nature11564 (pp. 6, 124, 130).
42. L. Di Michele, F. Varrato, J. Kotar, S. H. Nathan, G. Foffi and E. Eiser, 'Multistep kinetic self-assembly of DNA-coated colloids', *Nat. Comm.* **4**, 2007 (2013) DOI: 10.1038/ncomms3007 (p. 7).
43. V. Meester, R. W. Verweij, C. van der Wel and D. J. Kraft, 'Colloidal recycling: reconfiguration of random aggregates into patchy particles', *ACS Nano* **10**, 4322 (2016) DOI: 10.1021/acsnano.5b07901 (pp. 7, 12, 102, 124).
44. I. Chakraborty, V. Meester, C. van der Wel and D. J. Kraft, 'Colloidal joints with designed motion range and tunable joint flexibility', *Nanoscale* **9**, 7814 (2017) DOI: 10.1039/C6NR08069C (pp. 7, 52, 124, 130, 133).
45. Q. Chen, S. C. Bae and S. Granick, 'Directed self-assembly of a colloidal kagome lattice', *Nature* **469**, 381 (2011) DOI: 10.1038/nature09713 (pp. 7, 102).
46. S. A. J. van der Meulen, G. Helms and M. Dogterom, 'Solid colloids with surface-mobile linkers', *J. Phys. Condens. Mat.* **27**, 233101 (2015) DOI: 10.1088/0953-8984/27/23/233101 (pp. 7, 52).
47. Y. Wang, Y. Wang, X. Zheng, É. Ducrot, J. S. Yodh, M. Weck and D. J. Pine, 'Crystallization of DNA-coated colloids', *Nat. Commun.* **6**, 7253 (2015) DOI: 10.1038/ncomms8253 (pp. 7, 52, 102, 115).
48. M. Hadorn, E. Boenzli, K. T. Sorensen, H. Fellermann, P. Eggenberger Hotz and M. M. Hanczyc, 'Specific and reversible DNA-directed self-assembly of oil-in-water emulsion droplets', *P. Natl. Acad. Sci. USA* **109**, 20320 (2012) DOI: 10.1073/pnas.1214386109 (pp. 7, 128).
49. L. Feng, L.-L. Pontani, R. Dreyfus, P. Chaikin and J. Brujic, 'Specificity, flexibility and valence of DNA bonds guide emulsion architecture', *Soft Matter* **9**, 9816 (2013) DOI: 10.1039/c3sm51586a (p. 7).
50. S. Sacanna, W. T. M. Irvine, P. M. Chaikin and D. J. Pine, 'Lock and key colloids', *Nature* **464**, 575 (2010) DOI: 10.1038/nature08906 (pp. 7, 102, 103, 115).
51. D. J. Kraft, J. W. J. De Folter, B. Luigjes, S. I. R. Castillo, S. Sacanna, A. P. Philipse and W. K. Kegel, 'Conditions for equilibrium solid-stabilized emulsions', *J. Phys. Chem. B* **114**, 10347 (2010) DOI: 10.1021/jp102659b (pp. 7, 103, 104).

-
52. C. A. Murray and D. G. Grier, 'Video microscopy of monodisperse colloidal systems', *Annu. Rev. Phys. Chem.* **47**, 421 (1996) DOI: 10.1146/annurev.physchem.47.1.421 (p. 12).
 53. E. R. Weeks, J. C. Crocker, A. C. Levitt, A. Schofield and D. A. Weitz, 'Three-dimensional direct imaging of structural relaxation near the colloidal glass transition', *Science* **287**, 627 (2000) DOI: 10.1126/science.287.5453.627 (pp. 12, 102).
 54. W. K. Kegel and A. van Blaaderen, 'Direct observation of dynamical heterogeneities in colloidal hard-sphere suspensions', *Science* **287**, 290 (2000) DOI: 10.1126/science.287.5451.290 (p. 12).
 55. A. D. Dinsmore, E. R. Weeks, V. Prasad, A. C. Levitt and D. A. Weitz, 'Three-dimensional confocal microscopy of colloids', *Appl. Optics* **40**, 4152 (2001) DOI: 10.1364/AO.40.004152 (p. 12).
 56. G. Meng, J. Paulose, D. R. Nelson and V. N. Manoharan, 'Elastic instability of a crystal growing on a curved surface', *Science* **343**, 634 (2014) DOI: 10.1126/science.1244827 (p. 12).
 57. F. C. MacKintosh and C. F. Schmidt, 'Microrheology', *Curr. Opin. Colloid In.* **4**, 300 (1999) DOI: 10.1016/S1359-0294(99)90010-9 (p. 12).
 58. Y. Tseng, T. P. Kole and D. Wirtz, 'Micromechanical mapping of live cells by multiple-particle-tracking microrheology', *Biophys. J.* **83**, 3162 (2002) DOI: 10.1016/S0006-3495(02)75319-8 (pp. 12, 84).
 59. K. C. Neuman and A. Nagy, 'Single-molecule force spectroscopy: optical tweezers, magnetic tweezers and atomic force microscopy', *Nat. Methods* **5**, 491 (2008) DOI: 10.1038/nmeth.1218 (p. 12).
 60. J. Gelles, B. J. Schnapp and M. P. Sheetz, 'Tracking kinesin-driven movements with nanometre-scale precision', *Nature* **331**, 450 (1988) DOI: 10.1038/331450a0 (p. 12).
 61. A. Yildiz, J. N. Forkey, S. A. McKinney, T. Ha, Y. E. Goldman and P. R. Selvin, 'Myosin V walks hand-over-hand: single fluorophore imaging with 1.5-nm localization', *Science* **300**, 2061 (2003) DOI: 10.1126/science.1084398 (p. 12).
 62. E. Betzig, G. H. Patterson, R. Sougrat, O. W. Lindwasser, S. Olenych, J. S. Bonifacino, M. W. Davidson, J. Lippincott-Schwartz and H. F. Hess, 'Imaging intracellular fluorescent proteins at nanometer resolution', *Science* **313**, 1642 (2006) DOI: 10.1126/science.1127344 (p. 12).
 63. S. T. Hess, T. P. K. Girirajan and M. D. Mason, 'Ultra-high resolution imaging by fluorescence photoactivation localization microscopy', *Biophys. J.* **91**, 4258 (2006) DOI: 10.1529/biophysj.106.091116 (p. 12).
 64. B. Huang, W. Wang, M. Bates and X. Zuang, 'Three-dimensional super-resolution imaging by stochastic optical reconstruction microscopy', *Science* **319**, 810 (2007) DOI: 10.1126/science.1153529 (p. 12).

65. J. C. Crocker and D. G. Grier, 'Methods of digital video microscopy for colloidal studies', *J. Colloid Interf. Sci.* **179**, 298 (1996) DOI: 10.1006/jcis.1996.0217 (pp. 12, 13, 16, 21, 27, 32, 40, 72).
66. T. Savin and P. S. Doyle, 'Static and dynamic errors in particle tracking microrheology', *Biophys. J.* **88**, 623 (2005) DOI: 10.1529/biophysj.104.042457 (pp. 12, 16).
67. R. N. Ghosh and W. W. Webb, 'Automated detection and tracking of individual and clustered cell surface low density lipoprotein receptor molecules', *Biophys. J.* **66**, 1301 (1994) DOI: 10.1016/S0006-3495(94)80939-7 (p. 12).
68. M. J. Saxton and K. Jacobson, 'Single-particle tracking: applications to membrane dynamics', *Annu. Rev. Bioph. Biom.* **26**, 373 (1997) DOI: 10.1146/annurev.biophys.26.1.373 (p. 12).
69. R. J. Ober, S. Ram and E. S. Ward, 'Localization accuracy in single-molecule microscopy', *Biophys. J.* **86**, 1185 (2004) DOI: 10.1016/S0006-3495(04)74193-4 (pp. 12, 16).
70. C. S. Smith, N. Joseph, B. Rieger and K. A. Lidke, 'Fast, single-molecule localization that achieves theoretically minimum uncertainty', *Nat. Methods* **7**, 373 (2010) DOI: 10.1038/nmeth.1449 (pp. 12, 26).
71. V. N. Manoharan, M. T. Elsesser and D. J. Pine, 'Dense packing and symmetry in small clusters of microspheres', *Science* **301**, 483 (2003) DOI: 10.1126/science.1086189 (pp. 12, 19, 102, 124).
72. D. J. Kraft, J. Groenewold and W. K. Kegel, 'Colloidal molecules with well-controlled bond angles', *Soft Matter* **5**, 3823 (2009) DOI: 10.1039/b910593j (p. 12).
73. G. L. Hunter, K. V. Edmond, M. T. Elsesser and E. R. Weeks, 'Tracking rotational diffusion of colloidal clusters', *Opt. Express* **19**, 17189 (2011) DOI: 10.1364/OE.19.017189 (p. 12).
74. K. V. Edmond, M. T. Elsesser, G. L. Hunter, D. J. Pine and E. R. Weeks, 'Decoupling of rotational and translational diffusion in supercooled colloidal fluids', *P. Natl. Acad. Sci. USA* **109**, 17891 (2012) DOI: 10.1073/pnas.1203328109 (p. 12).
75. M. K. Cheezum, W. F. Walker and W. H. Guilford, 'Quantitative comparison of algorithms for tracking single fluorescent particles', *Biophys. J.* **81**, 2378 (2001) DOI: 10.1016/S0006-3495(01)75884-5 (pp. 12, 16, 24).
76. M. C. Jenkins and S. U. Egelhaaf, 'Confocal microscopy of colloidal particles: towards reliable, optimum coordinates', *Adv. Colloid Interfac.* **136**, 65 (2008) DOI: 10.1016/j.cis.2007.07.006 (pp. 12, 13, 17, 25, 26).
77. A. van Blaaderen and P. Wiltzius, 'Real-space structure of colloidal hard-sphere glasses', *Science* **270**, 1177 (1995) DOI: 10.1126/science.270.5239.1177 (p. 12).

-
78. R. Besseling, L. Isa, E. R. Weeks and W. C. K. Poon, 'Quantitative imaging of colloidal flows', *Adv. Colloid Interfac.* **146**, 1 (2009) doi: 10.1016/j.cis.2008.09.008 (p. 12).
 79. A. Sergé, N. Bertaux, H. Rigneault and D. Marguet, 'Dynamic multiple-target tracing to probe spatiotemporal cartography of cell membranes', *Nat. Methods* **5**, 687 (2008) doi: 10.1038/nmeth.1233 (p. 12).
 80. K. Jaqaman, D. Loerke, M. Mettlen, H. Kuwata, S. Grinstein, S. L. Schmid and G. Danuser, 'Robust single-particle tracking in live-cell time-lapse sequences', *Nat. Methods* **5**, 695 (2008) doi: 10.1038/nmeth.1237 (p. 12).
 81. K. Althoff, J. Degerman and T. Gustavsson, 'Combined segmentation and tracking of neural stem-cells', *Lect. Notes Comput. Sc.* **3540**, 282 (2005) doi: 10.1007/11499145_30 (p. 13).
 82. C. Tang and E. Bengtsson, 'Segmentation and tracking of neural stem cell', *Lect. Notes Comput. Sc.* **3645**, 851 (2005) doi: 10.1007/11538356_88 (p. 13).
 83. J. Baumgartl, J. L. Arauz-Lara and C. Bechinger, 'Like-charge attraction in confinement: myth or truth?', *Soft Matter* **2**, 631 (2006) doi: 10.1039/B603052A (pp. 13, 21).
 84. M. P. Gordon, T. Ha and P. R. Selvin, 'Single-molecule high-resolution imaging with photobleaching', *P. Natl. Acad. Sci. USA* **101**, 6462 (2004) doi: 10.1073/pnas.0401638101 (pp. 13, 16).
 85. X. Qu, D. Wu, L. Mets and N. F. Scherer, 'Nanometer-localized multiple single-molecule fluorescence microscopy', *P. Natl. Acad. Sci. USA* **101**, 11298 (2004) doi: 10.1073/pnas.0402155101 (pp. 13, 16).
 86. D. B. Allan, T. A. Caswell, N. C. Keim and C. van der Wel, 'Trackpy v0.3.1', Zenodo **55143** (2016) doi: 10.5281/zenodo.55143 (pp. 13, 14, 16, 19, 56, 63, 86).
 87. S. Maneewongvatana and D. M. Mount, 'It's okay to be skinny, if your friends are fat', *Proc. 4th Ann. W. Comput. Geometry* **2** (1999) (pp. 14, 17).
 88. D. Kraft, *A software package for sequential quadratic programming*, tech. rep. (DLR German Aerospace Center, DFVLR-FB 88-28, 1988) (p. 17).
 89. E. Jones, T. Oliphant, P. Peterson et al., *SciPy: Open source scientific tools for Python*, 2001 (p. 17).
 90. T. H. Besseling, J. Jose and A. van Blaaderen, 'Methods to calibrate and scale axial distances in confocal microscopy as a function of refractive index', *J. Microsc.* **257**, 142 (2015) doi: 10.1111/jmi.12194 (p. 19).
 91. D. J. Kraft, R. Wittkowski, B. Ten Hagen, K. V. Edmond, D. J. Pine and H. Löwen, 'Brownian motion and the hydrodynamic friction tensor for colloidal particles of complex shape', *Phys. Rev. E* **88**, 050301 (2013) doi: 10.1103/PhysRevE.88.050301 (pp. 19, 26).

92. A. Ramírez-Saito, C. Bechinger and J. L. Arauz-Lara, 'Optical microscopy measurement of pair correlation functions', *Phys. Rev. E* **74**, 030401 (2006) DOI: 10.1103/PhysRevE.74.030401 (p. 21).
93. J. C. Crocker, J. A. Matteo, A. D. Dinsmore and A. G. Yodh, 'Entropic attraction and repulsion in binary colloids probed with a line optical tweezer', *Phys. Rev. Lett.* **82**, 4352 (1999) DOI: 10.1103/PhysRevLett.82.4352 (p. 25).
94. C. Zhang, G. Brügger and F. Scheffold, 'Tracking of colloids close to contact', *Opt. Express* **23**, 22579 (2015) DOI: 10.1364/OE.23.022579 (p. 25).
95. P. R. Bevington and D. K. Robinson, *Data reduction and error analysis for the physical sciences*, 3rd (McGraw-Hill Higher Education, 2003), ISBN: 0-07-247227-8 (p. 26).
96. A. V. Abraham, S. Ram, J. Chao, E. S. Ward and R. J. Ober, 'Quantitative study of single molecule location estimation techniques', *Opt. Express* **17**, 23352 (2009) DOI: 10.1364/OE.17.023352 (p. 26).
97. J. Fung and V. N. Manoharan, 'Holographic measurements of anisotropic three-dimensional diffusion of colloidal clusters', *Phys. Rev. E* **88**, 020302 (2013) DOI: 10.1103/PhysRevE.88.020302 (p. 27).
98. G. M. Kepler and S. Fraden, 'Attractive potential between confined colloids at low ionic strength', *Phys. Rev. Lett.* **73**, 356 (1994) DOI: 10.1103/PhysRevLett.73.356 (pp. 32, 33, 35).
99. J. C. Crocker and D. G. Grier, 'Microscopic measurement of the pair interaction potential of charge-stabilized colloid', *Phys. Rev. Lett.* **73**, 352 (1994) DOI: 10.1103/PhysRevLett.73.352 (pp. 32, 36, 40, 44).
100. S. H. Behrens and D. G. Grier, 'Pair interaction of charged colloidal spheres near a charged wall', *Phys. Rev. E* **64**, 050401 (2001) DOI: 10.1103/PhysRevE.64.050401 (pp. 32, 35).
101. B. J. Park and E. M. Furst, 'Attractive interactions between colloids at the oil-water interface', *Soft Matter* **7**, 7676 (2011) DOI: 10.1039/c1sm00005e (p. 32).
102. N. Hoze, D. Nair, E. Hosity, C. Sieben, S. Manley, A. Herrmann, J.-B. Sibarita, D. Choquet and D. Holcman, 'Heterogeneity of AMPA receptor trafficking and molecular interactions revealed by superresolution analysis of live cell imaging', *P. Natl. Acad. Sci. USA* **109**, 17052 (2012) DOI: 10.1073/pnas.1204589109 (p. 32).
103. S. K. Sainis, V. Germain and E. R. Dufresne, 'Statistics of particle trajectories at short time intervals reveal fN-scale colloidal forces', *Phys. Rev. Lett.* **99**, 018303 (2007) DOI: 10.1103/PhysRevLett.99.018303 (pp. 32, 36, 38, 40).
104. R. Sarfati and E. R. Dufresne, 'Long-range attraction of particles adhered to lipid vesicles', *Phys. Rev. E* **94**, 012604 (2016) DOI: 10.1103/PhysRevE.94.012604 (pp. 32, 38, 52, 78, 84, 97).

-
105. I. C. Jenkins, J. C. Crocker and T. Sinno, 'Interaction potentials from arbitrary multi-particle trajectory data', *Soft Matter* **11**, 6948 (2015) DOI: 10.1039/c5sm01233c (p. 35).
 106. H. Risken, *The Fokker-Planck Equation*, 2nd (Springer, 1996), ISBN: 978-3-540-61530-9, DOI: 10.1007/978-3-642-61544-3 (pp. 37, 39, 43, 48).
 107. S. M. Carroll, *Spacetime and geometry: an introduction to general relativity* (Addison Wesley, 2004), ISBN: 0-8053-8732-3 (pp. 44, 48).
 108. S. M. Kay, *Fundamentals of statistical signal processing: estimation theory* (Prentice Hall PTR, 1993), ISBN: 978-0133457117 (p. 46).
 109. Y. Nagasaki, H. Kobayashi, Y. Katsuyama, T. Jomura and T. Sakura, 'Enhanced immunoresponse of antibody/mixed-PEG co-immobilized surface construction of high-performance immunomagnetic ELISA system', *J. Colloid Interf. Sci.* **309**, 524 (2007) DOI: 10.1016/j.jcis.2006.12.079 (p. 52).
 110. M. Kamimura, D. Miyamoto, Y. Saito, K. Soga and Y. Nagasaki, 'Design of poly(ethylene glycol)/streptavidin coimmobilized upconversion nanophosphors and their application to fluorescence biolabeling', *Langmuir* **24**, 8864 (2008) DOI: 10.1021/la801056c (p. 52).
 111. A. Vonarbourg, C. Passirani, P. Saulnier and J. P. Benoit, 'Parameters influencing the stealthiness of colloidal drug delivery systems', *Biomaterials* **27**, 4356 (2006) DOI: 10.1016/j.biomaterials.2006.03.039 (pp. 52, 58, 84, 88).
 112. A. E. Nel, L. Mädler, D. Velegol, T. Xia, E. M. V. Hoek, P. Somasundaran, F. Klaessig, V. Castranova and M. Thompson, 'Understanding biophysicochemical interactions at the nano-bio interface', *Nat. Mater.* **8**, 543 (2009) DOI: 10.1038/nmat2442 (pp. 52, 84, 88).
 113. A. Jain and K. Cheng, 'The principles and applications of avidin-based nanoparticles in drug delivery and diagnosis', *J. Control. Release* **245**, 27 (2016) DOI: 10.1016/j.jconrel.2016.11.016 (p. 52).
 114. J. Dai and M. P. Sheetz, 'Mechanical properties of neuronal growth cone membranes studied by tether formation with laser optical tweezers', *Biophys. J.* **68**, 988 (1995) DOI: 10.1016/S0006-3495(95)80274-2 (p. 52).
 115. G. Koster, A. Cacciuto, I. Derényi, D. Frenkel and M. Dogterom, 'Force barriers for membrane tube formation', *Phys. Rev. Lett.* **94**, 068101 (2005) DOI: 10.1103/PhysRevLett.94.068101 (pp. 52, 96, 97).
 116. R. Dimova, C. Dietrich, A. Hadjiisky, K. Danov and B. Pouligny, 'Falling ball viscosimetry of giant vesicle membranes: finite-size effects', *Eur. Phys. J. B* **12**, 589 (1999) DOI: 10.1007/s100510051042 (pp. 52, 90, 97).
 117. T. T. Hormel, S. Q. Kurihara, M. K. Brennan, M. C. Wozniak and R. Parthasarathy, 'Measuring lipid membrane viscosity using rotational and translational probe diffusion', *Phys. Rev. Lett.* **112**, 188101 (2014) DOI: 10.1103/PhysRevLett.112.188101 (pp. 52, 90, 97).

118. N. Li, N. Sharifi-Mood, F. Tu, D. Lee, R. Radhakrishnan, T. Baumgart and K. J. Stebe, 'Curvature-driven migration of colloids on tense lipid bilayers', *Langmuir* **33**, 600 (2016) doi: 10.1021/acs.langmuir.6b03406 (p. 52).
119. S. A. J. van der Meulen and M. E. Leunissen, 'Solid colloids with surface-mobile DNA linkers', *J. Am. Chem. Soc.* **135**, 15129 (2013) doi: 10.1021/ja406226b (pp. 52, 130).
120. S. Angioletti-Uberti, P. Varilly, B. M. Mognetti and D. Frenkel, 'Mobile linkers on DNA-coated colloids: valency without patches', *Phys. Rev. Lett.* **113**, 128303 (2014) doi: 10.1103/PhysRevLett.113.128303 (p. 52).
121. S. A. Lauer and J. P. Nolan, 'Development and characterization of Ni-NTA-bearing microspheres', *Cytometry* **48**, 136 (2002) doi: 10.1002/cyto.10124 (p. 52).
122. U. Wattendorf and H. P. Merkle, 'PEGylation as a tool for the biomedical engineering of surface modified microparticles', *J. Pharm. Sci.* **97**, 4655 (2008) doi: 10.1002/jps.21350 (pp. 52, 58).
123. R. J. Macfarlane, B. Lee, M. R. Jones, N. Harris, G. C. Schatz and C. A. Mirkin, 'Nanoparticle superlattice engineering with DNA', *Science* **334**, 204 (2011) doi: 10.1126/science.1210493 (p. 52).
124. G. Wu, J. Majewski, C. Ege, K. Kjaer, M. J. Weygand and K. Y. C. Lee, 'Lipid corralling and poloxamer squeeze-out in membranes', *Phys. Rev. Lett.* **93**, 028101 (2004) doi: 10.1103/PhysRevLett.93.028101 (p. 52).
125. T. Demina, I. Grozdova, O. Krylova, A. Zhirnov, V. Istratov, H. Frey, H. Kautz and N. Melik-Nubarov, 'Relationship between the structure of amphiphilic copolymers and their ability to disturb lipid bilayers', *Biochemistry* **44**, 4042 (2005) doi: 10.1021/bi048373q (p. 52).
126. J.-Y. Wang, J. Chin, J. D. Marks and K. Y. C. Lee, 'Effects of PEO-PPO-PEO triblock copolymers on phospholipid membrane integrity under osmotic stress', *Langmuir* **26**, 12953 (2010) doi: 10.1021/la101841a (p. 52).
127. S. Nawaz, M. Redhead, G. Mantovani, C. Alexander, C. Bosquillon and P. Carbone, 'Interactions of PEO-PPO-PEO block copolymers with lipid membranes: a computational and experimental study linking membrane lysis with polymer structure', *Soft Matter* **8**, 6744 (2012) doi: 10.1039/c2sm25327e (p. 52).
128. F. Rusmini, Z. Zhong and J. Feijen, 'Protein immobilization strategies for protein biochips', *Biomacromolecules* **8**, 1775 (2007) doi: 10.1021/bm061197b (pp. 52, 60).
129. B. R. Coad, T. Scholz, K. Vasilev, J. D. Hayball, R. D. Short and H. J. Griesser, 'Functionality of proteins bound to plasma polymer surfaces', *ACS Appl. Mater. Interfaces* **4**, 2455 (2012) doi: 10.1021/am300128n (pp. 52, 60).
130. S. C. B. Gopinath, T.-H. Tang, M. Citartan, Y. Chen and T. LakshmiPriya, 'Current aspects in immunosensors', *Biosens. Bioelectron.* **57**, 292 (2014) doi: 10.1016/j.bios.2014.02.029 (p. 52).

-
131. F. Meng, G. H. M. Engbers and J. Feijen, 'Polyethylene glycol-grafted polystyrene particles', *J. Biomed. Mater. Res. A* **70A**, 49 (2004) DOI: 10.1002/jbm.a.30056 (pp. 52, 54, 58, 59, 70, 85).
 132. J. Appel, S. Akerboom, R. G. Fokink and J. Sprakel, 'Facile one-step synthesis of monodisperse micron-sized latex particles with highly carboxylated surfaces', *Macromol. Rapid Comm.* **34**, 1284 (2013) DOI: 10.1002/marc.201300422 (pp. 53, 54, 70, 85).
 133. P. Cuatrecasas and I. Parikh, 'Absorbents for affinity chromatography. Use of N-hydroxysuccinimide esters of agarose', *Biochemistry* **11**, 2291 (1972) DOI: 10.1021/bi00762a013 (p. 55).
 134. G. Kada, H. Falk and H. J. Gruber, 'Accurate measurement of avidin and streptavidin in crude biofluids with a new, optimized biotin-fluorescein conjugate', *Biochim. Biophys. Acta* **1427**, 33 (1999) DOI: 10.1016/S0304-4165(98)00178-0 (p. 55).
 135. M. I. Angelova and D. S. Dimitrov, 'Liposome electroformation', *Faraday Discuss. Chem. Soc.* **81**, 303 (1986) DOI: 10.1039/DC9868100303 (pp. 56, 70, 85).
 136. P. G. de Gennes, 'Polymers at an interface; a simplified view', *Adv. Colloid Interfac.* **27**, 189 (1987) DOI: 10.1016/0001-8686(87)85003-0 (pp. 58, 130).
 137. S. Upadhyayula et al., 'Coatings of polyethylene glycol for suppressing adhesion between solid microspheres and flat surfaces', *Langmuir* **28**, 5059 (2012) DOI: 10.1021/la300545v (pp. 58, 76).
 138. R. Gref, M. Lück, P. Quellec, M. Marchand, E. Dellacherie, S. Harnisch, T. Blunk and R. H. Müller, "'Stealth' corona-core nanoparticles surface modified by polyethylene glycol (PEG): influences of the corona (PEG chain length and surface density) and of the core composition on phagocytic uptake and plasma protein adsorption', *Coll. Surface B* **18**, 301 (2000) DOI: 10.1016/S0927-7765(99)00156-3 (p. 59).
 139. B. Pelaz, P. del Pino, P. Maffre, R. Hartmann, M. Gallego, S. Rivera-Fernández, J. M. de la Fuente, G. U. Nienhaus and W. J. Parak, 'Surface functionalization of nanoparticles with polyethylene glycol: effects on protein adsorption and cellular uptake', *ACS Nano* **9**, 6996 (2015) DOI: 10.1021/acsnano.5b01326 (p. 59).
 140. V. T. Moy, E.-L. Florin and H. E. Gaub, 'Intermolecular forces and energies between ligands and receptors', *Science* **266**, 257 (1994) DOI: 10.1126/science.7939660 (pp. 60, 73, 75, 88).
 141. F. A. de Wolf and G. M. Brett, 'Ligand-binding proteins: their potential for application in systems for controlled delivery and uptake of ligands', *Pharmacol. Rev.* **52**, 207, ISSN: 0031-6997 (2000) (p. 60).
 142. K. E. Sapsford, W. R. Algar, L. Berti, K. B. Gemmill, B. J. Casey, E. Oh, M. H. Stewart and I. L. Medintz, 'Functionalizing nanoparticles with biological molecules: developing chemistries that facilitate nanotechnology', *Chem. Rev.* **113**, 1904 (2013) DOI: 10.1021/cr300143v (pp. 60, 128).

143. S.-C. Huang, H. Swerdlow and K. D. Caldwell, 'Binding the biotinylated DNA to streptavidin-coated polystyrene latex', *Anal. Biochem.* **222**, 441 (1994) doi: 10.1006/abio.1994.1514 (p. 60).
144. J. J. Gray and R. T. Bonnecaze, 'Adsorption of colloidal particles by Brownian dynamics simulation: kinetics and surface structures', *J. Chem. Phys.* **114**, 1366 (2001) doi: 10.1063/1.1319317 (p. 63).
145. C. van der Wel, 'Circletracking v1.0', Zenodo **47216** (2016) doi: 10.5281/zenodo.47216 (pp. 63, 72, 86).
146. M. Saleemuddin and Q. Husain, 'Concanavalin A: a useful ligand for glycoenzyme immobilization—a review', *Enzyme Microb. Tech.* **13**, 290 (1991) doi: 10.1016/0141-0229(91)90146-2 (p. 65).
147. D. R. Phillips, 'Effect of trypsin on the exposed polypeptides and glycoproteins in the human platelet membrane', *Biochemistry* **11**, 4582 (1972) doi: 10.1021/bi00774a025 (p. 65).
148. D. Freche, U. Pannasch, N. Rouach and D. Holcman, 'Synapse geometry and receptor dynamics modulate synaptic strength', *Plos One* **6**, e25122 (2011) doi: 10.1371/journal.pone.0025122 (p. 68).
149. C. M. Pfefferkorn, Z. Jiang and J. C. Lee, 'Biophysics of α -synuclein membrane interactions', *Biochim. Biophys. Acta* **1818**, 162 (2012) doi: 10.1016/j.bbamem.2011.07.032 (p. 68).
150. K. S. Kim, J. Neu and G. Oster, 'Curvature-mediated interactions between membrane proteins', *Biophys. J.* **75**, 2274 (1998) doi: 10.1016/S0006-3495(98)77672-6 (p. 68).
151. M. M. Müller, M. Deserno and J. Guven, 'Interface-mediated interactions between particles: a geometrical approach', *Phys. Rev. E* **72**, 061407 (2005) doi: 10.1103/PhysRevE.72.061407 (pp. 68, 78).
152. C. Yolcu, R. C. Haussman and M. Deserno, 'The effective field theory approach towards membrane-mediated interactions between particles.', *Adv. Colloid Interfac.* **208**, 89 (2014) doi: 10.1016/j.cis.2014.02.017 (pp. 68, 91).
153. J. C. Pàmies and A. Cacciuto, 'Reshaping elastic nanotubes via self-assembly of surface-adhesive nanoparticles', *Phys. Rev. Lett.* **106**, 045702 (2011) doi: 10.1103/PhysRevLett.106.045702 (p. 68).
154. A. Šarić and A. Cacciuto, 'Self-assembly of nanoparticles adsorbed on fluid and elastic membranes', *Soft Matter* **9**, 6677 (2013) doi: 10.1039/c3sm50188d (pp. 68, 78).
155. M. Simunovic, A. Srivastava and G. A. Voth, 'Linear aggregation of proteins on the membrane as a prelude to membrane remodeling', *P. Natl. Acad. Sci. USA* **110**, 20396 (2013) doi: 10.1073/pnas.1309819110 (p. 68).
156. A. Vahid and T. Idema, 'Pointlike inclusion interactions in tubular membranes', *Phys. Rev. Lett.* **117**, 138102 (2016) doi: 10.1103/PhysRevLett.117.138102 (p. 68).

-
157. S. Semrau, T. Idema, T. Schmidt and C. Storm, 'Membrane-mediated interactions measured using membrane domains', *Biophys. J.* **96**, 4906 (2009) DOI: 10.1016/j.bpj.2009.03.050 (p. 68).
 158. J. C. Loudet, A. M. Alsayed, J. Zhang and A. G. Yodh, 'Capillary interactions between anisotropic colloidal particles', *Phys. Rev. Lett.* **94**, 018301 (2005) DOI: 10.1103/PhysRevLett.94.018301 (pp. 69, 78).
 159. M. Cavallaro, Jr., L. Botto, E. P. Lewandowski, M. Wang and K. J. Stebe, 'Curvature-driven capillary migration and assembly of rod-like particles', *P. Natl. Acad. Sci. USA* **108**, 20923 (2011) DOI: 10.1073/pnas.1116344108 (pp. 69, 78).
 160. D. Vella and L. Mahadevan, 'The "Cheerios effect"', *Am. J. Phys.* **73**, 817 (2005) DOI: 10.1119/1.1898523 (p. 69).
 161. Y. Tamba, H. Terashima and M. Yamazaki, 'A membrane filtering method for the purification of giant unilamellar vesicles', *Chem. Phys. Lipids* **164**, 351 (2011) DOI: 10.1016/j.chemphyslip.2011.04.003 (pp. 70, 77).
 162. A. W. C. Lau, A. Prasad and Z. Dogic, 'Condensation of isolated semi-flexible filaments driven by depletion interactions', *Europhys. Lett.* **87**, 48006 (2009) DOI: 10.1209/0295-5075/87/48006 (pp. 70, 75).
 163. D. B. Allan, T. A. Caswell, N. C. Keim and C. van der Wel, 'Trackpy v0.3.0', *Zenodo* **34028** (2015) DOI: 10.5281/zenodo.34028 (p. 72).
 164. A. H. Bahrami, M. Raatz, J. Agudo-Canalejo, R. Michel, E. M. Curtis, C. K. Hall, M. Gradzielski, R. Lipowsky and T. R. Weigl, 'Wrapping of nanoparticles by membranes', *Adv. Colloid Interfac.* **208**, 214 (2014) DOI: 10.1016/j.cis.2014.02.012 (p. 74).
 165. J. Pécéréaux, H.-G. Döbereiner, J. Prost, J.-F. Joanny and P. Bassereau, 'Refined contour analysis of giant unilamellar vesicles', *Eur. Phys. J. E* **13**, 277 (2004) DOI: 10.1140/epje/i2004-10001-9 (pp. 75, 86, 87).
 166. W. Rawicz, K. C. Olbrich, T. McIntosh, D. Needham and E. Evans, 'Effect of chain length and unsaturation on elasticity of lipid bilayers', *Biophys. J.* **79**, 328 (2000) DOI: 10.1016/S0006-3495(00)76295-3 (pp. 75, 79, 96).
 167. B. P. Binks and T. S. Horozov, *Colloidal particles at liquid interfaces* (Cambridge University Press, 2008), ISBN: 978-0-521-07131-4 (p. 78).
 168. N. Sharifi-mood, I. B. Liu and K. J. Stebe, 'Curvature capillary migration of microspheres', *Soft Matter* **11**, 6768 (2015) DOI: 10.1039/C5SM00310E (p. 78).
 169. H. K. Lin, R. Zandi, U. Mohideen and L. P. Pryadko, 'Fluctuation-induced forces between inclusions in a fluid membrane under tension', *Phys. Rev. Lett.* **107**, 228104 (2011) DOI: 10.1103/PhysRevLett.107.228104 (p. 78).
 170. A. Callan-Jones, B. Sorre and P. Bassereau, 'Curvature-driven lipid sorting in biomembranes', *Cold Spring Harb. Persp. Biol.* **3**, a004648 (2011) DOI: 10.1101/cshperspect.a004648 (p. 81).

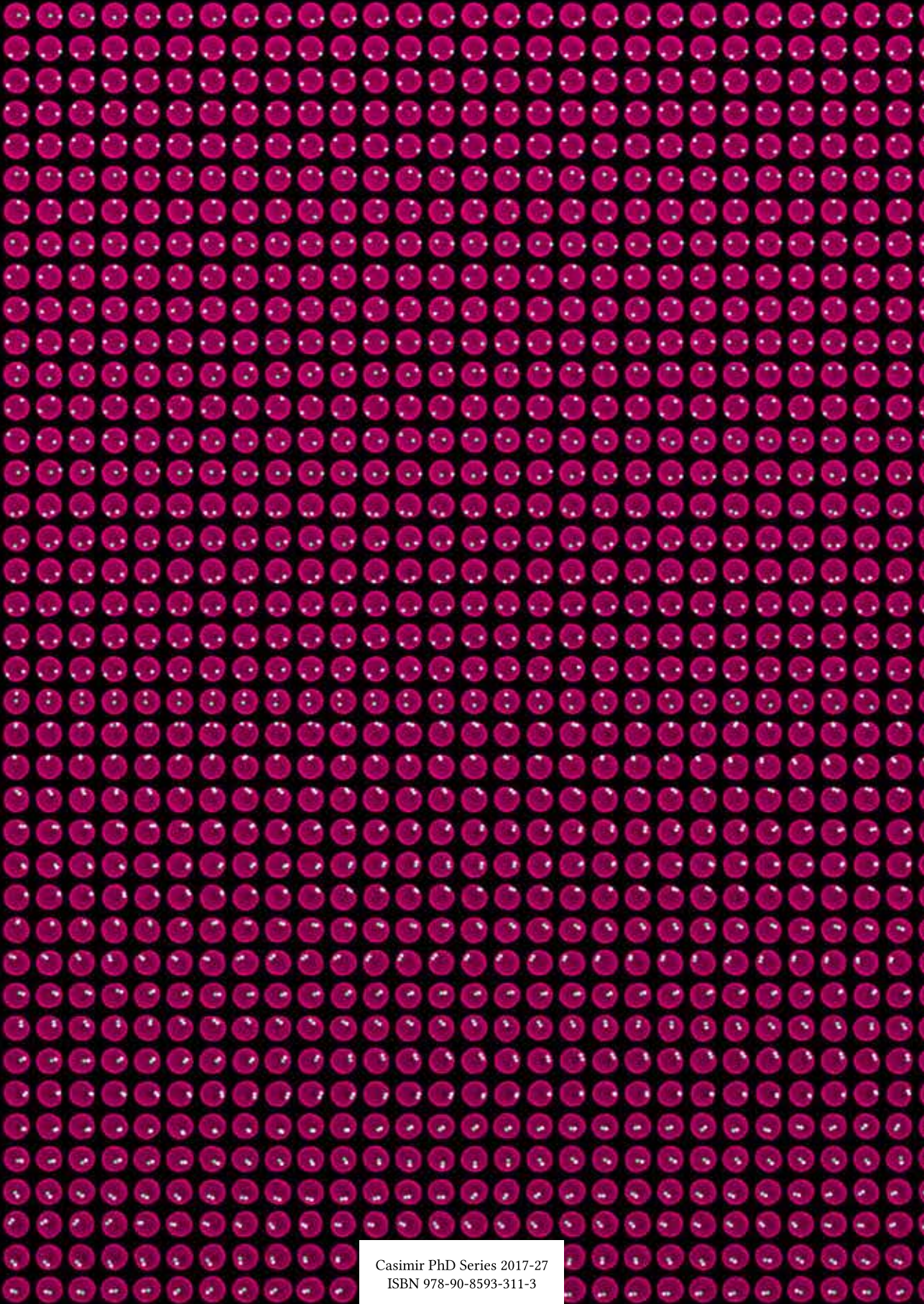
171. F. Tang, L. Li and D. Chen, 'Mesoporous silica nanoparticles: Synthesis, biocompatibility and drug delivery', *Adv. Mater.* **24**, 1504 (2012) DOI: 10.1002/adma.201104763 (p. 84).
172. M. Mahmoudi et al., 'Interaction of stable colloidal nanoparticles with cellular membranes', *Biotechnol. Adv.* **32**, 679 (2014) DOI: 10.1016/j.biotechadv.2013.11.012 (pp. 84, 88).
173. J. Rejman, V. Oberle, I. S. Zuhorn and D. Hoekstra, 'Size-dependent internalization of particles via the pathways of clathrin- and caveolae-mediated endocytosis', *Biochem. J.* **377**, 159 (2004) DOI: 10.1042/bj20031253 (pp. 84, 95).
174. S. Paquay and R. Kusters, 'A method for molecular dynamics on curved surfaces', *Biophys. J.* **110**, 1226 (2016) DOI: 10.1016/j.bpj.2016.02.017 (p. 87).
175. H. Qian, M. P. Sheetz and E. L. Elson, 'Single particle tracking. Analysis of diffusion and flow in two-dimensional systems', *Biophys. J.* **60**, 910 (1991) DOI: 10.1016/S0006-3495(91)82125-7 (p. 87).
176. D. Ernst and J. Köhler, 'Measuring a diffusion coefficient by single-particle tracking: statistical analysis of experimental mean squared displacement curves', *Phys. Chem. Chem. Phys.* **15**, 845 (2013) DOI: 10.1039/c2cp43433d (p. 87).
177. R. Lipowsky, H.-G. Döbereiner, C. Hiergeist and V. Indrani, 'Membrane curvature induced by polymers and colloids', *Physica A* **249**, 536 (1998) DOI: 10.1016/S0378-4371(97)00513-X (p. 88).
178. R. Lipowsky and H.-G. Döbereiner, 'Vesicles in contact with nanoparticles and colloids', *Europhys. Lett.* **43**, 219 (1998) DOI: 10.1209/epl/i1998-00343-4 (p. 88).
179. M. Raatz, R. Lipowsky and T. R. Weigl, 'Cooperative wrapping of nanoparticles by membrane tubes', *Soft Matter* **10**, 3570 (2014) DOI: 10.1039/c3sm52498a (pp. 88, 93).
180. J. Agudo-Canalejo and R. Lipowsky, 'Critical particle sizes for the engulfment of nanoparticles by membranes and vesicles with bilayer asymmetry', *ACS Nano* **9**, 3704 (2015) DOI: 10.1021/acsnano.5b01285 (p. 88).
181. P. G. Saffman and M. Delbrück, 'Brownian motion in biological membranes', *P. Natl. Acad. Sci. USA* **72**, 3111 (1975) (p. 90).
182. B. D. Hughes, B. A. Pailthorpe and L. R. White, 'The translational and rotational drag on a cylinder moving in a membrane', *J. Fluid Mech.* **110**, 349 (1981) DOI: 10.1017/S0022112081000785 (p. 90).
183. E. P. Petrov and P. Schwille, 'Translational diffusion in lipid membranes beyond the Saffman-Delbrück approximation', *Biophys. J.* **94**, L41 (2008) DOI: 10.1529/biophysj.107.126565 (p. 90).
184. K. Danov, R. Aust, F. Durst and U. Lange, 'Influence of the surface viscosity on the hydrodynamic resistance and surface diffusivity of a large Brownian particle', *J. Colloid Interf. Sci.* **175**, 36 (1995) DOI: 10.1006/jcis.1995.1426 (pp. 90, 97).

-
185. C. Herold, P. Schwille and E. P. Petrov, 'DNA condensation at freestanding cationic lipid bilayers', *Phys. Rev. Lett.* **104**, 148102 (2010) doi: 10.1103/PhysRevLett.104.148102 (pp. 90, 97).
 186. A. H. Bahrami, R. Lipowsky and T. R. Weikl, 'Tubulation and aggregation of spherical nanoparticles adsorbed on vesicles', *Phys. Rev. Lett.* **109**, 188102 (2012) doi: 10.1103/PhysRevLett.109.188102 (pp. 91, 93).
 187. A. Šarić and A. Cacciuto, 'Soft elastic surfaces as a platform for particle self-assembly', *Soft Matter* **7**, 8324 (2011) doi: 10.1039/c1sm05773a (pp. 92, 95).
 188. A. Gunnarsson, L. Dexlin, P. Wallin, S. Svedhem, P. Jönsson, C. Wingren and F. Höök, 'Kinetics of ligand binding to membrane receptors from equilibrium fluctuation analysis of single binding events', *J. Am. Chem. Soc.* **133**, 14852 (2011) doi: 10.1021/ja2047039 (p. 95).
 189. M. Terasaki, L. B. Chen and K. Fujiwara, 'Microtubules and the endoplasmic reticulum are highly interdependent structures', *J. Cell Biol.* **103**, 1557 (1986) doi: 10.1083/jcb.103.4.1557 (p. 96).
 190. C. R. Hopkins, A. Gibson, M. Shipman and K. Miller, 'Movement of internalized ligand-receptor complexes along a continuous endosomal reticulum', *Nature* **346**, 335 (1990) doi: 10.1038/346335a0 (p. 96).
 191. D. Heinrich, M. Ecke, M. Jasnin, U. Engel and G. Gerisch, 'Reversible membrane pearling in live cells upon destruction of the actin cortex', *Biophys. J.* **106**, 1079 (2014) doi: 10.1016/j.bpj.2013.12.054 (p. 96).
 192. I. Derényi, F. Jülicher and J. Prost, 'Formation and interaction of membrane tubes', *Phys. Rev. Lett.* **88**, 238101 (2002) doi: 10.1103/PhysRevLett.88.238101 (p. 96).
 193. P. M. Shaklee, T. Idema, G. Koster, C. Storm, T. Schmidt and M. Dogterom, 'Bidirectional membrane tube dynamics driven by nonprocessive motors', *P. Natl. Acad. Sci. USA* **105**, 7993 (2008) doi: 10.1073/pnas.0709677105 (p. 96).
 194. Y. Li, R. Lipowsky and R. Dimova, 'Membrane nanotubes induced by aqueous phase separation and stabilized by spontaneous curvature', *P. Natl. Acad. Sci. USA* **108**, 4731 (2011) doi: 10.1073/pnas.1015892108 (p. 97).
 195. R. Lipowsky, 'Spontaneous tubulation of membranes and vesicles reveals membrane tension generated by spontaneous curvature', *Faraday Discuss.* **161**, 305 (2013) doi: 10.1039/c2fd20105d (p. 97).
 196. H.-G. Döbereiner, O. Selchow and R. Lipowsky, 'Spontaneous curvature of fluid vesicles induced by trans-bilayer sugar asymmetry', *Eur. Biophys. J.* **28**, 174 (1999) doi: 10.1007/s002490050197 (p. 97).
 197. K. D. Danov, R. Dimova and B. Pouligny, 'Viscous drag of a solid sphere straddling a spherical or flat surface', *Phys. Fluids* **12**, 2711 (2000) doi: 10.1063/1.1289692 (p. 97).
 198. A. van Blaaderen, R. Ruel and P. Wiltzius, 'Template-directed colloidal crystallization', *Nature* **385**, 321 (1997) doi: 10.1038/385321a0 (p. 102).

199. P. N. Pusey, 'The effect of polydispersity on the crystallization of hard spherical colloids', *J. Physique* **48**, 709 (1987) DOI: 10.1051/jphys:01987004805070900 (p. 102).
200. S. Sacanna, M. Korpics, K. Rodriguez, L. Colón-Meléndez, S.-H. Kim, D. J. Pine and G.-R. Yi, 'Shaping colloids for self-assembly', *Nat. Commun.* **4**, 1688 (2013) DOI: 10.1038/ncomms2694 (pp. 102, 103, 115).
201. W. Stöber, A. Fink and E. Bohn, 'Controlled growth of monodisperse silica spheres in the micron size range', *J. Colloid Interf. Sci.* **26**, 62 (1968) DOI: 10.1016/0021-9797(68)90272-5 (p. 102).
202. J. W. Goodwin, J. Hearn, C. C. Ho and R. H. Ottewill, 'Studies on the preparation and characterisation of monodisperse polystyrene latices, III. Preparation without added surface active agents', *Colloid Polym. Sci.* **252**, 464 (1974) DOI: 10.1007/BF01554752 (p. 102).
203. L. Antl, J. W. Goodwin, R. D. Hill, R. H. Ottewill, S. M. Owens, S. Papworth and J. A. Waters, 'The preparation of poly(methyl methacrylate) latices in non-aqueous media', *Colloids Surf.* **17**, 67 (1986) DOI: 10.1016/0166-6622(86)80187-1 (p. 102).
204. Y. Liu, K. V. Edmond, A. Curran, C. Bryant, B. Peng, D. G. A. L. Aarts, S. Sacanna and R. P. A. Dullens, 'Core-shell particles for simultaneous 3D imaging and optical tweezing in dense colloidal materials', *Adv. Mater.* **28**, 8001 (2016) DOI: 10.1002/adma.201602137 (pp. 102, 103, 115).
205. T. M. Obey and B. Vincent, 'Novel monodisperse "silicone oil"/water emulsions', *J. Colloid Interf. Sci.* **163**, 454 (1994) DOI: 10.1006/jcis.1994.1124 (pp. 103, 104, 110).
206. S. Sacanna, W. K. Kegel and A. P. Philipse, 'Thermodynamically stable pickering emulsions', *Phys. Rev. Lett.* **98**, 158301 (2007) DOI: 10.1103/PhysRevLett.98.158301 (pp. 103, 113).
207. S. Sacanna, W. K. Kegel and A. P. Philipse, 'Spontaneous oil-in-water emulsification induced by charge-stabilized dispersions of various inorganic colloids', *Langmuir* **23**, 10486 (2007) DOI: 10.1021/la701311b (pp. 103, 110, 112, 113).
208. S. Sacanna and A. P. Philipse, 'A generic single-step synthesis of monodisperse core/shell colloids based on spontaneous Pickering emulsification', *Adv. Mater.* **19**, 3824 (2007) DOI: 10.1002/adma.200700865 (pp. 103, 113).
209. J. D. Miller, K.-P. Hoh and H. Ishida, 'Studies of the simulation of silane coupling agent structures on particulate fillers; the pH effect', *Polym. Compos.* **5**, 18 (1984) DOI: 10.1002/pc.750050106 (pp. 104, 110).
210. B. Arkles, J. R. Steinmetz, J. Zazyczny and P. Mehta, 'Factors contributing to the stability of alkoxy silanes in aqueous solution', *J. Adhes. Sci. Technol.* **6**, 193 (1992) DOI: 10.1163/156856192X00133 (pp. 104, 105).
211. K. Piana and U. Schubert, 'Catalyst influence on the molar mass distribution of hydrolyzed (3-glycidoxypropyl)trimethoxysilane and (3-methacryloxypropyl)trimethoxysilane', *Chem. Mater.* **6**, 1504 (1994) DOI: 10.1021/cm00045a006 (pp. 104, 110, 112, 113).

-
212. S. Altmann and J. Pfeiffer, 'The hydrolysis/condensation behaviour of methacryloyloxyalkylfunctional alkoxy silanes: structure-reactivity relations', *Monatsh. Chem.* **134**, 1081 (2003) DOI: 10.1007/s00706-003-0615-y (pp. 104, 110, 112).
213. M.-C. Brochier-Salon, P.-A. Bayle, M. Abdelmouleh, S. Boufi and M. N. Belgacem, 'Kinetics of hydrolysis and self condensation reactions of silanes by NMR spectroscopy', *Colloid Surf. A* **312**, 83 (2008) DOI: 10.1016/j.colsurfa.2007.06.028 (p. 104).
214. S. Sacanna, L. Rossi and A. P. Philipse, 'Oil-in-water emulsification induced by ellipsoidal hematite colloids: evidence for hydrolysis-mediated self-assembly', *Langmuir* **23**, 9974 (2007) DOI: 10.1021/la701427s (pp. 104, 105, 113).
215. J. Šefčík and A. V. McCormick, 'Thermochemistry of aqueous silicate solution precursors to ceramics', *AIChE J.* **43**, 2773 (1997) DOI: 10.1002/aic.690431324 (pp. 104, 110).
216. J. Šefčík, S. E. Rankin, S. J. Kirchner and A. V. McCormick, 'Esterification, condensation, and deprotonation equilibria of trimethylsilanol', *J. Non-Cryst. Solids* **258**, 187 (1999) DOI: 10.1016/S0022-3093(99)00418-4 (pp. 104, 110, 112, 113).
217. C. J. Morin, L. Geulin, A. Desbène and P. L. Desbène, 'Study of the acid hydrolysis of (3-methacryloxypropyl)trimethoxysilane by capillary electrophoresis-ion-trap mass spectrometry', *J. Chromatogr. A* **1032**, 327 (2004) DOI: 10.1016/j.chroma.2004.01.002 (pp. 105, 112).
218. D. J. Kraft, B. Luigjes, J. W. J. de Folter, A. P. Philipse and W. K. Kegel, 'Evolution of equilibrium Pickering emulsions—a matter of time scales', *J. Phys. Chem. B* **114**, 12257 (2010) DOI: 10.1021/jp104662g (pp. 105, 113).
219. S. Sacanna, W. T. M. Irvine, L. Rossi and D. J. Pine, 'Lock and key colloids through polymerization-induced buckling of monodisperse silicon oil droplets', *Soft Matter* **7**, 1631 (2011) DOI: 10.1039/C0SM01125H (p. 106).
220. A. van Blaaderen and A. Vrij, 'Synthesis and characterization of colloidal dispersions of fluorescent, monodisperse silica spheres', *Langmuir* **8**, 2921 (1992) DOI: 10.1021/la00048a013 (p. 107).
221. N. A. M. Verhaegh and A. van Blaaderen, 'Dispersions of rhodamine-labeled silica spheres: synthesis, characterization, and fluorescence confocal scanning laser microscopy', *Langmuir* **10**, 1427 (1994) DOI: 10.1021/la00017a019 (p. 107).
222. R. W. Verweij and C. van der Wel, 'semtracking: determining the size distribution of particles in SEM images', *Zenodo* **45575** (2016) DOI: 10.5281/zenodo.45575 (p. 107).
223. J. Zwanikken, K. Ioannidou, D. Kraft and R. van Roij, 'Reversible emulsification controlled by ionic surfactants and responsive nanoparticles', *Soft Matter* **7**, 11093 (2011) DOI: 10.1039/c1sm05779k (p. 113).

224. E. Sackmann, 'Supported membranes: scientific and practical applications', *Science* **271**, 43 (1996) DOI: 10.1126/science.271.5245.43 (p. 124).
225. R. P. Richter, R. Bérat and A. R. Brisson, 'Formation of solid-supported lipid bilayers: an integrated view', *Langmuir* **22**, 3497 (2006) DOI: 10.1021/la052687c (p. 124).
226. E. Castellana and P. S. Cremer, 'Solid supported lipid bilayers: from biophysical studies to sensor design', *Surf. Sci. Rep.* **61**, 429 (2006) DOI: 10.1016/j.surfrep.2006.06.001 (p. 124).
227. K. Ben M'Barek, D. Molino, S. Quignard, M.-A. Plamont, Y. Chen, P. Chavrier and J. Fattaccioli, 'Phagocytosis of immunoglobulin-coated emulsion droplets', *Biomaterials* **51**, 270 (2015) DOI: 10.1016/j.biomaterials.2015.02.030 (pp. 124, 128, 129, 134).
228. L.-L. Pontani, I. Jorjadze, V. Viasnoff and J. Brujic, 'Biomimetic emulsions reveal the effect of mechanical forces on cell-cell adhesion', *P. Natl. Acad. Sci. USA* **109**, 9839 (2012) DOI: 10.1073/pnas.1201499109 (p. 124).
229. S. Leptihn, O. K. Castell, B. Cronin, E.-H. Lee, L. C. M. Gross, D. P. Marshall, J. R. Thompson, M. Holden and M. I. Wallace, 'Constructing droplet interface bilayers from the contact of aqueous droplets in oil', *Nature Protocols* **8**, 1048 (2013) DOI: 10.1038/nprot.2013.061 (p. 124).
230. C. L. Phillips, E. Jankowski, B. J. Krishnatreya, K. V. Edmond, S. Sacanna, D. G. Grier, D. J. Pine and S. C. Glotzer, 'Digital colloids: Reconfigurable clusters as high information density elements', *Soft Matter* **10**, 7468 (2014) DOI: 10.1039/C4SM00796D (p. 124).
231. D. B. Miracle, W. S. Sanders and O. N. Senkov, 'The influence of efficient atomic packing on the constitution of metallic glasses', *Philos. Mag.* **83**, 2409 (2003) DOI: 10.1080/1478643031000098828 (pp. 124, 130).
232. N. B. Schade, M. C. Holmes-Cerfon, E. R. Chen, D. Aronzon, J. W. Collins, J. A. Fan, F. Capasso and V. N. Manoharan, 'Tetrahedral colloidal clusters from random parking of bidisperse spheres', *Phys. Rev. Lett.* **110**, 148303 (2013) DOI: 10.1103/PhysRevLett.110.148303 (pp. 124, 130).
233. D. Axelrod, D. E. Koppel, J. Schlessinger, E. Elson and W. W. Webb, 'Mobility measurement by analysis of fluorescence photobleaching recovery kinetics', *Biophys. J.* **16**, 1055 (1976) DOI: 10.1016/S0006-3495(76)85755-4 (p. 128).
234. D. Marsh, *Handbook of Lipid Bilayers*, second ed. (CRC Press, 2013), ISBN: 978-1-4200-8832-8 (p. 128).
235. M. E. Leunissen, R. Dreyfus, F. C. Cheong, D. G. Grier, R. Sha, N. C. Seeman and P. M. Chaikin, 'Switchable self-protected attractions in DNA-functionalized colloids', *Nat. Mater.* **8**, 590 (2009) DOI: 10.1038/nmat2471 (p. 128).



Casimir PhD Series 2017-27
ISBN 978-90-8593-311-3